Journal of
*Marine Science
and Engineering*

Special Issue Reprint

Wave Loads on Offshore Structure

Edited by
Piguang Wang and Kai Wei

mdpi.com/journal/jmse

MDPI

Wave Loads on Offshore Structure

Wave Loads on Offshore Structure

Guest Editors

Piguang Wang
Kai Wei

Basel • Beijing • Wuhan • Barcelona • Belgrade • Novi Sad • Cluj • Manchester

Guest Editors

Piguang Wang	Kai Wei
Faculty of Architecture, Civil and Transportation Engineering Beijing University of Technology Beijing China	Department of Bridge Engineering Southwest Jiaotong University Chengdu China

Editorial Office
MDPI AG
Grosspeteranlage 5
4052 Basel, Switzerland

This is a reprint of the Special Issue, published open access by the journal *Journal of Marine Science and Engineering* (ISSN 2077-1312), freely accessible at: https://www.mdpi.com/journal/jmse/special_issues/RI49S9R25D.

For citation purposes, cite each article independently as indicated on the article page online and as indicated below:

Lastname, A.A.; Lastname, B.B. Article Title. *Journal Name* **Year**, *Volume Number*, Page Range.

ISBN 978-3-7258-6452-2 (Hbk)
ISBN 978-3-7258-6453-9 (PDF)
https://doi.org/10.3390/books978-3-7258-6453-9

Contents

About the Editors

Piguang Wang

Piguang Wang is a Professor and Doctoral Supervisor with the College of Architecture and Civil Engineering at Beijing University of Technology. He is a recipient of grants from the Beijing Natural Science Foundation. His research focuses on structural resilience, earthquake engineering, wind engineering, and the multi-hazard performance of infrastructure. He has led and participated in numerous national and provincial research projects on the seismic safety of major engineering structures, offshore and nearshore infrastructure protection, and the performance-based design of resilient communities. His recent innovative contributions include developing highly efficient analysis methods for water–structure–soil coupled systems under earthquake loading and establishing simplified added mass models for fluid–structure interaction, providing essential tools for large-scale nonlinear analysis of offshore structures. He has published over 100 SCI-indexed papers in leading journals such as *Journal of Engineering Mechanics*, *Computers and Geotechnics*, and *Engineering Structures*, authored 3 monographs, and holds 12 national invention patents. Additionally, he serves as the Deputy Secretary-General of the Nearshore and Offshore Engineering Disaster and Environmental Protection Committee of the Seismological Society of China and is on the Editorial Boards of several journals. He was also the winner of the Seismological Society of China Natural Science Award.

Kai Wei

Kai Wei is a Professor and Doctoral Supervisor within the Department of Bridge Engineering at Southwest Jiaotong University. He is the recipient of the National Excellent Youth Fund, the Young Talent of the Sichuan "Tianfu Emei" Program, and a Member of the Sichuan May Fourth Youth Medal Collective. He has long been engaged in theoretical and applied basic research on bridge hydrodynamics, presided over four projects of the National Natural Science Foundation of China, three sub-projects of regional joint fund and national key research and development projects, and led several scientific and technological research projects of some major bridges, including Changtai Yangtze River Bridge, Hangzhou Bay High-speed Railway Bridge, Xihoumen Rail-cum-road Bridge, etc. He serves as a Section Board Member of the journal *Sustainability*, an Editorial Board Member of the *Journal of Civil and Environmental Engineering*, and a Young Editorial Board Member of the *China Journal of Highway and Transport* and *Journal of Southeast University*. He has published two monographs and more than one hundred journal articles. He was also the winner of the Special Prize in the 2022 Science and Technology Award of the China Highway and Transportation Society, and the second prize in the 2017 Shanghai Science and Technology Awards.

Journal of
Marine Science and Engineering

MDPI

Article

Numerical Simulation and Tests of Lateral Bearing Capacity of Sloped Offshore Monopile Under Vertical Load and Lateral Cyclic Load

Yongqing Lai [1], Gen Xiong [1], Ben He [1], Yilong Sun [2,3,4,*], Lin Guo [2,4] and Kaiyuan Liu [5,6]

[1] Power China Huadong Engineering Co., Ltd., Hangzhou 311100, China
[2] College of Civil Engineering and Architecture, Wenzhou University, Wenzhou 325035, China
[3] Key Laboratory of Engineering and Technology for Soft Soil Foundation and Tideland Reclamation of Zhejiang Province, Wenzhou 325035, China
[4] Zhejiang Engineering Research Center of Disaster Prevention and Mitigation for Coastal Soft Soil Foundation, Wenzhou 325035, China
[5] China Three Gorges Corporation, Wuhan 430010, China
[6] China Three Gorges Corporation, Institute of Science and Technology, Beijing 100038, China
* Correspondence: sunyilong@wzu.edu.cn

Abstract: Offshore monopile foundations endure complex loads during service. They bear vertical loads from the superstructure's self-weight and lateral cyclic loads (e.g., wind, waves), while near-coastal seabeds are usually sloped. To resolve these issues, model pile tests under combined vertical and lateral cyclic loads were carried out to study how slope angle and vertical load affect monopile deformation. A numerical model was validated via comparison with test results and then used to reveal the development of cumulative deformation in offshore sloped monopiles under the above combined loads. The results show that, below 1000 cycles, the cumulative displacement of the pile increases logarithmically with the number of cycles. As the slope angle increases, the cumulative deformation increases. In these tests, the cumulative deformation of the pile increases by 114% compared to the results of the flat site, but it decreases with an increase in vertical load. As such, when a 3 N vertical load is applied to the pile top, its deformation at the flat site decreases by 20%, but its deformation at a 20° slope site decreases by 10%. Finally, a predicted formula is proposed for offshore monopiles with the effect of slope angle, and this formula can provide a preliminary assessment method of cumulative.

Keywords: offshore wind turbine; monopile; lateral bearing capacity; vertical load and lateral cyclic load

1. Introduction

Ocean environmental loads are very complex, especially for pile foundations in offshore engineering. On the one hand, monopiles are acted by vertical–lateral load combinations; on the other hand, the seafloor can be sloped [1]. In this condition, monopiles are acted by considerable vertical gravity combined with lateral cyclic loading from wind and waves. At the same time, the seafloor slope has a non-negligible effect on the stability of the monopile. Therefore, understanding the lateral response of offshore monopile to slope, vertical load and lateral cyclic load is highly significant.

It is well known that slopes cause asymmetric stress distributions. The lateral bearing capacity and responses of piles on slopes have been revealed by many researchers. Jiang et al. [2] and Georgiadis [3,4] investigated the effect of slope on soil's ultimate resistance using a theoretical method. According to the law of soil's ultimate resistance, an analysis method for a rigid pile was then proposed. Liu et al. [5] investigated the difference in soil's ultimate resistance between front and back piles under the effect of lateral load. Peng et al. presented an asymmetric failure mode of soil to investigate the bearing capacity of laterally loaded piles at the slope crest [6]. In some studies, model tests were conducted to evaluate the bearing capacity of piles on a slope. Rathod et al. [7] conducted sloped pile model tests to investigate the effect of slenderness ratio and slope angle on the lateral deformation of a sloped pile. It was found that, when the slope angle was less than 11.3°, the slope effect was negligible. Zhang et al. [8] conducted model tests to study the effect of slope on the cyclic lateral response of a pile. Yue et al. [9] compared the cyclic lateral response of a pile on a downslope and an upslope by using the test method and found that the slope effect is significant in the downslope condition. Numerical simulations are also used to study the bearing capacity of slope piles. Sawant et al. [10] and Ng et al. [11] analyzed slope-induced pile model deformation via numerical calculations. Numerical simulations further explored how relative soil stiffness affects sloped pile response. Pang et al. [12] meanwhile studied slope angle's impact on soil ultimate resistance and p-y curve initial stiffness. A nonlinear method was proposed for calculating the initial stiffness of p-y curves. In the above studies, the effect of slope was among the lateral response characteristics of piles. Nevertheless, in practical offshore monopile projects, pile foundations bear combined vertical loads derived from gravity and lateral loads induced by waves, and they are situated in sloped areas—these conditions call for further investigation.

The lateral bearing capacity of piles under vertical–lateral load combinations has been studied by some researchers. It was found that the P-Δ effect was caused by vertical load, meaning an additional bending moment was introduced, so the lateral deformation of the pile was increased and the lateral ultimate capacity was decreased. Based on model analyses, Goryunov et al. [13] and Liang et al. [14] found that the lateral deformation of a pile increases with an increase in vertical load. Zhang et al. [15] proposed an elastoplastic solution for calculating the lateral deformation of a pile under vertical–lateral load using the subgrade reaction method, and found that the lateral deformation and bending moment of the pile increased with an increase in vertical load. Vertical–lateral cyclic load pile model tests were conducted by Liu et al. [16], who found that vertical load increases the lateral cyclic deformation of a pile. However, some researchers found that vertical compression decreased the deformation and bending moment of a pile to some degree. Lu et al. [17] conducted a series of vertical–lateral load pile centrifuge tests, and by comparing the pile deformation and bending moment, they found that soil densification was caused by vertical compression. Drawing on findings from model experiments, Mu et al. [18] concluded that pre-imposed vertical loads enhance the soil's resistance stress; analogous outcomes were observed in field-based pile experiments conducted by Karasev et al. [19] and Bartolomey [20]. Through numerical simulations, Karthigeyan et al. [21], Taheri et al. [22], and Lu et al. [23] demonstrated that the ultimate soil resistance associated with the p-y curve rises as the vertical load increases. The influence of vertical loads on the horizontal deformation of pile foundations has been systematically investigated in the above studies, the majority of these studies concentrated on pile foundations situated on flat ground. The impact of vertical load on the lateral displacement of pile foundations located on sloped terrain remains unstudied.

In summary, the influence of vertical load and slope angle on the lateral bearing capacity of offshore monopiles should be revealed, but little research has been performed in this area. As such, a series of vertical–lateral load pile model tests were conducted. The effect of vertical load and slope angle on the lateral cyclic deformation of a pile was investigated. Then, a numerical model was created and validated by comparing the results of model tests. Finally, by using this numerical model, the effects of slope angle, vertical load, and pile diameter on the cyclic deformation were revealed, and the cumulative deformation characteristics were studied.

2. Model Tests of Pile Under Vertical Load and Lateral Load

2.1. Apparatus of Model Tests

A specific apparatus was made to conduct model tests of a pile, as shown in Figure 1. This apparatus consists of a model box, a model pile, an actuator system, and a monitoring system. The dimensions of the model box are 600 mm in length, 600 mm in width, and 800 mm in height. This model pile is used to simulate an offshore monopile. The prototype size of the steel monopile is 50 m in length and 3 m in diameter. Within the present research, the 1:100 scale ratio was employed to underpin core analytical and validation processes. The model pile is made of aluminum, with dimensions of 30 mm in diameter and 500 mm in length. The actuator system applies lateral cyclic loading, while the monitoring system measures the lateral displacement and strain. As reported by Leblanc et al. [24], the relative stiffness of the prototype pile and model pile was determined to be 0.00776 and 0.00853, respectively. This near-identical stiffness characteristic translates to consistent deformation responses between the two, and the specific relational parameters are tabulated in Table 1.

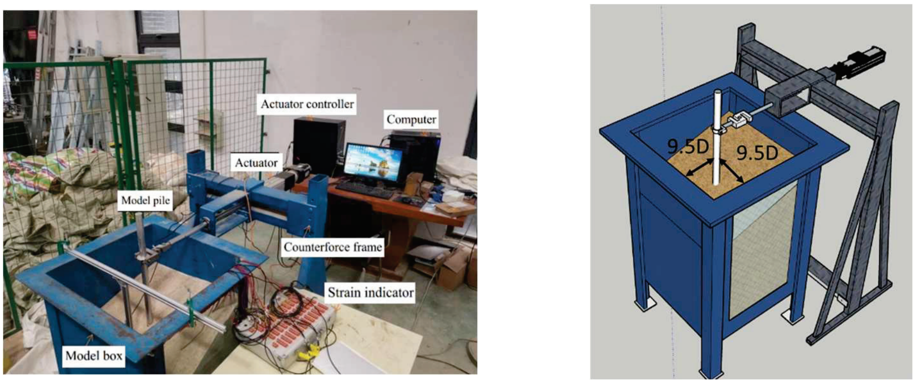

(**a**) Diagram of test device (**b**) Diagram of model pile position

Figure 1. Apparatus of model tests.

Table 1. Similar relation of prototype pile and model pile.

Parameter	Prototype Pile	Model Pile	Similar Ratio
Diameter/m	3.0	0.03	100
Length/m	50	0.5	100
Burial depth/m	30	0.32	93.75
Bending stiffness/kN·m^2	1.23×10^{11}	1788.32	7×10^7
Stiffness ratio of pile–soil	7.76×10^{-3}	8.53×10^{-3}	0.91
Mass of supper structure/kg	3×10^5	0.3	10^6

A concentrated mass block was applied to the top of the model pile, as shown in Figure 2. The capacity of the prototype wind turbine is 5 MW, and the mass of the blade and turbine is about 300 t. The same scale reduction ratio as the test pile (1:100) was used; accordingly, the mass of the upper structure was about 3 N.

For the model test program, Fujian standard sand was selected as the foundation soil material, with a mean particle size of 0.47 mm and a void ratio of 0.68. This sand's key physical properties, including additional detailed parameters, are summarized in Table 2. Distribution curve of the sand particle sizes is shown in Figure 3. The rainfall method was used for layering and filling sand, with a 50 mm filling depth for each layer. The relative density of sand in the model tests was controlled at 65%. After completing the filling of sand, the test soil was left stationary for one hour. The influence of soil stress on the model tests was eliminated. If the sand in the model tests was sloped, the slope was adjusted to a specific angle. After this step, sand was again subjected to static conditions for one hour.

(**a**) Concentrated mass block (**b**) Connection device of loader and pile

Figure 2. Diagram of vertical load application method.

Table 2. Basic parameters of sand in model test.

G_s	d_{50}/mm	C_u	C_c	$\rho_{\max}$/(g/cm^3)	$\rho_{\min}$/(g/cm^3)	$e_{\max}$	$e_{\min}$
2.626	0.75	2.63	1.04	1.745	1.55	0.77	0.519

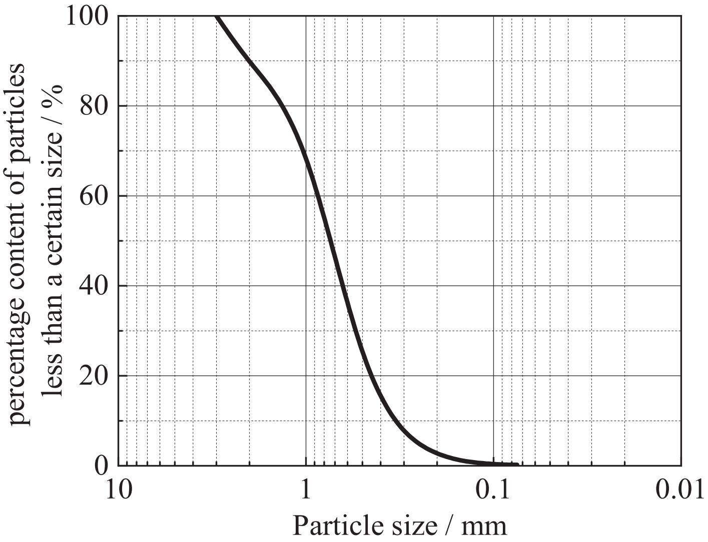

Figure 3. Particle size distribution curve for Fujian standard sand.

In the model tests, a strain gauge, soil pressure sensor, and displacement sensor were used to measure the displacement of the pile and the change in soil stress. Six pairs of strain gauges were attached to the surface of the pile body at a spacing of 60 mm, and three pairs of soil pressure sensors were placed in the soil surrounding the pile. A layout diagram of the sensors is shown in Figure 4.

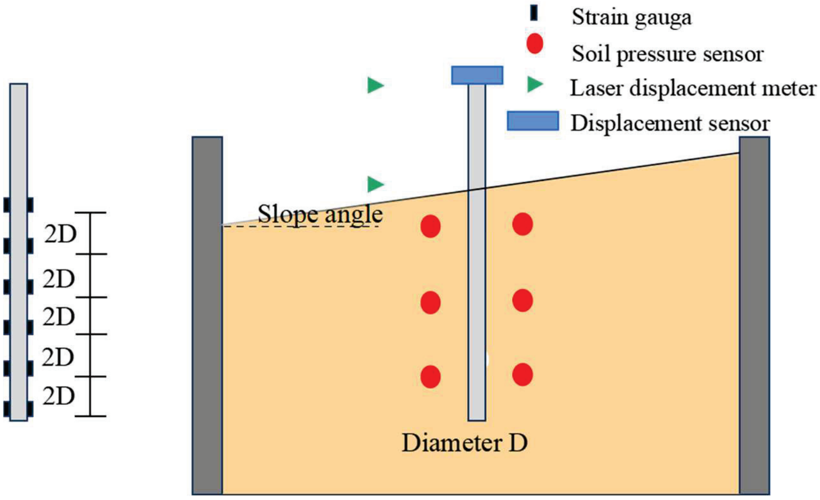

Figure 4. Sensor positional layout for model tests.

2.2. Scheme of Model Tests

Wind turbine structures are usually knocked by cyclic loads such as wind and waves. Under this cyclic loading condition, the pile foundation is within the serviceability limit [25]. Cyclic load ratio ξ is used to define the magnitude of cyclic load. A value of ξ within the range of 0 to 0.3 represents frequent wind and wave loads [26]. In this study, a cyclic load ratio ξ of 0.3 is chosen. According to static load tests, the lateral limit bearing capacity is about 53 N, so the amplitude of cyclic load is about 16 N. Andersen [27] and Nikitas et al. [28] found that the period of cyclic load is about 10 s, so its frequency is determined to be 0.1 Hz. A waveform diagram of the cyclic load is shown in Figure 5.

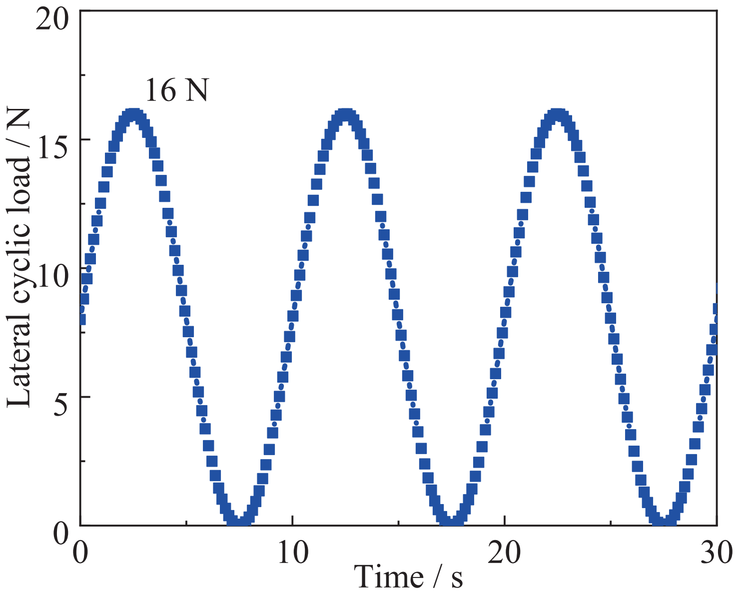

Figure 5. Cyclic lateral loading schematic.

In the model pile tests with combined vertical and lateral cyclic loads, slope angles of 0°, 10°, and 20° were used for the soil foundation. A vertical load of 3 N and 0 N was applied to the pile top. This vertical load was used to simulate the mass of the superstructure. The detailed test program is shown in Table 3.

Table 3. Program of model pile tests under vertical load and lateral cyclic load.

No	Lateral Cyclic Load		Vertical Load/N	Slope Angle/°	Cyclic Number
	Amplitude/N	**Frequency/Hz**			
C1~2	16	0.1	0 3	0	5000
C3~4	16			10	
C5~6	16			20	

3. Analysis of Model Test Results

3.1. Effect of Vertical Load

The effect of vertical load on the lateral displacement of the pile top is shown in Figure 6. After the first cyclic load, the lateral displacement of the pile top without the effect of vertical load was 55 mm. However, when a vertical load of 3 N was applied to the pile top, the lateral displacement of the pile top was 0.44 mm. It was found that vertical load induced a decrease in the lateral displacement. After the 5000th cyclic load, the lateral displacement of the pile top without the effect of vertical load was 2.73 mm. However, the lateral displacement of the pile top with vertical load was 2.19 mm, indicating that lateral load increases the lateral bearing capacity.

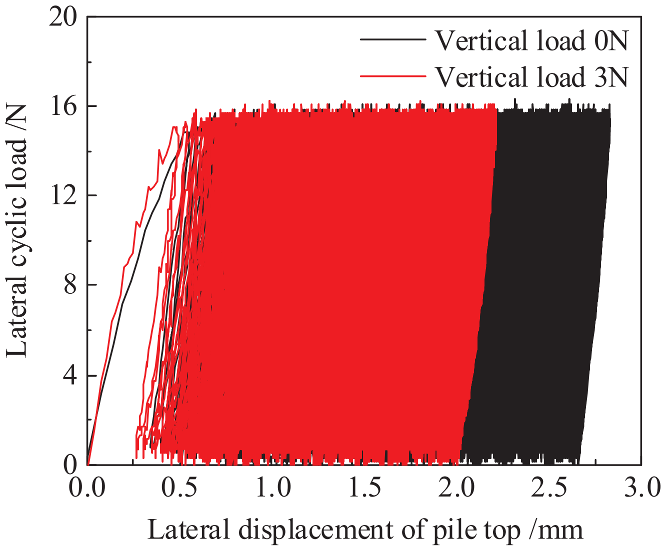

Figure 6. Accumulated lateral displacement at the pile top under vertical load action.

3.2. Effect of Slope Angle

A comparison of the lateral displacement of the pile top under the effect of slope angle is shown in Figure 7. It shows that as the slope angle increases, the cumulative lateral displacement of the pile top increases. When the cyclic number is 5000, the lateral displacement of the pile top is 2.73 mm on flat ground. The lateral displacement values of the pile top on the 10° slope and 20° slope are 3.76 mm and 6.06 mm, respectively. Compared with the displacement of the pile top at the flat site, the displacement at the top of the pile increased by 32.8% and 114.8%, respectively. The reason is that as the slope angle increases, the loss of soil in front of the pile becomes more obvious, and the slope effect has a more pronounced influence on lateral bearing capacity.

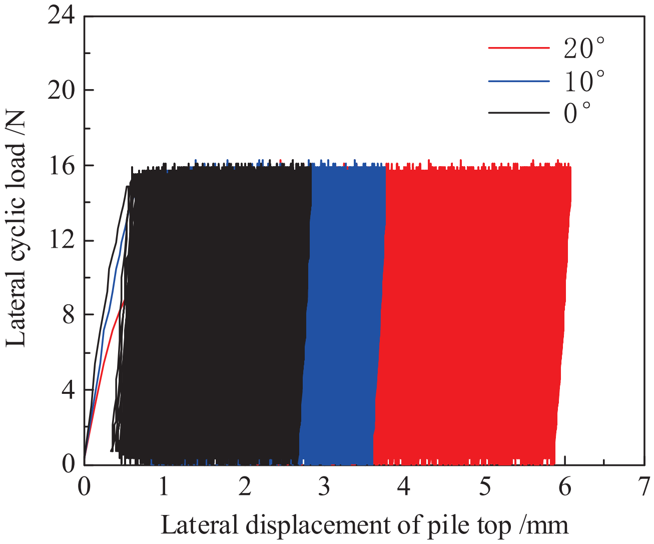

Figure 7. Cumulative lateral displacement at the pile top under slope angle action.

4. Numerical Model of Pile Under Vertical Load and Lateral Load

4.1. Establishment of the Numerical Model

Based on the results of model tests, a numerical model is created to investigate the development of cumulative lateral displacement of the pile at different slope angles. In the established numerical model, structured grids are adopted. The soil grids adjacent to the pile body are dense, whereas those distant from it are sparse. The model comprises a total of 40,040 nodes and 43,056 elements.A schematic diagram of the numerical model is shown in Figure 8. The surrounding boundaries and the bottom boundary are fixed. The Mohr–Coulomb model is used to simulate the stress–strain relationship of the soil. An elastic model is used to reflect the deformation of the pile, with an elastic modulus of 50 GPa and a Poisson ratio of 0.3. An interface element is adopted to simulate nonlinear pile–soil interactions. The parameters of the interface are 0.5 times those of the soil parameters. In the numerical model, Equation (1) is embedded to reflect the nonlinear relationship between the elastic modulus and the confining pressure [29]. Detailed parameters of the soil and pile in the numerical model are shown in Table 4.

$$E_s = k \cdot \sigma_{\mathrm{at}} \cdot \left(\frac{\sigma_3}{\sigma_{\mathrm{at}}} \right)^{\lambda} \tag{1}$$

where k is the influence coefficient of the soil elastic modulus, λ is the influence coefficient of depth, σ_3 is the minimum principal stress of soil (kPa), and σ_{at} is the atmospheric pressure (101 kPa).

A vertical load is applied to the pile top using a concentrated mass. The cumulative deformation of the pile due to the effect of cyclic load is calculated by using the stiffness attenuation model, which was proposed by Achmus et al. [30] using the attenuation modulus obtained from a cyclic triaxial test. The relationship of the attenuation modulus with cyclic number is shown in Equation (2).

$$\frac{E_{\mathrm{s}N}}{E_{\mathrm{s}1}} = \frac{\varepsilon_{\mathrm{p},N=1}}{\varepsilon_{\mathrm{p},N}} = N^{-b_1 (X)^{b_2}} \tag{2}$$

where N is the cyclic number, $E_{\mathrm{s}N}$ is the elastic modulus after the Nth cycle, E_{s1} is the elastic modulus after the 1st cycle, $\varepsilon_{\mathrm{p},N=1}$ is the axial strain after the 1st cycle, $\varepsilon_{\mathrm{p},N}$ is the axial strain after the Nth cycle, X is the stress ratio of soil, and b_1 and b_2 are the relevant parameters.

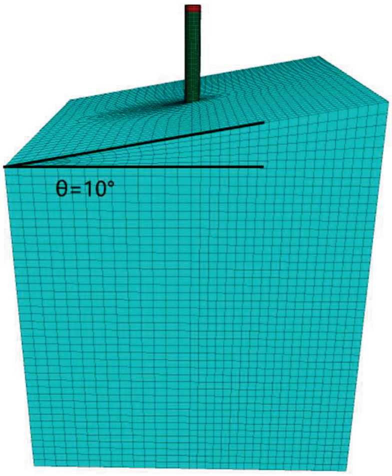

Figure 8. Diagram of the numerical model.

Table 4. Parameters of soil in the model tests.

Influence Coefficient of Modulus/λ	Influence Coefficient of Depth/*k*	Poisson Ratio	Dilatancy Angle/°	Friction Angle/°
450	0.65	0.275	5	36

In accordance with Achmus et al. [30] and Yang et al. [31], the characteristic cyclic stress ratio X_c is defined to reflect the change in soil stress under the effect of cyclic load.

$$X_c = \frac{X^{(1)} - X^{(0)}}{1 - X^{(0)}} \tag{3}$$

$$X^{(0)} = \frac{\sigma_1}{\sigma_{1,sf}} \tag{4}$$

$$X^{(1)} = \frac{\sigma_{1,cyc}}{\sigma_{1,sf}} \tag{5}$$

$$\sigma_{1,sf} = \left(1 + \frac{2\sin\phi}{1 - \sin\phi}\right)\sigma_3 \tag{6}$$

where $X^{(0)}$ is the stress ratio of the initial condition in the numerical model, $X^{(1)}$ is the stress ratio of the initial condition in the load stage, σ_1 is the major principal stress in the numerical model, σ_1, sf is the major principal stress at the static failure state, σ_3 is the minor principal stress in the numerical model, and φ is the internal friction angle of soil.

Based on the above theory and equations, modulus attenuation due to the effect of cyclic load is embedded in the numerical model. The numerical model is then used to calculate the cumulative deformation of the pile. The detailed flow diagram is shown in Figure 9.

4.2. Validation of the Numerical Model

In this section, the established numerical model is validated by comparing its results with those of model tests. The lateral deformation of the pile top in 0° and 10° model tests is reproduced with the established numerical model, and the comparison is shown in Figure 10. When there is no vertical load, the differences between model tests and numerical results are about 8% and 3%, respectively, for the 0° and 10° sites. When a 3 N vertical load is applied to the pile top, the differences between model tests and numerical results are about 6% and 4%, respectively, for the 0° and 10° sites. This indicates that the numerical results are in good agreement with the results of model tests.

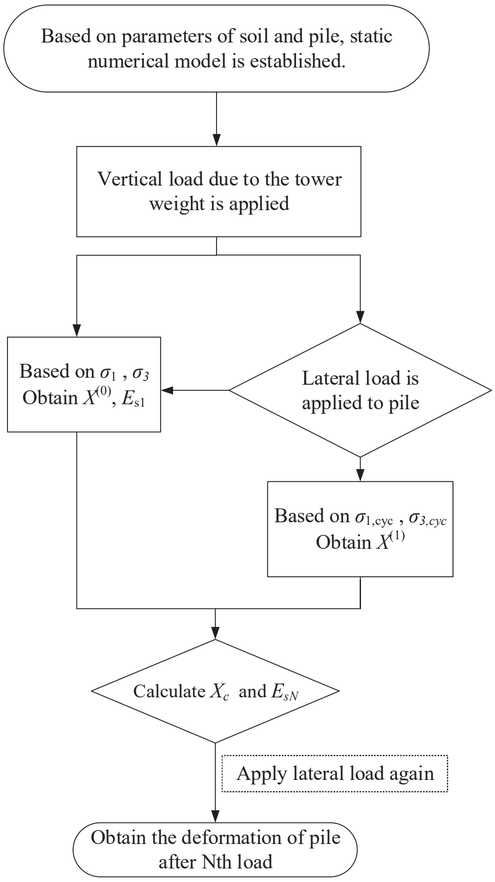

Figure 9. Flow diagram of the calculated cumulative deformation.

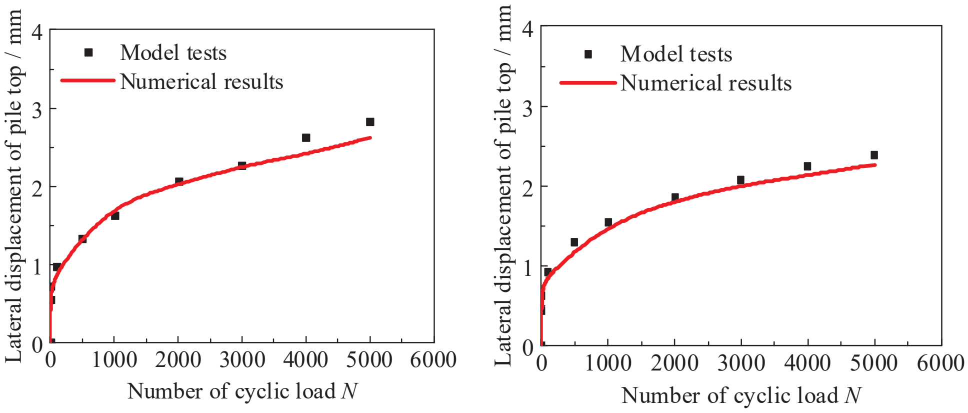

(**a**) 0 N vertical load at 0° site (**b**) 3 N vertical load at 0° site

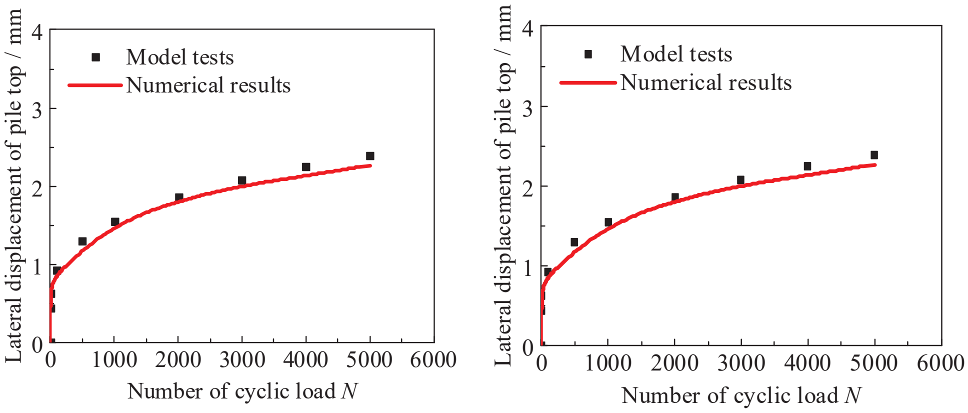

(**c**) 0 N vertical load at 10° site (**d**) 3 N vertical load at 10° site

Figure 10. Comparative analysis of outcomes between model experiments and numerical computations.

4.3. Numerical Model of Offshore Monopile

Based on the verified numerical model, a numerical model of an offshore monopile under vertical and lateral loads is established. The cumulative deformation of the offshore monopile is investigated at different relative densities of sand and slope angles. The numerical model of different slope angles is shown in Figure 11.

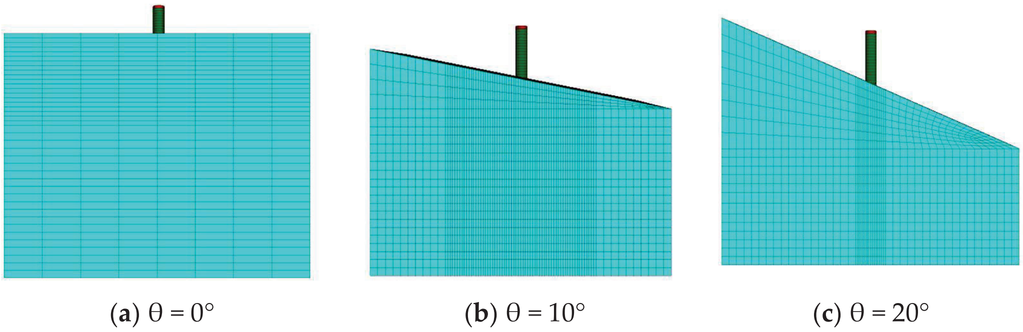
(**a**) θ = 0° (**b**) θ = 10° (**c**) θ = 20°

Figure 11. Numerical model of different slope angles.

This numerical model uses relative densities of 60%, 75%, and 90%, and slope angles of 0°, 10°, and 20°. The monopile's dimensions are 50 m in length, 5 m in diameter, and 5 cm in wall thickness, and its elastic modulus is 210 GPa. Vertical loads of 1 MN and 3 MN are applied on the pile top. The detailed parameters of sand are shown in Table 5.

Table 5. Parameters of sand with different relative densities.

Relative Density/%	Influence Coefficient of Modulus/λ	Influence Coefficient of Depth/*k*	Poisson Ratio	Dilatancy Angle/°	Friction Angle/°
60	400	0.6	0.250	5	35
75	500	0.55	0.225	7.5	37.5
90	700	0.5	0.200	10	40

5. Influence Analysis of Large-Diameter Monopile Under Vertical Load and Lateral Load

5.1. Influence of Relative Density

A pile of 5 m diameter at the flat site is chosen to investigate the effect of relative density on the cumulative deformation of the pile. Firstly, the lateral ultimate bearing capacity is calculated to define the magnitude of cyclic load. The lateral displacement of the pile under different lateral loads is shown in Figure 12. In accordance with Barari et al. [26], lateral displacement of 0.1 times the diameter (0.1 D) is used to determine the lateral ultimate force. The ultimate forces at 60%, 75%, and 90% relative density are about 18 MN, 21 MN, and 26 MN. It is found that as the relative density increases, the ultimate force increases. When compared with 60% relative density, there is an increase of 15% and 40%.

Based on the study by Sun et al. [32], a lateral ultimate force of 0.3 times was chosen as the amplitude of the cyclic load. The amplitudes of the cyclic load for different relative densities are 5.4 MN, 6.3 MN, and 7.8 MN. The cumulative displacement of the pile at different relative densities is shown in Figure 13, which shows that most of the cumulative deformation is produced within 1000 cyclic loads. After that, the growth rate of cumulative deformation decreases. At the same amplitude level of cyclic load, as the relative density increases, the cumulative deformation of the pile decreases. At the 10,000th cyclic load, the cumulative deformations of the pile at relative densities of 60%, 75%, and 90% are 0.37 m, 0.28 m, and 0.19 m. Compared with the deformation of the pile at the 60% site, the deformation at the 75% and 90% sites decreases by 24% and 48%.

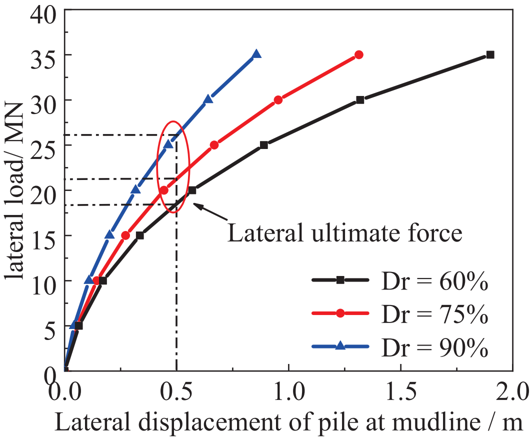

Figure 12. Load–displacement curve of pile at different relative densities.

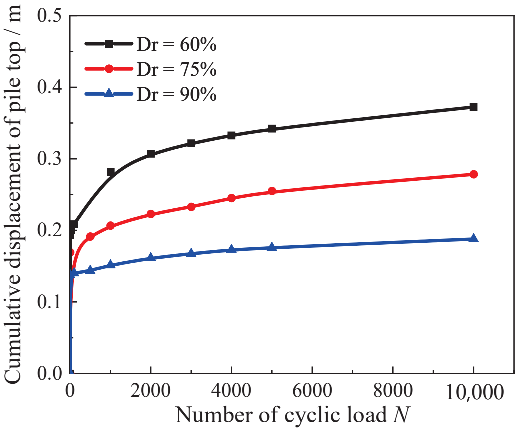

Figure 13. Cumulative displacement curve of the pile at different relative densities.

5.2. Influence of Slope Angle

Sand of 75% relative density is used to calculate the cumulative deformation at different slope angles. The same method is used in this section. The lateral ultimate force of the pile at different slope angles is calculated, revealing values of about 21 MN, 18 MN, and 15 MN for 0°, 10°, and 20°. Based on the results of lateral ultimate force, the amplitudes of cyclic load at different slope angles are determined to be 6.3 MN, 5.4 MN, and 4.5 MN. The cumulative deformation of the pile is shown in Figure 14. It can be seen that the cumulative deformation of the pile at the 0° and 10° sites is mostly stable after the 1000th cyclic load, but that of the pile at the 20° site still increases with the number of cyclic loads. At the 1000th cyclic load, the deformation of the pile at the 0° and 10° sites is about 0.28 m and 0.54 m. However, the deformation of the pile at the 20° site is up to 1.28 m. It is indicated that, below 10°, the slope has no remarkable effect on the deformation of the pile. At the 20° site, the cumulative deformation of the pile remarkably increases due to the slope effect.

To further explore the influence of slope angle on pile deformation, the scenario with a cyclic load of 6.3 MN and a cyclic number of 6000 was selected to compare the range of soil deformation, as illustrated in Figure 15. It is observed that with the increase in slope angle, the range of identical soil deformation expands, which suggests that the extent of soil stiffness attenuation is enhanced. Specifically, the extent of stiffness attenuation at a slope angle of 20° is 50% greater than that at the flat site. These results demonstrate that an increase in slope angle aggravates the stiffness attenuation of the surrounding soil.

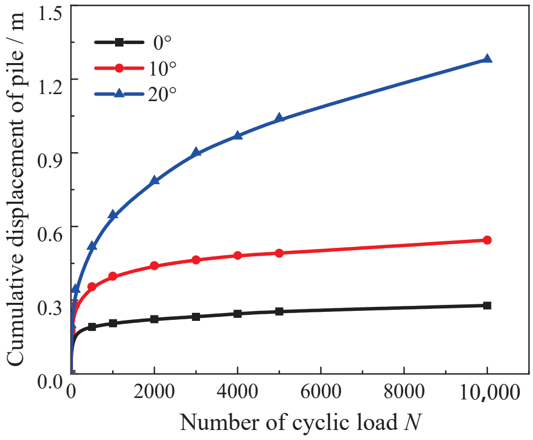

Figure 14. Cumulative displacement curve of pile at different slope angles.

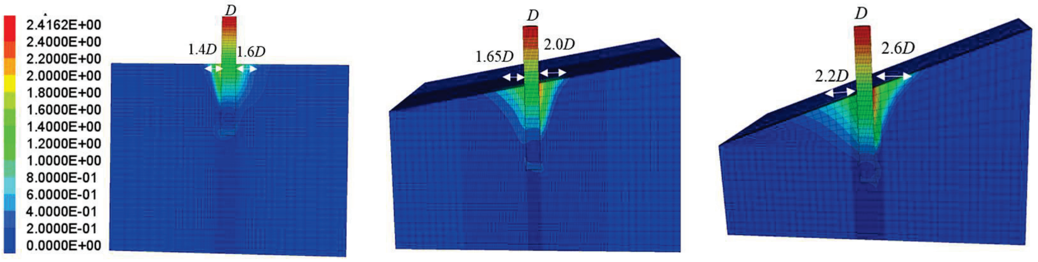

(**a**) θ = 0° (**b**) θ = 10° (**c**) θ = 20°

Figure 15. Analysis results of numerical models for different slope angles.

5.3. Influence of Vertical Load

Sand of 75% relative density is used to calculate the cumulative deformation with different vertical loads. The cumulative deformation of the pile is shown in Figure 16. Most of the cumulative deformation of the pile at different vertical loads is produced within 1000 cyclic loads. The effect of vertical load is a decrease in the cumulative deformation of the pile. At the 10,000th cyclic load, the deformation of the pile is about 0.35 m under a 1 MN vertical load, whereas under a 3 MN vertical load, the cumulative deformation of the pile is 0.28 m, a decrease of 20%.

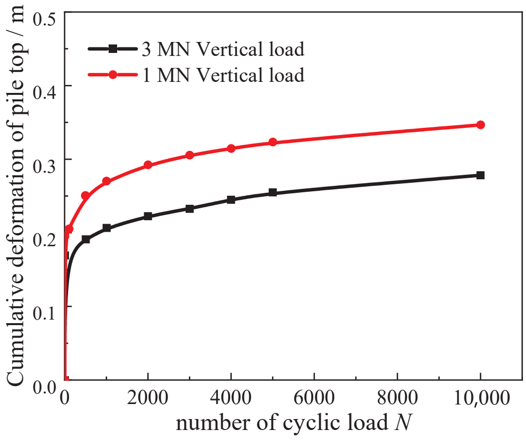

Figure 16. Cumulative displacement curve of pile at different vertical loads.

6. Prediction of Cumulative Displacement for Large-Diameter Monopile

Based on the results of the above numerical calculations, the relationship between cumulative deformation of the pile top and the number of cyclic loads is investigated. When dividing by the lateral displacement of the pile top under the first lateral cyclic load, its cumulative deformation is dimensionless. The detailed equation is shown in Equation (7).

$$y_{0,N} = \frac{y_N}{y_1} \tag{7}$$

where $y_{0,N}$ is the dimensionless displacement of the pile top, y_N is the displacement of the pile top after the Nth cyclic load, and y_1 is the displacement of the pile top after the first cyclic load.

As shown in Figure 17, as the logarithm of the number of cyclic loads increases, the dimensionless displacement of the pile top linearly increases. At the same time, with an increase in the relative density, the slope of the line decreases. As the slope angle increases, the slope of the line increases. Based on these results, the cumulative deformation can be predicted using the following proposed equation:

$$y_N = y_1 N^t \tag{8}$$

where t is the exponential parameter of the cumulative deformation formula.

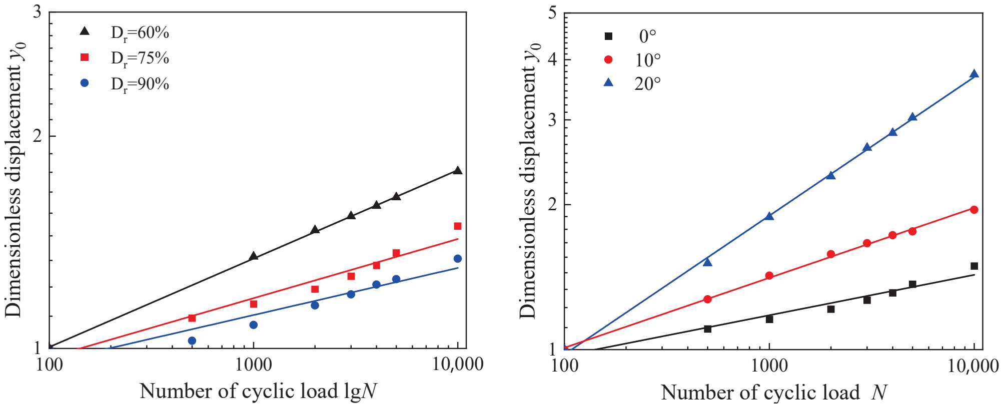

(**a**) Different relative density (**b**) Different slope angle

Figure 17. Relationship curve of non-dimensional displacement y_0 and number of cyclic loads.

By conducting a regression analysis of the above results, the parameters of the predicted formula are determined, and the results are shown in Figure 18. The relationship between the exponential parameter and relative density is shown in Equation (9). The relationship between the exponential parameter and slope angle is shown in Equation (10). In engineering design, the calculated results of piles are obtained for flat sites without accounting for the slope. By incorporating the relative density of sand and slope angle into the proposed formula, the cumulative deformation of slope-side piles can be rapidly derived based on the calculated results of piles in flat sites.

$$\mathrm{t} = 2.37\mathrm{e}^{-\frac{Dr}{17.3}} + 0.05 \tag{9}$$

$$\mathrm{t} = 0.79\mathrm{e}^{0.065\theta} \tag{10}$$

where D_r is the relative density of sand and θ is the slope angle.

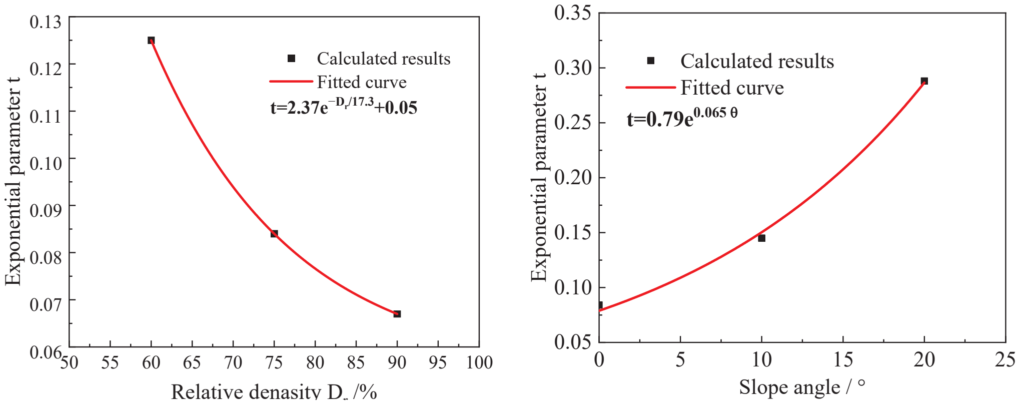

(**a**) Different relative density (**b**) Different slope angle

Figure 18. Parameter analysis of exponential parameter for cumulative deformation formula.

7. Conclusions

Model tests of a pile under vertical and lateral cyclic loads are conducted to determine the effects of slope angle and vertical load on its cumulative deformation. Based on the results of model tests, a numerical model of the pile is verified. A numerical model of an offshore monopile is then created. A series of numerical calculations are performed to determine the effect of relative density, slope angle, and vertical load on the cumulative deformation of the pile top. Finally, the development of cumulative deformation is investigated and a formula for predicting the cumulative deformation of a pile is proposed. The main conclusions are as follows:

(1). The cumulative displacement of the pile increases logarithmically with the number of cyclic loads. Deformation of the pile is produced within 1000th cycles. After the 1000th cycle, the deformation of the pile is largely stable.

(2). As the slope angle increases, the cumulative horizontal displacement of the single-pile foundation also increases. Compared to flat ground, the cumulative displacement of the pile at 10° and 20° slope sites increases by 32.8% and 114.8%, respectively.

(3). As the vertical load increases, the cumulative horizontal displacement of the single-pile foundation decreases. When the vertical load is 3 N, the cumulative displacement at 0°, 10°, and 20° decreases by 19.7%, 17.6%, and 10.7%.

(4). For large-diameter offshore monopiles situated on sloped sites under vertical-horizontal combined loading, cumulative displacement demonstrates a logarithmic growth characteristic with the increment of cycle counts. A predictive formula for cumulative deformation is developed, serving as a preliminary evaluation approach for such deformation. On account of insufficient cases from numerical computations and model tests, additional investigations are needed to optimize the developed model.

Author Contributions: Conceptualization, Y.L. and G.X.; methodology, B.H. and Y.S.; software, Y.S., K.L. and Y.L.; validation, Y.S. and G.X.; formal analysis, L.G.; investigation, Y.S. and K.L.; resources, Y.L.; data curation, Y.S.; writing—original draft preparation, Y.S.; writing—review and editing, L.G.; visualization, Y.L.; supervision, L.G. All authors have read and agreed to the published version of the manuscript.

Funding: This research was funded by the National Natural Science Foundation of China (Grant No.: 52301343), the Natural Science Foundation of Zhejiang Province (Grant No.: LQ23E090003), the "Leading Goose" R&D Program of Zhejiang (Grant No.: 2023C03122), the National Natural Science Foundation of China (Grant No.: 52408387), and the Zhejiang Provincial Natural Science Foundation of China (Grant No.: LQ24E080013) and Zhejiang Provincial Department of Education Project (Grant No.: Y202351968).

Data Availability Statement: The original contributions presented in this study are included in the article. Further inquiries can be directed to the corresponding author(s).

Acknowledgments: The findings presented in this article were made possible through the diligent. guidance of the authors' supervisor and the invaluable assistance of classmates, as well as the care and help of the teachers in the research group. With their collective help, the authors were able to obtain the lake test data. The unwavering support of the family and girlfriend of one of the authors was also instrumental. The authors extend sincere gratitude to all of them.

Conflicts of Interest: Authors Yongqing Lai, Gen Xiong and Ben He were employed by the company Power China Huadong Engineering Co., Ltd. Author Kaiyuan Liu was employed by the company China Three Gorges Corporation. The remaining authors declare that the research was conducted in the absence of any commercial or financial relationships that could be construed as a potential conflict of interest.

References

1. Lin, M.; Jiang, C.; Chen, Z.; Liu, P.; Pang, L. A method for calculating lateral response of offshore rigid monopile in sand underslope effect. *Ocean Eng.* **2022**, *259*, 111812. [CrossRef]
2. Jiang, C.; Zhang, Z.; He, J. Nonlinear analysis of combined loaded rigid piles in cohesionless soil slope. *Comput. Geotech.* **2020**, *117*, 103225. [CrossRef]
3. Georgiadis, K.; Georgiadis, M. Undrained lateral pile response in sloping ground. *J. Geotech. Geoenviron. Eng.* **2010**, *136*, 1489–1500. [CrossRef]
4. Georgiadis, K.; Georgiadis, M.; Anagnostopoulos, C. Lateral bearing capacity of rigid piles near clay slopes. *Soils Found.* **2013**, *53*, 144–154. [CrossRef]
5. Liu, P.; Jiang, C.; Lin, M.; Chen, L.; He, J. Nonlinear analysis of laterally loaded rigid piles at the crest of clay slopes. *Comput. Geotech.* **2020**, *126*, 103715. [CrossRef]
6. Peng, W.; Zhao, M.; Zhao, H.; Yang, C. Effect of slope on bearing capacity of laterally loaded pile based on asymmetric failure mode. *Comput. Geotech.* **2021**, *140*, 104469. [CrossRef]
7. Rathod, D.; Muthukkumaran, K.; Thallak, S. Experimental Investigation on Behavior of a Laterally Loaded Single Pile Located on Sloping Ground. *Int. J. Geomech.* **2019**, *19*, 04019021. [CrossRef]
8. Zhang, L.; Yue, S.; Peng, W.; Zhou, S. Experimental study on cyclic lateral response of piles in sandy sloping ground. *Ocean Eng.* **2023**, *282*, 115056. [CrossRef]
9. Yue, S.; Zhang, L.; Zhou, S.; Peng, W.; Wu, G.; Zhao, M. Experimental investigation into effects of slope and loading characteristics on cyclic laterally loaded monopile in sand. *Ocean Eng.* **2024**, *294*, 116784. [CrossRef]
10. Sawant, V.; Shukla, S. Three-dimensional finite element analysis of laterally loaded piles in sloping ground. *Indian Geotech. J.* **2012**, *42*, 278–286. [CrossRef]
11. Ng, C.W.W.; Zhang, L. Three-dimensional analysis of performance of laterally loaded sleeved piles in sloping ground. *J. Geotech. Geoenviron. Eng.* **2001**, *127*, 499–509. [CrossRef]
12. Pang, L.; Jiang, C.; Chen, L.J. Nonlinear Predictive Framework of the Undrained Clay Slope Effect on the Initial Stiffness of py Curves of Laterally Loaded Piles by FEM. *J. Mar. Sci. Eng.* **2022**, *10*, 1684. [CrossRef]
13. Goryunov, B. Analysis of piles subjected to the combined action of vertical and horizontal loads (discussion). *Soil Mech. Found. Eng.* **1973**, *10*, 10–13. [CrossRef]
14. Liang, F.Y.; Liao, C.C.; Mao, L.; Bai, W. Model tests on the behavior of a single pile under vertical-horizontal load. *Build. Struct.* **2013**, *43*, 92–94.
15. Zhang, L.; Gong, X.-N.; Yang, Z.-X.; Yu, J.-L. Elastoplastic solutions for single piles under combined vertical and lateral loads. *J. Cent. South Univ. Technol.* **2011**, *18*, 216–222. [CrossRef]
16. Liu, T.; Lai, Y.; He, B.; Lv, N. Influence of Vertical Load on the Lateral Response of Piles in Normally Consolidated and Over-Consolidated Clay: Centrifuge and Numerical Modelling. *Front. Phys.* **2022**, *10*, 908181. [CrossRef]
17. Lu, W.; Zhang, G. Influence mechanism of vertical-horizontal combined loads on the response of a single pile in sand. *Soils Found.* **2018**, *58*, 1228–1239. [CrossRef]
18. Mu, L.; Kang, X.; Feng, K.; Huang, M.; Cao, J. Influence of Vertical Loads on Lateral Behaviour of Monopiles in Sand. *Eur. J. Environ. Civ. Eng.* **2018**, *22* (Suppl. S1), s286–s301. [CrossRef]
19. Karasev, O.; Talanov, G.; Benda, S. Investigation of the Work of Single Situ-cast Piles Under Different Load Combinations. *Soil Mech. Found. Eng.* **1977**, *14*, 173–177. [CrossRef]

20. Bartolomey, A. Experimental Analysis of Pile Groups Under Lateral Loads. In Proceedings of the Special Session 10 of the Ninth International Conference on Soil Mechanics and Foundation Engineering, Tokyo, Japan, 10–15 July 1977; pp. 187–188.
21. Karthigeyan, S.; Ramakrishna, V.; Rajagopal, K. Influence of vertical load on the lateral response of piles in sand. *Comput. Geotech.* **2006**, *33*, 121–131. [CrossRef]
22. Taheri, O.; Moayed, R.Z.; Nozari, M. Lateral soil-pile stiffness subjected to vertical and lateral loading. *J. Geotech. Transp. Eng.* **2015**, *1*, 30–37.
23. Lu, W.; Zhang, G. New *p-y* curve model considering vertical loading for piles of offshore wind turbine in sand. *Ocean Eng.* **2020**, *203*, 107228. [CrossRef]
24. Leblanc, C.; Houlsby, G.; Byrne, B. Response of stiff piles in sand to long-term cyclic lateral loading. *Géotechnique* **2010**, *60*, 79–90. [CrossRef]
25. *DNV-OS-J101*; Offshore Standard: Design of Offshore Wind Turbine Structures. Det Norske Veritas: Hovek, Norway, 2013.
26. Barari, A.; Bagheri, M.; Rouainia, M.; Ibsen, L.B. Deformation mechanisms for offshore monopile foundations accounting for cyclic mobility effects. *Soil Dyn. Earthq. Eng.* **2017**, *97*, 439–453. [CrossRef]
27. Andersen, K. Cyclic soil parameters for offshore foundation design. *Front. Offshore Geotech. III* **2015**, *5*, 5–82.
28. Nikitas, G.; Arany, L.; Aingaran, S.; Vimalan, J.; Bhattacharya, S. Predicting long term performance of offshore wind turbines using cyclic simple shear apparatus. *Soil Dyn. Earthq. Eng.* **2017**, *92*, 678–683. [CrossRef]
29. Duncan, J.M.; Chang, C.Y. Nonlinear analysis of stress and strain in soils. *J. Soil Mech. Found. Div.* **1970**, *96*, 1629–1653. [CrossRef]
30. Achmus, M.; Kuo, Y.; Abdel-Rahman, K. Behavior of monopile foundations under cyclic lateral load. *Comput. Geotech.* **2009**, *36*, 725–735. [CrossRef]
31. Yang, Y.; Sun, Y.; Xu, C.; Iqbal, K.; DU, X. Predicting accumulated deformation of offshore large-diameter monopile using hollow cylinder apparatus. *Ocean Eng.* **2022**, *261*, 111984. [CrossRef]
32. Sun, Y.; Xu, C.; Naggar, M.H.E.; Du, X.; Dou, P. Cumulative cyclic response of offshore monopile in sands. *Appl. Ocean Res.* **2023**, *133*, 103481. [CrossRef]

Journal of
Marine Science and Engineering

MDPI

Article

A Time-Domain Substructure Method for Simulating Water–Cylinder Interaction Under Dynamic Loadings Considering Boundary Condition of Free Surface Waves

Piguang Wang [1], Hao Fu [1], Hao Liu [2,*], Zhenyun Tang [1] and Xiuli Du [1]

[1] Key Laboratory of Urban Security and Disaster Engineering of Ministry of Education, Beijing University of Technology, Beijing 100124, China; wangpiguang1985@bjut.edu.cn (P.W.); s202364174@emails.bjut.edu.cn (H.F.); tzy@bjut.edu.cn (Z.T.)
[2] International Research Institute of Disaster Science, Tohoku University, Sendai 980-0845, Japan
* Correspondence: hao.liu.e5@tohoku.ac.jp

Abstract: The dynamic interaction between water and cylindrical structures can significantly affect the dynamic responses and properties of offshore structures. Among the key factors, the free-surface boundary condition plays a crucial role in determining the hydrodynamic forces on cylinders, leading to frequency-dependent added mass and damping effects. Although the dynamic responses of the cylinder can be readily obtained using frequency-domain methods, their computational efficiency is much lower than that of the time-domain methods, and they are not well suited for nonlinear structure analysis. To address this, this study proposes a time-domain substructure method for simulating water–cylinder interaction considering the boundary condition of free surface waves, where the frequency-dependent added mass and added damping are equivalently represented by a spring-dashpot-mass model in time domain. The results indicated that the calculation efficiency of the proposed method has improved by approximately two orders of magnitude compared with the frequency-domain finite element method. Moreover, the water–cylinder interaction can markedly influence the seismic responses with small mass ratios, whereas its effect on wave-induced responses becomes negligible when the wave period exceeds 5 s. The effects of the free-surface boundary condition on the wave responses of the cylinder can be generally negligible, except when the wave period approaches the natural vibration period of the cylinder. In addition, its influence on seismic responses can be ignored when the damping ratio of the cylinder exceeds 0.02.

Keywords: water-cylinder interaction; hydrodynamic force; added mass; added damping; time-domain substructure method

1. Introduction

Circular cylinders have been widely used in offshore structures, such as offshore wind turbines, cross-sea bridges, and wharves [1–3]. Usually, wind load and ocean wave load are the two most important environmental loads for the design of offshore structures, while earthquake loading becomes dominant in regions with high seismic intensity. It is well known that cylinders immersed in water are subjected to additional hydrodynamic forces under dynamic loading due to fluid–structure interaction. These hydrodynamic forces can change the dynamic properties and responses of the structures [4–6]. Therefore, water–cylinder interaction must be given particular attention in the design of offshore structures.

The water–cylinder interaction during earthquakes has been well studied in recent decades. Based on the radiation wave theory, the earthquake-induced hydrodynamic force on a circular cylinder, varying uniformly from the bedrock to the water surface, can be derived strictly from the governing equation of the fluid and boundary conditions [7]. The existing studies indicated that the effect of water–cylinder interaction during earthquakes can be replaced by an additional mass, which is called "added mass" [5]. Based on the analytical solutions of the earthquake-induced hydrodynamic force on circular and elliptical cylinders, the simplified formulas of the added mass to simulate the water–cylinder were developed by Li and Yang [8], Jiang et al. [9], and Wang et al. [10]. Furthermore, using highly efficient and accurate numerical methods, Wang et al. [11–13] proposed simplified added mass formulations for simulating the dynamic interaction of waves with circular tapered cylinders, inclined circular cylinders, round-ended cylinders, and rectangular cylinders.

The wave–cylinder interaction has also been investigated by many researchers. The Morison equation proposed by Morison et al. [14] and the diffraction wave theory proposed by MacCamy and Fuchs [15] are two major methods to calculate the wave forces on cylinders. The Morison equation is a semi-empirical and semi-theoretical formula to evaluate the wave forces acting on slender cylinders [16–18], which is made up of a drag force and a virtual mass force. The diffraction wave theory is mainly used to calculate the wave forces on larger cylinders [19–21]. Wave-induced forces can also deform the cylinder, and this deformation generates additional hydrodynamic forces that can be evaluated using radiation wave theory. In addition, Newman [22] provided the fundamental theoretical basis, covering potential flow theory, radiation–diffraction methods, and added-mass and damping formulations, while Molin [23] offers an updated and detailed account of nonlinear wave–structure interactions, including modern issues such as gap resonance and moonpool dynamics. Due to the boundary condition of free surface waves, the effects of the radiated waves generated by cylinder motion can be characterized by frequency-dependent added mass and damping. The closed-form solutions of the added mass and damping coefficients for an oscillating circular cylinder were given by Rahman and Bhatta [24]. The results indicated that the added mass approaches a constant value and becomes frequency-independent, while the added damping converges to zero as the oscillation frequency tends to infinity.

Existing studies have shown that the damping effects of free surface waves can be neglected and the water–cylinder interaction can be approximated by a frequency-independent added mass when the load frequency is high [20]. However, since ocean waves generally occur at relatively low frequencies, both added mass and damping vary significantly within the relevant frequency range. In this case, the dynamic responses of cylinders can be readily evaluated using frequency-domain methods [5]. Nevertheless, the computational efficiency of the frequency-domain methods is much lower than that of the time-domain methods, and they are not well suited for nonlinear structural analysis. The main purpose of this paper is to develop a substructure method in the time domain with high precision and efficiency for simulating water–cylinder interaction while explicitly considering the free-surface boundary condition. In this approach, the frequency-dependent added mass and damping are equivalently represented by a spring–dashpot–mass model in the time domain. This method is both stable and efficient and can be seamlessly integrated with the explicit finite element method. Furthermore, the proposed method is applied to evaluate the effects of the added mass and damping on the dynamic responses of the circular cylinder subjected to wave and earthquake loads.

2. Theoretical Formulation and Solution

The water–cylinder interaction problem under horizontal loading is shown in Figure 1, where the signs (r, θ, z), h and a denote the cylindrical coordinate system, water depth, radius of the cylinder, respectively. The cylinder has a horizontal displacement time history

$u(t)$, which induces a radiated hydrodynamic pressure $p_r(r,\theta,z,t)$. In the analysis of hydrodynamic forces acting on offshore structures, two main approaches are generally employed. The first is Morison's equation, which is suitable for small-diameter slender structures. In this method, the fluid forces are expressed using empirical inertia and drag coefficients, which are typically dependent on Reynolds number and flow conditions. Morison's equation enables rapid computation of fluid forces with relatively low computational cost, but its applicability is mainly limited to structures whose dimensions are small compared to the wavelength. The second approach is potential flow theory, which is more suitable for large-scale structures. This theory assumes that the fluid is irrotational, inviscid, and incompressible, and it avoids reliance on empirical lift or drag coefficients. Since this study focuses on large-scale offshore structures, potential flow theory is adopted to solve the water–cylinder interaction.

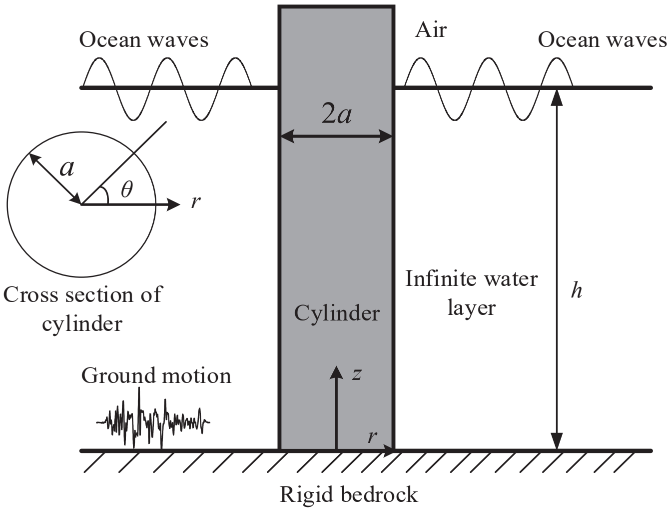

Figure 1. A circular cylinder surrounding by water overlying rigid bedrock.

The governing equation for hydrodynamic pressure $p_r(r,\theta,z,t)$ is expressed as:

$$\frac{\partial^2 P_r}{\partial r^2} + \frac{1}{r}\frac{\partial P_r}{\partial r} + \frac{1}{r^2}\frac{\partial^2 P_r}{\partial \theta^2} + \frac{\partial^2 P_r}{\partial z^2} = 0 \tag{1}$$

where $P_r = \int_{-\infty}^{\infty} p_r e^{-\mathrm{i}\omega t}\mathrm{d}t$ is the Fourier transformation of p_r and ω is the load frequency.

The boundary conditions for the radiation wave at bottom, free surface, infinity and interface of cylinder and water can be written as:

$$\left.\frac{\partial P_r}{\partial z}\right|_{z=0} = 0 \tag{2}$$

$$\frac{\partial P_r}{\partial z} = \frac{\omega^2}{g} P_r \ \ z = h \tag{3}$$

$$\lim_{r\to\infty} \sqrt{r}\left(\frac{\partial P_r}{\partial r} - \mathrm{i}kP_r\right) = 0 \tag{4}$$

$$\left.\frac{\partial P_r}{\partial r}\right|_{r=a} = \rho\omega^2 U\cos\theta \tag{5}$$

where $U = \int_{-\infty}^{\infty} u e^{-\mathrm{i}\omega t}\mathrm{d}t$ denotes the displacement of the cylinder in frequency domain, ρ is the fluid density, and g is the gravitational acceleration.

Using separation of variables and according to boundary conditions in Equations (2)–(5), the hydrodynamic pressure can be obtained by:

$$P_r = -\rho a \omega^2 \cos\theta \sum_{j=0}^{\infty} d_j S_j \cosh k_j z \int_0^h U \cosh k_j z \mathrm{d}z \tag{6}$$

$$S_j = \frac{-H_1^{(1)}\left(k_j a\right)}{k_j a H_1^{(1)\prime}\left(k_j a\right)} \tag{7}$$

$$d_j = \frac{2}{h + \left(\omega^2/g\right)^{-1} \sinh^2\left(k_j h\right)} \tag{8}$$

where $H_n^{(1)}(\cdot)$ is Hankel function of the first kind of order n; for j = 1,2,3... $k_j = i\kappa_j$, k_0 and κ_j can be obtained by the following equations:

$$k_0 \tanh(k_0 h) = \frac{\omega^2}{g} \text{and } \kappa_j \tan\left(\kappa_j h\right) = -\frac{\omega^2}{g} \tag{9}$$

For a circular cylinder with a rigid motion, the hydrodynamic force component per unit length can be obtained as:

$$F_x^r = -\int_0^{2\pi} P_r a \cos\theta \mathrm{d}\theta = \rho \pi a^2 \omega^2 U \sum_{j=0}^{J} d_j S_j \frac{\cosh k_j z}{k_j \sinh k_j h} \tag{10}$$

where J denotes the number of modes. It should be noted that Equation (10) will be used to obtain the discrete hydrodynamic force on the nodes of the circular cylinder, and the corresponding added mass and damping due to the water–cylinder interaction will be further obtained.

3. Method of Rational Function Approximation

It should be noted that the radiation force (F_{Rad}) due to the water–structure interaction can be defined as follows for a single-frequency motion in frequency domain:

$$F_{Rad} = M_h(\omega)\omega^2 U - \mathrm{i}\omega C_h(\omega) U \tag{11}$$

where $M_h(\omega)$ and $C_h(\omega)$ denote the frequency-dependent added mass and damping, respectively. Figure 2 show the typical frequency-dependent added mass and damping coefficients for the water–cylinder interaction, where the added mass becomes constant and frequency-independent whereas the added damping converges to zero when the load frequency tends to infinity. Therefore, the added mass $M_h(\omega)$ can be further rewritten as:

$$M_h(\omega) = m_h(\omega) + M_h(\infty) \tag{12}$$

where $M_h(\infty)$ represents the added mass with load frequency tends to infinity.

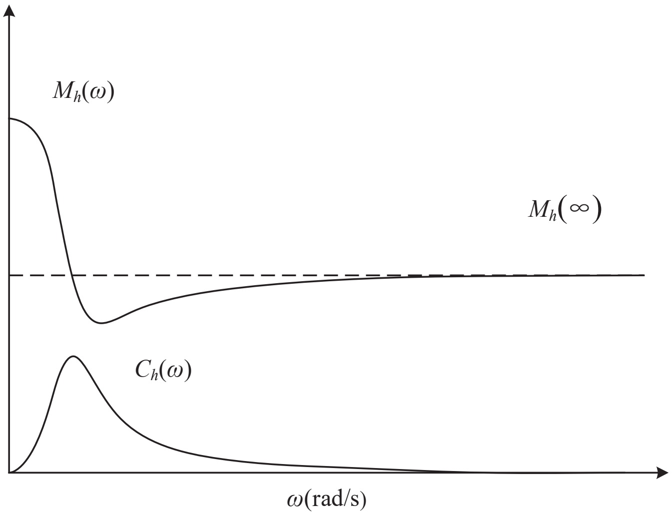

Figure 2. Typical frequency-dependent added mass and damping coefficients for water–cylinder interaction.

Therefore, the radiation force F_{Rad} can be rewritten as the following dynamic stiffness relationship:

$$F_{Rad} = -S_h(\omega)U = -H_h(\omega)U + M_h(\infty)\omega^2 U \tag{13}$$

$$H_h(\omega) = -m_h(\omega)\omega^2 + \mathrm{i}\omega C_h(\omega) \tag{14}$$

where $S_h(\omega)$ and $H_h(\omega)$ denote the dynamic stiffness coefficient.

Correspondingly, the discrete hydrodynamic force on the circular cylinder at ith node with vertical coordinate equal to z_i ($F^r_{x,i}$) can be expressed as:

$$F^r_{x,i}(z_i) = -S_{h,i}(\omega)U_i(\omega) = -\left[H_{h,i}(\omega) - M_{h,i}(\infty)\omega^2\right]U_i(\omega) \tag{15}$$

$$H_{h,i}(\omega) = -m_{h,i}(\omega)\omega^2 + \mathrm{i}\omega C_{h,i}(\omega) \tag{16}$$

According to Equation (10), $M_{h,i}(\infty)$, $m_{h,i}(\omega)$ and $C_{h,i}(\omega)$ can be expressed as:

$$M_{h,i}(\infty) = \mathrm{Re}\left[w_i \rho \pi a^2 \sum_{j=0}^{\infty} d_j S_j \frac{\cosh(k_j \times \infty)}{k_j \sinh k_j h}\right] \tag{17}$$

$$m_{h,i}(\omega) = \mathrm{Re}\left[w_i \rho \pi a^2 \sum_{j=0}^{\infty} d_j S_j \frac{\cosh k_j z_i}{k_j \sinh k_j h}\right] - M_i(\infty) \tag{18}$$

$$C_{h,i}(\omega) = -\mathrm{Im}\left[w_i \rho \pi a^2 \omega \sum_{j=0}^{\infty} d_j S_j \frac{\cosh k_j z_i}{k_j \sinh k_j h}\right] \tag{19}$$

where Re and Im denote extracting the real part and imaginary part; and $w_i = |z_{i+1} - z_{i-1}|/2$.

Although the solution in the frequency domain in Equation (15) can be transformed back into time domain by the inverse Fourier transform, the convolution involved in this process introduces temporal globality. As a result, the response at a given instant is dependent on the responses at all the preceding instants. This significantly increases the computational cost, particularly for long-duration simulations, compared with direct time-domain integration methods. In addition, the frequency-domain method has limitations in accounting for structural nonlinearities. To overcome these issues, a high-order time-domain approximation based on the temporal localization method is adopted to solve

Equaiton (16). Specifically, the frequency-independent added mass $M_{h,i}(\omega)$ is replaced by a mass element. Then, the frequency-dependent dynamic stiffness coefficient $H_{h,i}(\omega)$ are approximated as a rational function as given in Equation (20). Finally, the rational function is equivalently transformed into time domain equivalently by introducing the auxiliary variables, which will be elaborately introduced in Section 4.

The rational approximation function of the dynamic stiffness coefficient $H_{h,i}(\omega)$ can be expressed as

$$H_{h,i}(\omega) \approx \widetilde{H}_{h,i}(\omega) = \rho\pi a^2 \frac{p_0 + p_1(\mathrm{i}\omega) + \cdots + p_{N+1}(\mathrm{i}\omega)^{N+1}}{q_0 + q_1(\mathrm{i}\omega) + \cdots + q_N(\mathrm{i}\omega)^N} \tag{20}$$

where N is the order number of the rational function, with higher values of N leading to improved approximation accuracy; and p_n (n = 0,. . ., N + 1) and q_n (n = 0,. . ., N) are the undetermined real constants.

Furthermore, the dynamic stiffness coefficient $S_{h,i}(\omega)$ is rewritten as

$$S_{h,i}(\omega) \approx \rho\pi a^2 \frac{p_0 + p_1(\mathrm{i}\omega) + \cdots + p_{N+1}(\mathrm{i}\omega)^{N+1}}{q_0 + q_1(\mathrm{i}\omega) + \cdots + q_N(\mathrm{i}\omega)^N} - M_h(\omega)\omega^2 \tag{21}$$

To identify the coefficients of the rational function in Equation (20), numerical methods are required. The least-squares method is commonly employed to approximate the frequency-domain data obtained from Equation (16) by the rational function form expressed in Equation (20) [25]. By substituting $s = i\omega$, Equation (20) can be expressed in transfer function form without altering its coefficients, which facilitates stability analysis. According to modern control theory [26], a stable transfer function requires all poles to have negative real parts, as indicated in Equation (22). However, conventional identification methods [25] do not guarantee this condition and may yield transfer functions with poles in the right-half complex plane, leading to instability. For water–cylinder interaction systems, such unstable transfer function would cause divergent structural responses and physically unrealistic results. To avoid this, stability constraints-such as those defined in Equation (22)—must be enforced during the identification process.

$$\mathrm{Re}(\text{roots of } q) < 0 \tag{22}$$

To this end, a more flexible identification method capable of incorporating nonlinear constraints is needed. Inspired by the strategy proposed by Tang et al. [27] for identifying frequency response functions in semi-infinite media, this study adopts a hybrid identification method combining Genetic Algorithm (GA) and Sequential Quadratic Programming (SQP). The method takes advantage of GA's global search capability and SQP's high local optimization accuracy to ensure both stability and precision. Specifically, GA is used to explore the global parameter space and locate promising solutions, though its accuracy is limited. On the other hand, SQP can refine these solutions with high precision, but it is sensitive to initial guesses and may become trapped in local optima or even fail to converge if poor initial solutions are used. The hybrid method first employs GA for global exploration and selects a few well-performing individuals as initial guesses for SQP, which then performs independent local optimization. Moreover, this hybrid framework allows the stability constraint in Equation (22) to be flexibly incorporated as a nonlinear constraint in the optimization process. The overall identification procedure used in this study is illustrated in Figure 3.

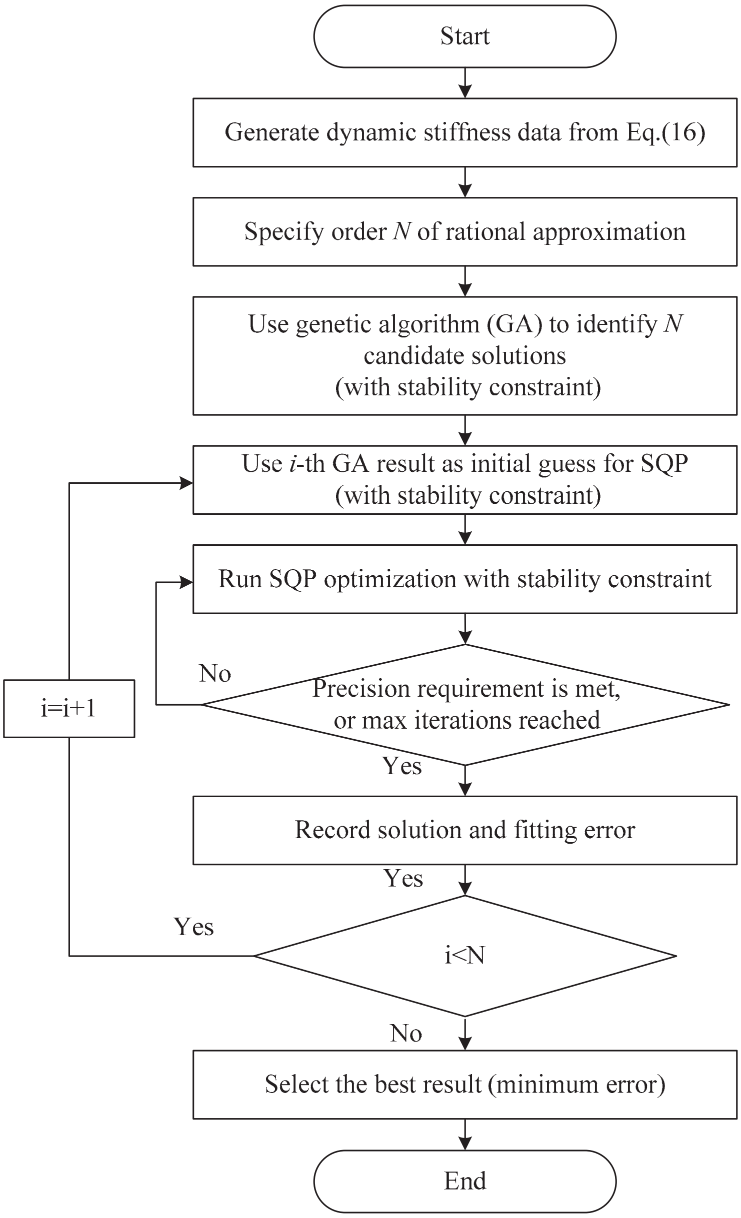

Figure 3. Schematic of the hybrid identification method combining Genetic Algorithm (GA) and Sequential Quadratic Programming (SQP).

To evaluate the effectiveness of the proposed method, a numerical simulation case is conducted. The cylindrical structure is defined with a radius of a = 2 m and a water depth of h = 40 m, where the number of modes is J = 20. Based on this configuration, frequency-domain dynamic stiffness data are generated from Equation (16) and used as input for the identification procedure. The order N of the rational approximation function is set to 7. The GA is configured with a population size of 50, from which the top 20 individuals are chosen as initial solutions for SQP refinement. Each candidate is then independently optimized using SQP, with a maximum iteration limit of 5000 and a convergence tolerance of 10^{-12}. Such a strict tolerance is intentionally chosen to fully exploit the allowed iterations and achieve the highest possible refinement accuracy for each candidate, thereby enhancing the overall identification precision. It should be noted that these settings are provided as an illustrative example; researchers can adjust the parameters according to their specific objectives and practical requirements. Figure 4 presents the comparison between the identified and target dynamic stiffness-both magnitude and phase-at various vertical locations.

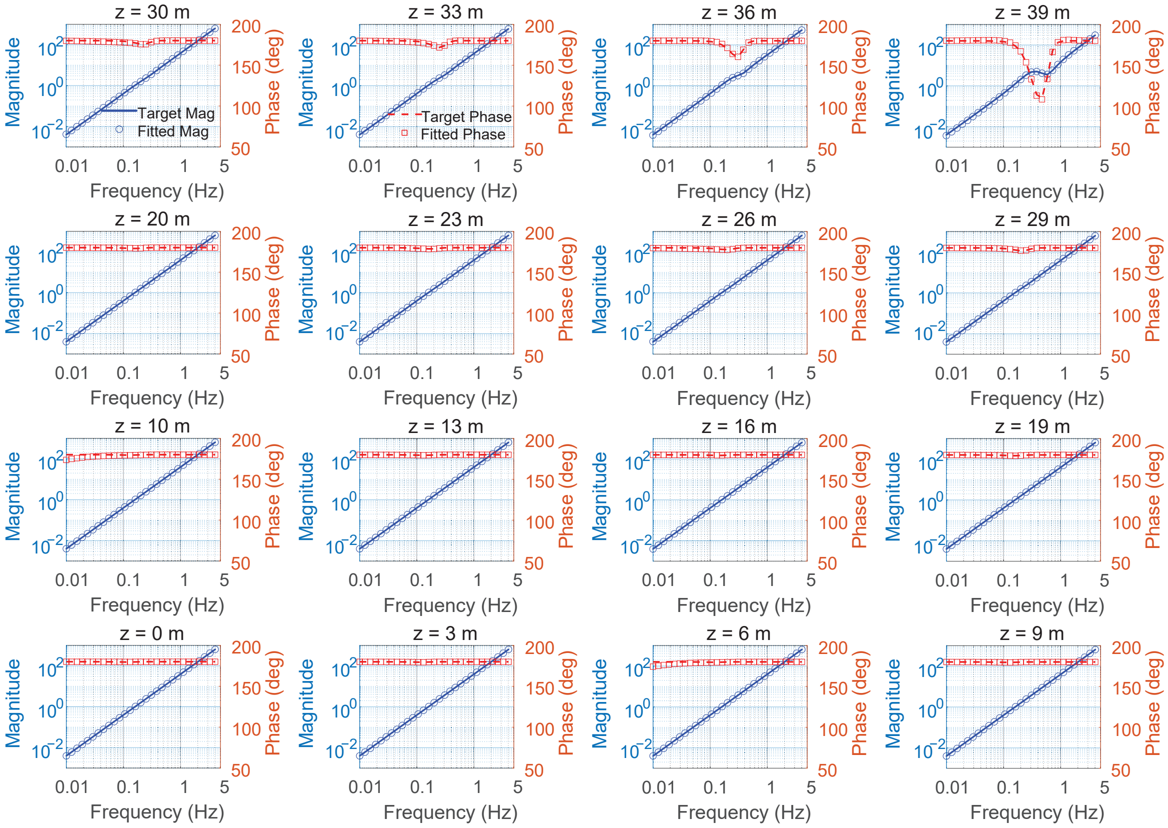

Figure 4. Comparison of the magnitude and phase of dynamic stiffness at different vertical positions with those of the fitted rational approximation.

Blue circles represent the fitted magnitude, and blue solid lines denote the target magnitude. Red squares indicate the fitted phase, while red dashed lines correspond to the target phase. The results show that at lower vertical positions, the dynamic stiffness behaves approximately as added inertia, with magnitude proportional to the square of frequency and phase close to 180°. Above approximately 30 m height, the dynamic stiffness exhibits significant variations due to wave motion effects. The proposed identification method accurately captures both magnitude and phase across these positions, confirming its effectiveness in modeling frequency-dependent hydrodynamic behavior.

4. Method of Auxiliary Variable Realization

According to the time-domain mechanical model proposed by the authors [28,29], the dynamic stiffness relation in Equation (15) with the dynamic stiffness replaced by the rational function in Equation (21) can be equivalently transformed into a spring-dashpot-mass model shown in Figure 5. It should be noted that the spring-dashpot-mass model by the authors [28,29] has been used to solve the artificial boundary condition absorbing scattered waves and pile–soil interaction. However, this model does not take into account the frequency-independent added mass in Equation (21). Therefore, the new spring-dashpot-mass model in the present study added a parallel mass element ($M_{m,0}$), as shown in Figure 5.

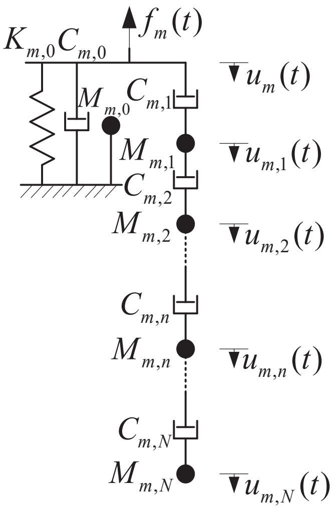

Figure 5. The spring-dashpot-mass model.

For the hydrodynamic force acting on the cylinder at node *m*, the dynamic equation in the time domain can be expressed as follows:

$$M_{m,0}\ddot{u}_m + (C_{m,0} + C_{m,1})\dot{u}_m + K_{m,0}u_m - C_{m,1}u_{m,1} = -f_m \tag{23}$$

$$\mathbf{M}_m^{\infty}\ddot{\mathbf{u}}_m + \mathbf{C}_m^{\infty}\dot{\mathbf{u}}_m + \mathbf{f}_m = \mathbf{0} \tag{24}$$

with

$$\mathbf{u}_m = \begin{Bmatrix} u_{m,1} & u_{m,2} & \cdots & u_{m,N} \end{Bmatrix}^{\mathrm{T}} \tag{25}$$

$$\mathbf{f}_m = \begin{Bmatrix} C_{m,1}\dot{u}_m & 0 & \cdots & 0 \end{Bmatrix}^{\mathrm{T}} \tag{26}$$

$$\mathbf{M}_m^{\infty} = \begin{bmatrix} M_{m,1} & 0 & 0 & \cdots & 0 & 0 \\ 0 & M_{m,2} & 0 & \cdots & 0 & 0 \\ 0 & 0 & M_{m,3} & \cdots & 0 & 0 \\ \vdots & \vdots & \vdots & \ddots & \vdots & \vdots \\ 0 & 0 & 0 & \cdots & M_{m,N-1} & 0 \\ 0 & 0 & 0 & \cdots & 0 & M_{m,N} \end{bmatrix} \tag{27}$$

$$\mathbf{C}_m^{\infty} = \begin{bmatrix} C_{m,1} + C_{m,2} & -C_{m,2} & 0 & \cdots & 0 & 0 \\ -C_{m,2} & C_{m,2} + C_{m,3} & -C_{m,3} & \cdots & 0 & 0 \\ 0 & -C_{m,3} & C_{m,3} + C_{m,4} & \cdots & 0 & 0 \\ \vdots & \vdots & \vdots & \ddots & \vdots & \vdots \\ 0 & 0 & 0 & \cdots & C_{m,N-1} + C_{m,N} & -C_{m,N} \\ 0 & 0 & 0 & \cdots & -C_{m,N} & C_{m,N} \end{bmatrix} \tag{28}$$

where u_m and f_m are the time-domain values of U_m and F_m, respectively; $u_{m,n}$ ($n = 0,\ldots, N$) are the real auxiliary variables corresponding to the auxiliary degrees of freedom in the time-domain mechanical model; $M_{m,0} = M_m(\infty)$; and $K_{m,0}$, $C_{m,0}$ for $n = 0,\ldots, N$ as well as $M_{m,\mathrm{n}}$ ($n = 0,\ldots, N$) are the undetermined real constants, respectively. These dimensionless constants can be obtained from the coefficients of the rational function, as detailed in [30]. It should be noted that the damping matrix $\mathbf{C}_m$ denotes the radiative damping of the fluid due to the radiation waves generated by the motion of the cylinder at node with number *m*.

Time-Domain Mechanical Model

The finite element equation in the time domain for a cylinder vibrating in water can be expressed as a partitioned matrix form:

$$\begin{bmatrix} \mathbf{M}_I & 0 \\ 0 & \mathbf{M}_B \end{bmatrix} \begin{Bmatrix} \ddot{\mathbf{u}}_I \\ \ddot{\mathbf{u}}_B \end{Bmatrix} + \begin{bmatrix} \mathbf{C}_I & \mathbf{C}_{IB} \\ \mathbf{C}_{BI} & \mathbf{C}_B \end{bmatrix} \begin{Bmatrix} \dot{\mathbf{u}}_I \\ \dot{\mathbf{u}}_B \end{Bmatrix} + \begin{bmatrix} \mathbf{K}_I & \mathbf{K}_{IB} \\ \mathbf{K}_{BI} & \mathbf{K}_B \end{bmatrix} \begin{Bmatrix} \mathbf{u}_I \\ \mathbf{u}_B \end{Bmatrix} = \begin{Bmatrix} 0 \\ \mathbf{f}_W \end{Bmatrix} + \begin{Bmatrix} \mathbf{f}_I \\ \mathbf{f}_B \end{Bmatrix} \tag{29}$$

where the subscripts I and B denote the nodes of the cylinder in air and water, respectively; $\mathbf{u}$ is the displacement vector, and the dot over the variable denotes the derivative with respect to time; **M**, **K,** and **C** represent the lumped mass, stiffness, and damping matrices, respectively. **f** denotes the node force vector; $\mathbf{f}_I$ and $\mathbf{f}_B$ are the discrete all external loads on the nodes in air and water, respectively; $\mathbf{f}_W$ is the discrete hydrodynamic force on the nodes in water due to the motion of the cylinder.

The element mass and stiffness matrices of the cylinder used in the present study are expressed as follows:

$$\mathbf{M_e} = m_e \begin{bmatrix} \frac{1}{2} & 0 & 0 & 0 \\ 0 & \frac{l^2}{78} & 0 & 0 \\ 0 & 0 & \frac{1}{2} & 0 \\ 0 & 0 & 0 & \frac{l^2}{78} \end{bmatrix} \tag{30}$$

$$\mathbf{K_e} = \frac{EI_e}{l^3} \begin{bmatrix} 12 & 6l & -12 & 6l \\ 6l & 4l^2 & -6l & 2l^2 \\ -12 & -6l & 12 & -6l \\ 6l & 2l^2 & -6l & 4l^2 \end{bmatrix} \tag{31}$$

where $\mathbf{M}_e$ and $\mathbf{K}_e$ are the element mass and stiffness matrices, respectively; l is the length of the element; E is the elasticity modulus of the pile; m_e is the unit mass; and I_e is the unit moment of inertia.

For a cylinder with Q nodes in water, the vector $\mathbf{f}_W$ can be expressed as follows:

$$\mathbf{f}_W = \begin{Bmatrix} f_1 & \cdots & f_m & \cdots & f_Q \end{Bmatrix}^{\mathrm{T}} \tag{32}$$

where the nodal hydrodynamic force f_m is obtained by Equation (19).

Substituting Equation (23) into Equation (32), we can obtain the following:

$$-\left[\mathbf{M}_B^{\infty}\ddot{\mathbf{u}}_B + \mathbf{C}_B^{\infty}\dot{\mathbf{u}}_B + \mathbf{K}_B^{\infty}\mathbf{u}_B + \mathbf{C}_{Q1B}^{\infty}\mathbf{u}_{Q1}^{\infty}\right] = \mathbf{f}_W \tag{33}$$

$$\mathbf{M}_B^{\infty} = \begin{bmatrix} m_{w,1} & 0 & 0 & 0 & 0 \\ 0 & m_{w,2} & 0 & 0 & 0 \\ 0 & 0 & \ddots & 0 & 0 \\ 0 & 0 & 0 & m_{w,M-1} & 0 \\ 0 & 0 & 0 & 0 & m_{w,M} \end{bmatrix} \tag{34}$$

$$\mathbf{K}_B^{\infty} = \begin{bmatrix} K_{1,0} & 0 & 0 & 0 & 0 \\ 0 & K_{2,0} & 0 & 0 & 0 \\ 0 & 0 & \ddots & 0 & 0 \\ 0 & 0 & 0 & K_{M-1,0} & 0 \\ 0 & 0 & 0 & 0 & K_{M,0} \end{bmatrix} \tag{35}$$

$$\mathbf{C}_B^{\infty} = \begin{bmatrix} C_{1,0}+C_{1,1} & 0 & 0 & 0 & 0 \\ 0 & C_{2,0}+C_{2,1} & 0 & 0 & 0 \\ 0 & 0 & \ddots & 0 & 0 \\ 0 & 0 & 0 & C_{M-1,0}+C_{M-1,1} & 0 \\ 0 & 0 & 0 & 0 & C_{M,0}+C_{M,1} \end{bmatrix} \tag{36}$$

$$\mathbf{C}_{Q1B}^{\infty} = \begin{bmatrix} -C_{1,1} & 0 & 0 & 0 & 0 \\ 0 & -C_{2,1} & 0 & 0 & 0 \\ 0 & 0 & \ddots & 0 & 0 \\ 0 & 0 & 0 & -C_{Q-1,1} & 0 \\ 0 & 0 & 0 & 0 & -C_{Q,1} \end{bmatrix} \tag{37}$$

$$\mathbf{u}_{Q1}^{\infty} = \begin{Bmatrix} u_{1,1} & u_{2,1} & \dots & u_{Q,1} \end{Bmatrix}^{\mathrm{T}} \tag{38}$$

By substituting Equation (33) into Equation (29), the dynamic equation can be rewritten as the following:

$$\begin{bmatrix} \mathbf{M}_I & 0 \\ 0 & \mathbf{M}_B+\mathbf{M}_B^{\infty} \end{bmatrix} \begin{Bmatrix} \ddot{\mathbf{u}}_I \\ \ddot{\mathbf{u}}_B \end{Bmatrix} + \begin{bmatrix} \mathbf{C}_I & \mathbf{C}_{IB} \\ \mathbf{C}_{BI} & \mathbf{C}_B+\mathbf{C}_B^{\infty} \end{bmatrix} \begin{Bmatrix} \dot{\mathbf{u}}_I \\ \dot{\mathbf{u}}_B \end{Bmatrix} + \begin{bmatrix} \mathbf{K}_I & \mathbf{K}_{IB} \\ \mathbf{K}_{BI} & \mathbf{K}_B\mathbf{K}_B^{\infty} \end{bmatrix} \begin{Bmatrix} \mathbf{u}_I \\ \mathbf{u}_B \end{Bmatrix} = \begin{Bmatrix} 0 \\ -\mathbf{C}_{Q1B}^{\infty}\mathbf{u}_{Q1}^{\infty} \end{Bmatrix} + \begin{Bmatrix} \mathbf{f}_I \\ \mathbf{f}_B \end{Bmatrix} \tag{39}$$

According to Equation (24), we can obtain the following dynamic equation:

$$\mathbf{M}_Q\ddot{\mathbf{u}}_Q + \mathbf{C}_Q\dot{\mathbf{u}}_Q + \mathbf{f}_{QB} = 0 \tag{40}$$

$$\mathbf{M}_Q = \begin{bmatrix} \mathbf{M}_1^{\infty} & \mathbf{0} & \mathbf{0} & \mathbf{0} & \mathbf{0} \\ \mathbf{0} & \mathbf{M}_2^{\infty} & \mathbf{0} & \mathbf{0} & \mathbf{0} \\ \vdots & \vdots & \ddots & \vdots & \vdots \\ \mathbf{0} & \mathbf{0} & \cdots & \mathbf{M}_{Q-1}^{\infty} & \mathbf{0} \\ \mathbf{0} & \mathbf{0} & \cdots & \mathbf{0} & \mathbf{M}_Q^{\infty} \end{bmatrix} \tag{41}$$

$$\mathbf{C}_Q = \begin{bmatrix} \mathbf{C}_1^{\infty} & \mathbf{0} & \mathbf{0} & \mathbf{0} & \mathbf{0} \\ \mathbf{0} & \mathbf{C}_2^{\infty} & \mathbf{0} & \mathbf{0} & \mathbf{0} \\ \vdots & \vdots & \ddots & \vdots & \vdots \\ \mathbf{0} & \mathbf{0} & \cdots & \mathbf{C}_{Q-1}^{\infty} & \mathbf{0} \\ \mathbf{0} & \mathbf{0} & \cdots & \mathbf{0} & \mathbf{C}_Q^{\infty} \end{bmatrix} \tag{42}$$

$$\mathbf{f}_{QB} = \begin{Bmatrix} \mathbf{f}_1 & \mathbf{f}_2 & \cdots & \mathbf{f}_Q \end{Bmatrix}^{\mathrm{T}} \tag{43}$$

$$\mathbf{u}_Q = \begin{Bmatrix} \mathbf{u}_1 & \mathbf{u}_2 & \cdots & \mathbf{u}_Q \end{Bmatrix}^{\mathrm{T}} \tag{44}$$

According to Equations (25), (26), (37)–(44), the final dynamic equation can be expressed as follows:

$$\mathbf{M}\ddot{\mathbf{u}} + \mathbf{C}\dot{\mathbf{u}} + \mathbf{K}\mathbf{u} = \mathbf{f} \tag{45}$$

where $\mathbf{u}$, $\mathbf{M}$, $\mathbf{C}$, and $\mathbf{K}$ are the total displacement vector, mass matrix, damping matrix, and stiffness matrix, respectively. It should be noted that the damping matrix $\mathbf{C}$ denotes the total damping effects due to the structural damping and the radiative damping of the fluid. The detailed process of obtaining $\mathbf{u}$, $\mathbf{M}$, $\mathbf{C}$ and $\mathbf{K}$ can be expressed as:

$$\mathbf{u} = \begin{Bmatrix} \mathbf{u}_I^{\mathrm{T}} & \mathbf{u}_B^{\mathrm{T}} & \mathbf{u}_1^{\mathrm{T}} & \mathbf{u}_2^{\mathrm{T}} & \dots & \mathbf{u}_M^{\mathrm{T}} \end{Bmatrix}^{\mathrm{T}} \tag{46}$$

$$\mathbf{f} = \begin{Bmatrix} \mathbf{f}_I & \mathbf{f}_B & \mathbf{0} & \mathbf{0} & \cdots & \mathbf{0} \end{Bmatrix}^{\mathrm{T}} \tag{47}$$

$$\mathbf{M} = \begin{bmatrix} \mathbf{M}_I & \mathbf{0} & \mathbf{0} & \mathbf{0} & \cdots & \mathbf{0} & \mathbf{0} \\ \mathbf{0} & \mathbf{M}_B + \mathbf{M}_B^\infty & \mathbf{0} & \mathbf{0} & \cdots & \mathbf{0} & \mathbf{0} \\ \mathbf{0} & \mathbf{0} & \mathbf{M}_1^\infty & \mathbf{0} & \cdots & \mathbf{0} & \mathbf{0} \\ \mathbf{0} & \mathbf{0} & \mathbf{0} & \mathbf{M}_2^\infty & \cdots & \mathbf{0} & \mathbf{0} \\ \vdots & \vdots & \vdots & \vdots & \ddots & \vdots & \vdots \\ \mathbf{0} & \mathbf{0} & \mathbf{0} & \mathbf{0} & \cdots & \mathbf{M}_{M-1}^\infty & \mathbf{0} \\ \mathbf{0} & \mathbf{0} & \mathbf{0} & \mathbf{0} & \cdots & \mathbf{0} & \mathbf{M}_M^\infty \end{bmatrix} \tag{48}$$

$$\mathbf{C} = \begin{bmatrix} \mathbf{C}_I & \mathbf{C}_{IB} & \mathbf{0} & \mathbf{0} & \cdots & \mathbf{0} & \mathbf{0} \\ \mathbf{C}_{BI} & \mathbf{C}_B + \mathbf{C}_B^\infty & \mathbf{C}_{B1}^\infty & \mathbf{C}_{B2}^\infty & \cdots & \mathbf{C}_{B(M-1)}^\infty & \mathbf{C}_{BM}^\infty \\ \mathbf{0} & \mathbf{C}_{1B}^\infty & \mathbf{C}_1^\infty & \mathbf{0} & \cdots & \mathbf{0} & \mathbf{0} \\ \mathbf{0} & \mathbf{C}_{2B}^\infty & \mathbf{0} & \mathbf{C}_2^\infty & \cdots & \mathbf{0} & \mathbf{0} \\ \vdots & \vdots & \vdots & \vdots & \ddots & \vdots & \vdots \\ \mathbf{0} & \mathbf{C}_{(M-1)B}^\infty & \mathbf{0} & \mathbf{0} & \cdots & \mathbf{C}_{M-1}^\infty & \mathbf{0} \\ \mathbf{0} & \mathbf{C}_{MB}^\infty & \mathbf{0} & \mathbf{0} & \cdots & \mathbf{0} & \mathbf{C}_M^\infty \end{bmatrix} \tag{49}$$

$$\mathbf{K} = \begin{bmatrix} \mathbf{K}_I & \mathbf{K}_{IB} & \mathbf{0} & \mathbf{0} & \cdots & \mathbf{0} & \mathbf{0} \\ \mathbf{K}_{BI} & \mathbf{K}_B + \mathbf{K}_B^\infty & \mathbf{0} & \mathbf{0} & \cdots & \mathbf{0} & \mathbf{0} \\ \mathbf{0} & \mathbf{0} & \mathbf{0} & \mathbf{0} & \cdots & \mathbf{0} & \mathbf{0} \\ \mathbf{0} & \mathbf{0} & \mathbf{0} & \mathbf{0} & \cdots & \mathbf{0} & \mathbf{0} \\ \vdots & \vdots & \vdots & \vdots & \ddots & \vdots & \vdots \\ \mathbf{0} & \mathbf{0} & \mathbf{0} & \mathbf{0} & \cdots & \mathbf{0} & \mathbf{0} \\ \mathbf{0} & \mathbf{0} & \mathbf{0} & \mathbf{0} & \cdots & \mathbf{0} & \mathbf{0} \end{bmatrix} \tag{50}$$

$$\mathbf{C}_{Bm}^\infty = \mathbf{C}_{mB}^{\infty\mathrm{T}} = -C_{m,1} \begin{bmatrix} 1 & 0 & \cdots & 0 & 0 \end{bmatrix} \tag{51}$$

Equation (45) can be solved by the standard direct time integration algorithms, such as the implicit Newmark and Wilson algorithms and the explicit central difference algorithm. In this study, the Newmark-β method is adopted to solve Equation (45).

Based on the above developments, the order of computing each component of the developed model can be summarized as follows. First, the discrete added mass $M_{h,i}(\infty)$ and $m_{h,i}(\omega)$, as well as the added damping $C_{h,i}(\omega)$, are obtained by Equations (17)–(19). Correspondingly, the dynamic stiffness coefficient $H_{h,i}(\omega)$ is calculated by Equation (16). Second, the exact dynamic stiffness coefficient $H_{h,i}(\omega)$ is then transformed into the form of rational approximation shown in Equation (20) by using the hybrid identification method combining Genetic Algorithm and Sequential Quadratic Programming. Third, the real constants p_n and q_n obtained in Equation (20) are used to calculate the value of spring, dashpot, and mass in Equations (23) and (24). Fourth, the element mass and stiffness matrices of the cylinder are obtained by Equations (30) and (31). Fifth, the finite element equation, Equation (45), is obtained by integrating external loads and boundary conditions, the element mass and stiffness matrices of the cylinder, and the spring, dashpot and mass matrices of the water–cylinder interaction. Finally, the finite element equation, Equation (45), is solved using the Newmark-β method.

5. Results and Discussions

In this section, the developed method is applied to investigate the effects of free surface waves on the dynamic responses of the circular cylinder subjected to wave and earthquake loadings. The water density is ρ = 1000 kg/m^3 and the water depth is h = 40 m. The radius of the cylinder is a = 2 m, and its length is equal to the water depth. The cylinder is uniformly discretized into twenty elements along the vertical direction. The elastic modulus and density of the cylinder are 30 GPa and 2500 kg/m^3, respectively. The variation in the natural vibration period is achieved by adjusting the mass of the upper structure, where the mass ratio R_m, defined as the ratio of the structural mass to the mass of displaced water, was used to denote variation in structural mass. Rayleigh damping is used to consider the damping effect of the structure, with the damping ratio denoted by ξ.

The analytical solution of the wave force on a circular cylinder developed by MacCamy and Fuchs [15] is adopted in this study. The resultant circumferential wave force on the circular cylinder at height z (f^I) is expressed as follows:

$$f^I(z) = \rho \frac{2gH_w \cosh(kz)}{k\cosh(kh)} A(ka)\sin(\omega_0 t) \tag{52}$$

$$A(ka) = \frac{1}{\sqrt{\left[J_1'(ka)\right]^2 + \left[Y_1'(ka)\right]^2}} \tag{53}$$

$$gk_0 \tanh(k_0 h) = \omega_0^2 \tag{54}$$

where k denotes the wave number, $\omega_0 = 2\pi/T_w$ is the wave angular frequency, T_w denotes the wave period, H_w denotes the wave height, $J_1(\cdot)$ is the Bessel function of order one of the first kind, $Y_n(\cdot)$ is the Bessel function of order one of the second kind, and the prime denotes a derivative with respect to the argument. The wave height is $H_w = 4$ m in the present study.

To investigate the effects of water–cylinder interaction on seismic responses, three seismic waves—Chichi, El-Centro, and Christchurch earthquakes—are considered. The acceleration time history and frequency spectrum of the three seismic waves are shown in Figure 6, with a peak acceleration of 0.1 g. The time history of the corresponding ground displacement can be extracted by integration of acceleration.

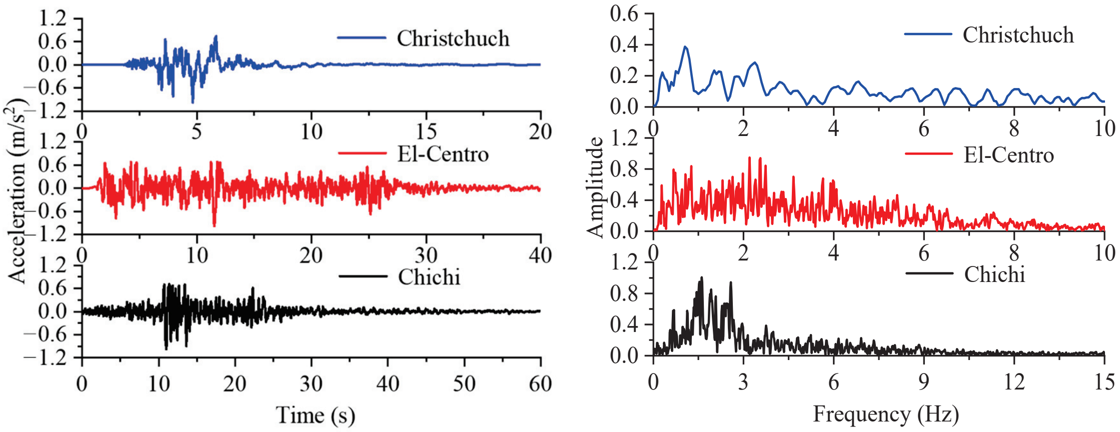

(**a**) (**b**)

Figure 6. Acceleration curves of seismic waves: (**a**) time history; and (**b**) amplitude of the frequency spectrum.

The dynamic responses of the cylinder are analyzed under three scenarios: neglecting water–cylinder interaction, considering water–cylinder interaction with the boundary condition of free surface waves, and considering water–cylinder interaction while neglecting the boundary condition of free surface waves. For brevity, these cases are denoted as "No water–cylinder interaction", "With free waves," and "Without free waves," respectively. The simulation parameters used in the present study are given in Table 1. In addition, the simulated cases for the wave and earthquake loads are given in Table 2. The convergence tests for time step sizes and mesh independence are first conducted in the case of a cylinder under wave load with wave period $T_w = 8$ s, mass ratio $R_m = 5.08$, and damping ratio ξ

= 0.02. The results of the convergence test for time step sizes and mesh independence verification are given in Tables 3 and 4, respectively. It can be seen that the time step size for the Newmark-β method set as 0.01 s, and the element size set as 2 m are sufficient in the present study.

Table 1. The simulation parameters used in the present study.

Parameter	Value
Water density	1000 kg/m^3
Water depth	40 m
Radius of the cylinder	2 m
Elastic modulus of the cylinder	30 GPa
Density of the cylinder	2500 kg/m^3
Peak acceleration of seismic waves	0.1 g
Wave height	4 m

Table 2. The simulated cases for the wave and earthquake loads.

Case	Mass Ratio	Damping Ratio
Wave load: wave period set as 3 s to 10 s	2.5, 5.08, 7.66, 12.82	0.0, 0.005, 0.01, 0.02, 0.05
Seismic waves: Chichi, El-Centro, Christchurch	2.5 to 12.82	0.0, 0.005, 0.01, 0.02, 0.05

Table 3. Convergence test for time step sizes.

Time Step (s)	Displacement (m)	Acceleration (m·s^{-2})
0.05	0.01743	−0.01802
0.02	0.01738	−0.01743
0.01	0.01737	−0.01733

Table 4. Mesh independence verification.

Mesh Size (m)	Displacement (m)	Acceleration (m·s^{-2})
4	0.01742	−0.01597
2	0.01737	−0.01734
1	0.01732	−0.01735

5.1. Verification

A cylinder with a mass ratio R_m = 5.08 and a damping ratio ξ = 0.02 is used to verify the proposed method. The results are compared with those obtained from the frequency-domain finite element method (FEM) [5]. Figure 7 shows the comparison of these two methods under wave load with a wave period equal to 8 s, and Figure 8 shows the comparison of these two methods under the El-Centro seismic wave, where the time history of the displacement on the cylinder head is given. It can be seen that the proposed time-domain substructure method agrees well with the frequency-domain FEM. Notably, the computational efficiency of the time-domain substructure method is much higher than that of frequency-domain FEM. For a wave load of 100 s duration, the computation times for the proposed method and frequency-domain FEM are 0.147 s and 18.234 s, respectively. For the El-Centro seismic wave with a duration of 50 s, the corresponding computation times are 0.056 s and 9.048 s, respectively.

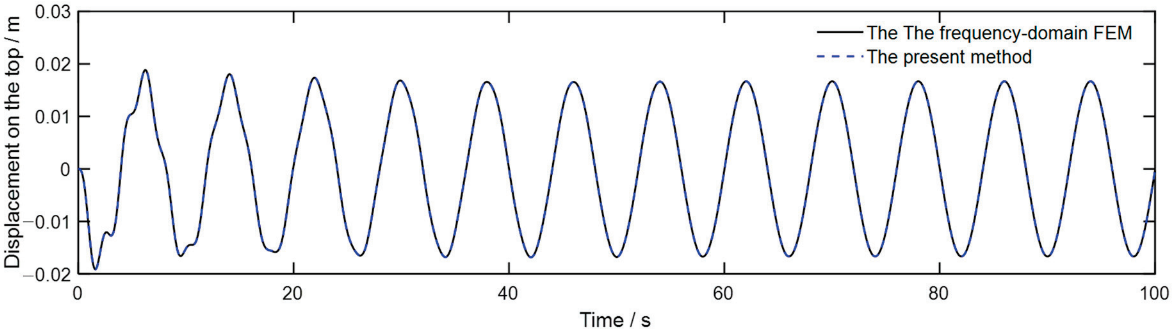

Figure 7. The comparison of proposed method and frequency-domain FEM under wave load with wave period 8 s.

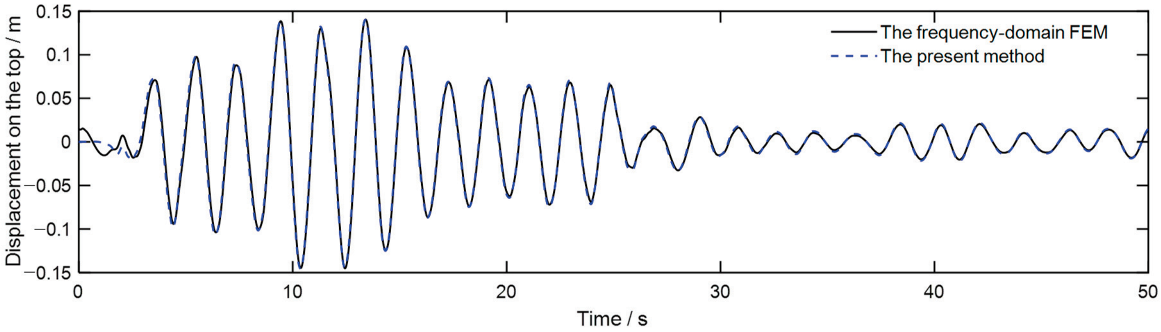

Figure 8. The comparison of proposed method and frequency-domain FEM under *El-Centro* seismic wave.

5.2. Wave Loading

The dynamic responses of the cylinder with the first-order natural vibration period of the cylinder T_s = 3.5 s and mass ratio R_m = 12.83 are first studied, where the wave periods are set as 7 s and 8 s. Figure 9 shows the time history of the displacement on the cylinder head for a damping ratio of 0 and 0.02. Figures 10 and 11 show the maximum bending moment, acceleration, and displacement along the cylinder length with wave periods equal to 3.7 s and 8 s, respectively, where the damping ratio is 0.01. It can be seen that the effects of water–cylinder interaction and free surface waves on the wave responses of the cylinder significantly decrease as the damping ratio of the cylinder increases. Notably, water–cylinder interaction can significantly increase the wave response of the cylinder when its natural frequencies are close to the wave periods. In contrast, this influence is minimal when the wave period is far from the cylinder's natural vibration periods. Moreover, the added damping resulting from the free surface waves can significantly decrease the wave responses of the cylinders when the effects of water–cylinder interaction are large.

A quantitative analysis is further conducted to study the effects of water–cylinder interaction on the dynamic responses of the cylinder, varied with wave period and the first-order natural vibration period of the cylinder (mass ratio). Two dimensionless coefficients, including R_{u1} and R_{M1}, are defined as follows:

$$\begin{aligned} R_{u1} &= \frac{(u_2 - u_1)}{u_1}\%, \\ R_{M1} &= \frac{(M_2 - M_1)}{M_1}\% \end{aligned} \tag{55}$$

where u_1 and M_1 denote the peak top displacement and base bending moment of the cylinder without considering water–cylinder interaction; u_2 and M_2 denote the peak displacement of the cylinder top and bending moment at the base of the cylinder, considering the boundary condition of free surface waves. Figures 12 and 13 show the variation of R_{u1} and R_{M1} with wave period for different mass ratios and damping ratios, respectively. Generally, the water–cylinder interaction tends to increase the displacement and bending moment of the cylinder, and this influence diminishes as the damping ratio increases. However, when the wave period is close to the cylinder's natural vibration period, water–cylinder interaction can significantly reduce the dynamic responses. It can also be seen that the effects of water–cylinder interaction on the dynamic responses of the cylinder become negligible when the wave period exceeds 5 s.

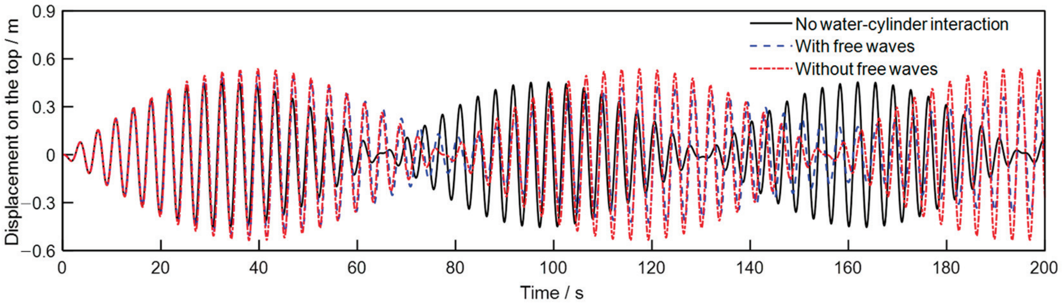

(**a**) $\xi = 0.0$, $T_w = 3.7$ s

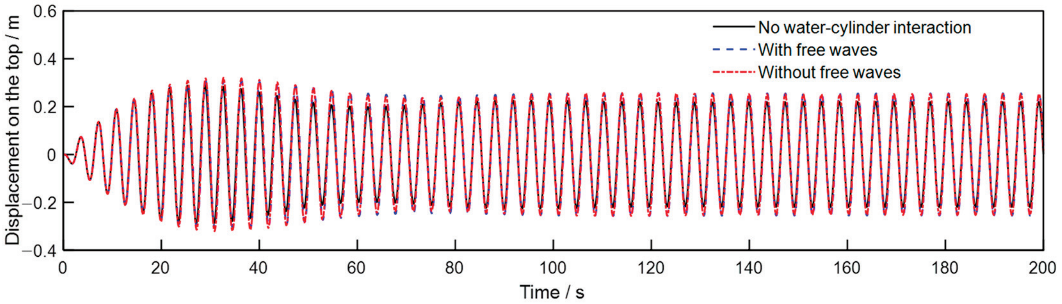

(**b**) $\xi = 0.02$, $T_w = 3.7$ s

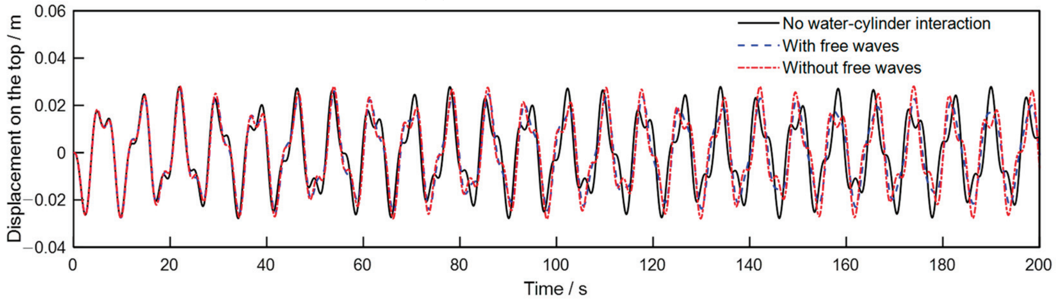

(**c**) $\xi = 0.02$, $T_w = 3.7$ s

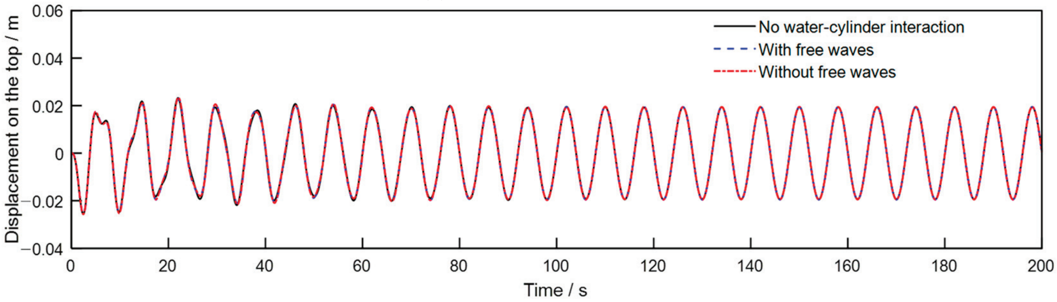

(**d**) $\xi = 0.02$, $T_w = 8$ s

Figure 9. Time history of the displacement on the cylinder head with different wave period and damping ratio: (**a**) damping ratio = 0, wave period = 3.7 s; (**b**) damping ratio = 0.02, wave period = 3.70 s; (**c**) damping ratio = 0, wave period = 8 s; and (**d**) damping ratio = 0.02, wave period = 8 s.

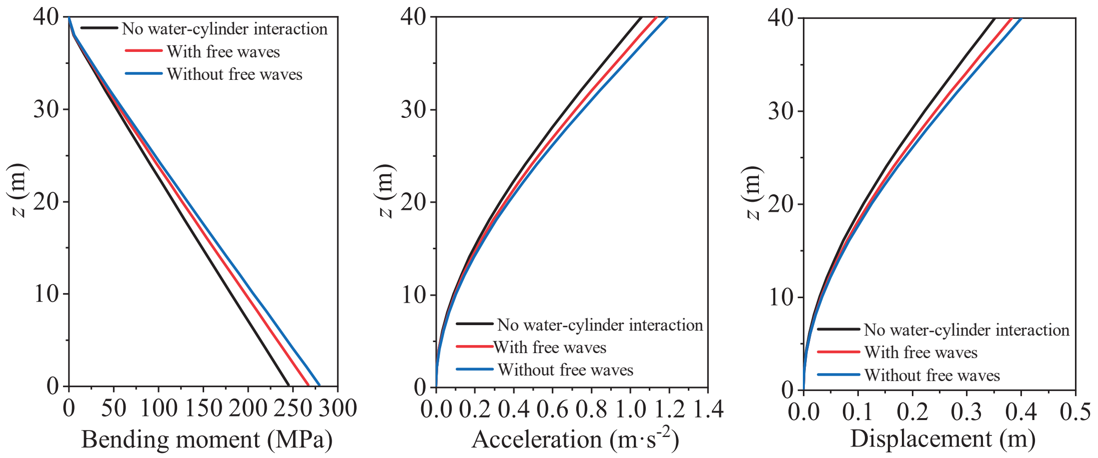

(**a**) Bending moment (**b**) Acceleration (**c**) Displacement

Figure 10. The maximum responses along the length of the cylinder with wave period equal to 3.7 s: (**a**) peak bending moment response; (**b**) peak acceleration response; and (**c**) peak displacement response.

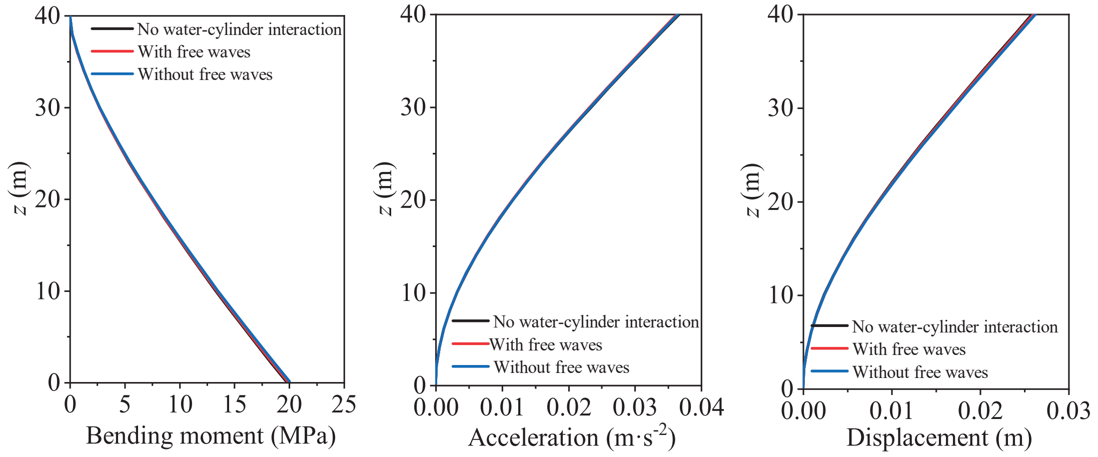

(**a**) Bending moment (**b**) Acceleration (**c**) Displacement

Figure 11. The maximum responses along the length of the cylinder with wave period equal to 8 s: (**a**) peak bending moment response; (**b**) peak acceleration response; and (**c**) peak displacement response.

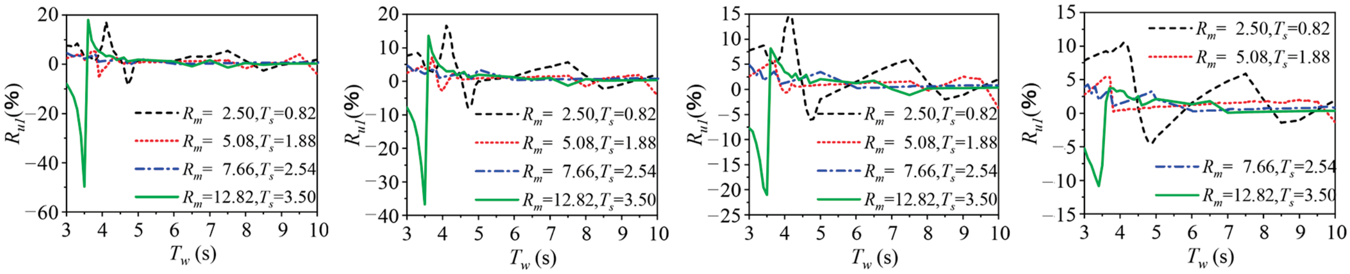

(**a**) $\xi = 0.005$ (**b**) $\xi = 0.01$ (**c**) $\xi = 0.02$ (**d**) $\xi = 0.05$

Figure 12. The dimensionless coefficient R_{u1} varied with wave period for different mass ratio and damping ratio: (**a**) damping ratio = 0.005; (**b**) damping ratio = 0.01; (**c**) damping ratio = 0.02; and (**d**) damping ratio = 0.05.

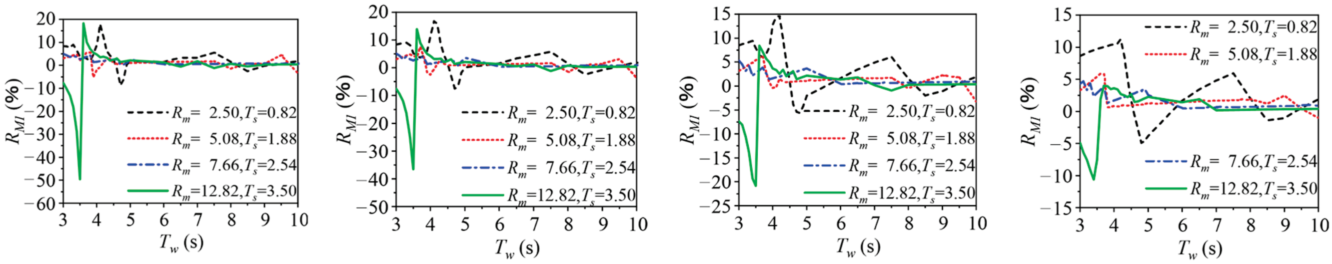

(**a**) ξ = 0.005 (**b**) ξ = 0.01 (**c**) ξ = 0.02 (**d**) ξ = 0.05

Figure 13. The dimensionless coefficient R_{M1} varied with wave period for different mass ratio and damping ratio: (**a**) damping ratio = 0.005; (**b**) damping ratio = 0.01; (**c**) damping ratio = 0.02; and (**d**) damping ratio = 0.05.

Finally, the effects of the boundary condition of free surface waves on the dynamic responses of the cylinder are quantitatively studied, where three dimensionless coefficients, including R_{u2} and R_{M2}, are defined as the following:

$$\begin{aligned} R_{u2} &= \frac{(u_3 - u_2)}{u_2}\%, \\ R_{M2} &= \frac{(M_3 - M_2)}{M_2}\% \end{aligned} \tag{56}$$

where u_3 and M_3 denote the peak top displacement and bending moment of the cylinder without considering the boundary condition of free surface waves. Figures 14 and 15 show the variation of R_{u2} and R_{M2} with wave period for different mass ratios and damping ratios, respectively. Generally, the boundary condition of free surface waves tends to reduce the wave-induced dynamic responses of the cylinder due to the added damping effect, while this influence is less than 5%. However, the boundary condition of free surface waves can significantly decrease the dynamic responses of the cylinder when the wave period is close to the natural vibration period of the cylinder.

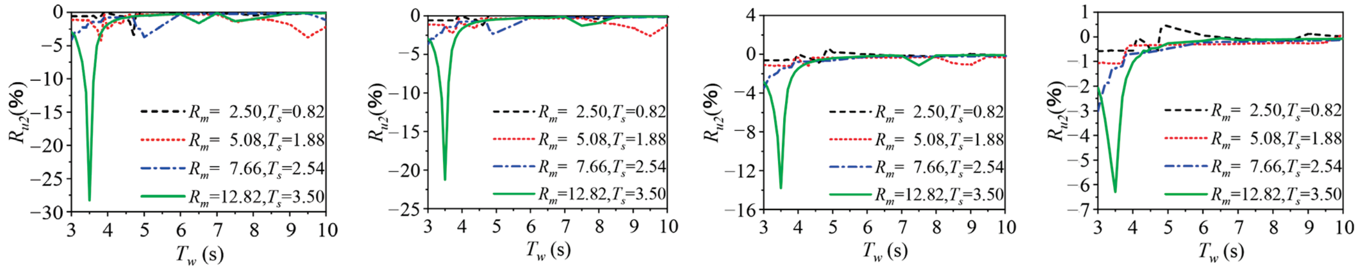

(**a**) ξ = 0.005 (**b**) ξ = 0.01 (**c**) ξ = 0.02 (**d**) ξ = 0.05

Figure 14. The dimensionless coefficient R_{u2} varied with wave period for different mass ratio and damping ratio: (**a**) damping ratio = 0.005; (**b**) damping ratio = 0.01; (**c**) damping ratio = 0.02; and (**d**) damping ratio = 0.05.

5.3. Earthquake Loading

Figures 16–18 show the time history of the displacements at the cylinder head for first-order natural vibration periods of T_s= 0.866 s, 1.88 s, and 3.5 s (R_m = 2.5, 5.0, and 12.83) under Chichi, El-Centro, and Christchurch earthquakes, respectively, with the damping ratio set as 0.02. Figures 19 and 20 show the maximum bending moment, acceleration, and displacement along the length of the cylinder for the Christchurch wave, for mass ratios of 2.5 and 12.83, respectively. It can be seen that the effects of water–cylinder interaction on the seismic responses of the cylinder significantly decrease as the natural vibration period of the cylinder decreases. The water–cylinder interaction may either amplify or reduce the peak responses of the cylinder, depending closely on the frequency spectrum of the seismic wave, as well as the cylinder's natural vibration period and damping ratio. Additionally, the water–cylinder interaction tends to increase the natural vibration period of the cylinder, whereas the free surface waves have little influence on the natural vibration period. It can also be seen that the boundary condition of free surface waves has minimal influence on the seismic responses of the cylinder in the case of $\xi = 0.02$.

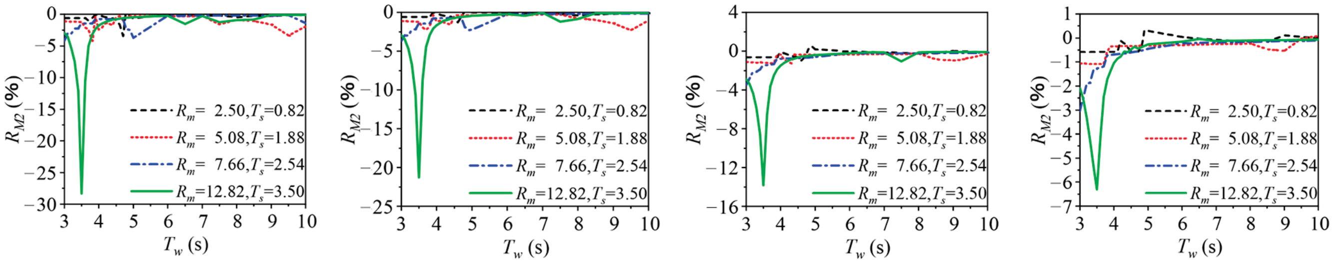

(**a**) $\xi = 0.005$ (**b**) $\xi = 0.01$ (**c**) $\xi = 0.02$ (**d**) $\xi = 0.05$

Figure 15. The dimensionless coefficient R_{M2} varied with wave period for different mass ratio and damping ratio: (**a**) damping ratio = 0.005; (**b**) damping ratio = 0.01; (**c**) damping ratio = 0.02; and (**d**) damping ratio = 0.05.

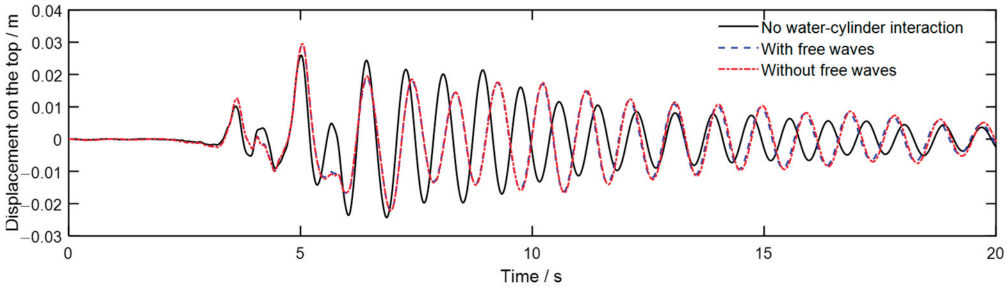

(**a**) $T_s = 0.866$ s

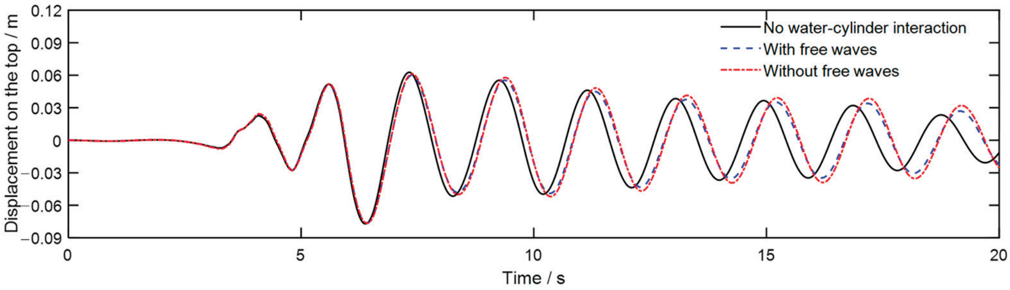

(**b**) $T_s = 1.88$ s

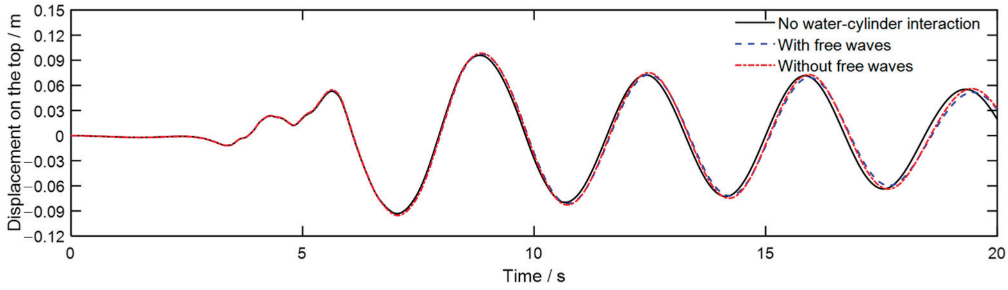

(**c**) $T_s = 3.5$ s

Figure 16. Time history of the displacement on the cylinder head under Christchurch seismic wave: (**a**) the first-order natural vibration period of the cylinder = 0.866 s; (**b**) the first-order natural vibration period of the cylinder = 1.88 s; and (**c**) the first-order natural vibration period of the cylinder = 3.5 s.

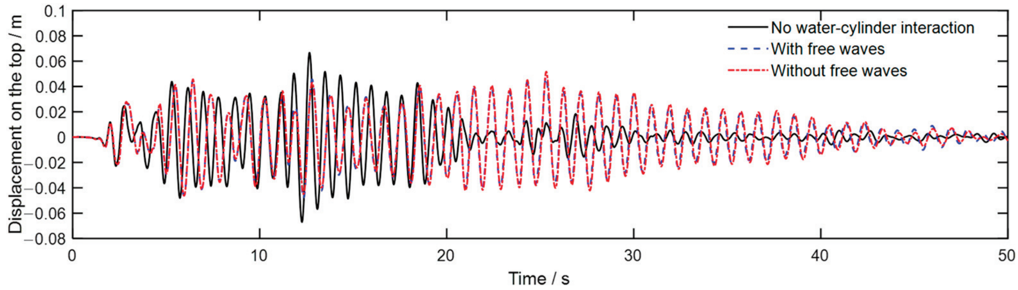

(**a**) $T_s = 0.866$ s

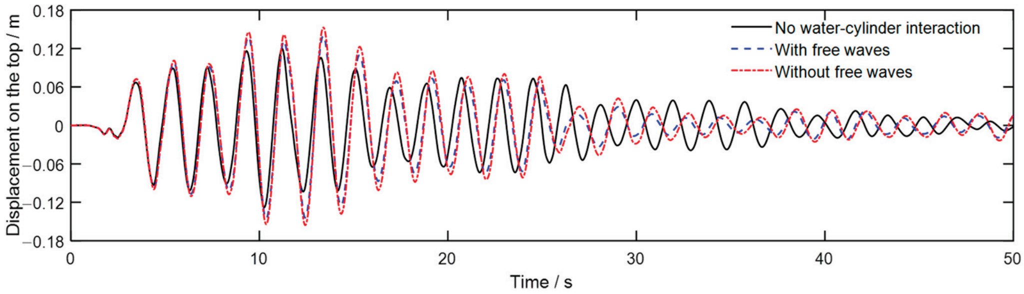

(**b**) $T_s = 1.88$ s

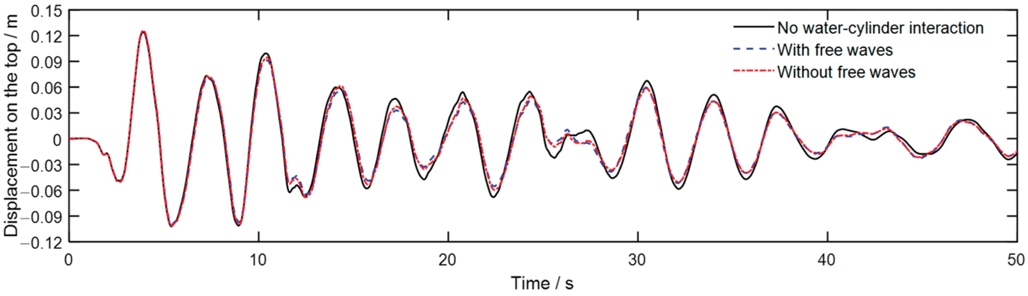

(**c**) $T_s = 3.5$ s

Figure 17. Time history of the displacement on the cylinder head under El-Centro seismic wave: (**a**) the first-order natural vibration period of the cylinder = 0.866 s; (**b**) the first-order natural vibration period of the cylinder = 1.88 s; and (**c**) the first-order natural vibration period of the cylinder = 3.5 s.

A quantitative analysis is furtherly conducted to study the effects of water–cylinder interaction and boundary condition of free surface waves on the seismic responses of the cylinder varied with mass ratio. Figures 21 and 22 show the variation of R_{u1} and R_{M1} with mass ratio and damping ratio, respectively. It can be seen that water–cylinder interaction can significantly influence the seismic responses of the cylinder, especially when the mass ratio is small. Generally, the effects of water–cylinder interaction decrease with increasing damping ratio. Figures 23 and 24 show the variation of R_{u2} and R_{M2} with mass ratio for different damping ratios, respectively. It can be seen that the boundary condition of free surface waves reduces the seismic responses of the cylinder due to the added damping effect, and this influence significantly decreases as the damping ratio increases. Moreover, the effect of the boundary condition of free surface waves on the bending moment is considerably larger than that on displacement, and this influence on the bending moment is less than 5% when the damping ratio is larger than 0.02. In general, the effects of the boundary condition of free surface waves on the seismic responses of the cylinder can be considered negligible when the damping ratio of the cylinder is larger than 0.02.

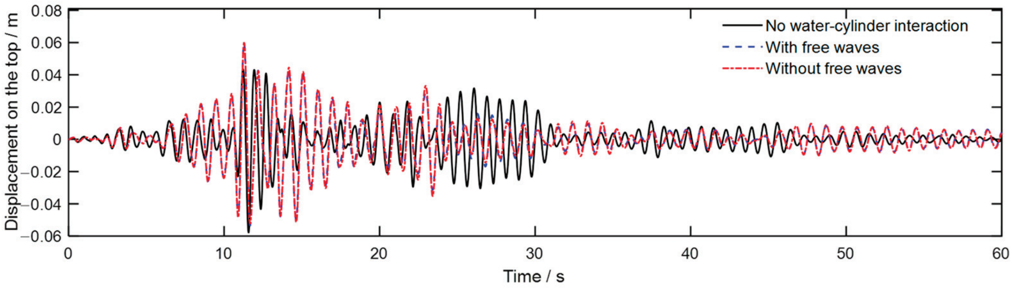

(**a**) $T_s = 0.866$ s

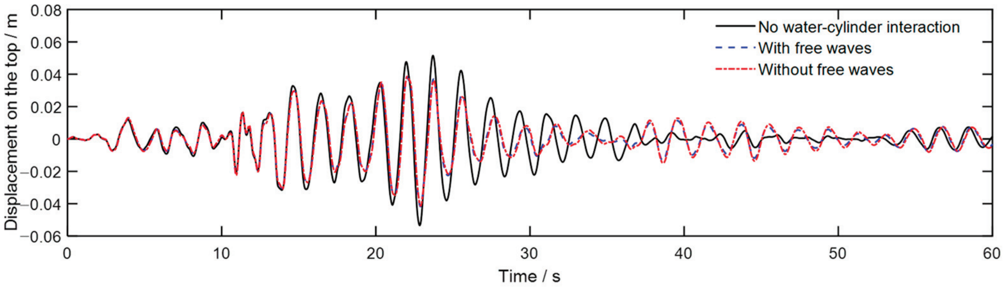

(**b**) $T_s = 1.88$ s

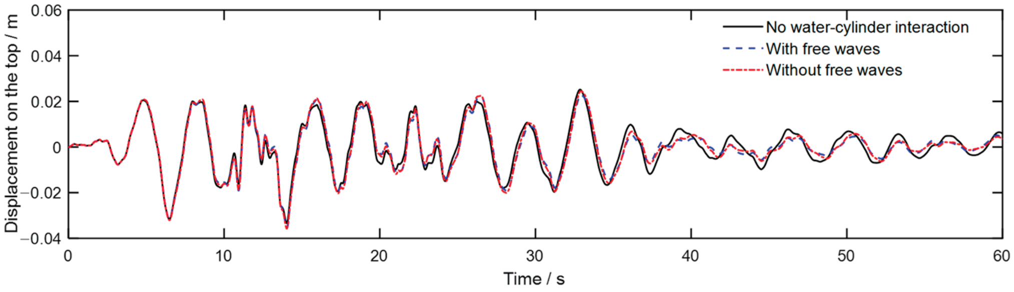

(**c**) $T_s = 3.5$ s

Figure 18. Time history of the displacement on the cylinder head under Chichi seismic wave: (**a**) the first-order natural vibration period of the cylinder = 0.866 s; (**b**) the first-order natural vibration period of the cylinder = 1.88 s; and (**c**) the first-order natural vibration period of the cylinder = 3.5 s.

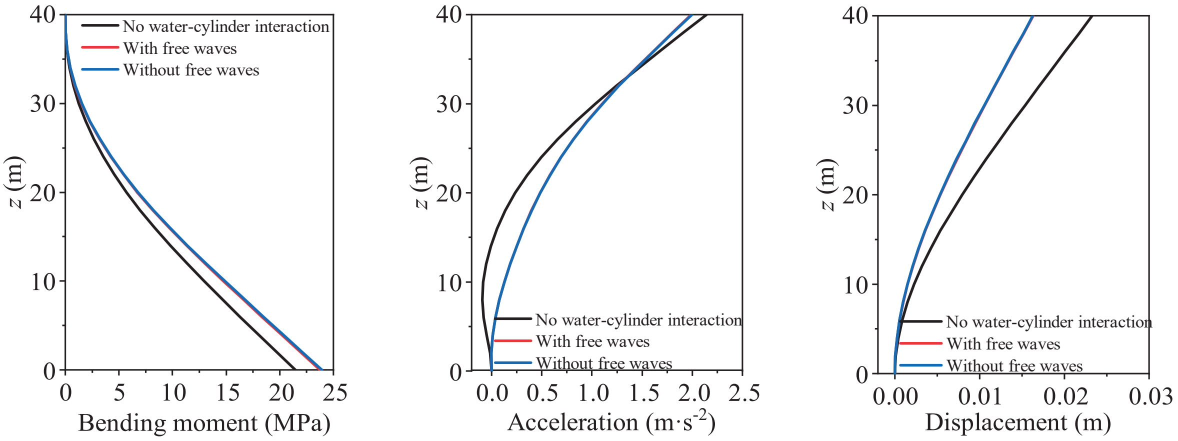

(**a**) Bending moment (**b**) Acceleration (**c**) Displacement

Figure 19. The maximum responses along the length of the cylinder for Christchurch wave with mass ratio equal to 2.5: (**a**) peak bending moment response; (**b**) peak acceleration response; and (**c**) peak displacement response.

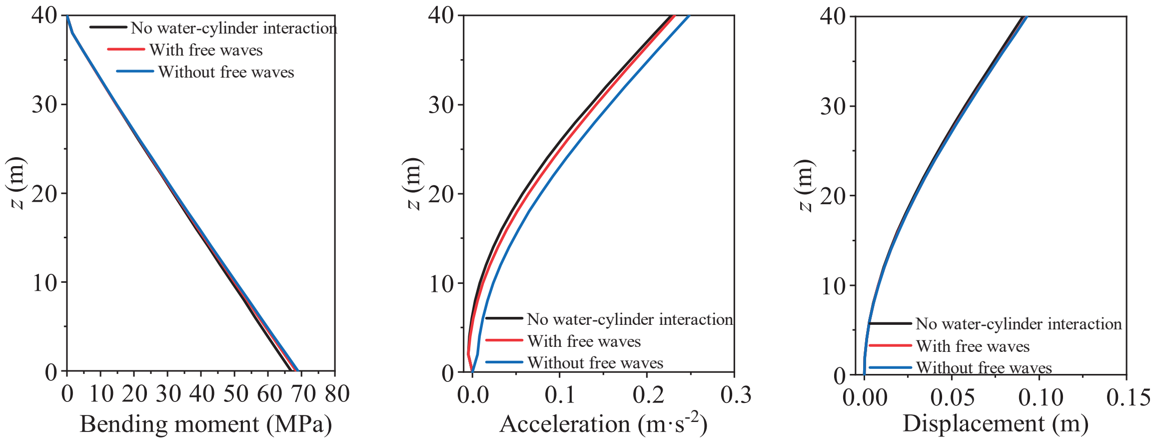

(**a**) Bending moment (**b**) Acceleration (**c**) Displacement

Figure 20. The maximum responses along the length of the cylinder for Christchurch wave with mass ratio equal to 12.83: (**a**) peak bending moment response; (**b**) peak acceleration response; and (**c**) peak displacement response.

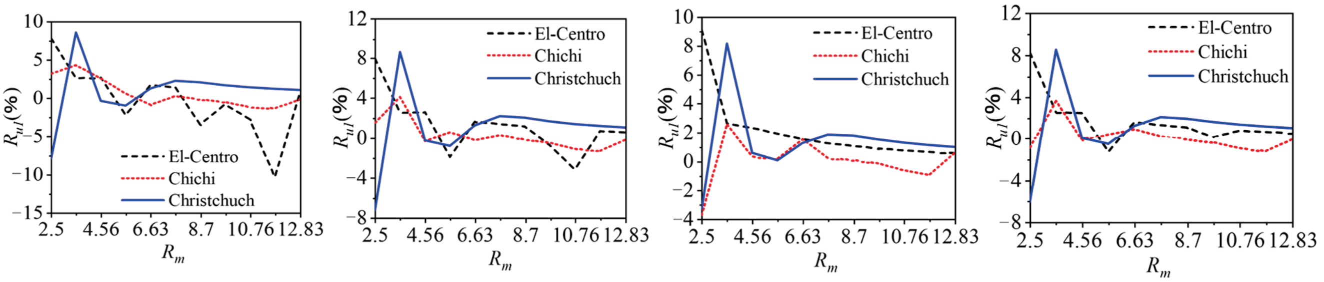

(**a**) $\xi = 0.005$ (**b**) $\xi = 0.01$ (**c**) $\xi = 0.02$ (**d**) $\xi = 0.05$

Figure 21. The dimensionless coefficient R_{u1} varied with mass ratio for different damping ratio: (**a**) damping ratio = 0.005; (**b**) damping ratio = 0.01; (**c**) damping ratio = 0.02; and (**d**) damping ratio = 0.05.

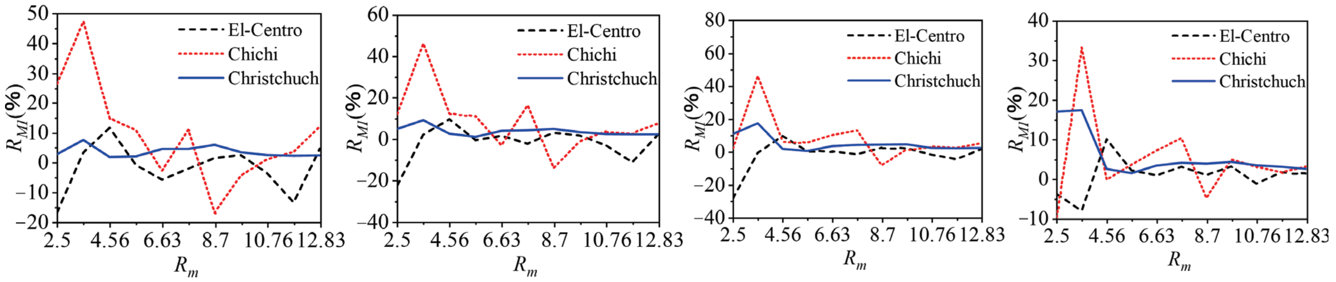

(**a**) $\xi = 0.005$ (**b**) $\xi = 0.01$ (**c**) $\xi = 0.02$ (**d**) $\xi = 0.05$

Figure 22. The dimensionless coefficient R_{M1} varied with mass ratio for different damping ratio: (**a**) damping ratio = 0.005; (**b**) damping ratio = 0.01; (**c**) damping ratio = 0.02; and (**d**) damping ratio = 0.05.

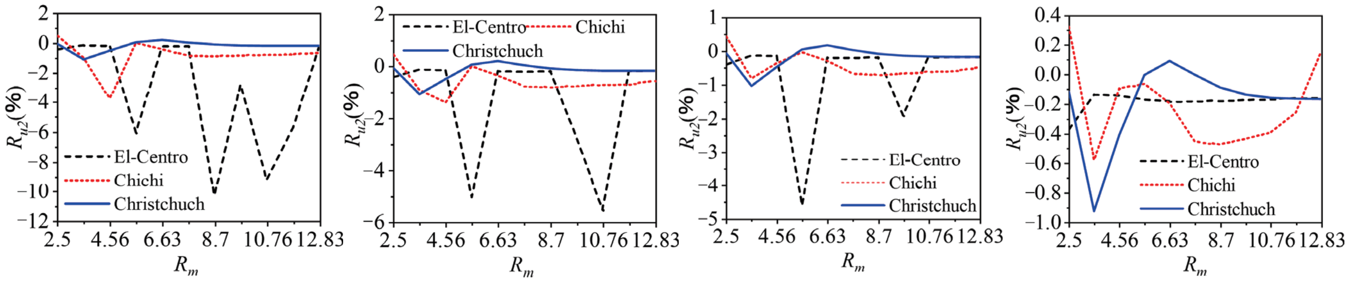

(**a**) $\xi = 0.005$ (**b**) $\xi = 0.01$ (**c**) $\xi = 0.02$ (**d**) $\xi = 0.05$

Figure 23. The dimensionless coefficient R_{u2} varied with mass ratio for different damping ratio: (**a**) damping ratio = 0.005; (**b**) damping ratio = 0.01; (**c**) damping ratio = 0.02; and (**d**) damping ratio = 0.05.

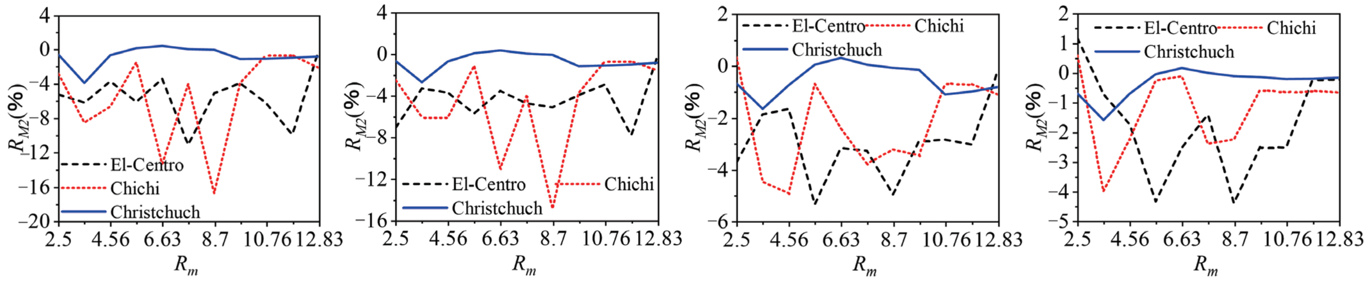

(**a**) $\xi = 0.005$ (**b**) $\xi = 0.01$ (**c**) $\xi = 0.02$ (**d**) $\xi = 0.05$

Figure 24. The dimensionless coefficient R_{M2} varied with mass ratio for different damping ratio: (**a**) damping ratio = 0.005; (**b**) damping ratio = 0.01; (**c**) damping ratio = 0.02; and (**d**) damping ratio = 0.05.

6. Conclusions

In the present study, a high-precision and efficient time-domain substructure method is developed to simulate water–cylinder interaction considering the boundary condition of free surface waves. The frequency-dependent added mass and added damping are equivalent as a spring-dashpot-mass model in the time domain, which is stable, efficient and can be seamlessly coupled with the explicit finite element method. The proposed method is further applied to evaluate the effects of added mass and damping on the dynamic responses of the circular cylinder subjected to wave and earthquake loads. From all the results presented in this study, the main conclusions are summarized as follows:

1. The proposed time-domain substructure method agrees well with the frequency-domain FEM, while the calculation efficiency is improved by approximately two orders of magnitude.
2. Water–cylinder interaction generally increases the displacement and bending moment of the cylinder under wave loads, while it can markedly decrease the dynamic responses when the wave period is close to the natural vibration period. The effects of water–cylinder interaction can be neglected for wave periods greater than 5 s.
3. The boundary condition of free surface waves has a negligible effect (<5%) on wave responses of the cylinder in most cases, while its added damping effect can significantly decrease the dynamic responses of the cylinder when the wave period is near the natural vibration period of the cylinder.
4. The water–cylinder interaction can significantly influence the seismic responses of the cylinder, especially when the mass ratio is small. Generally, the effects of water–cylinder interaction decrease as the damping ratio increases.
5. The boundary condition of free surface waves can decrease the seismic responses of the cylinder, and this influence significantly decreases as the damping ratio increases.

In general, this effect can be neglected when the damping ratio of the cylinder is larger than 0.02.

6. Water–cylinder interaction tends to increase the natural vibration period of the cylinder, while the free surface waves have little influence on it.

Author Contributions: Conceptualization, Z.T. and X.D.; Methodology, P.W.; Software, H.F. and H.L.; Validation, H.L.; Writing—original draft, P.W.; Supervision, Z.T. and X.D. All authors have read and agreed to the published version of the manuscript.

Funding: This work is supported by the Beijing Natural Science Foundation (JQ24050) and the National Natural Science Foundation of China (52478479).

Data Availability Statement: The original contributions presented in this study are included in the article. Further inquiries can be directed at the corresponding author.

Conflicts of Interest: The authors declare no conflict of interest.

References

1. Chaudhari, V.; Somala, S.N. Fragility of offshore wind turbines variation with pulse-period and amplitude: Directivity and Fling step. *Structures* **2022**, *41*, 66–76. [CrossRef]
2. Bai, X.Y.; Jiang, H.; Song, G.S.; Li, X. Extreme responses of sea-crossing bridges subjected to offshore ground motion and correlated extreme wind and wave. *Ocean Eng.* **2022**, *247*, 110710. [CrossRef]
3. Ur Rehman, S.S.; Cui, Y.; Wang, Z.X.; Ang, Y. Performance assessment of pile supported wharves with seismic isolation system considering pile-soil interaction. *Ocean Eng.* **2024**, *312*, 119219. [CrossRef]
4. Han, R.P.S.; Xu, H. A simple and accurate added mass model for hydrodynamic fluid-structure interaction analysis. *J. Frankl. Inst.* **1996**, *333*, 929–945. [CrossRef]
5. Liaw, C.Y.; Chopra, A.K. Dynamics of towers surrounded by water. *Earthq. Eng. Struct. Dyn.* **1974**, *3*, 33–49. [CrossRef]
6. Wei, K.; Yuan, W.C.; Bouaanani, N. Experimental and numerical assessment of the three dimensional modal dynamic response of bridge pile foundations submerged in water. *J. Bridge Eng.* **2013**, *18*, 1032–1041. [CrossRef]
7. Du, X.; Wang, P.; Zhao, M. Simplified formula of hydrodynamic pressure on circular bridge piers in the time domain. *Ocean Eng.* **2014**, *85*, 44–53. [CrossRef]
8. Li, Q.; Yang, W.L. An improved method of hydrodynamic pressure calculation for circular hollow piers in deep water under earthquake. *Ocean Eng.* **2013**, *72*, 241–256. [CrossRef]
9. Jiang, H.; Wang, B.; Bai, X.; Zeng, C.; Zhang, H. Simplified expression of hydrodynamic pressure on deep water cylindrical bridge piers during earthquakes. *Bridge Eng.* **2017**, *22*, 04017014. [CrossRef]
10. Wang, P.; Zhao, M.; Du, X. Analytical solution and simplified formula for earthquake induced hydrodynamic pressure on elliptical hollow cylinders in water. *Ocean Eng.* **2018**, *148*, 149–160. [CrossRef]
11. Wang, P.; Zhao, M.; Du, X. Simplified formula for earthquake-induced hydrodynamic pressure on round-ended and rectangular cylinders surrounded by water. *J. Eng. Mech. ASCE* **2019**, *145*, 04018137. [CrossRef]
12. Wang, P.; Zhao, M.; Du, X.; Liu, J.; Chen, J. Simplified evaluation of earthquake-induced hydrodynamic pressure on circular tapered cylinders surrounded by water. *Ocean Eng.* **2018**, *164*, 105–113. [CrossRef]
13. Wang, P.G.; Wang, X.J.; Zhao, M.; Cheng, X.L.; Du, X.L. A numerical model for earthquake-induced hydrodynamic forces and wave forces on inclined circular cylinder. *Ocean Eng.* **2020**, *207*, 107382. [CrossRef]
14. Morison, J.R.; O'Brien, M.P.; Johnson, J.W.; Schaff, S.A. The force exerted by surface waves on piles. *AIME Pet. Trans.* **1950**, *189*, 149–154. [CrossRef]
15. MacCamy, R.C.; Fuchs, R.A. *Wave Forces on Piles: A Diffraction Theory*; Report No.TM-69; U.S. Army Corps of Engineers, Beach Erosion Board: Washington, DC, USA, 1954.
16. Fish, P.R.; Dean, R.B.; Heaf, N.J. Fluid-structure interaction in Morison's equation for the design of offshore structures. *Eng. Struct.* **1980**, *2*, 15–26. [CrossRef]
17. Penzien, J.; Kaul, M.K. Response of offshore towers to strong motion earthquakes. *Earthq. Eng. Struct. Dyn.* **1972**, *1*, 55–68. [CrossRef]
18. Song, B.; Zheng, F.; Li, Y. Study on a simplified calculation method for hydrodynamic pressure to slender structures under earthquakes. *J. Earthq. Eng.* **2013**, *17*, 720–735. [CrossRef]
19. Jian, Y.; Zhan, J.; Zhu, Q. Short crested wave-current forces around a large vertical circular cylinder. *Eur. J. Mech. B-Fluids* **2008**, *27*, 346–360. [CrossRef]

20. Wang, P.G.; Zhao, M.; Du, X.L.; Liu, J.B. Dynamic response of bridge pier under combined earthquake and wave-current action. *J. Bridge Eng.* **2019**, *24*, 04019095. [CrossRef]
21. Wang, P.G.; Zhao, M.; Du, X.L.; Liu, J.B. Analytical solution for the short-crested wave diffraction by an elliptical cylinder. *Eur. J. Mech. B-Fluids* **2019**, *74*, 399–409. [CrossRef]
22. Newman, J.N. *Marine Hydrodynamics*; MIT Press: Cambridge, MA, USA, 2018.
23. Molin, B. *Offshore Structure Hydrodynamics*; Cambridge University Press: Cambridge, UK, 2023.
24. Rahman, M.; Bhatta, D.D. Evaluation of added mass and damping coefficients of an osciallating circular cylinder. *Appl. Math. Model.* **1993**, *17*, 70–79. [CrossRef]
25. Wolf, J.P. Consistent lumped-parameter models for unbounded soil: Physical representation. *Earthq. Eng. Struct. Dyn.* **1991**, *20*, 11–32. [CrossRef]
26. Bubnicki, Z. *Modern Control Theory*; Springer: Berlin/Heidelberg, Germany, 2005.
27. Tang, Z.Y.; Li, X.; Wang, Z.Y. Stable parameters identification for rational approximation of single-degree-of-freedom frequency response function of semi-infinite medium. *Int. J. Numer. Methods Eng.* **2023**, *124*, 5596–5615. [CrossRef]
28. Wang, P.G.; Zhang, W.Q.; Xu, H.B.; Zhao, M.; Du, X.L. A high-accuracy substructure method in the time domain for simulating pile-soil dynamic interaction in horizontal vibration. *Comput. Geotech.* **2021**, *140*, 104479. [CrossRef]
29. Wang, P.G.; Zhao, M.; Li, H.F.; Du, X.L. An accurate and efficient time-domain model for simulating water-cylinder dynamic interaction during earthquakes. *Eng. Struct.* **2018**, *166*, 263–273. [CrossRef]
30. Zhao, M.; Du, X.; Liu, J.; Li, H. Explicit finite element artificial boundary scheme for transient scalar waves in two-dimensional unbounded waveguide. *Int. J. Numer. Methods Eng.* **2011**, *87*, 1074–1104. [CrossRef]

Journal of
Marine Science and Engineering

Article

Analysis of the Main Influencing Factors of Marine Environment on the Nuclear Pressure Vessel of Floating Nuclear Power Plants

Fuxuan Ma [1,2], Meng Zhang [1,2,3,*] and Xianqiang Qu [2]

[1] College of Shipbuilding Engineering, Harbin Engineering University, Harbin 150001, China; mafuxuan@hrbeu.edu.cn
[2] Yantai Research Institute, Harbin Engineering University, Yantai 264000, China; quxianqiang@hrbeu.edu.cn
[3] College of Power and Energy Engineering, Harbin Engineering University, Harbin 150001, China
* Correspondence: zhangmeng@hrbeu.edu.cn

Abstract: Nuclear energy inherently possesses both immense utility and significant risks. To ensure global safety, designers of floating nuclear power plants (FNPPs) must thoroughly consider the influence of the marine environment on the reactor pressure vessel (RPV). Wave loads act on the hull of an FNPP, causing structural deformation, which is subsequently transferred to the RPV. Additionally, wave-induced forces generate six degrees of freedom (6-DOF) motion in the hull, resulting in inertial loads. Consequently, the RPV is subjected to both deformation loads transmitted from the hull and inertial loads associated with the 6-DOF motion. To accurately account for the effects of the marine environment while minimizing the computational cost of RPV fatigue analysis, it is essential to identify the primary influencing factors. This study determined that the predominant factors affecting RPV fatigue in an FNPP were the hull's pitch, roll, and yaw motions. In mechanical analyses of the RPV, including ultimate strength and fatigue assessments, only rotational inertial loads need to be considered, while the influence of translational inertial loads and hull deformation can be neglected.

Keywords: floating nuclear power plant; reactor pressure vessel; marine environment; key influencing factors; hull deformation; inertial load

1. Introduction

With the continuous optimization of the global energy structure and the ongoing promotion of green and low-carbon development strategies, traditional fossil fuels, along with renewable energy sources such as wind, wave, and solar power, are increasingly exhibiting limitations in meeting the growing energy demand. As a clean, efficient, and highly flexible offshore power generation technology, the floating nuclear power plant (FNPP) has garnered widespread attention from governments worldwide. Compared with conventional power generation methods, FNPPs offer advantages such as environmental friendliness, cost-effectiveness, and reduced susceptibility to weather conditions, making them particularly suitable for remote offshore areas, offshore resource development, and polar scientific research. The realization of FNPPs relies on the integration of mobile small-scale nuclear reactor technology with ship and offshore engineering to construct mobile floating marine platforms equipped with nuclear reactors and power generation systems.

The concept of FNPPs was first proposed by the United States, which subsequently converted the Liberty Ship Charles H. Cugle into the world's first FNPP, the Sturgis, to supply power to military bases in the Panama Canal region [1]. Russia has since made significant advancements in this field, with its first floating nuclear power plant, the Akademik

Lomonosov, completing reactor installation in 2013 and commencing commercial operations in May 2020. This facility provides energy for the Far East and Siberian regions while also supporting electricity demands for Arctic gas extraction. The power plant is equipped with two KLT-40S reactors, each with a rated electrical output of 35 MW [2]. Russia continues to develop nuclear reactors for icebreakers and FNPPs, including the RITM-200M, ABVD, SVBR, and VBER series, covering power ranges from 8 MW to 300 MW [3].

Apart from Russia, countries such as France, South Korea, and the United States have proposed their own FNPP concepts but have yet to implement them on a large scale. Since 2005, China has actively pursued FNPP development, accelerating research on small floating nuclear power plants. The China National Nuclear Corporation (CNNC) has developed two FNPP models, ACP100S and ACP25S, which can be deployed in single- or dual-reactor configurations to achieve power outputs ranging from 25 MW to 250 MW. Meanwhile, the China General Nuclear Power Corporation (CGN) has independently developed the ACPR50S floating nuclear power plant, featuring a thermal power output of 200 MW and an electrical power output of approximately 60 MW, currently under experimental reactor construction [3]. Additionally, the China Shipbuilding Industry Corporation’s 719 Research Institute has proposed the HHP25 offshore nuclear power platform, with a thermal power output of 100 MW and an electrical power output of 25 MW, which has completed preliminary design [4].

As a typical marine and offshore engineering structure, FNPPs operate in highly stochastic oceanic environments and must withstand complex cyclic loads, including wind, wave, and current forces. These loads subject the structure to millions of stress cycles, leading to significant fatigue damage. Extensive research indicates that fatigue failure is one of the primary failure modes of marine and offshore structures [5,6]. Reports from the International Maritime Organization (IMO) have highlighted that certain maritime engineering failures may be initiated by cracks in side-shell structures [7].

In FNPPs, the reactor pressure vessel (RPV) and associated pressure-bearing components (e.g., pressure pipelines) are critical components of the nuclear island [8,9]. The RPV encloses the radioactive core, internal structures, and heat transfer medium, operating under high temperature, high pressure, fluid erosion, and neutron irradiation for prolonged periods [10,11]. Moreover, dynamic variations in temperature and pressure induce cyclic stresses that exacerbate fatigue damage. The RPV and pressure pipelines in FNPPs are enclosed within a steel containment vessel and are structurally supported by both lower and upper supports connected to the hull. In the marine environment, these pressure-bearing components must withstand not only high temperature, high pressure, fluid erosion, and neutron irradiation but also the combined effects of wave, wind, and current loads. Compared with single-load conditions, coupled loads induce greater hot spot stress ranges, significantly reducing the RPV’s fatigue life. Due to differences in the frequency and amplitude of random loads, along with potential high correlation between them, assessing fatigue damage becomes increasingly complex.

Fatigue analysis methods for ship structures and RPVs belong to two distinct engineering disciplines [12–14], presenting significant methodological differences and making fatigue analysis of FNPP pressure-bearing components particularly challenging. To address this issue, Ma proposed a method that converts structural stress spectra induced by wave loads into stress-time histories, which are then superimposed with thermal-pressure stress histories, thereby reducing finite element computation costs and enhancing the efficiency of multi-load coupling analysis [15]. Yuan employed the equivalent design wave method, converting long-term sea states into equivalent regular wave conditions while simultaneously applying both regular wave loads and thermal-pressure loads to analyze structural fatigue behavior, further considering different initial phase combinations [16]. Shen comprehensively accounted for the interactions among multiple loads and proposed a damage combination formula for thermal-pressure conditions and wave conditions, simplifying FNPP fatigue analysis procedures [17].

In RPV structural ultimate strength assessments, the influence of the marine environment on stress distribution must also be considered. Ship structural strength is typically evaluated using either rule-based analysis or direct strength analysis, where wave load design values can be obtained through regulatory calculations [12,18] or the equivalent design wave method [19]. Additionally, wave loads acting on the hull can be identified through structural response monitoring data, and structural health monitoring technologies can be employed to detect environmental loads in real time, thereby enhancing the operational safety of FNPP structures.

Based on this background, this study investigates the structural response of RPVs in marine environments, analyzing the impact of various dynamic loads on RPV fatigue and structural strength. The primary objectives of this research include the following:

1. Utilizing spectral analysis methods to examine the influence of marine environmental loads (such as hull deformation and six-degree-of-freedom inertial forces) on RPV fatigue damage and identifying the dominant damage factors.
2. Applying the equivalent design wave method to analyze the stress distribution of RPVs under extreme sea conditions and identifying key stress factors.
3. Proposing optimization strategies for FNPP operation to mitigate RPV fatigue damage and enhance structural safety based on the analytical results.

2. Marine Environment and Structural Model

2.1. Operational Waters and Sea State Parameters

The FNPP examined in this study is planned to operate near Bayzikou Village, Xingang Subdistrict, Penglai City, Shandong Province. The offshore facility is located approximately 3.35 km from the onshore facility, bordering the Bohai Sea to the north. The specific location is shown in Figures 1 and 2.

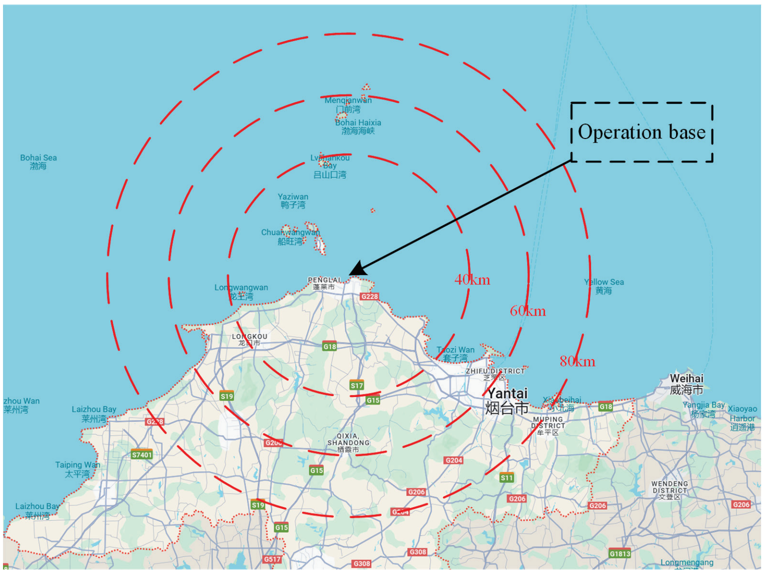

Figure 1. FNPP operational site location.

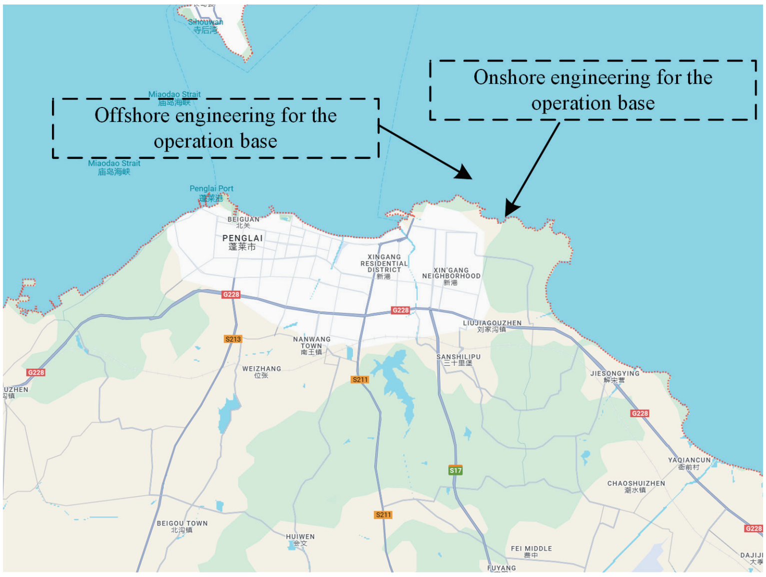

Figure 2. Offshore and onshore facility locations.

The operational site is situated in the Miaodao Strait, a shallow nearshore channel predominantly influenced by waves and tidal currents. The geomorphological units of the Miaodao Strait include submarine erosion trenches, a central uplift, and southern and northern shallow zones, with seabed sediments consisting of rock fragments, gravel, sand, silt, and soft mud in sequence. The regional topography is illustrated in Figure 3.

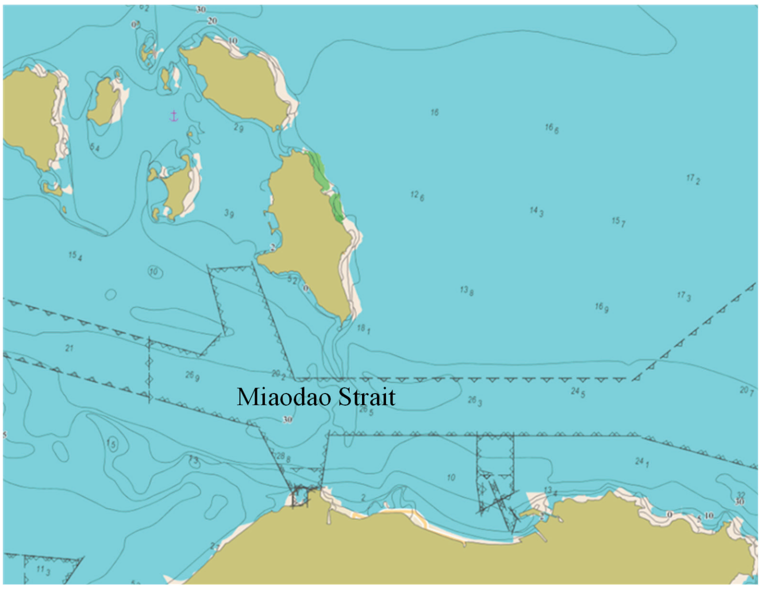

Figure 3. Topographic features of the operational region.

To characterize the wave conditions within the FNPP's operational area, this study adopted wave scatter diagrams from the Yellow and Bohai Seas [15]. Using extreme value analysis methods [20], the wave parameters near the operational site were statistically analyzed, yielding the extreme maximum wave height (Hmax), significant wave height (Hs), mean zero-crossing period (Tz), and mean up-crossing period (Ts) for return periods of 1, 10, 50, 100, and 500 years, as summarized in Table 1.

Table 1. Extreme wave heights and related parameters for different return periods.

Return Period	Hs (m)	Hmax (m)	Tz (s)	Ts (s)
1 year	3.7	6.4	6.4	7.3
10 years	4.3	7.5	6.9	7.9
50 years	4.6	8.0	7.3	8.3
100 years	4.8	8.4	7.4	8.4
500 years	5.2	9.0	7.8	8.9

2.2. Structural Model

The FNPP has a length of 230 m, a beam of 36 m, and a depth of 16.9 m. The FNPP consists of several primary structural components, including the hull, containment vessel, and reactor pressure vessel (RPV). The hull comprises inner and outer shell plating, strong framing, longitudinal girders, and stiffeners. A finite element model was established in ANSYS version 2022, where the primary structures were modeled using shell elements, while the secondary structures were modeled using beam and link elements. Specifically, shell elements were used for high-web frames, corrugated bulkheads, and T-stiffened panels; beam elements were used for structural stiffeners subjected to lateral loads, and link elements were used for non-load-bearing stiffeners. During mesh generation, quadrilateral elements were prioritized over triangular elements in high-stress regions (e.g., near openings, bracket connections, and sharp corners) to enhance the computational accuracy. The aspect ratio of the elements was controlled to be ≤ 3, and in high-stress areas, it was adjusted to be close to 1. Additionally, grid attributes were defined based on the actual arrangement of hull members (e.g., ribs, longitudinal girders, and stiffeners), ensuring that the mesh alignment, spacing, and geometry accurately reflected the structural layout characteristics. The finite element model of the hull consisted of 1,123,194 elements, as illustrated in Figure 4.

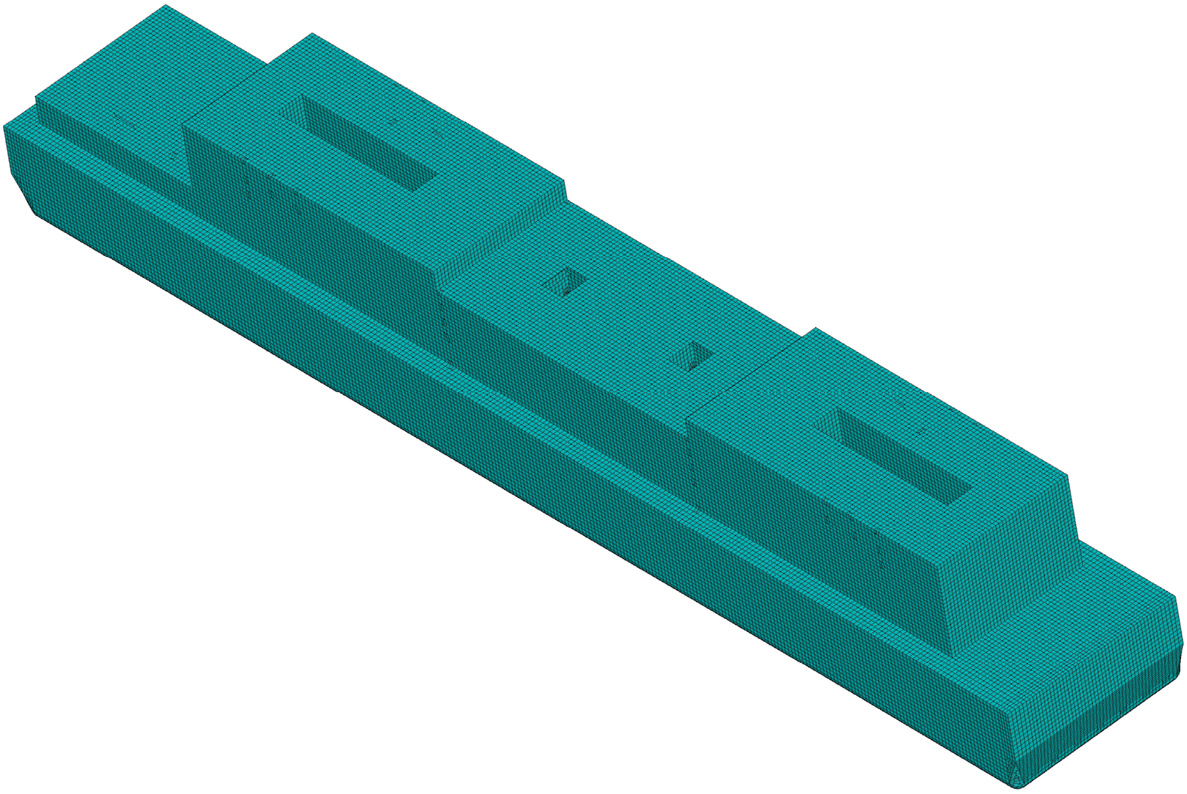

Figure 4. Finite element model of the FNPP hull.

The RPV is located inside the FNPP's containment vessel, serving as a sealed enclosure for the nuclear reactor, designed to withstand operational pressure and thermal loads. The positions of the containment vessel and RPV are shown in Figures 5 and 6.

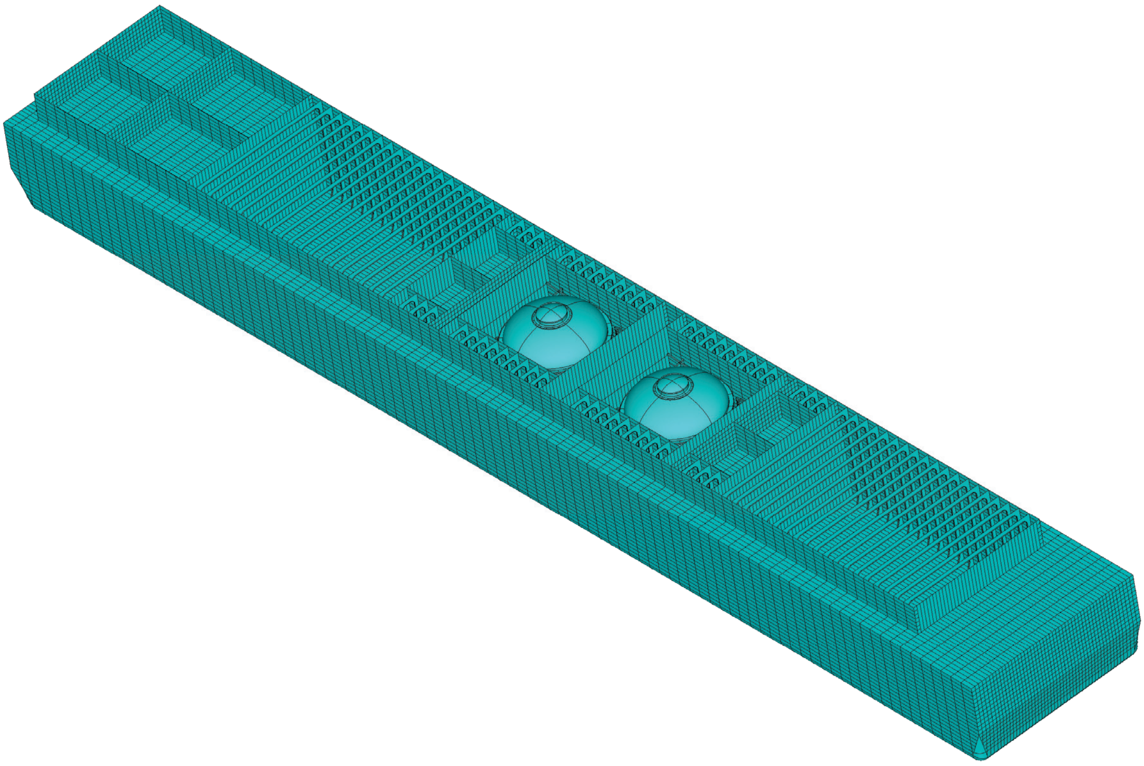

Figure 5. Internal structure of the FNPP hull.

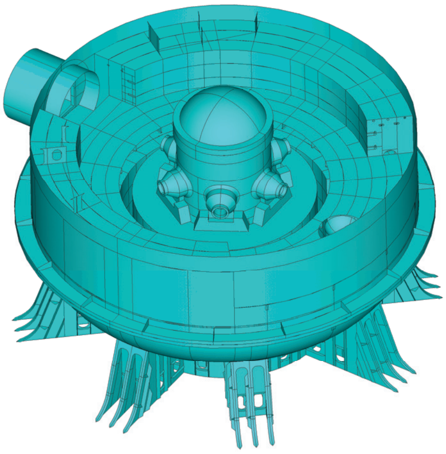

Figure 6. Internal structure of the containment vessel.

The RPV's geometric specifications are as follows: height, 10.66 m; outer diameter, 4.42 m; material, 16MnD5 steel; and total weight (including internal components), 568 tons. The RPV finite element model was developed using solid elements, ensuring an accurate representation of stress distribution and deformation under operational conditions. To improve the stress calculation precision, the thickness direction was meshed with at least six layers of elements. The RPV finite element model consisted of 214,265 elements, as shown in Figure 7.

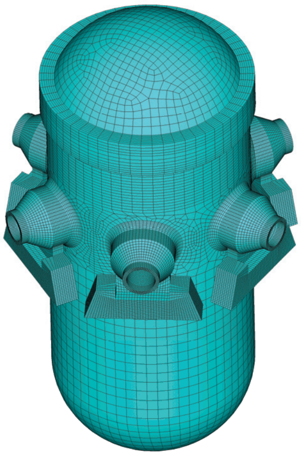

Figure 7. Finite element model of the RPV.

A binding constraint was applied between the bottom of the limiting groove and the surface of the bearing platform. Additionally, coupling degrees of freedom were set between the RPV supports and the limiting groove, ensuring that the RPV supports were circumferentially fixed while allowing free radial sliding, as illustrated in Figure 8.

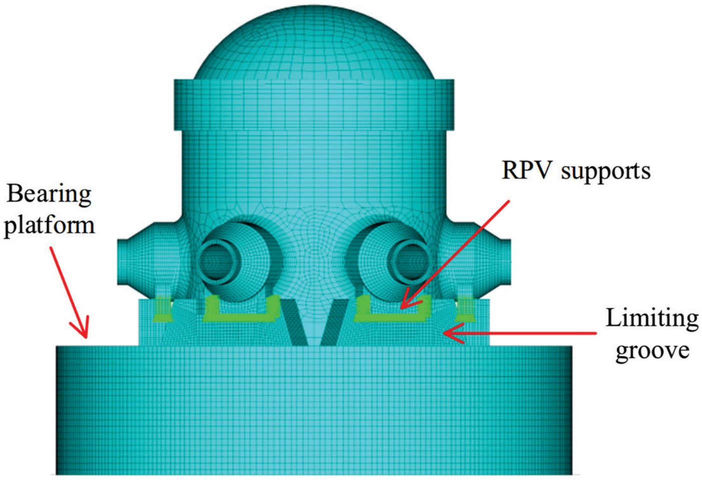

Figure 8. Connection between the RPV and the FNPP.

For analyzing the RPV response under wave loads, a global model was employed, where both ends of the hull were simply supported [15]. For evaluating the RPV response under inertial forces, a local model was used, with the bottom of the limiting groove being fixed [15].

The hydrodynamic model of the FNPP was constructed in AQWA. The computational model had a length of 230 m, a beam of 36 m, and a depth of 16.9 m, which were consistent with the finite element structure. Only the outer hull of the floater was modeled. The total mass of the FNPP was 83,000 tons, with the center of gravity located at (0.328 m, 0.003 m, −0.38 m). The calculated natural periods were as follows: roll, approximately 10.96 s; heave, approximately 9.87 s; and pitch, approximately 8.71 s. The FNPP was moored to the sea surface using 16 anchor chains, as shown in Figure 9.

The hydrodynamic analysis was conducted using AQWA. The wave directions were set from 0° to 180° with an interval of 30°. The frequency range was set from 0.001 Hz to 0.4 Hz, with 50 evenly spaced frequency points. The calculated RAO (response amplitude operator) results for different wave directions are presented in Figure 10.

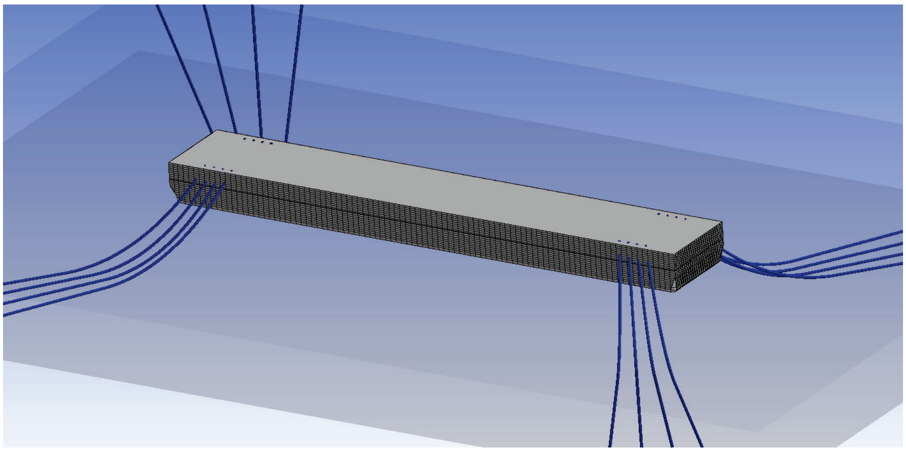

Figure 9. Hydrodynamic analysis model.

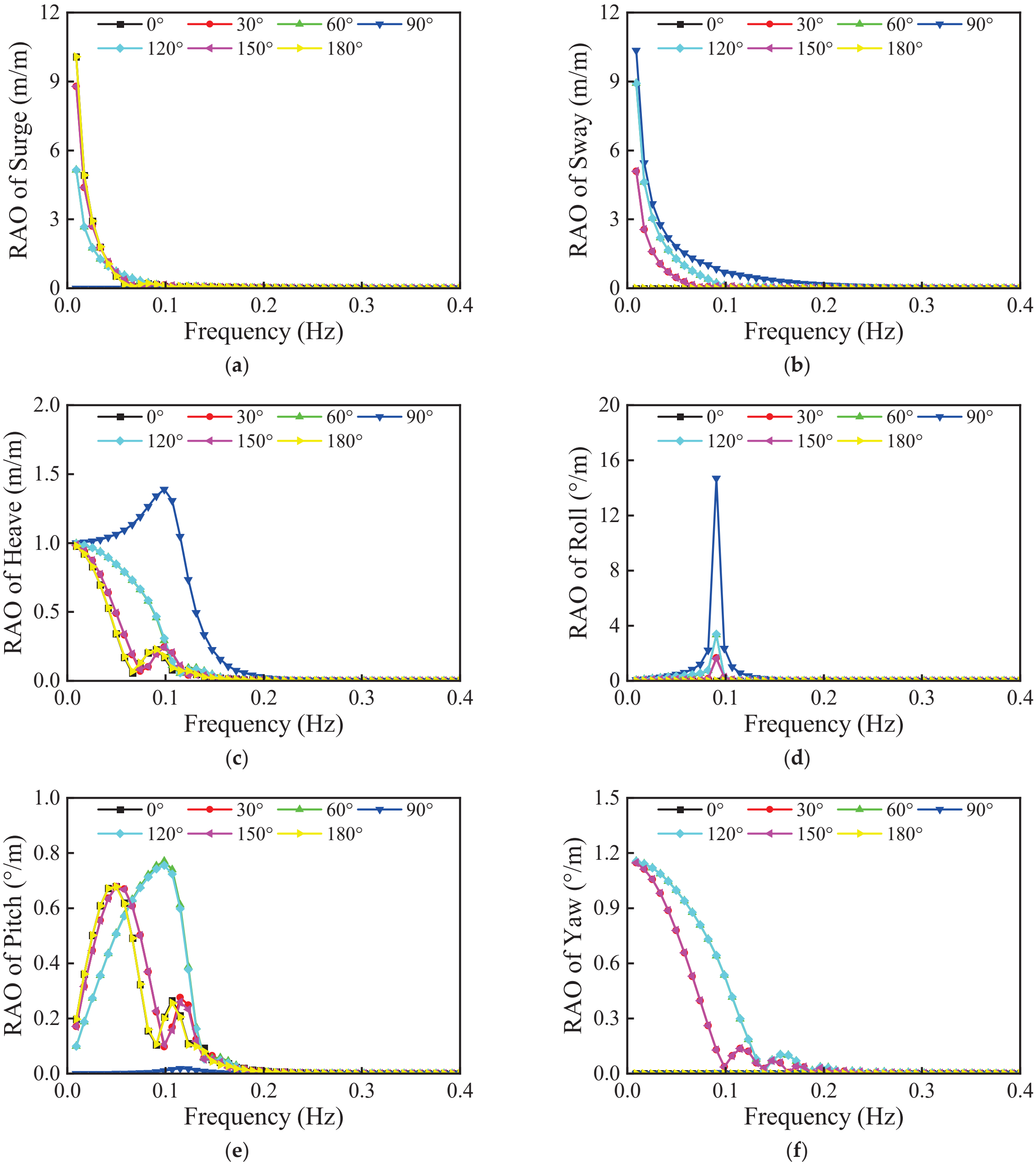

Figure 10. Motion RAO. (**a**) Surge. (**b**) Sway. (**c**) Heave. (**d**) Roll. (**e**) Pitch. (**f**) Yaw.

3. Structural Damage Analysis Induced by Various Inputs

In the marine environment, wave-induced loads significantly affect the fatigue of the hull structure as they are alternating loads. In contrast, current-induced loads are typically horizontal forces acting on the hull surface over extended periods, exerting a limited impact on fatigue. Additionally, the effect of current-induced loads on the stress in the RPV structure of FNPP is relatively small. As a result, the RPV is primarily subjected to the following dynamic loads: hull deformation (D_S) due to wave-induced dynamic pressure and inertial forces generated by the six-degree-of-freedom (6-DOF) motion of the hull. These inertial forces include the following: surge inertial force (F_X), sway inertial force (F_Y), heave inertial force (F_Z), pitch inertial force (F_{RY}), roll inertial force (F_{RX}), and yaw inertial force (F_{RZ}). These dynamic loads cause the RPV structure to experience cyclic stresses, leading to fatigue damage. Therefore, it is essential to systematically analyze the structural damage induced by these dynamic loads, particularly by assessing the effects of wave-induced pressure and hull motion on RPV fatigue damage individually. By comparing the fatigue damage caused by different factors, the dominant influencing factors can be identified.

3.1. Spectral Analysis Method

In ship and offshore engineering, long-term ocean wave conditions are typically represented by multiple short-term sea states, each characterized by specific wave parameters and occurrence frequencies. Each short-term sea state is considered a stationary Gaussian random process, and the resulting cyclic stress process in the structure is also regarded as an accumulation of multiple short-term sea states.

For a single short-term sea state, the cyclic stress process is generally assumed to be a zero-mean stationary Gaussian random process, with its stress range distribution (i.e., short-term distribution) expressed by a probability density function. According to random process theory, the peak stress in a short-term distribution follows a Rayleigh distribution, given by

$$f_X(x) = \frac{x}{\sigma_X^2} \exp\left(-\frac{x^2}{2\sigma_X^2}\right) \tag{1}$$

where x represents the peak stress value, and σ is the standard deviation of the cyclic stress process.

To obtain the stress transfer function, unit-amplitude wave-induced hydrodynamic pressures or inertial forces at different frequencies are applied to the structural model. The corresponding stress amplitudes at specific nodal points are extracted, allowing for the derivation of the stress transfer function. The power spectral density function $G(f)$ of the cyclic stress process is obtained using spectral analysis methods:

$$G(f) = |H(f)|^2 S(f) \tag{2}$$

where $H(f)$ is the stress transfer function, and $S(f)$ is the wave spectrum.

The 0th and 2nd moments of the power spectral density function are defined as

$$m_j = \int_0^\infty f^j G(f) df \quad (j = 0, 2) \tag{3}$$

The standard deviation σ_X of the stress response is then

$$\sigma_X = \sqrt{m_0} \tag{4}$$

To determine the number of stress cycles within a given period, the zero-crossing rate n_0 must be calculated, which represents the average number of times the stress process crosses its zero mean with a positive slope per unit time:

$$n_0 = \sqrt{\frac{m_2}{m_0}} \tag{5}$$

Under the narrow-band assumption, each zero-crossing corresponds to a stress peak, establishing a relationship between stress range S and stress peaks X:

$$S = 2X \tag{6}$$

Thus, the probability density function for stress range is

$$f_S(S) = \frac{S}{4\sigma_X^2} \exp\left(-\frac{S^2}{8\sigma_X^2}\right) \tag{7}$$

Given an exposure time T_i for the ith short-term sea state, with an average zero-crossing rate n_{0i}, the cumulative fatigue damage D_i is

$$D_i = T_i n_{0i} \int_0^\infty \frac{f_S(S)}{N(S)} dS \tag{8}$$

where $N(S)$ is the S–N curve for the material.

The RPV material in this study was low-alloy structural steel (16MnD5), and the S–N curve was based on the RCC code [14], as illustrated in Figure 11. Sa represents half of the alternating stress intensity range, and N represents the corresponding allowable cycles.

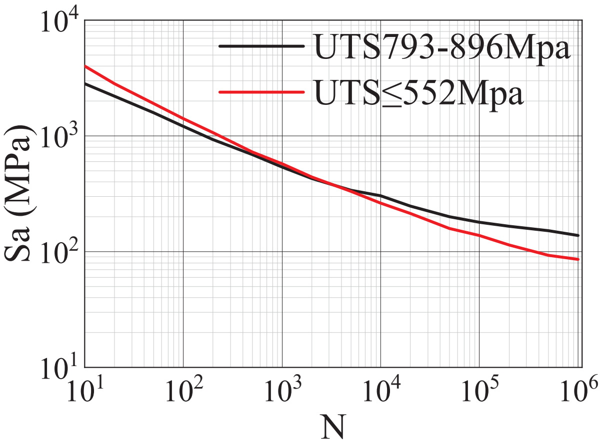

Figure 11. S–N curve for the RPV material.

For long-term fatigue analysis, the total accumulated fatigue damage is obtained by summing all short-term sea state damages:

$$D_{total} = \sum_{i=1}^{M} D_i \tag{9}$$

where M represents the number of short-term sea states in the long-term fatigue analysis.

3.2. Structural Damage Evaluation

To analyze the effects of different dynamic loads on RPV fatigue damage, the spectral analysis method was used to calculate the fatigue damage induced by each factor individually. Two typical fatigue load conditions were selected based on the wave scatter diagram of the FNPP's operational waters [15]:

Condition 1: significant wave height, 4 m; peak spectral period, 8 s; wave directions, 0° to 180°, in 30° increments; and exposure time per direction, 3 h.

Condition 2: significant wave height, 6 m; peak spectral period, 10 s; wave directions, 0° to 180°, in 30° increments; and exposure time per direction, 3 h.

The inner side of the RPV's closure head cap and nozzle are locations prone to fatigue [15]. Therefore, fatigue evaluation points were selected on the inner surface of the RPV structure, as shown in Figure 12.

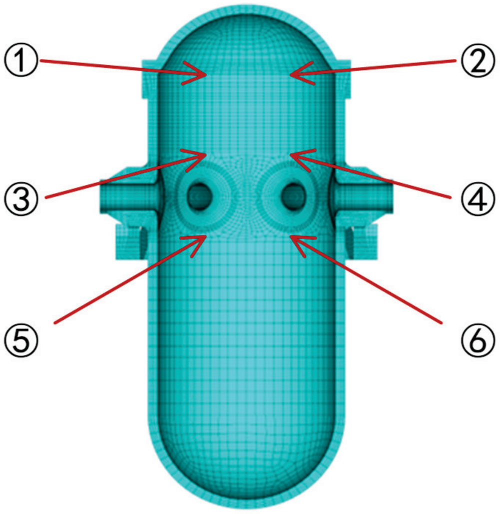

Figure 12. Locations of fatigue evaluation points.

For condition 1, the fatigue damage results across different wave directions (0–180°) are presented in Figure 13.

The results indicated the following: Roll-induced inertial forces F_{RX} had the most significant impact on RPV fatigue damage. Pitch-induced inertial forces F_{RY} had the second-largest impact. The effects of other factors on RPV fatigue damage were relatively minor. Roll-induced fatigue damage was maximized in beam seas (wave direction, 90°) and minimized in head seas (wave direction, 0°). Pitch-induced fatigue damage was maximized in head seas (0°) and minimized in beam seas (90°). Yaw-induced fatigue damage peaked in oblique wave conditions. Hull deformation-induced fatigue damage peaked in beam wave conditions.

For condition 2, the fatigue damage results are shown in Figure 14.

A comparison between Figures 13 and 14 shows the following: Roll motion F_{RX} remained the dominant factor affecting RPV fatigue. Pitch motion F_{RY} continued to be the second-largest contributor. Wave direction significantly influenced the fatigue damage distribution, with roll-induced damage peaking in beam seas and pitch-induced damage peaking in head seas.

Since the RPV was a large, mass-concentrated onboard structure with constrained movement, hull deformation had minimal impact on the fatigue damage, while roll and pitch inertial forces dominated the fatigue damage. Therefore, when analyzing RPV fatigue under marine conditions, only roll and pitch inertial forces needed to be considered.

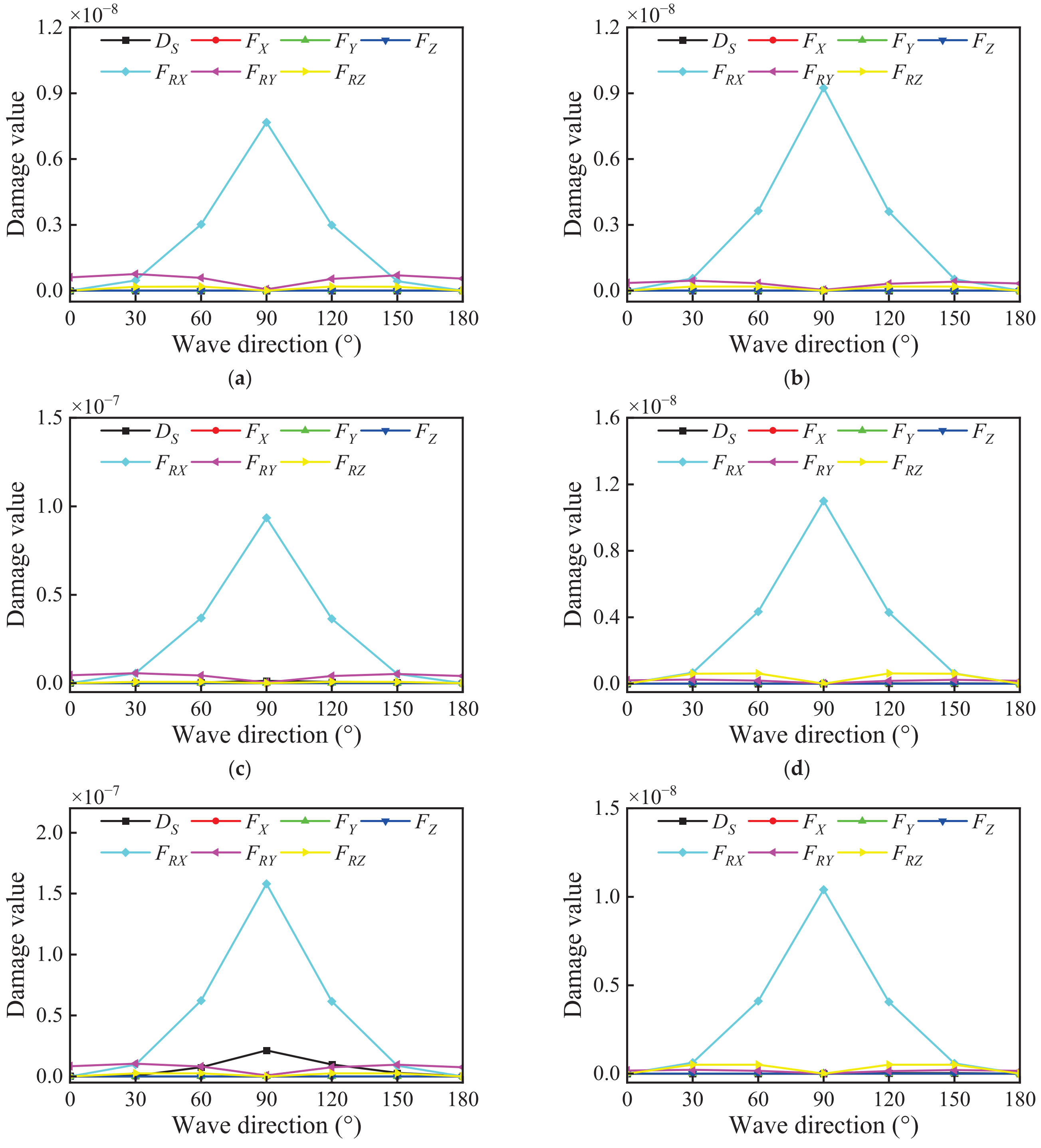

(**a**) (**b**) (**c**) (**d**) (**e**) (**f**)

Figure 13. Fatigue damage at different evaluation points under condition 1. (**a**) Check point 1. (**b**) Check point 2. (**c**) Check point 3. (**d**) Check point 4. (**e**) Check point 5. (**f**) Check point 6.

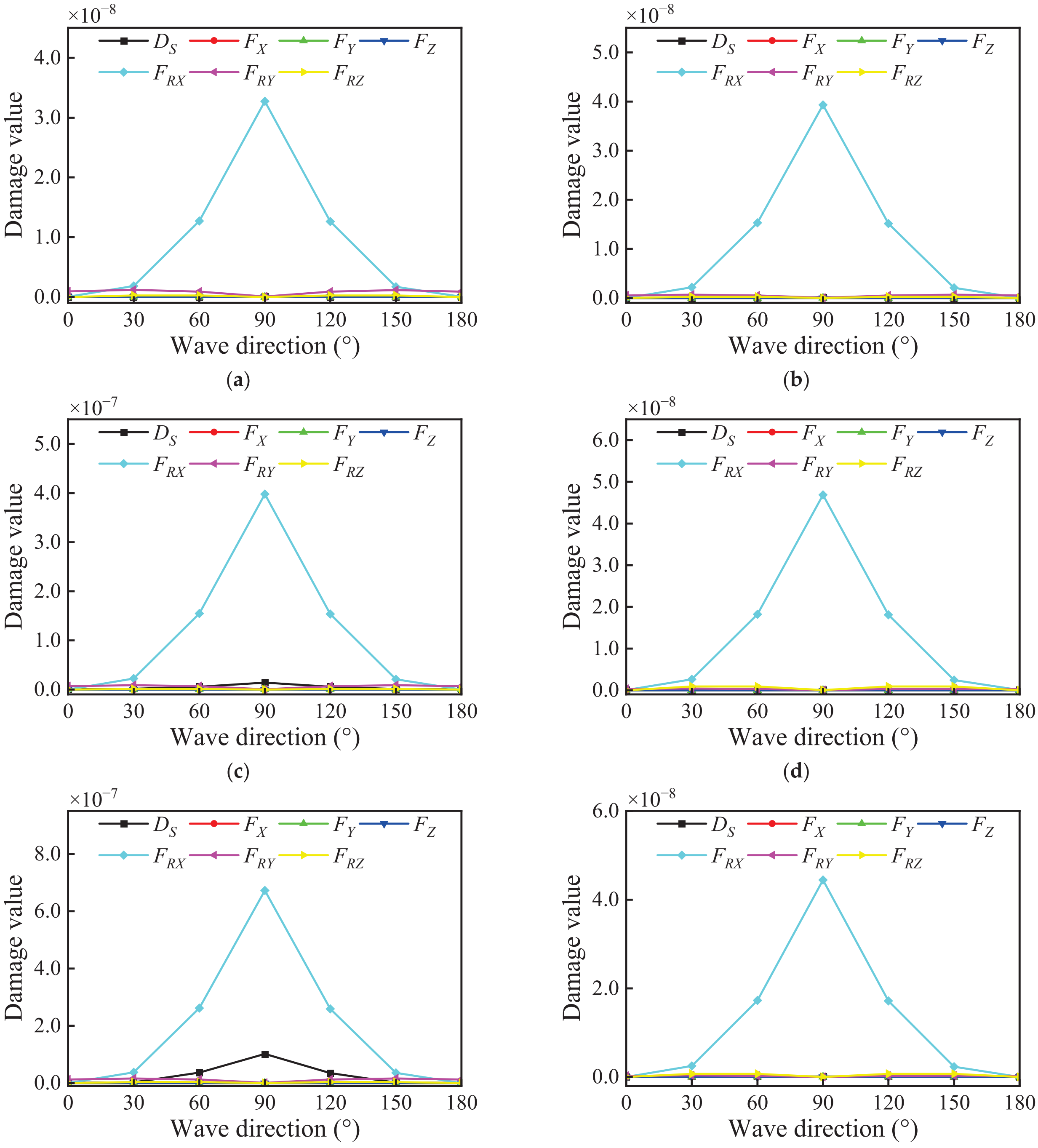

(a)

(b)

(c)

(d)

(e)

(f)

Figure 14. Fatigue damage at different evaluation points under condition 2. (**a**) Check point 1. (**b**) Check point 2. (**c**) Check point 3. (**d**) Check point 4. (**e**) Check point 5. (**f**) Check point 6.

4. Structural Strength Analysis Under Various Inputs

The structural strength analysis of ship structures under marine environmental loads is typically conducted using direct calculation methods, where wave loads are determined using the design wave method. Based on the design sea state, the corresponding design wave parameters were identified, and the resulting wave dynamic pressure and inertial forces were applied to the finite element model of the FNPP to compute the stress distribution and evaluate the structural strength. By comparing the stress distribution under different loading conditions, the dominant factors affecting the RPV structure could be identified.

4.1. Design Wave Method

The 100-year return period extreme sea state was selected as the design sea condition for strength assessment. The corresponding significant wave height and peak spectral period were determined from Table 1, while seven representative wave directions were chosen: 0° (head seas), 30°, 60°, 90° (beam seas), 120°, 150°, and 180° (following seas). The primary controlling load parameter was set as the vertical bending moment at midship, and its transfer function was calculated under different wave directions.

The response spectrum of the vertical bending moment under the design sea state was obtained using Equation (2). Under the narrow-band assumption, the short-term distribution of the response amplitude followed a Rayleigh distribution, and the exceedance probability of a given response threshold is given by

$$P(\overline{X} > \overline{x}) = \exp\left(-\frac{\overline{x}^2}{2\sigma_X^2}\right) \tag{10}$$

where $P(\overline{X} > \overline{x})$ is the probability that the response amplitude exceeded the threshold, and $\overline{x}$ is the target exceedance threshold.

A probability level of 10^{-8} was selected for determining the 100-year extreme vertical bending moment at midship. The resulting predicted values for different wave directions are listed in Table 2.

Table 2. Predicted vertical bending moments at midship for different wave directions.

Wave Direction (°)	Predicted Vertical Bending Moment (10^8·N·m)	Max Response Under Unit Wave Amplitude (10^8·N)
0	12.89	6.19
30	18.96	5.42
60	26.74	4.32
90	3.17	0.56
120	25.50	4.13
150	18.98	5.43
180	13.06	6.21

The design wave height is then computed as

$$H = \frac{2R}{RAO_c} \tag{11}$$

where H is the design wave height, R is the predicted extreme vertical bending moment, and RAO_c is the maximum response under unit wave amplitude.

Using the transfer function, the wave period and phase corresponding to the maximum response under unit wave amplitude were determined, defining the design wave parameters for the 100-year return period sea state, as summarized in Table 3.

Table 3. Design wave parameters for 100-year return period.

Wave Direction (°)	Wave Height (m)	Period (s)	Phase (°)
0	4.2	16.3	172.9
30	7.0	15.0	168.8
60	12.4	9.0	128.7
90	11.2	9.0	−74.7
120	12.4	9.5	135.2
150	7.0	15.0	170.7
180	4.2	16.3	174.6

4.2. Structural Stress Distribution

To analyze the stress distribution in the RPV under different load conditions, the design wave method was applied to compute the first principal stress distribution in the 100-year return period sea state. The wave-induced dynamic pressure and 6-DOF motion inertial forces were applied separately to assess their contributions to RPV stress, as shown in Figures 15–21.

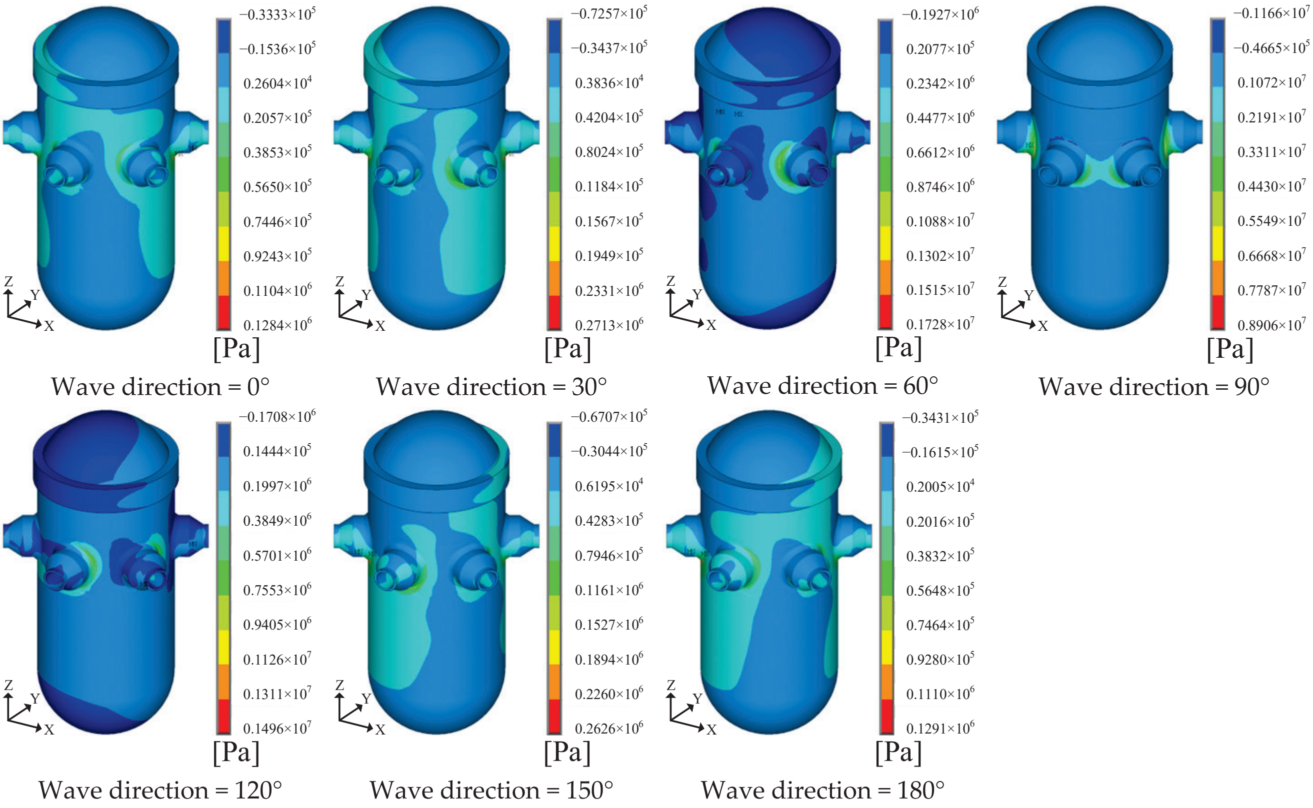

Wave direction = 0°
Wave direction = 30°
Wave direction = 60°
Wave direction = 90°
Wave direction = 120°
Wave direction = 150°
Wave direction = 180°

Figure 15. Stress distribution due to wave dynamic pressure.

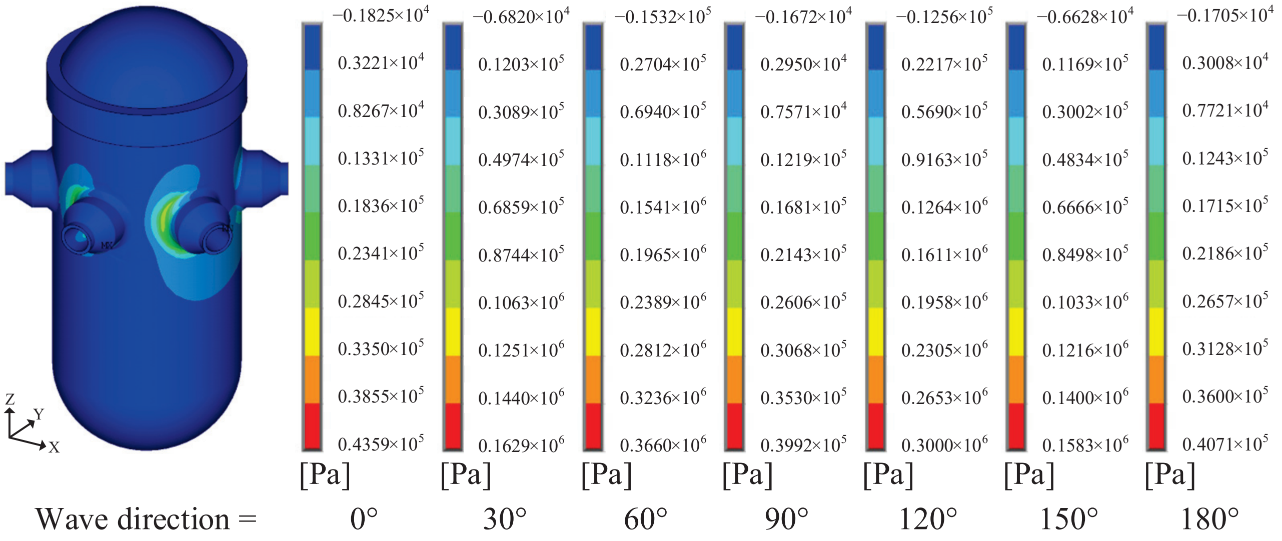

Wave direction = 0° 30° 60° 90° 120° 150° 180°

Figure 16. Stress distribution due to surge inertial force.

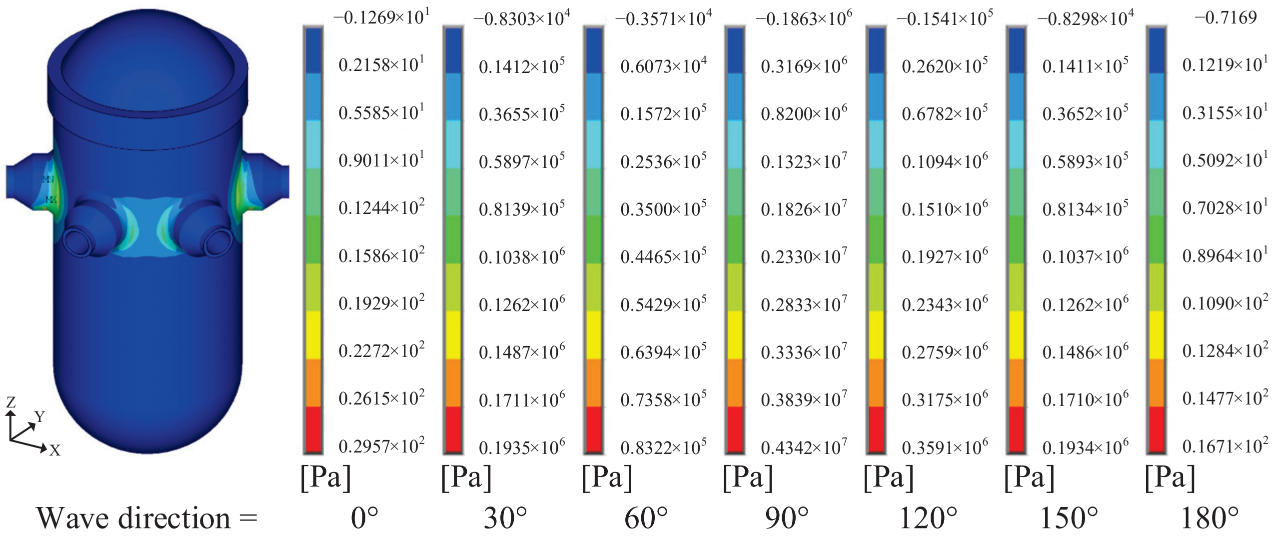

Figure 17. Stress distribution due to sway inertial force.

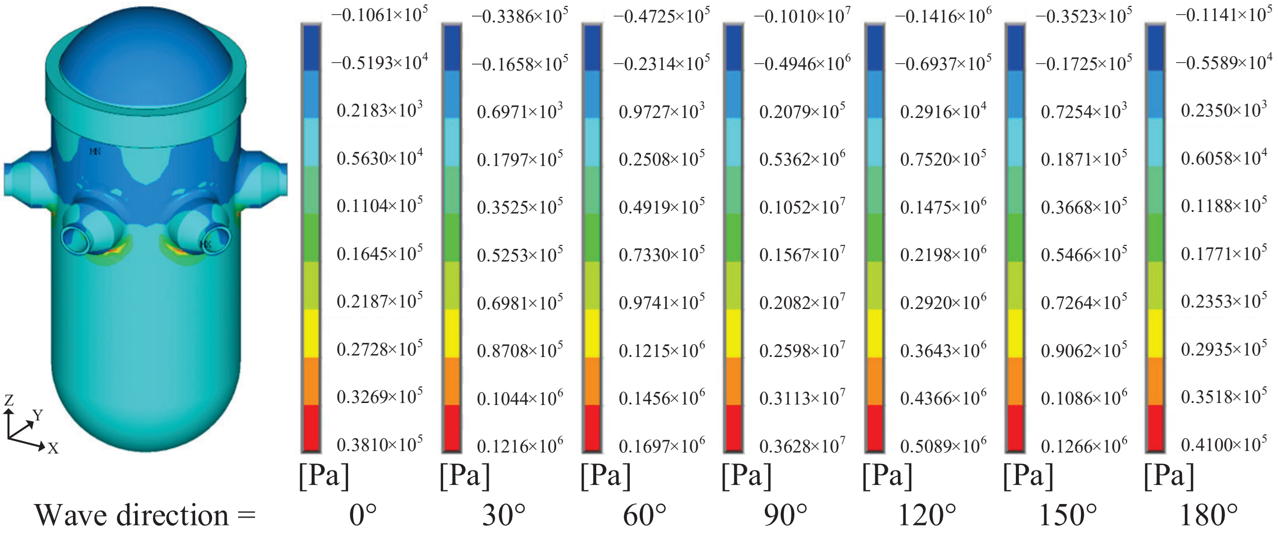

Figure 18. Stress distribution due to heave inertial force.

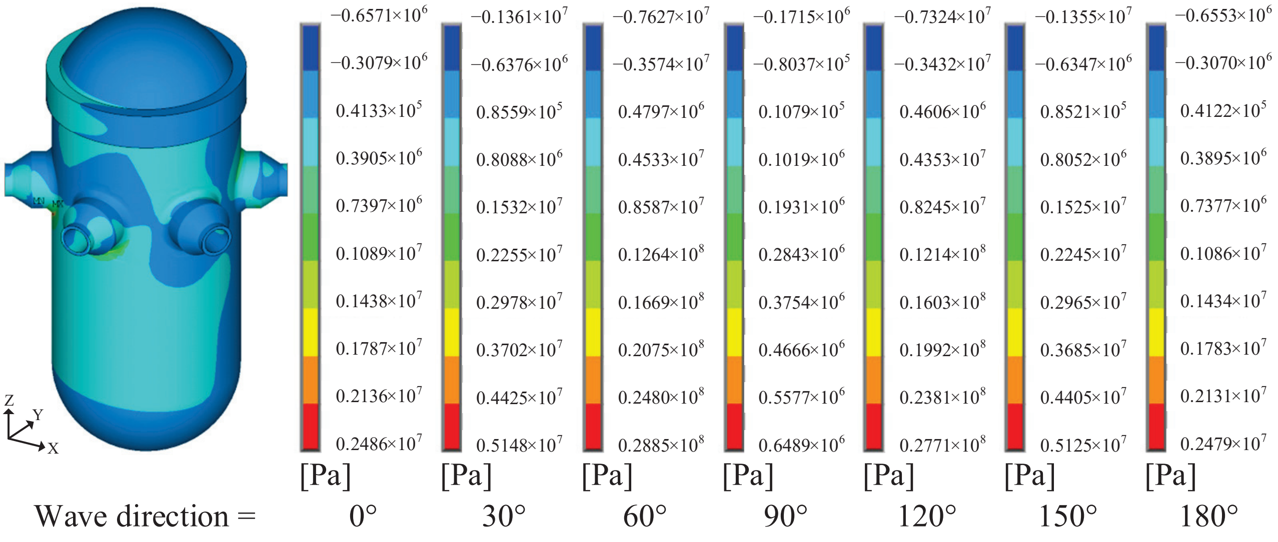

Figure 19. Stress distribution due to pitch inertial force.

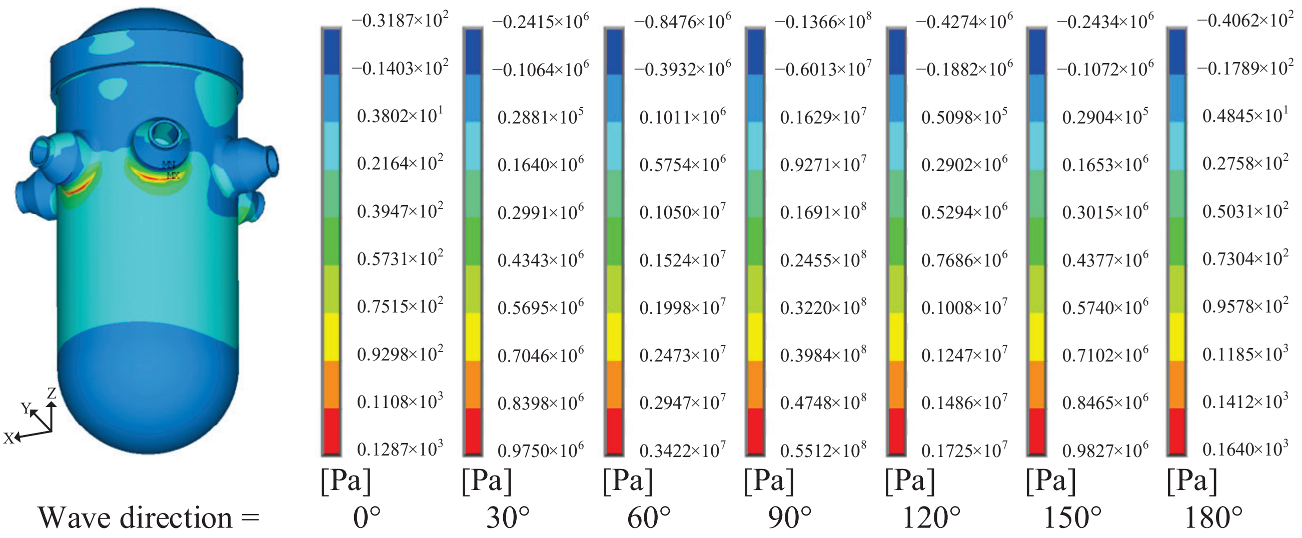

Figure 20. Stress distribution due to roll inertial force.

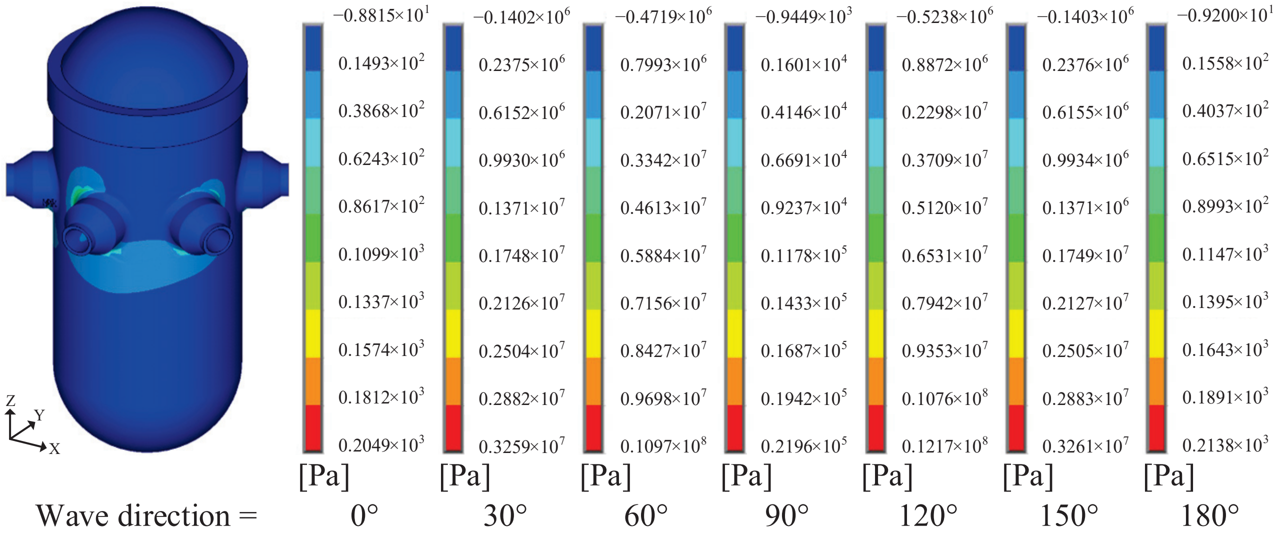

Figure 21. Stress distribution due to yaw inertial force.

Figures 15–21 indicate the following: Wave dynamic pressure resulted in varying stress distributions depending on the wave direction. Inertial forces from the 6-DOF motion produced similar stress distributions across different wave directions in the ship-fixed coordinate system, with only magnitude variations. The maximum RPV stress occurred at the nozzle connection. Rotational inertial forces (F_{RX}, F_{RY}, and F_{RZ}) induced higher stress levels than wave pressure and translational inertial forces. Roll motion under beam seas (90°) led to the highest stress levels.

As rotational inertial forces dominated RPV stress, structural strength assessments could be simplified by considering only these forces while neglecting wave-induced deformation and translational inertial forces. Furthermore, the maximum stress remained well below the material's yield strength (340 MPa) [14], suggesting that thermal-pressure loads had a greater impact on RPV strength. Therefore, in ultimate strength assessments, appropriate load cases should be selected based on the combined effects of thermal-pressure and inertial loads.

5. Conclusions

This study systematically analyzed the structural response of the RPV in an FNPP under marine environmental conditions. A detailed hull structure model, RPV structure model, and hydrodynamic model were constructed. Using spectral analysis and the design wave method, the fatigue damage and stress distribution of the RPV under various dynamic loads were assessed. The study focused on the impacts of hull deformation and 6-DOF inertial forces on the RPV. The results indicated that rotational inertial forces were the dominant factors affecting both fatigue damage and structural strength, whereas other dynamic loads had relatively minor effects. The main conclusions were as follows:

1. Among the dynamic loads induced by the marine environment, roll inertial force had the most significant impact on RPV fatigue damage, followed by pitch inertial force, while the effects of translational inertial forces and hull deformation were relatively minor.
2. The contribution of different dynamic loads to RPV fatigue damage varied significantly with wave direction. In beam seas, roll inertial force caused the highest fatigue damage. In head seas, pitch inertial force caused the highest fatigue damage.
3. Under the 100-year return period extreme sea state, stress analysis based on the design wave method showed the following: The maximum stress occurred at the nozzle connection of the RPV. Rotational inertial forces induced significantly higher stresses than wave pressure and translational inertial forces, making them the dominant contributors to RPV structural strength.
4. Unlike land-based nuclear power plants, the RPV in an FNPP must account for additional dynamic loads from the marine environment in strength and fatigue analyses. In addition to conventional thermal-pressure loads, hull deformation and inertial forces must be considered. Due to the large geometric scale of FNPPs, full-scale ship models must be used for hull deformation calculations, leading to high computational costs in RPV strength and fatigue analysis. To reduce computational expense, simplified models should be adopted, considering only the primary influencing factors.
5. This study focused exclusively on the effects of the marine environment on the RPV structure, without considering thermal-pressure loads. Therefore, under a 100-year return period sea state, the calculated RPV stress was far below the yield strength of the material. Under typical sea conditions, the calculated fatigue damage of the RPV was also minimal, indicating an almost infinite fatigue life. This suggested that with the current structural design, the RPV did not face strength or fatigue failure issues when considering only marine environmental effects. In actual structural assessments, thermal-pressure loads must be incorporated, along with long-term operational conditions, for a more comprehensive evaluation.

Author Contributions: F.M., conceptualization, methodology, software, formal analysis, writing-original draft, validation, data curation, and visualization; M.Z., funding acquisition, project administration, investigation, and writing—review and editing; X.Q., supervision and resources. All authors have read and agreed to the published version of the manuscript.

Funding: This work was sponsored and supported by the Leading Innovation Project of China National Nuclear Corporation (KY90200220002).

Data Availability Statement: The original contributions presented in this study are included in the article material. Further inquiries can be directed to the corresponding author.

Conflicts of Interest: The authors declare no conflicts of interest.

References

1. Mcginty, F.C. Nuclear Power Plants and Maintainability. *Hum. Factors* **1965**, *7*, 355–361. [CrossRef] [PubMed]
2. Vujić, J.; Bergmann, R.M.; Škoda, R.; Miletić, M. Small Modular Reactors: Simpler, Safer, Cheaper? *Energy* **2012**, *45*, 288–295. [CrossRef]
3. Zhao, S.; Song, Y. A Development Overview of National and International Floating Nuclear Power Plant. *Prog. Rep. China Nucl. Sci. Technol.* **2017**, *5*, 93–98.
4. Li, Q.; Song, D.; Zeng, W.; Chen, Z.; Liu, J.; Wang, D.; Xiao, R. Overall Design and Verification of ACP100S Floating Nuclear Power Plant. *Nucl. Power Eng.* **2020**, *41*, 189–192.
5. Collins, J.A. *Failure of Materials in Mechanical Design: Analysis, Prediction, Prevention*; John Wiley: Hoboken, NJ, USA, 1993.
6. Li, Z.; Mao, W.; Ringsberg, J.W.; Johnson, E.; Storhaug, G. A Comparative Study of Fatigue Assessments of Container Ship Structures Using Various Direct Calculation Approaches. *Ocean. Eng.* **2014**, *82*, 65–74. [CrossRef]
7. Garbatov, Y.; Ås, S.K.; Den Besten, H.; Haselbach, P.; Kahl, A.; Karr, D.; Kim, M.H.; Liu, J.; Lourenço de Souza, M.I.; Mao, W. Committee III. 2: Fatigue and Fracture. In Proceedings of the International Ship and Offshore Structures Congress, Vancouver, BC, Canada, 11–15 September 2022; p. D011S001R007.
8. Mukhtar, A.; Khattak, M.A.; Rafique, A.F.; Zareen, N. Reactor Pressure Vessel (RPV) Design and Fabrication: A Literature Review. *J. Adv. Res. Appl. Mech.* **2016**, *22*, 1–12.
9. Tachibana, Y.; Nakagawa, S.; Iyoku, T. Reactor Pressure Vessel Design of the High Temperature Engineering Test Reactor. *Nucl. Eng. Des.* **2004**, *233*, 103–112. [CrossRef]
10. Törrönen, K.; Cullen, W.H. *Effect of Light-Water Reactor Environments on Fatigue Crack Growth Rate in Reactor Pressure Vessel Steels*; ASTM International: West Conshohocken, PA, USA, 1982. [CrossRef]
11. Seifert, H.P.; Ritter, S. Stress Corrosion Cracking of Low-Alloy Reactor Pressure Vessel Steels under Boiling Water Reactor Conditions. *J. Nucl. Mater.* **2008**, *372*, 114–131. [CrossRef]
12. *DNV-CG-0129*; Fatigue Assessment of Ship Structures. DNV AS: Høvik, Norway, 2021.
13. ASME. *Code Boiler and Pressure Vessel Code*; ASME: New York, NY, USA, 2001.
14. RCC-MR. Design and Manufacturing Rules for Fast Reactors. In *AFCEN (June 1985), in Sell to AFNOR*; AFNOR: Paris, France, 1985.
15. Ma, F.; Li, H.; Zhang, M.; Qu, X. A Quasi Time-Domain Method for Fatigue Analysis of Reactor Pressure Vessels in Floating Nuclear Power Plants in Marine Environments. *J. Mar. Sci. Eng.* **2024**, *12*, 2085. [CrossRef]
16. Yuan, J.; Ma, F.; Zhang, M.; Shen, K.; Tang, J. The Time-Domain Design Stress Method for Fatigue Analysis of the Reactor Pressure Vessel in Floating Nuclear Power Plants. *J. Mar. Sci. Eng.* **2025**, *13*, 235. [CrossRef]
17. Shen, K.; Ma, F.; Yuan, J.; Zhang, M. A Damage Combination Method for Fatigue Analysis of Pressure Equipment in Floating Nuclear Power Plants. *J. Mar. Sci. Eng.* **2025**, *13*, 236. [CrossRef]
18. Veritas, D.N. Hull Structural Design Ships with Length 100 Metres and Above. In *DNV Rules for Classification of Ships*; DNV: Byrum, Norway, 2009.
19. Phelps, B.P. *Determination of Wave Loads for Ship Structural Analysis*; Aeronautical and Maritime Research Laboratory: Melbourne, Australia, 1997.
20. You, Z. Unified Approach for Estimation of Return Ocean Wave Height. *Oceanol. Limnol. Sin.* **2022**, *53*, 1015–1025.

Journal of
Marine Science and Engineering

Article

Modeling and Investigation of Long-Term Performance of High-Rise Pile Cap Structures Under Scour and Corrosion

Shilei Niu [1], Zhongxiang Liu [1,2,*], Tong Guo [2,3], Anxin Guo [4] and Sudong Xu [1]

[1] School of Transportation, Southeast University, Nanjing 210096, China; niushilei@seu.edu.cn (S.N.); sudongxu@seu.edu.cn (S.X.)
[2] Advanced Ocean Institute, Southeast University, Nantong 226000, China; guotong@seu.edu.cn
[3] Key Laboratory of Concrete and Prestressed Concrete Structures, Ministry of Education, Southeast University, Nanjing 210096, China
[4] Ministry-of-Education Key Laboratory of Structural Dynamic Behavior and Control, School of Civil Engineering, Harbin Institute of Technology, Harbin 150090, China; guoanxin@hit.edu.cn
* Correspondence: zhongxiang@seu.edu.cn

Abstract: High-rise pile cap structures, such as sea-crossing bridges, suffer from long-term degradation due to continuous corrosion and scour, which seriously endangers structural safety. However, there is a lack of research on this topic. This study focused on the long-term performance and dynamic response of bridge pile foundations, considering scour and corrosion effects. A refined modeling method for bridge pile foundations, considering scour-induced damage and corrosion-induced degradation, was developed by adjusting nonlinear soil springs and material properties. Furthermore, hydrodynamic characteristics and long-term performance, including hydrodynamic phenomena, wave force, energy, displacement, stress, and acceleration responses, were investigated through fluid–structure coupling analysis and pile–soil interactions. The results show that the horizontal wave forces acting on the high-rise pile cap are greater than the vertical wave forces, with the most severe wave-induced damage occurring in the wave splash zone. Steel and concrete degradation in the wave splash zone typically occurs sooner than in the atmospheric zone. The total energy of the structure at each moment under load is equal to the sum of internal energy and kinetic energy. Increased corrosion time and scour depth result in increased displacement and stress at the pile cap connection. The long-term dynamic response is mainly influenced by the second-order frequency (62 Hz).

Keywords: dynamic performance; scour depth; *p*–*y* springs; corrosion damage; fluid–structure interaction; finite element analysis; bridge pile foundation

1. Introduction

Sea-crossing bridges, as a key node and important component of the transportation network, play a pivotal role in advancing the development of the marine transportation infrastructure and hold significant strategic importance [1–3]. Numerous sea-crossing bridges worldwide have adopted a high-rise pile cap substructure [4], such as the San Francisco Bay Area Bridge in the United States [5], the Akashi Strait Bridge in Japan [6], the Sydney Harbor Bridge in Australia [7], and the Donghai Bridge in China [8]. Unlike land bridges, marine bridges are situated in complex and dynamic marine environments, typically characterized by deep water and large waves [9,10]. Wave action is often one of the key loads influencing the structural design of sea-crossing bridges [11,12]. Deep-water high-rise pile cap foundations are highly flexible and are susceptible to damage from foundation

J. Mar. Sci. Eng. **2025**, *13*, 450 https://doi.org/10.3390/jmse13030450

scour and dynamic forces from the water medium. Effectively analyzing dynamic damage has always been a challenge for the safe and healthy operation of sea-crossing bridges.

Bridge structures typically enjoy extended longevity; however, in marine settings, reinforced concrete bridges experience considerable degradation due to environmental elements such as alternating wet–dry conditions, chloride ion corrosion, and carbonation, resulting in a notable decline in their durability [13–15]. Among these factors, chloride ion corrosion stands out as a major culprit for reinforcement corrosion as it initiates the deterioration process. This corrosion compromises the concrete's protective layer, hastening the corrosion of internal reinforcement, consequently diminishing the load-bearing capacity of the bridge components and ultimately culminating in reduced durability [16,17]. As shown in Figure 1, the reinforced concrete column under chloride ion erosion reveals that the rust expansion of the reinforcement leads to the detachment of the protective concrete cover. Additionally, with the increase in service time, the column exhibits a significant occurrence of longitudinal rust spots.

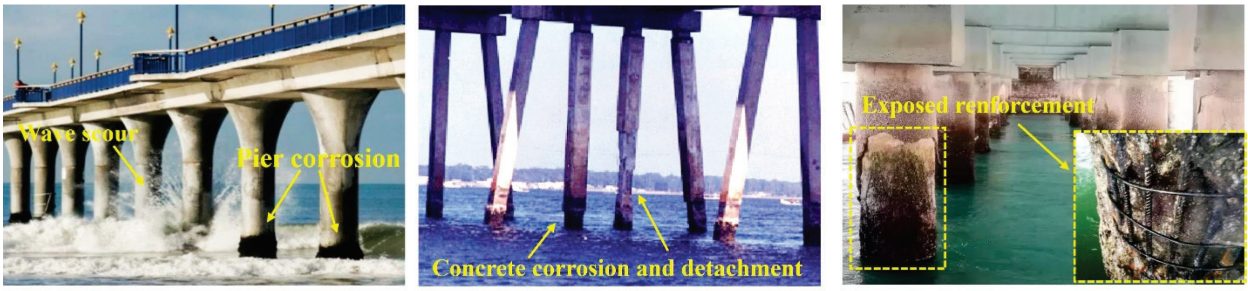

Figure 1. Corrosion damage to the substructures of sea-crossing bridges.

In recent years, researchers both domestically and abroad have investigated the mechanism, rate, and influencing factors of steel reinforcement corrosion through experiments and theoretical models. Yuan et al. [18] accelerated the corrosion rate of steel bars in concrete by adding chloride salt, finding that the cracking of the concrete has a significant effect on the corrosion rate. However, a reasonable model has not been established to simulate the accelerated process of steel bar corrosion after concrete cracking. Ou et al. [19] conducted accelerated corrosion tests on the steel bars of large reinforced concrete beams using the method of applied current, and conducted cyclic load tests on corroded beams. It was concluded that the mass loss of stirrups is greater in the same accelerated corrosion time. As the corrosion progresses, the stirrups fracture, causing the beam to transition from bending failure to bending–shear failure. Akiyama et al. [20] used X-ray digital image processing to visualize the corrosion process in reinforced concrete members to estimate the reliability of these structures. Based on response surface theory and finite element model results, Fan et al. [21] examined the impact of corrosion and erosion on the brittleness of bridge structure barges. It was found that corrosion and erosion have a net positive impact on the dynamic response of the pier columns of sea-crossing bridges and cause greater damage to pile foundations.

While a considerable amount of research has focused on the effects of chloride ion corrosion on the performance and durability of sea-crossing bridges, studies on the dynamic failure processes and long-term mechanisms under wave action remain limited. Given the aging of sea-crossing bridges and the deterioration of their material and structural capacities, investigating fluid–solid coupling and conducting dynamic response analyses of high-rise pile caps under nonlinear pile–soil interactions is of significant importance.

Traditional methods often rely on simplified models and assumptions, such as basic static load analyses or empirical wave force calculations [22,23]. In contrast, this study employs more detailed models that account for the complex impacts of sediment erosion and corrosion, and examines long-term dynamic responses through fluid–solid coupling analysis and pile–soil interaction. In Section 2, the fluid domain model is established based on the wave principle, and the feasibility of the numerical flume is verified. In addition, the modeling process of high-rise pile cap is introduced in detail. A simulation of the scouring effect and the degradation of structural strength due to corrosion are also introduced into the model. Finally, the results of numerical simulation are discussed and analyzed in Section 3. This section includes a discussion of the hydrodynamic analysis of the cap; the degradation of the performance parameters of the structural materials under corrosion; and the energy, displacement, stress, and acceleration response characteristics of the high-rise pile cap. This study provides key insights for early damage warning and guidance on protective measures, enhancing the resilience and durability of marine structures against scour and corrosion.

2. Refined Modeling with Scour- or Corrosion-Induced Effects

2.1. Fluid Domain Modeling

2.1.1. Governing Equations

When simulating wave motion in the study of wave–structure interactions, it is assumed that water is an incompressible viscous fluid [24,25]. The continuity equation and Reynolds time-averaged Navier–Stokes equation (RANS equation) are used as the control equations for wave motion [26].

$$\frac{\partial}{\partial x_i}(u_i A_i) = 0. \tag{1}$$

$$\frac{\partial u_i}{\partial t} + \frac{1}{V_F}(u_j A_j \frac{\partial u_i}{\partial x_j}) = -\frac{1}{\rho}\frac{\partial p}{\partial x_i} + G_i + f_i. \tag{2}$$

where i = 1, 2, 3, x_i represents the x, y, z coordinates; u_i represents the time-averaged velocity in each direction of the flow field; A_i represents the area fraction of the flowable fluid in each direction; V_F represents the volume fraction of the fluid; t represents the time; p represents the fluid pressure; ρ represents the fluid density; G_i represents the gravitational acceleration of the fluid in each direction; and f_i represents the acceleration due to viscous forces in each direction [26], expressed as follows:

$$f_i = \frac{1}{V_F}[\frac{\tau_{b,i}}{\rho} - \frac{\partial}{\partial x_j}(A_j S_{ij})]. \tag{3}$$

$$S_{ij} = -(v + v_T)[\frac{\partial u_i}{\partial x_j} + \frac{\partial u_j}{\partial x_i}]. \tag{4}$$

where $\tau_{b,i}$ denotes the fluid shear stress in each direction plane; S_{ij} denotes the strain rate tensor; v denotes the dynamic viscosity; and v_T denotes the turbulent viscosity.

A wave's free surface must satisfy both dynamic free surface boundary conditions and kinematic boundary conditions, meaning that the normal component of fluid velocity must match that of the boundary itself, and the stress vector component must be continuous [27,28]. Capturing the free surface of waves is crucial in establishing numerical wave flumes. The Volume of Fluid (VOF) method was used to monitor the interface between air and water [29–31]; this method defines the volume fraction function α for each phase of the two-phase fluid in every computational cell.

$$\alpha(x,t) = \begin{cases} 0, & air \\ 1, & water \\ 0 < \alpha_s < 1, & freesurface \end{cases}. \tag{5}$$

Once the volume fraction had been established, the two-phase flow was treated as a mixed-phase fluid, with its density ρ and dynamic viscosity μ expressed as

$$\begin{cases} \rho = \alpha\rho_1 + (1-\alpha)\rho_2 \\ \mu = \alpha\mu_1 + (1-\alpha)\mu_2 \end{cases}. \tag{6}$$

The volume fraction function was derived by solving the subsequent equation:

$$\frac{\partial \alpha}{\partial t} + \frac{\partial}{\partial x_i}(\alpha u_i) + \frac{\partial}{\partial x_i}[\alpha(1-\alpha)u_{\alpha i}] = 0. \tag{7}$$

where u_i is the relative compression velocity [32], and the final term on the left side of the equation serves as an artificial compression term, aiming to restrict numerical diffusion. α_{water} = 0.5 is taken for all free liquid levels in the numerical simulations of this study.

2.1.2. Numerical Model Setup

A three-dimensional numerical flume model, measuring 100 m × 54 m × 28 m (length × width × height), was established, as depicted in Figure 2. The design static water depth was set at 20 m. To eliminate the wave attenuation caused by the viscous effects of water and frictional interactions, the left edge of the pile cap was positioned 10 m from the inlet. Employing the boundary wave-making method, the wave-making boundary was set through the velocity inlet. The wave-absorbing region was set in a three-dimensional area within one wavelength at the end of the flume. The bottom and front/rear faces were designated as non-slip wall conditions, while the top face was represented as an atmospheric pressure outlet.

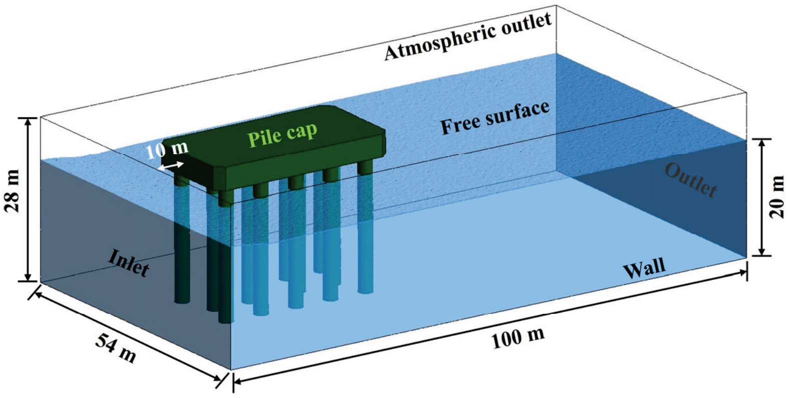

Figure 2. Wave-cap numerical flume model.

The model was meshed using a computational fluid dynamics (CFD) unstructured mesh; the mesh model is shown in Figure 3. To accurately capture wave motion and free-surface phenomena, grid refinement was applied within 3 m above and below the free surface and in the vicinity of the pile cap region. The global grid size was set at 0.5 m, with a refined grid size of 0.2 m in the specified regions, resulting in a total grid count of 18,684,462 cells. Wave gauges were positioned at 1 m and 10 m from the entrance to monitor the wave generation effects in the numerical flume.

The upper part of high pile cap fluid–structure coupling model is a rectangular pile cap of 3350 cm × 1750 cm × 400 cm. Detailed dimensions are shown in Figure 4. For the sake of esthetics, chamfers of 150 cm × 150 cm were set at the four corners of the pile cap. Since the selected wave conditions in this study do not directly impact the cap, the mitigating effect of the chamfers on wave-induced erosion was not a primary focus of the investigation.

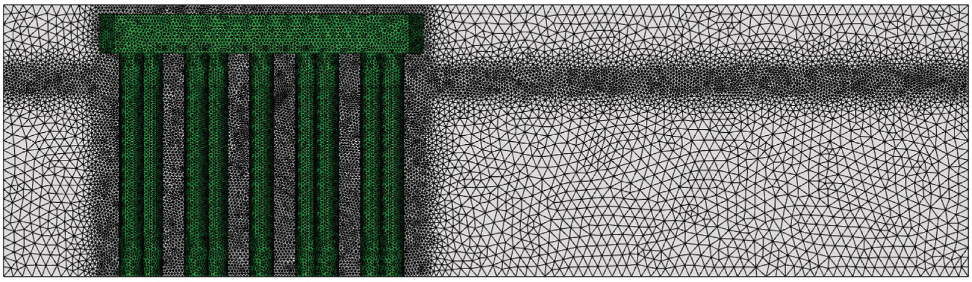

Figure 3. Detailed drawing of the grid division.

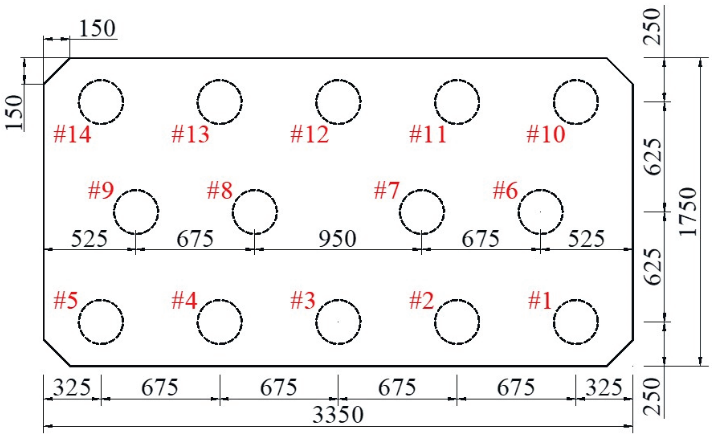

Figure 4. Detailed dimensional drawing of the pier cap (unit: cm).

During the computation process, multiphase flow handling was employed, where the fluids considered were gas phase and liquid phase, with their physical property parameters set as shown in Table 1. The VOF model was utilized to track the free surface, while the realizable *k*-ε model was chosen as the viscous model. A segregated solver was selected, with the pressure equation solved using the body-force-weighted method. The pressure–velocity coupling method employed the PISO algorithm, and the volume fraction was calculated using the Geo-Reconstruct method. In the operating environment, the pressure reference value was set to 101,325 Pa and the gravity acceleration was set to 9.81 $\mathrm{m/s^2}$. Considering both convergence issues and computational time, a time step of 0.05 s was set, and the transient calculation was conducted.

Table 1. Physical properties of fluid.

Fluid Type	Density (kg/m^3)	Dynamic Viscosity (kg/m·s)	Linear Attenuation Impedance (s^{-1})
Air	1.225	1.7894×10^{-5}	0
Water	998.2	0.001003	2.0367

The Stokes second-order wave was used to simulate ocean waves. According to the application range of the wave theory proposed by Maywalt [33], the relevant wave parameters of the Stokes second-order wave were taken in the following ranges:

$$H/gT^2 \in (0.001 \sim 0.0086). \tag{8}$$

$$H/L \in (0.00625 \sim 0.0503). \tag{9}$$

Here, H is the wave height, g is the gravitational acceleration, and T is the period. The hydrostatic depth was taken as D = 20 m, the wave height was taken as 1.2 m, and the period was taken as 4 s. The wavelength, period, and hydrostatic depth followed a diffuse relationship with each other during wave propagation [34], and the water depth and period of the wave had an effect on the wavelength in the process of wave propagation. Under the condition that the wave period and hydrostatic depth were known, the wavelength $L = 25$ m was calculated by Newton's iterative method based on Equation (10) for the wave velocity in finite water depth.

$$\frac{L}{T} = \sqrt{\frac{gL}{2\pi}\tanh\frac{2\pi D}{L}}. \tag{10}$$

2.1.3. Numerical Wave Verification

The accuracy of the numerical wave simulations in the numerical wave flume needed to be validated primarily through a comparative analysis of the spatiotemporal distribution of waveforms in the numerical wave flume with theoretical waveforms. In the numerical wave flume, wave gauges were set up at positions 1 m and 10 m from the inlet to monitor wave heights over time, which were then compared with the time-domain curves of the theoretical wave heights.

Figure 5 illustrates the variation of wave amplitudes over time at the horizontal wave gauge locations in the numerical wave flume. It can be observed that, during the motion of numerical waves, the ascent and descent of the waves exhibit good periodicity and stability. Once the numerical waves stabilize, their wave period aligns with the theoretical waveform period, and the crest and trough positions are essentially consistent. Comparing the time-domain curves of wave amplitudes at $x = 1$ m and $x = 10$ m locations, it is evident that the further the monitoring position is from the velocity inlet, the longer the development time of the waveforms, requiring more time to form stable waveforms. This phenomenon occurs because, at the initial moment, the water at the wave generation boundary undergoes periodic changes based on the wave generation function provided by the Stokes second-order wave. However, since the fluid is not a rigid body, it takes some time for the fluid motion patterns at the wave generation boundary to propagate to the corresponding monitoring positions, thus forming stable waves.

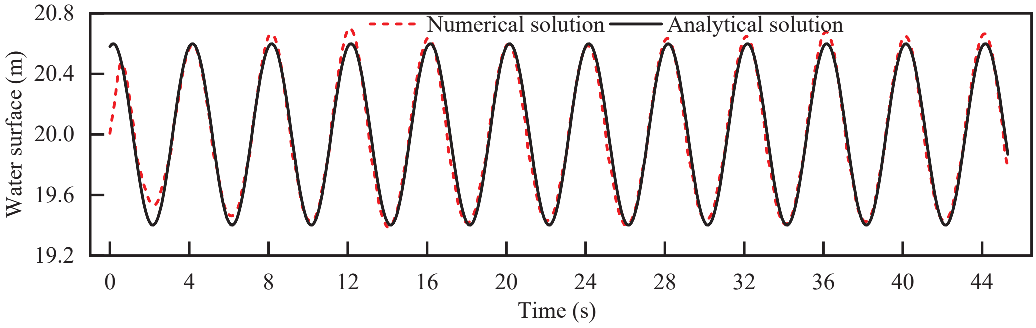

(**a**) 1 m.

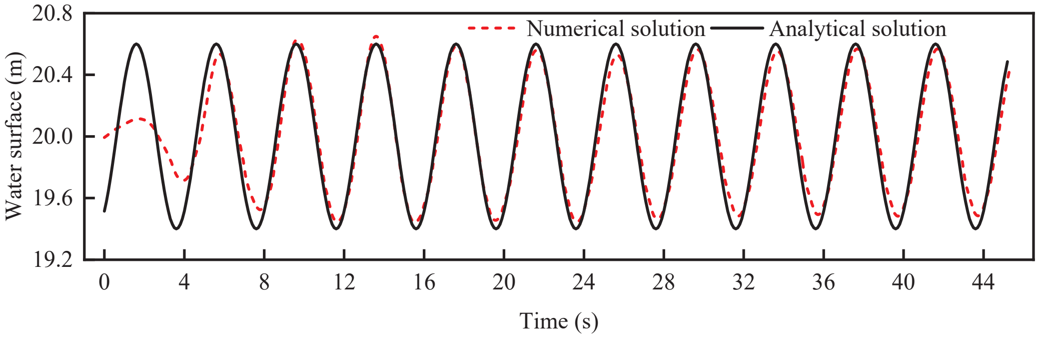

(**b**) 10 m.

Figure 5. Time variation curve of the wave surface at the wave height monitoring location.

2.2. Solid-Domain Modeling Considering Scour and Corrosion

2.2.1. High-Rise Pile Cap Modeling

The high-rise pile cap at the mid-span position of the 1000t-level auxiliary navigation hole continuous beam bridge of the Donghai Bridge was selected as the case analysis object, as shown in Figure 6. The height of the pile was 110 m, and the height of the pier cap was 4 m. The compressive strength of the concrete for the piles and pile cap was 30 MPa. There were 28 longitudinal bars arranged along the circumference of the pile, with a longitudinal bar diameter of 32 mm and a yield strength of 400 MPa. Along the longitudinal direction of the pile, there were 110 stirrups with a diameter of 16 mm and a yield strength of 335 MPa. The concrete protection layer thickness of the bridge pile was 50 mm. The soil depth of the pile was 87 m, and the depth of the seawater was set at 20 m. Based on the corrosion degree, the non-buried segment of the high-rise pile cap structure was divided into three zones: atmospheric area (4 m), wave splash area (3 m), and immersed area (20 m). This setup indicates that the structure is situated in a low-tide marine environment.

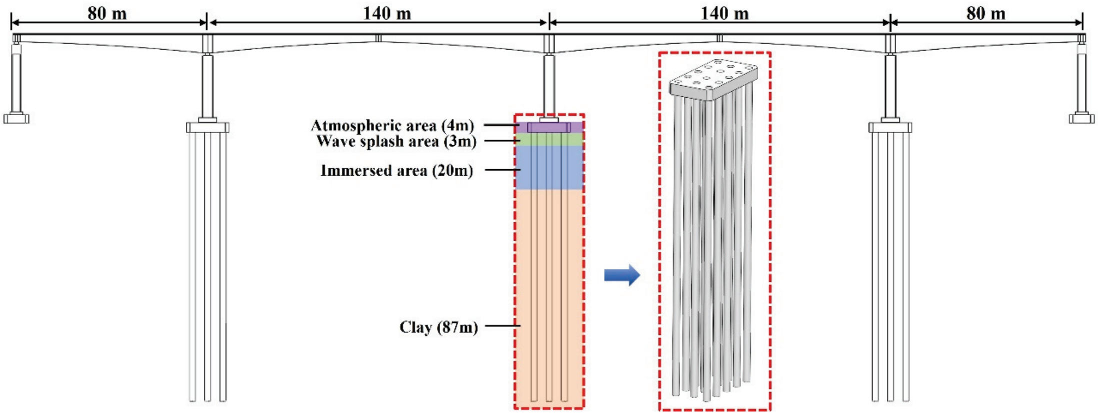

(a) High-rise pile cap of Donghai Bridge.

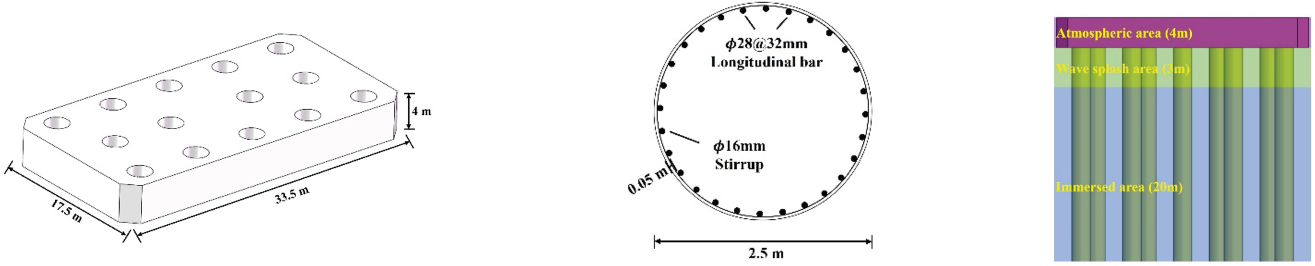

(b) Dimension of the cap. (c) Reinforcement arrangement of the pile. (d) Corrosion degree zoning.

Figure 6. Detailed structural diagrams for bridge and high-rise pile cap.

A refined model of the high-rise pile cap was established using the dynamic analysis software LS-DYNA (2020) to analyze the long-term dynamic response of the pile cap under different levels of corrosion and scour depth conditions. The material parameters used in this finite element model are shown in Table 2. Concrete was simulated using the *MAT_CSCM_CONCRETE (159) nonlinear material model, which can effectively simulate the dynamic response behavior of concrete materials. This model was developed by the U.S. Federal Highway Administration. It considers the strain rate effect of concrete materials through Equation (11), which reflects the strain rate characteristics of concrete materials in tensile and compressive cases, respectively, and embodies the enhancement of material strength by the strain rate effect. The model only needs to provide uniaxial compressive strength and maximum aggregate size to automatically generate the relevant parameters.

$$\begin{cases} f_{\mathrm{T}}^{\prime\mathrm{d}} = f_{\mathrm{T}}^{\prime} + E\varepsilon_e\eta \\ f_{\mathrm{C}}^{\prime\mathrm{d}} = f_{\mathrm{C}}^{\prime} + E\varepsilon_e\eta \end{cases}. \tag{11}$$

where $f_{\mathrm{T}}^{\prime\mathrm{d}}$ is the dynamic tensile strength of concrete; $f_{\mathrm{T}}^{\prime}$ is the static tensile strength of concrete; $f_{\mathrm{C}}^{\prime\mathrm{d}}$ is the dynamic compressive strength of concrete; $f_{\mathrm{C}}^{\prime}$ is the static compressive strength of concrete; E is the modulus of elasticity; ε_e is the equivalent strain rate; and η is the coefficient of dynamic increase associated with the strain rate parameter.

Table 2. Material parameters of high-rise pile cap components.

Component	Element	Constitutive Model	Parameters	Value
Concrete	SOLID	*MAT_CSCM_CONCRETE	Mass density	2400 kg/m^3
			Uniaxial compression strength	30 MPa
			Maximum aggregate size	20 mm
			Rate effects	Turn on
Longitudinal bar/stirrup	SOLID	*MAT_PLASTIC_KINEMATIC	Mass density	7850 kg/m^3
			Young's modulus	235,000 MPa
			Poisson's ratio	0.3
			Yield stress	310 MPa
			Failure strain	0.35
			C	40
			P	5

Steel reinforcement was modeled using the *MAT_PLASTIC_KINEMATIC (003) material [35], a bilinear elastic–plastic material model. The model is based on the elastic–plastic random dynamics model proposed by Cowper and Symonds, which can take into account strain rate effects and cell failure of the material. The Cowper–Symonds eigenequation is

$$\sigma_d = \left[1 + \left(\frac{\varepsilon_r}{C}\right)^{1/P}\right]\left(\sigma_s + \beta E_p \varepsilon_{eff}^{p}\right). \tag{12}$$

where σ_d is the ultimate yield stress; σ_s is the initial yield stress; ε_r is the strain rate; C and P are the strain rate parameters; β is the correction coefficient, where the kinematic reinforcement is taken as 0, and the isotropic reinforcement is taken as 1; E_p is the plastic reinforcement modulus; and ε_{eff}^{p} is the equivalent plastic strain.

The constitutive relationships for concrete and steel reinforcement selected in the numerical model are illustrated in Figure 7. Concrete remains in the elastic deformation stage until it reaches the ultimate load. After exceeding the ultimate load, the decay rate of the concrete's compressive strength increases rapidly. It is evident that the tensile capacity of the concrete is very limited. Reinforcement exhibits significant elastic–plastic behavior under axial tension. The hardening behavior of kinematic and isotropic reinforcement can be specified by adjusting the modification parameter β.

Additionally, the longitudinal bars and stirrups were discretized using Hughes–Liu beam elements (ELFORM = 1) with a mesh size of 10 mm. The keyword *CONSTRAINED_BEAM_IN_SOLID facilitated perfect bonding between the concrete and steel reinforcement. For the high-rise pile cap, a total of 533,448 solid elements and 134,504 beam elements were employed. Furthermore, to account for the impact of soil resistance on the bridge's dynamic response, p–y springs (*MATSPRING_INELASTIC) were strategically positioned 45° around the pile and at intervals of 1 m along the pile height to capture the nonlinear soil behavior under wave action, as shown in Figure 8.

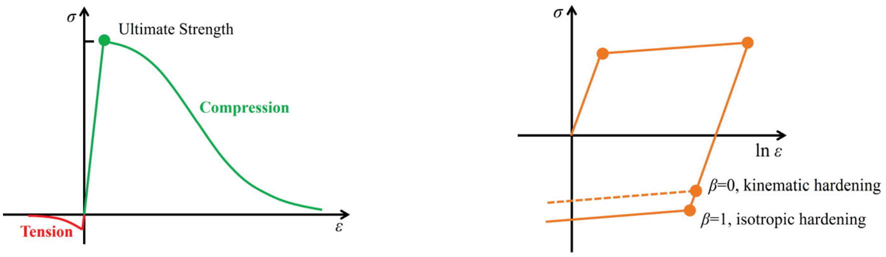

(**a**) Concrete. (**b**) Steel reinforcement.

Figure 7. Constitutive relationship of concrete and steel reinforcement in numerical modeling.

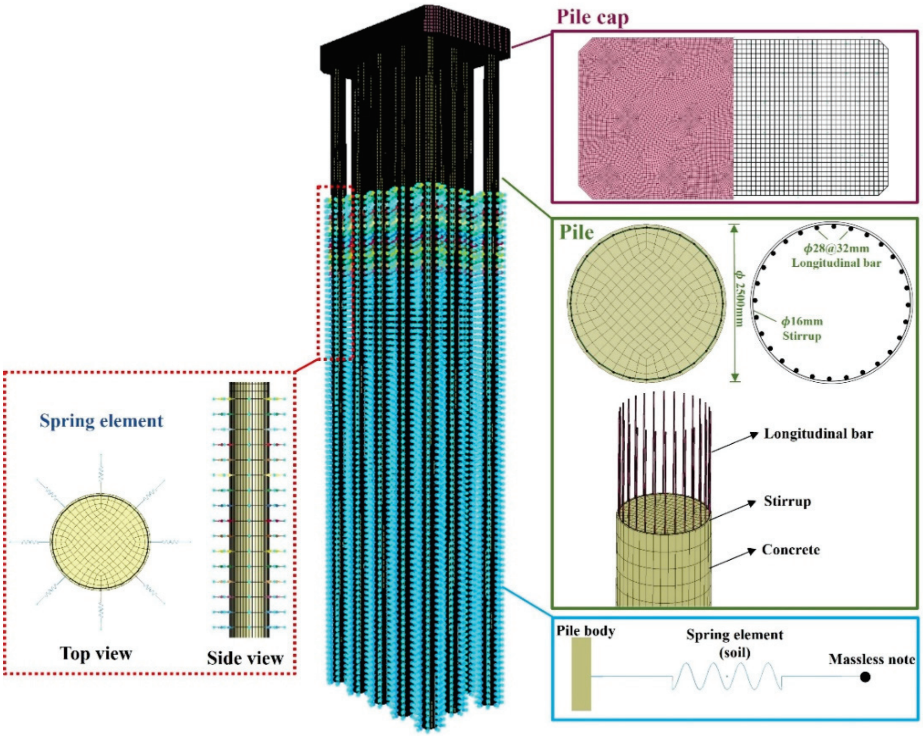

Figure 8. Finite element model of high-rise pile cap.

2.2.2. Pile–Soil Interaction Under Scour

In marine engineering, scour pits around pile foundations are formed as a result of wave action on the seabed. The energy from waves induces strong water flow and turbulence in the vicinity of the pile, leading to significant shear forces on the sediment. This process causes the erosion and displacement of seabed sediments surrounding the pile. As sediment is continuously removed due to wave-induced hydrodynamic forces, a localized depression, known as a scour pit, develops and expands over time. It is important to note that scour encompasses not only sediment transport, but also the wear and tear of concrete structures caused by the impact of waves. However, since the latter process occurs at a significantly slower rate, its influence was ignored in this study. The scour pit can compromise the stability of the pile foundation by reducing the lateral support provided by the surrounding soil, potentially leading to uneven settlement or structural instability. Understanding and accurately predicting this scour process is essential for ensuring the long-term stability and safety of marine structures.

The essence of the change in scour depth is the alteration of the pile–soil interaction. Therefore, accurately simulating the variation in bridge boundary conditions was crucial in this study. The soil resistance around the pile group acting on the pile was simplified as a sequence of two-point discrete nonlinear springs, as illustrated in Figure 7. The spring elements adopted the *MAT_SPRING_INELATSIC (MAT_S08) model of non-elastic material, connecting each pile and discrete spring elements spaced at 1 m. Since the soil cannot provide any tensile strength, this model only accounted for compressive response and excluded tensile response. The nonlinear compression stiffness of the springs followed the *p*–*y* curve specified in the "Code for Design of Port and Harbour Engineering Pile Foundations" (JTS 167-4-2012) [36–38]. The riverbed soil beneath the high-rise pile cap mainly consisted of clay. The depth of the clay was 87 m, its weight density γ was 17.64 kN/m^3, and the angle of internal friction α was 35°. The undrained shear strength C_u was 40 kPa.

The calculation formula for the standard value of ultimate horizontal resistance per unit area of clay pile side is

$$P_u = 3C_u + \gamma Z + (\zeta C_u Z/d). \tag{13}$$

$$P_u = 9C_u. \tag{14}$$

$$Zr = 6C_u d/(\gamma d + \zeta C_u). \tag{15}$$

where P_u represents the standard value of ultimate horizontal soil resistance per unit area of the pile at a depth beneath the mud surface (kPa); C_u represents the standard value of the undrained shear strength of clay in its original state (kPa); γ is the weight of the soil (kN/m^3); Z is any depth of the pile below the mud surface (m); ζ is a coefficient, taken as 0.250~50; d is the pile width or pile diameter (m); and Z_r is the depth at which the ultimate horizontal soil resistance turns (m).

For soft clay with an undrained shear strength standard value less than or equal to 96 kPa, the *p*–*y* curve under the non-reciprocating load is determined using the following formula:

$$\frac{P}{P_u} = 0.5(\frac{Y}{Y_{50}})^{1/3} \quad \frac{Y}{Y_{50}} < 8. \tag{16}$$

$$\frac{P}{P_u} = 1.0 \quad \frac{Y}{Y_{50}} \geq 8. \tag{17}$$

$$Y_{50} = \rho \varepsilon_{50} d. \tag{18}$$

where P is the standard value of horizontal soil resistance acting on the pile at a depth below the mud surface (kPa); Y is the transverse horizontal deformation of the pile below the mud surface depth (mm); Y_{50} is the lateral horizontal deformation of the pile at which the soil surrounding the pile reaches half of its ultimate horizontal soil resistance (mm); ρ is the correlation coefficient, taken as 2.5; and ε_{50} is the stress value at half the maximum principal stress difference in the triaxial test. For soft clay with high saturation, the strain value at half of the unconfined compressive strength can also be taken. If there are no test data, the value should be taken according to the following rules: if C_u is at 12~24 kPa, ε_{50} selects 0.020; if C_u is at 24~48 kPa, ε_{50} selects 0.010; if C_u is at 48~96 kPa, ε_{50} selects 0.007.

The soil surrounding an individual pile exhibits an infinite state when subjected to external horizontal loads, which means that the response of the soil is assumed to be unaffected by other factors, such as the influence of adjacent structures or boundary effects. However, in a cluster of piles, the proximity between piles alters the *p*–*y* curve of the soil surrounding the inner pile foundation, as it experiences reduced horizontal resistance compared to that of a single pile. Conversely, the soil surrounding the outer pile foundation maintains a semi-infinite state, resulting in a *p*–*y* curve similar to that of a single pile soil [39]. Therefore, the group pile foundation needs to consider the group pile effect. According to the JTS 167-4-2012, except for the pile farthest from the load point, the pile group effect should be considered for all other pile sections with a center distance of less than 8 times the pile diameter and a depth of less than 10 times the pile diameter. The commonly used method to consider the effect of pile group is to multiply the horizontal soil resistance of a single pile foundation by a reduction coefficient, which can be calculated using the following formula [36]:

$$\lambda_h = \left(\frac{(S_0/d) - 1}{7} \right)^{0.043(10 - Z/d)}. \tag{19}$$

where λ_h is the reduction coefficient of soil resistance; S_0 is the spacing between piles; Z is the arbitrary depth of the pile foundation below the mud surface; and d is the pile diameter.

The *p*–*y* curves of the soil layers before and after reduction at each depth, based on the above calculation data, are shown in Figure 9. Guo et al. [40] simulated varying scour depths by removing soil springs at corresponding locations within the scour hole. Although the material parameters of the soil used in their study differ from those adopted here, the variation in stiffness of the nonlinear soil springs with depth follows a consistent trend. Similarly, the reduction in soil spring stiffness due to pile group effects exhibits comparable behavior between the two studies. These findings collectively demonstrate the rationality of the soil spring parameters selected in this work, further validating the robustness of the proposed modeling approach.

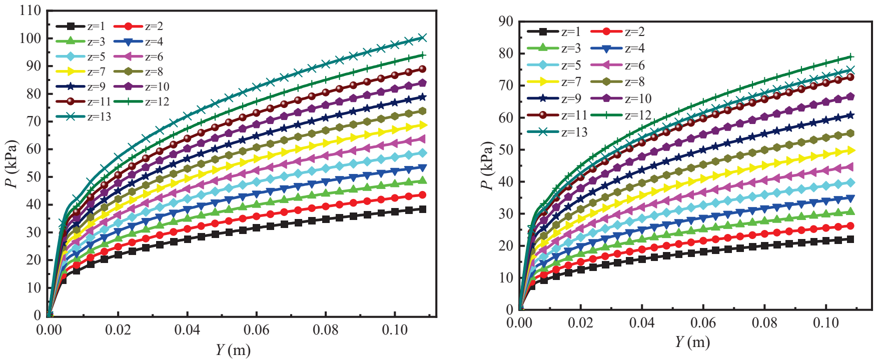

(**a**) Before reduction (**b**) After reduction

Figure 9. *P*–*y* curves of soil layers at different depths.

When simulating the process of foundation scouring, it is assumed that the actual scouring process is a riverbed soil erosion process and the scour depth of each pile is the same. When scouring occurs, the surface sediment is washed away by the water flow, and the pile body is exposed. The pile foundation at the washed-away soil layer loses transverse constraints. Therefore, when simulating the scouring process, the soil spring within the scouring depth range is removed, so that the transverse horizontal stiffness of the pile foundation within the corresponding range becomes zero. After scouring occurs, the depth of the lower soil layer changes, and the corresponding horizontal stiffness changes. Recalculations should be made to more finely simulate the entire foundation scouring process (as shown in Figure 10).

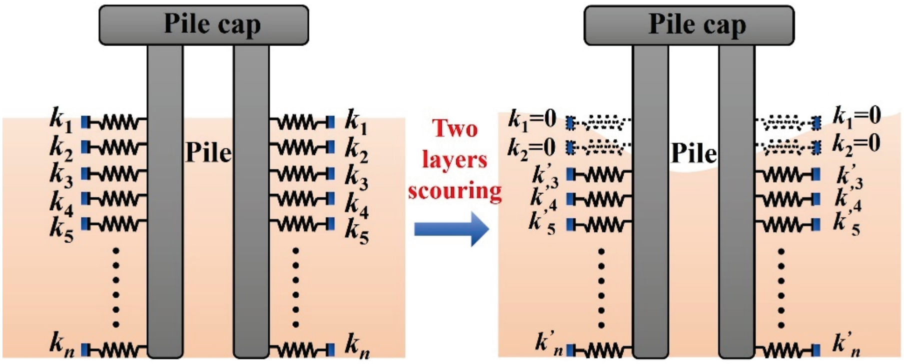

Figure 10. Simulation diagram of scouring process.

2.2.3. Structural Strength Deterioration Due to Corrosion

In marine environments, the aging and continuous degradation of reinforced concrete bridges are attributed to several factors, including the ingress of chloride ions, carbonation, temperature, and pollution [41]. This study specifically focuses on high-rise pile cap corrosion induced by chloride ions, while the microscopic electrochemical mechanism and molecular dynamics are not involved.

During the service life of a bridge, chloride ions from seawater continuously penetrate through the concrete protective layer and eventually reach the steel reinforcement. Upon reaching the steel surface, the chloride ions locally disrupt the passivating film surrounding the reinforcement. The sufficient accumulation of chloride ions on the steel surface leads to localized corrosion, with the expansion of corrosion products causing concrete cracking. Generally, the strength of reinforced concrete structures does not significantly deteriorate before the onset of steel corrosion. However, once corrosion initiates, it reduces the strength of both steel and concrete, thereby compromising the load-bearing capacity of the sea-crossing bridge.

(1) Corrosion initiation time

The bridge pile corrosion process in marine environments does not begin with construction. The duration between the finalization of the bridge piles and the initiation of corrosion follows a specific timeframe. A precise model can be employed to approximate the onset time of corrosion [42,43]:

$$T_i = \frac{c^2}{4D_c}\left[erf^{-1}\left(\frac{C_0 - C_{cr}}{C_0}\right)\right]^{-2}. \tag{20}$$

$$erf(x) = \frac{2}{\sqrt{\pi}}\int_0^x e^{-y^2}dy. \tag{21}$$

where T_i is the start time of the corrosion (year); c represents the thickness of the protective layer (cm); D_c denotes the chloride ion diffusion coefficient (cm^2/year); C_0 stands for the equilibrium chloride ion concentration on the concrete surface (kg/m^3 concrete); C_{cr} represents the critical chloride ion concentration at the onset of corrosion in kilograms per cubic meter of concrete; and *erf* is a Gaussian error function.

The parameters D_c, C_0, and C_{cr} are related to the environment in which the concrete bridge piles are located. The values of these parameters have been studied by many experts and scholars [44–46] and are shown in Table 3.

Table 3. Parameters affecting the corrosion initiation time.

D_c (cm^2/s)	C_0 (kg/m^3) Atmospheric Area	 Wave Splash Area	C_{cr} (kg/m^3)
2×10^{-8}	2.95	7.35	0.9

(2) Degradation of steel bar properties

The corrosion products of steel bars will reduce their own diameter and yield strength. Before T_i, the steel bars remain in their initial state. After T_i, the corrosion of the steel bars is closely related to the corrosion current density [20,47]. After the T_i moment, that is, after corrosion occurs, the degree of corrosion of the steel bars in the same area segment is uniform. The average cross-sectional area of the corroded steel bars A_s and the yield strength of the corroded steel bars f_s can be calculated using Equations (22)–(25) [48,49]:

$$A_s(t) = [1 - 0.01 \cdot Q_{corr}(t)]A_{s0}. \tag{22}$$

where A_{s0} is the initial cross-sectional area of uncorroded steel bars, and $Q_{corr}(t)$ represents the percentage of steel mass loss over time and can be determined using the following equation:

$$Q_{corr}(t) = \left[1 - \left(\frac{D(t)}{D_0}\right)^2\right] \times 100. \tag{23}$$

$$D(t) = D_0 - 0.023 i_{corr} \cdot t. \tag{24}$$

where D_0 and $D(t)$ are the initial diameter and remaining diameter of the steel reinforcement. i_{corr} denotes the corrosion current density of steel bars. According to Akiyama and Frangopol's suggested values for i_{corr} [20], the atmospheric area and wave splash area can be taken as 3 μA/cm^2 and 6 μA/cm^2, respectively.

The remaining yield strength of the steel bars can be calculated by

$$f_s(t) = \left(1 - \frac{Q_{corr}(t)}{200}\right) \times f_{s0}. \tag{25}$$

(3) Degradation of concrete strength

In this study, it is believed that the strength of the concrete remains unchanged when the crack width of the concrete protective layer reaches 1 mm. The diminished compressive strength of cracked concrete can be assessed as follows [50–52]:

$$f'_c(t) = \frac{f'_{c0}}{1 + K\varepsilon_1(t)/\varepsilon_{c0}}. \tag{26}$$

In the formula, K is the coefficient related to the diameter and roughness of the steel bar (K equals 0.1); f'_{c0} denotes the strength of the concrete at the beginning and $f'_c(t)$ denotes that after corroded time t; and ε_{c0} is the strain at f'_{c0}. $\varepsilon_1(t)$. The average tensile strain of the cracked concrete is calculated using the following equation:

$$\varepsilon_1(t) = \frac{b_f(t) - b_i}{b_i} = \frac{\Delta b(t)}{b_i}. \tag{27}$$

Here, b_i represents the width of the undamaged concrete section, while $b_f(t)$ represents the width post cracking. $\Delta b(t)$ can be derived using the following equation:

$$\Delta b(t) = n_{bars} \cdot w_{cr}(t). \tag{28}$$

where n_{bars} represents the quantity of steel bars within the compression layer. The average crack width of steel bar $w_{cr}(t)$ is derived by [53]

$$w_{cr}(t) = k_w[\delta_s(t) - \delta_{s0}]A_{s0}. \tag{29}$$

Here, k_w equals 0.0575, δ_{s0} denotes the quantity of steel damage necessary for crack initiation, and $\delta_s(t)$ serves as a dimensionless damage function, indicating the reduction in the cross-section within the interval of [0~1].

$$\delta_s(t) = \frac{A_{s0} - A_s(t)}{A_{s0}} = 0.01 \cdot Q_{corr}(t). \tag{30}$$

$$\delta_{s0} = 1 - \left[1 - \frac{R}{D_0}\left(7.53 + 9.32\frac{c}{D_0}\right) \times 10^{-3}\right]^2 \tag{31}$$

Here, R represents the pitting factor, which ranges between 4 and 8 for natural corrosion and between 5 and 13 for accelerated corrosion tests [54].

(4) Case study of the high-rise pile cap

The steel reinforcement and the concrete exhibit different characteristics of performance degradation in different corrosion zones. Equation (20) is utilized to calculate the corrosion initiation time. In this study, the high-rise pile cap's steel reinforcement is anticipated to begin corroding after approximately 8 years in the wave splash zone and around 19 years in the atmospheric zone. Subsequently, Equation (23) is applied to calculate the corrosion rate of the steel reinforcement. Based on the above estimated variables, Equations (22)–(31) were employed to determine the degradation curves of the material properties (such as steel reinforcement strength and diameter, concrete strength) over time. Under the specified conditions, the concrete protective layer is projected to develop a crack width of 1 mm at around the 11th year in the wave splash zone and approximately the 28th year in the atmospheric zone. At this moment, it is assumed that the strength of the concrete remains constant throughout the remaining service life.

Figure 11 illustrates the structural degradation caused by corrosion over time in two corrosion areas. From Figure 11a–c, it is evident that the steel reinforcement in the wave splash zone undergoes performance degradation earlier than that in the atmospheric zone, and the degree of degradation is more pronounced compared to the atmospheric zone. Since the steel reinforcement at the pile cap utilizes the same specification, the analysis exclusively focuses on the degradation pattern of the piles' stirrups located in the wave splash zone. Figure 11f reflects the degradation pattern of concrete. Similar to the steel reinforcement, the time at which the concrete strength starts to decrease is earlier in the wave splash zone compared to the atmospheric zone. However, the decline in concrete strength toward the end period is more pronounced in the atmospheric zone compared to the splash zone. This difference may be attributed to the complexity of reinforcement at the cap. Further fluid–structure coupling analysis was conducted using structural performance data extracted at service times of 8, 50, and 100 years. The performance indicators of steel reinforcement and concrete for different regions and years are presented in Table 4.

Fan et al. [35] employed a comparable model to investigate the corrosion-induced degradation of reinforced concrete bridges. Their results indicated that the initiation of steel corrosion in the splash-tidal zone and atmospheric zone occurred at 8 and 18 years, respectively, which aligns closely with the predictions of this study (8 and 19 years). Furthermore, the time-dependent corrosion behavior of both steel and concrete, as well as the resulting structural deterioration trends, exhibit remarkable consistency between the two studies. These comparative analyses substantiate the validity and reliability of the corrosion degradation model adopted in this work, demonstrating its capability to accurately simulate the long-term corrosion behavior of reinforced concrete structures.

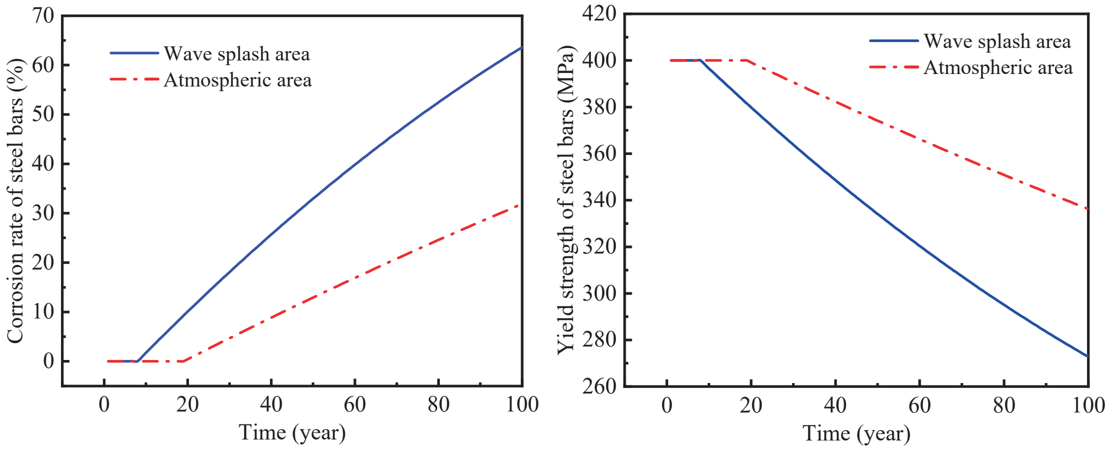

(**a**) Corrosion rate of steel bars (**b**) Yield strength of steel bars

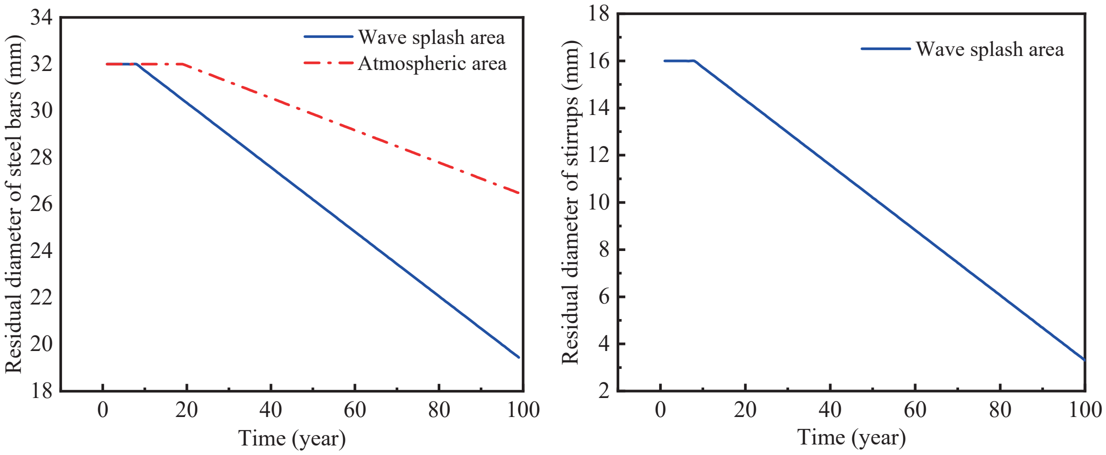

(**c**) Residual diameter of steel bars (**d**) Residual diameter of stirrups

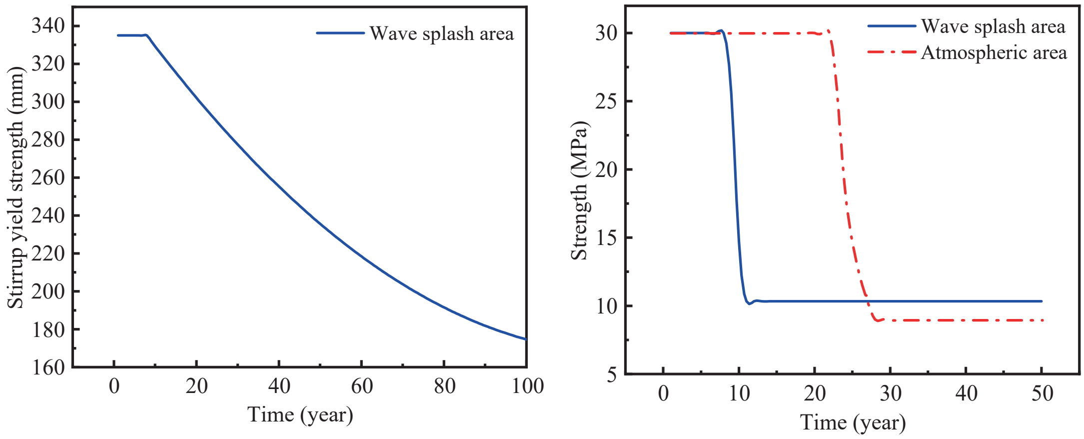

(**e**) Stirrup yield strength (**f**) Strength of concrete

Figure 11. Performance degradation curves of steel bars and concrete.

Table 4. Time-varying parameters considering non-uniform corrosion.

Area	Parameters	Service Time 8 Years	50 Years	100 Years
Wave splash area	Corrosion rate of steel bars	0	32.94%	63.61%
	Residual diameter of steel bars	32 mm	26.2 mm	19.3 mm
	Yield strength of steel bars	400 MPa	334.11 MPa	272.78 MPa
	Residual diameter of stirrups	16 mm	10.2 mm	3.3 mm
	Stirrup yield strength	335 MPa	235.63 MPa	174.64 MPa
	Concrete strength	30 MPa	10.34 MPa	10.34 MPa
Atmospheric area	Corrosion rate of steel bars	0	12.92%	31.88%
	Residual diameter of steel bars	32 mm	29.86 mm	26.41 mm
	Yield strength of steel bars	400 MPa	374.16 MPa	336.24 MPa
	Concrete strength	30 MPa	9.0 MPa	9.0 MPa

These findings can advance the design and maintenance of coastal infrastructure in corrosive environments by enabling the development of predictive corrosion management approaches, zone-specific protection strategies, and advanced corrosion-resistant materials. Overall, this research offers practical guidance for improving the resilience and sustainability of coastal infrastructure in corrosive environments.

3. Numerical Simulation Results

3.1. Analysis Strategy and Process

In the finite element modeling approach, numerical experiments were conducted as follows. In this study, wave parameters with a water depth of 20 m, a wave height of 1.2 m, and a period of 4 s were selected to extract the characteristics of wave forces. High-rise pile cap structures were subjected to three corrosion durations: 8 years, 50 years, and 100 years. Additionally, five local scour depths were considered: 0 m (pristine state), 3 m, 6 m, 9 m, and 12 m (maximum scour depth). In this study, the selection of the scour depth range referred to the empirical formula and the measured scour depth of the bridge site. Johnson et al. [55] introduced a model correction coefficient λ_s to consider the influence of uncertainty on the scour depth of the foundation. The adjusted HEC-18 formula can be expressed as follows:

$$y_s = 2.0\lambda_s y_0 K_1 K_2 K_3 K_4 \left(\frac{a}{y_0}\right)^{0.65} \left(\frac{V_0}{(gy_0)^{0.5}}\right)^{0.43}. \tag{32}$$

where K_1, K_2, K_3, and K_4 are the correction coefficients of pile foundation shape, angle of attack, flow field condition, and sediment particle size, respectively. $K_1 = K_2 = K_4 = 1.0$, $K_3 = 1.1$. The value of λ_s is 0.8. y_0 denotes the water depth upstream, g denotes the acceleration of gravity, and a denotes the width of the pier perpendicular to the flow direction.

In this work, the HEC-18 method was used to estimate the scour depth of the Donghai Bridge, in service for 100 years, to be 23 m. In 2020, it was reported that the average depth of the scour holes under the pier of the 17-year-old Donghai Bridge varied between 4 and 7 m, and the deepest was close to 20 m. Therefore, the scour depth was set to 0~12 m with an interval of 3 m. Here, 0 m represents intact state, 3 m and 6 m represent moderate scour, and 9 m and 12 m represent severe scour. Using nonlinear time history dynamic analysis, the study examined the temporal evolution of energy, displacement, stress, and acceleration of the high pile cap across the combinations of these parameters (three corrosion times and five scour depths). Note that the uncertainty of the corrosion and scour rate have not been considered here, and deserve attention in further study.

To facilitate the application of wave loads and improve computational efficiency, the resultant wave force from seconds 24 to 32 obtained through CFD analysis was applied to the high-rise pile cap structure. The LS-DYNA model applies the wave force to the relevant nodes through the *LOAD keyword. It is evident that the wave force is derived from two wave cycles, with a maximum positive resultant wave force of 119,712.5 N and a maximum negative resultant wave force of −77,618.4 N.

An implicit dynamic analysis procedure was adopted to investigate the dynamic response within eight seconds. The analysis process is outlined as follows and shown in Figure 12.

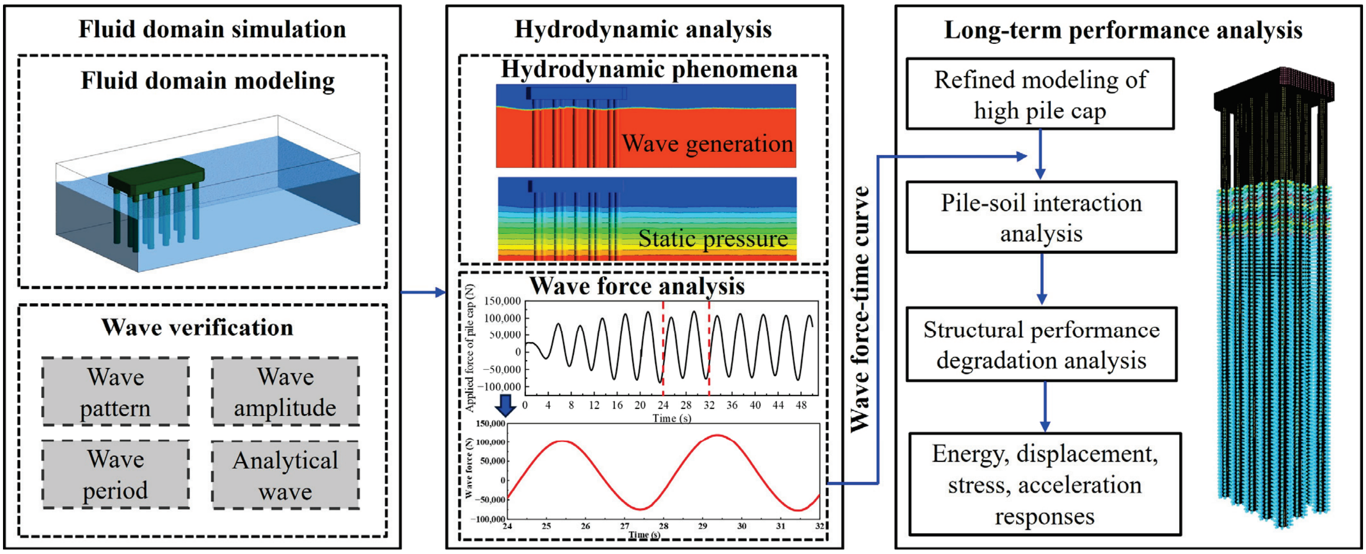

Figure 12. Flow diagram of dynamic response analysis of pile cap structure.

(1) Conduct a hydrodynamic analysis of the high-rise pile cap using ANSYS-FLUENT software (2022 R1) and extract the resultant wave force from two cycles within the 24–32 s duration;
(2) Apply the extracted resultant wave force as nodal forces to the corresponding nodes of the high-ride pile cap model established in the LS-DYNA software;
(3) Consider the performance degradation indicators of concrete, steel reinforcement, and stirrups of the high-rise pile cap at service times of 8, 50, and 100 years;
(4) Calculate the dynamic stiffness of nonlinear soil springs along the pile axis and simulate scour effects by varying the number of soil springs, considering scour depths of 0 m (pristine), 3 m, 6 m, 9 m, and 12 m;
(5) Extract dynamic responses such as stresses and the displacements of the high-rise pile cap to analyze its failure behavior.

3.2. Hydrodynamic Analysis

3.2.1. Hydrodynamic Phenomena

Under the wave parameter setting of wavelength $L = 25$ m and wave period $T = 4$ s, the wave propagation speed is 6.25 m/s. The whole length of the numerical flume is 100 m. Therefore, in an ideal case, starting from the initial time, after 16 s, the fluid at the wave-making boundary can propagate to the wave-absorbing area at the end of the flume, and then the whole flume forms a periodic and stable wave field. However, due to the obstruction of the pile groups and the viscosity of water, the wave propagation lags behind. Finally, the wave stabilization time appears after 24 s. Figure 13 shows the wave generation process in the numerical flume.

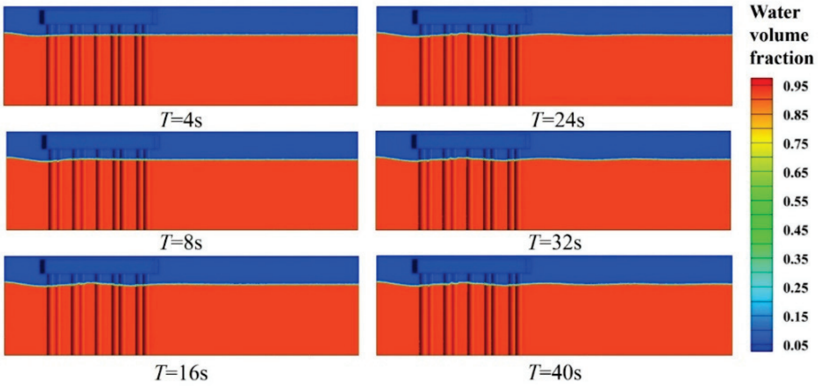

Figure 13. Wave generation process.

Figure 14 shows a static pressure cloud diagram of the numerical flume under the static water state and the wave motion state. The pressure distribution in the still water state is stratified, and the maximum pressure value at the bottom of the pool is roughly consistent with the theoretical pressure value obtained by the still water depth of 20 m. In the state of wave motion, on the same horizontal line, the water depth at the peak position is greater than the water depth at the trough position, so the net water pressure at the peak position is greater than the net water pressure at the trough position. With the increase in the water depth, the increasing pressure trend is consistent with the theoretical value. The pressure variation occurs primarily within the range of the wave height.

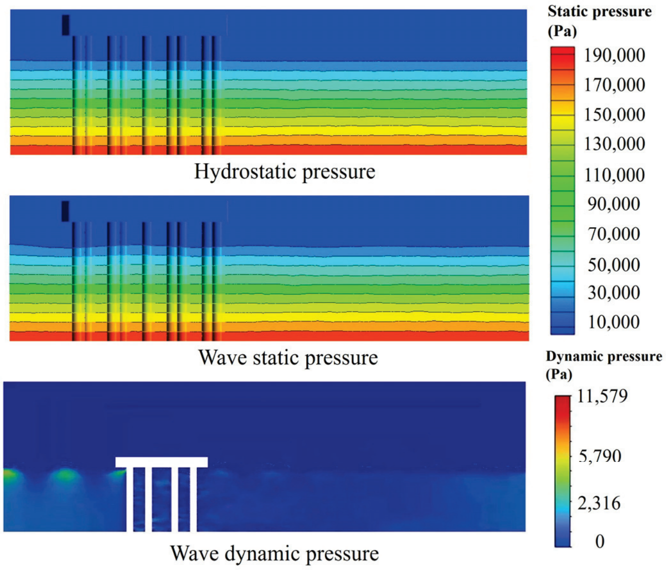

Figure 14. Pressure cloud diagram.

Turbulent kinetic energy reflects the intensity of fluid motion within turbulent regions and also signifies the transfer of energy within the fluid. During the development of turbulence, energy from the high-pressure region is transferred through turbulence to the low-pressure region, thereby redistributing the energy. Figure 15 illustrates the distribution of turbulent kinetic energy on the coupled fluid–structure interface at 32 s. Turbulent kinetic energy tends to concentrate predominantly within the wave splash zone, while other regions exhibit minimal turbulence. Additionally, the presence of group piles notably impacts the distribution of turbulent kinetic energy, resulting in lower turbulence being observed in the back compared to the front row. From the bottom view, it is evident that turbulence exists at the base of the platform, primarily distributed on the windward side.

Consequently, under wave action, the wave splash zone and the base of the high-rise pile cap are more susceptible to damage.

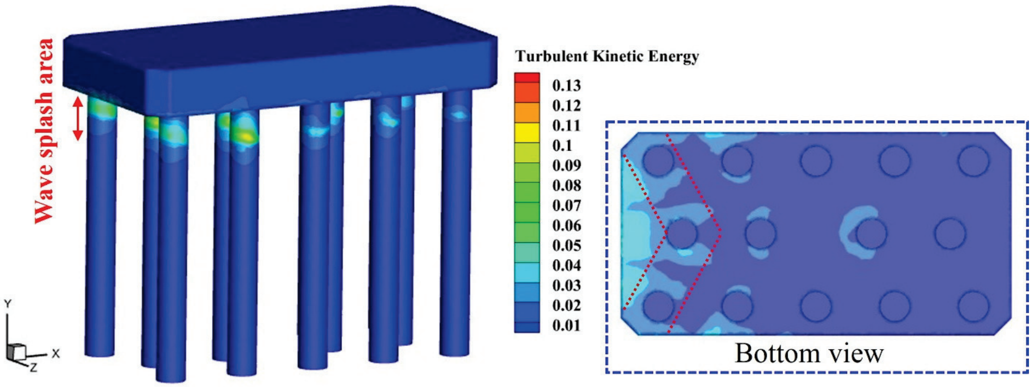

Figure 15. The distribution of turbulent kinetic energy on the fluid–structure interface at 32 s.

3.2.2. Wave Force Analysis

Analyzing the horizontal and vertical wave forces acting on a high-rise pile cap provides valuable insights into the nature of these forces. By integrating the fluid compressive stress and shear stress along the contact surface between the cap and the water, the resultant wave force exerted on the cap can be determined.

Figure 16 displays the temporal evolution of wave forces acting on the cap during wave action. According to Figure 16a, the horizontal wave force exhibits clear periodicity, and positive and negative wave forces are asymmetric. After 12 s, the fluctuation amplitude of the horizontal wave force maintains a stable value. The maximum positive horizontal wave force reaches 144,391.8 N, while the maximum negative horizontal wave force is registered at −149,788 N. As can be seen from Figure 16b, the vertical wave force displays a somewhat periodic pattern, although its periodicity is less pronounced compared to the horizontal wave force. At each wave summit, the wave force experiences varying degrees of sudden fluctuations, primarily because of the instantaneous reversal of the cap's action on the vertical wave force. When the wave summit impacts the high-rise pile cap, this abrupt reversal leads to an instantaneous surge in the vertical wave force. This phenomenon is particularly evident at 21 s, when the vertical wave force reaches its maximum value of 27,037.14 N.

As depicted in Figure 16c, the resultant wave force exerted on the high-rise pile cap demonstrates clear periodicity, suggesting that the cap's response to wave loads is predominantly influenced by the horizontal wave force aligned with the wave propagation direction. In comparison, the vertical wave force contributes relatively insignificantly to the resultant force. The maximum positive and negative resultant forces are 119,712.5 N and −88,255 N, respectively, which are lower than the peak value of the horizontal wave forces. This can be attributed to the phase difference between the variations in the horizontal and vertical forces. In the subsequent fluid–structure coupling analysis, the resultant wave force from 24 s to 32 s was selected for application on the high-rise pile cap structure.

The wave force of different wave conditions on high pile caps was not explored further in this study. Xu et al. [56] explored the influence of wave height on high pile caps through experiments, showing that when the wave height exceeds 0.18 m, the horizontal force increases with the increase in the wave height, and the vertical force increases first and then decreases, except for the case of complete submergence. The resultant wave force obtained from this simulation will be used as an external excitation load applied to the finite element model of the high pile cap.

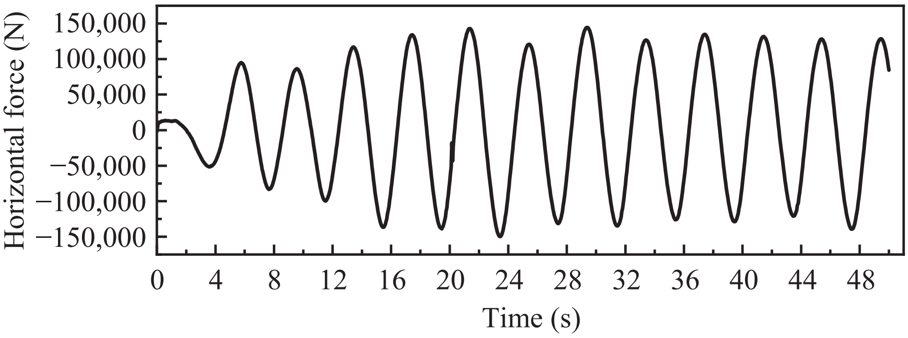

(**a**) Horizontal wave force

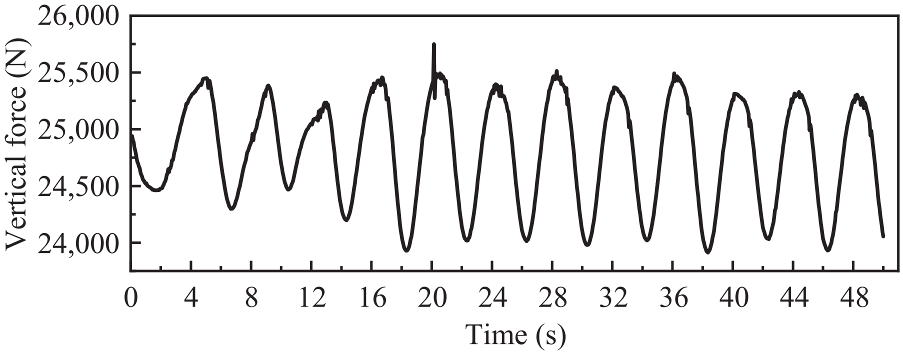

(**b**) Vertical wave force

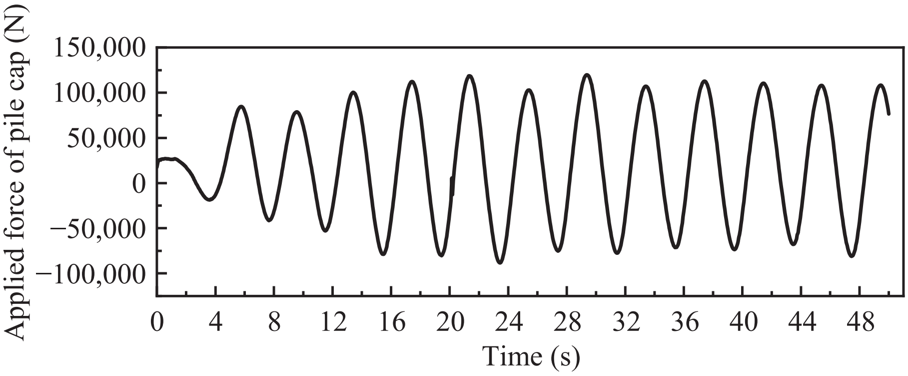

(**c**) Resultant wave force

Figure 16. Wave force–time history curve.

3.3. Long-Term Performance Analysis

3.3.1. Energy Analysis

Considering the high-rise pile cap and the *p*–*y* soil spring as a structural system, this study focuses on investigating the energy changes of the whole system. The energy change in the spring is also included in the change in the internal energy of the structural system. In addition, the damping effect of the system is not considered due to its negligible influence compared to other mechanical properties such as stiffness or mass. The total energy E_{total} is the sum of all of the energies in the model, the kinetic energy E_{kinetic} is the energy of all of the moving parts of the model, and the internal energy E_{internal} is the energy caused by the deformation of the material. The equations are as follows:

$$E_{\text{total}} = E_{\text{kinetic}} + E_{\text{internal}}. \tag{33}$$

$$E_{\text{kinetic}} = \frac{1}{2}\sum_i m_i v_i^2. \tag{34}$$

$$E_{\text{internal}} = \frac{1}{2}\sum_{i}\sigma_i\varepsilon_i \tag{35}$$

where m_i is the mass of the *i*th mass point, v_i is the velocity of the *i*th mass point, σ_i is the stress of the *i*th cell, and ε_i is the strain of the *i*th cell.

The changes in kinetic energy, internal energy, and total energy of the high-rise pile cap under wave action were analyzed and recorded. The structure with a corrosion time of 8 years and a scour depth of 12 m was selected to study its energy conversion law, as shown in Figure 17a. It can be found that the period of energy change is consistent with the period of wave load, and the period is 4 s, which means that the energy change in the high pile cap structure is mainly caused by external load. In two cycles (8 s), the change curve of each energy is the same. In the first second of each period, the value of kinetic energy, internal energy, and total energy is 0, indicating that the wave load has not caused the structure to deform during this period. In the process of energy conversion, it can be found that the sum of the internal energy and kinetic energy of the structure at each time point is equal to the total energy, which conforms to the law of energy conservation of the structure. This indicates that the energy change caused by the elastic–plastic deformation of the pile cap is equivalent to the change in internal energy. The internal energy of the structure reaches zero at 2.5 s and 6.4 s, while the kinetic energy peaks at 125 kJ during those instances. At this time, the total energy of the structure is equal to the kinetic energy, which indicates that the structure has entered a very dangerous time. Hence, appropriate measures should be taken to reduce the occurrence of all internal energy converted into kinetic energy.

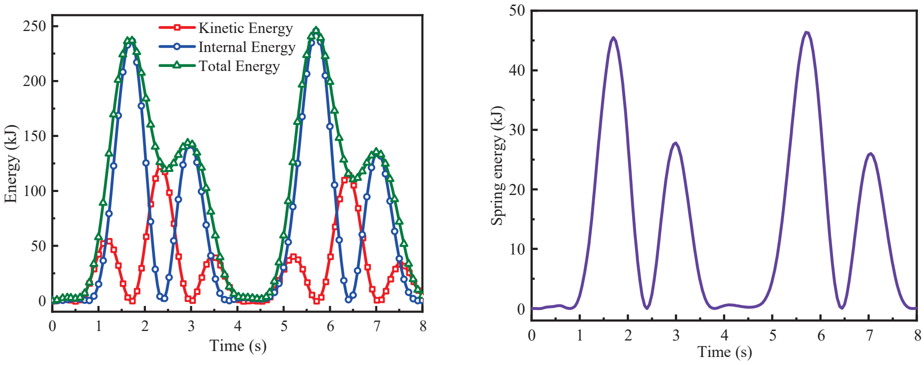

(**a**) Energy exchange (**b**) *P*–*y* spring energy

Figure 17. Energy analysis of high-rise pile cap.

Figure 17b shows the energy change in the *p*–*y* soil spring. The variation law of spring energy is similar to that of structural internal energy. The spring energy value is much smaller than that of internal energy, which indicates that the soil spring gives good restraint and support to the high pile cap under the action of waves. The nonlinear change in spring energy also implies the nonlinearity of structural dynamic response, which lays the foundation for the following dynamic analysis. By comparing the spring energy and internal energy changes in Figure 16, it is evident that the internal energy change induced by deformation contributes more significantly to the overall energy change in the structure.

3.3.2. Displacement Response Analysis

The transverse displacement of the cap was calculated under the action of waves. The high-rise pile cap model corroded for 8 years was selected for the comparative study. Figure 18a shows the time history curve depicting the overall transverse displacement of the cap as the wave load time varies across five different scouring conditions. It can be seen that the cap is roughly periodic under the action of wave load, and the transverse displacement increases first and then decreases in a period, which corresponds to the periodicity of the selected wave load. As the scour depth increases, the transverse displacement of the cap also rises accordingly. When the scour depth is 12 m, the transverse displacement value reaches the maximum, which is 0.0025 m. It can also be found that with the increase in the scour depth, the time of maximum transverse displacement is obviously delayed, which may be caused by the redistribution of the stiffness of the remaining nonlinear soil spring after scouring.

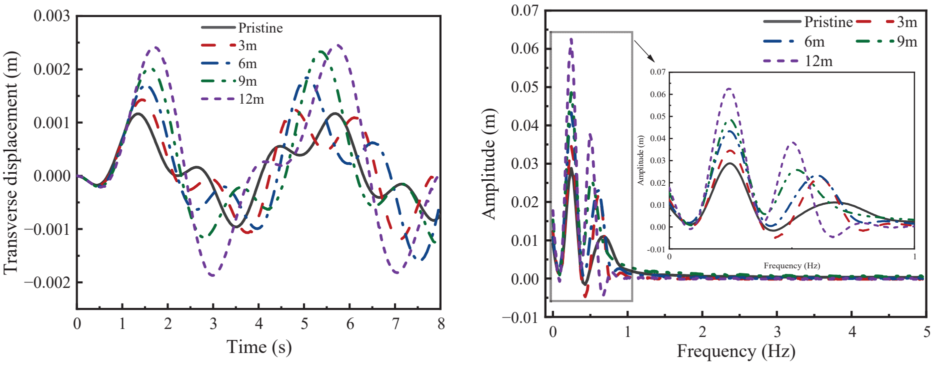

(**a**) Displacement–time history curve (**b**) Fourier spectrum

Figure 18. The displacement–time history curve and the Fourier analysis of the cap used for 8 years.

Figure 18b shows the Fourier analysis of the transverse displacement of the cap. The first two order frequencies of the cap under five kinds of scouring conditions are less than 1 Hz. The amplitude of the transverse displacement under the first-order frequency is 0.029 m, 0.035 m, 0.043 m, 0.049 m, and 0.062 m with the increase in the scour depth. Obviously, under the same external load, the pile cap with greater scour depth is more likely to be damaged.

Figure 19 shows a transverse displacement cloud diagram of the cap that has been in service for 8 years in two cycles (0–8 s) under the condition of a scour depth of 6 m. Through these cloud images, it can be seen that the maximum transverse displacement occurs near 1.9 s and 6.1 s. In the process of bearing wave load, the displacement of the pile cap is continuous and gradual, which is due to the constraint and bonding effect of the steel bar inside the pile cap.

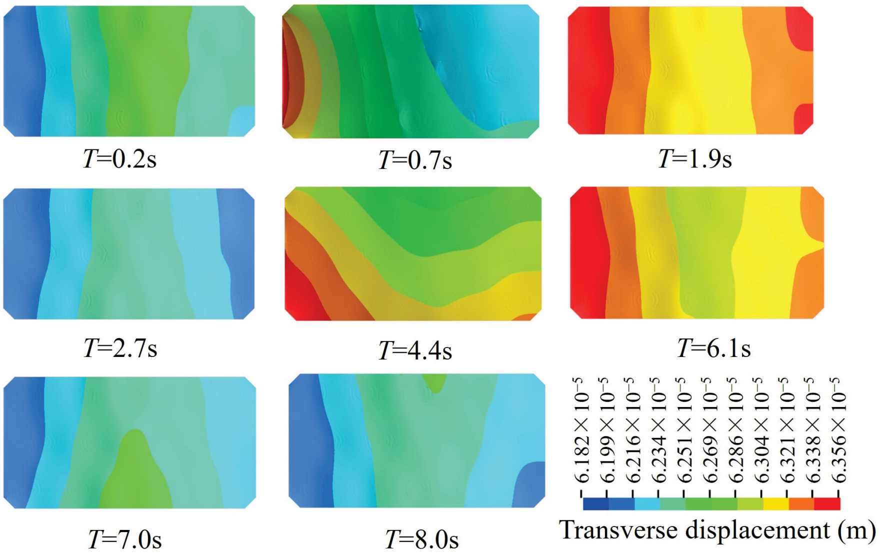

Figure 19. Transverse displacement cloud diagram of the cap under 6 m scouring.

Similarly, the study focused on the high-rise pile cap that had been in service for 8 years, with a scour depth of 6 m. The displacement–time curves of the top of 14 piles were extracted for analysis, as depicted in Figure 20. Figure 20a–d illustrate the transverse displacement, longitudinal displacement, vertical displacement, and combined displacement of the top of the 14 piles, respectively.

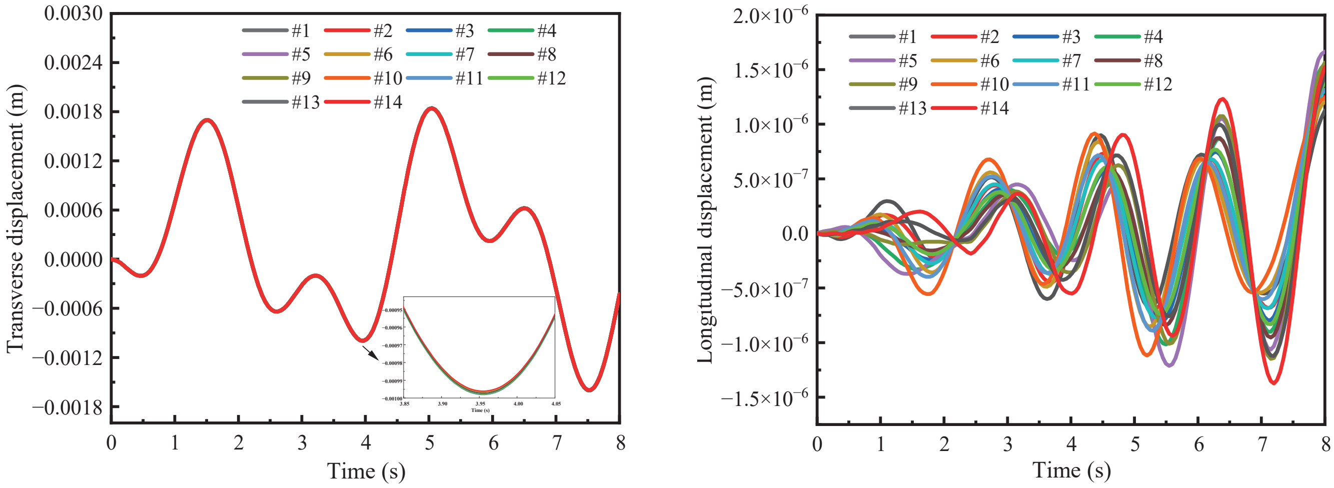

(**a**) Transverse displacement (**b**) Longitudinal displacement

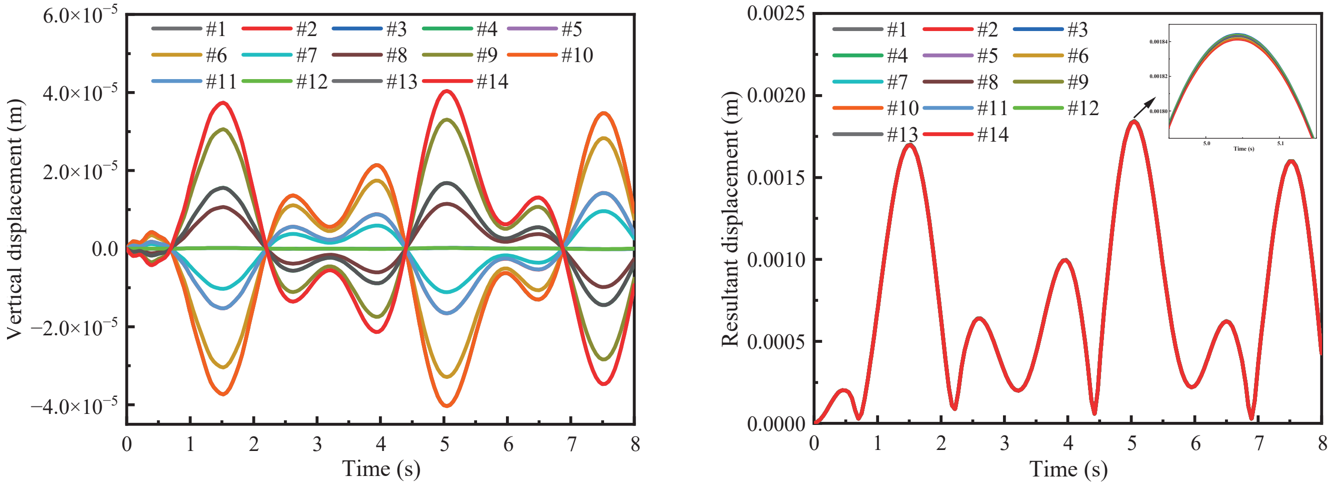

(**c**) Vertical displacement (**d**) Resultant displacement

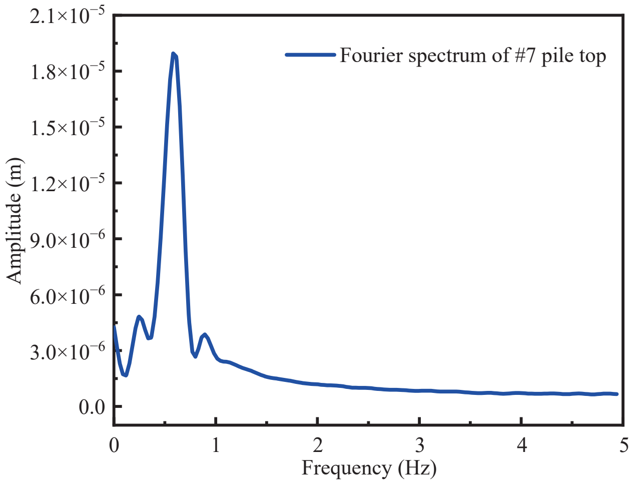

(**e**) Fourier spectrum of the longitudinal displacement

Figure 20. Displacement–time history curve of pile top and Fourier analysis.

It can be seen from Figure 20a–c that the displacements in all three directions exhibit roughly periodic behavior, following the cyclic variation of wave loading. Among the three directions, there are no significant differences in the transverse displacement of the pile top, indicating good coordination in transverse deformation for the high-rise pile cap with a group pile system. The magnitude of transverse displacement is much larger than that of longitudinal and vertical displacement, suggesting that, of the three directions, transverse displacement has the greatest impact on the deformation of the high-rise pile cap structure. A closer inspection of the local magnification of Figure 20a reveals that the transverse displacement of piles located in the middle (#3, #12) is slightly larger compared to the others, indicating the need for the enhanced monitoring and maintenance of central piles during service.

Figure 20b illustrates the variation pattern of longitudinal displacement at the pile tops. It is evident that, during the first cycle, there is no significant change in the longitudinal displacement of the pile tops, but in the second cycle, the displacement values noticeably increase, with pile #14 showing the most prominent variation. Due to the interaction between longitudinal reinforcement and stirrups inside the piles, there is a lag phenomenon in the variation of longitudinal displacement at the pile top. The longitudinal displacement variation of the piles on the left side of the longitudinal bridge (#4, #5, #8, #9, #13, and #14) precedes that of the piles on the right side (#1, #2, #6, #7, #10, and #11).

Figure 20c presents the variation in the vertical displacement at the pile top. The top vertical displacement in the middle piles (#3 and #12) remains almost unchanged, indicating that wave loading has little effect on the vertical displacement of the piles in the middle. Additionally, it is noted that the variation pattern of the vertical displacement on the left side of the longitudinal bridge is completely opposite to that of the piles on the right side. The top vertical displacement at piles #4, #5, #8, #9, #13, and #14 increases first and then decreases within one cycle, while for piles #1, #2, #6, #7, #10, and #11, it decreases first and then increases. The variation in the vertical displacement of piles near the edge is much greater than for those in the middle and near the middle.

Figure 20d illustrates the resultant displacement–time curve of the piles. The variation pattern of resultant displacement for the 14 piles is roughly the same, once again confirming that transverse displacement has the most significant influence on the deformation of the high-rise pile cap structure. The resultant displacement values within two cycles are all greater than zero, indicating that, under unidirectional wave action, the high-rise pile cap tends to offset in the direction of wave propagation.

To further investigate the relationship between the increasing longitudinal displacements and potential resonance, we conducted a Fourier analysis on the longitudinal displacement at the top of pile #7, as shown in Figure 20e. The maximum longitudinal displacement at the first natural frequency (0.6 Hz) is 1.52×10^{-5} m. Notably, the longitudinal displacements induced by wave are significantly smaller than this value. Therefore, the gradual increase in longitudinal displacement is attributed to the cumulative effect of wave-induced displacements rather than resonance.

Figure 21a shows the maximum transverse displacement of pile top #1 under different scour depths for 8 years, 50 years, and 100 years. It can be seen from the histogram that as the corrosion time increases, the maximum top transverse displacement of the pile gradually increases. Upon reaching the bridge’s service time limit, the maximum top transverse displacement of the pile is greater under various scour conditions compared to other corrosion periods. It can be concluded that when the service time and scour depth increase, the substructure of the sea-crossing bridge should be repaired and protected in time.

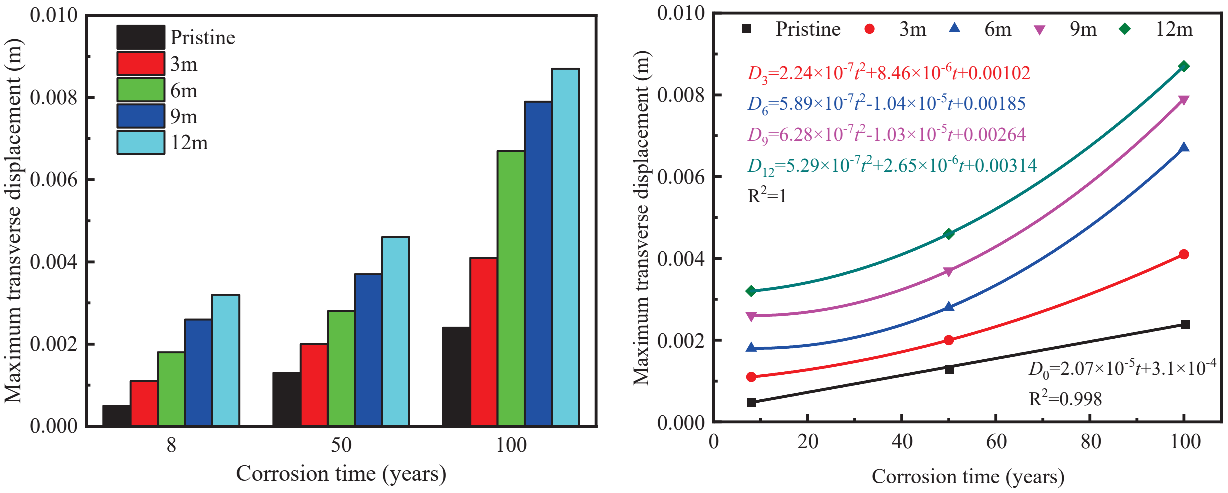

(**a**) Maximum transverse displacement (**b**) Fitting curve

Figure 21. Maximum transverse displacement and fitting curve for pile top #1.

Figure 21b illustrates the relationship between the maximum transverse displacement of pile #1 and the duration of corrosion at various scour depths through a fitted analysis. The fitted values of maximum transverse displacement and corrosion duration are displayed in the figure. A correlation coefficient greater than 0.95 indicates that the empirical formula fits accurately. When scour damage is absent, there is a nearly linear correlation between displacement and corrosion duration. As the scour depth increases, the relationship between transverse displacement and corrosion duration follows a nonlinear quadratic polynomial. Moreover, the displacement values increase exponentially with longer corrosion durations. Consequently, as the service life of a sea-crossing bridge extends, timely scour protection and material maintenance are crucial.

3.3.3. Stress Response Analysis

Nine points of concern were selected in the middle of the bottom of the cap to explore the variation law of the stress of the cap. As shown in Figure 22, the nine points of concern are respectively displaced at the middle edge of the cap bottom and the two sides of the pile cap connection. The relationship between the transverse stress and time of each concern is shown in Figure 23a. It can be seen that the stress at the edge shows a good period consistent with wave load. Although the cap edge will be in direct contact with the wave, the stress value is smaller than other concerns at the pile cap connection. The stress change trend on the left side of the pile (concern points C, E, G, and I) is opposite to that on the right side of the pile (concern points B, D, F, and H). Moreover, as the distance from the edge of the cap increases, the maximum amplitude of the transverse stress gradually decreases. The curve of the transverse stress of the pile cap at pile #1 with different scour depths was extracted, as shown in Figure 23b. With the increase in the scour depth, the variation amplitude of transverse stress shows an increasing trend. In the first cycle, when the scour depth reaches 12 m, the maximum transverse tensile stress is 25,020.52 Pa, and the maximum transverse compressive stress is 20,225.61 Pa. Moreover, with increasing scour depth, there is a delay in the occurrence of maximum transverse stress at this location, which indicates that a larger transverse displacement will occur.

Similarly, the high-rise pile cap with a corrosion time of 50 years was selected as the research object, and the vertical stress distribution along the pile body at 5.8 s of pile #1 under different scour conditions was extracted (Figure 24). The distribution of vertical stress is observed along the depth direction of the pile. There is vertical tensile stress at the pile top, and vertical compressive stress at the depth of 35 m. For reinforced concrete structures, where tensile stress exists, concrete is more likely to be destroyed, so it is necessary to increase the arrangement of steel bars at the pile cap connection. Below the buried depth of 60 m, the vertical stress value of the pile is very small and only compressive stress is exerted, so the pile in this area is not easily damaged. With the increase in the scour depth, the vertical tensile/compressive stress values at the pile top at the buried depth of 35 m gradually increase, so monitoring sediment scour is crucial to increase the service life of piles.

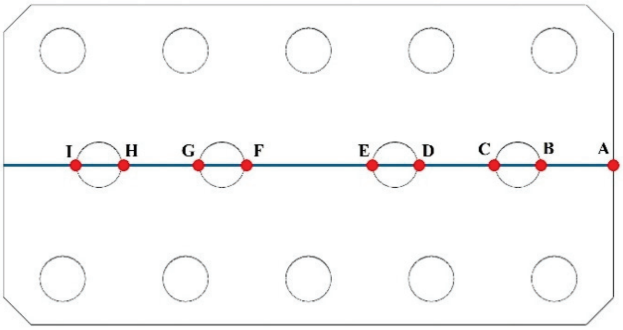

Figure 22. Location of the concern points.

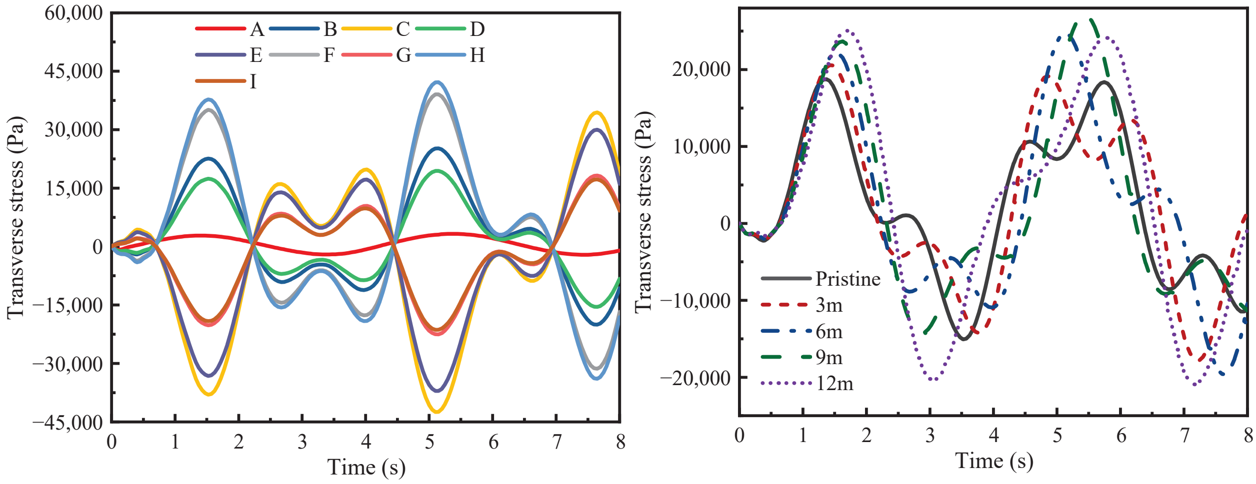

(**a**) Transverse stress of 9 concern points (**b**) Transverse stress of the pile cap at pile top #1

Figure 23. Transverse stress–time relationship.

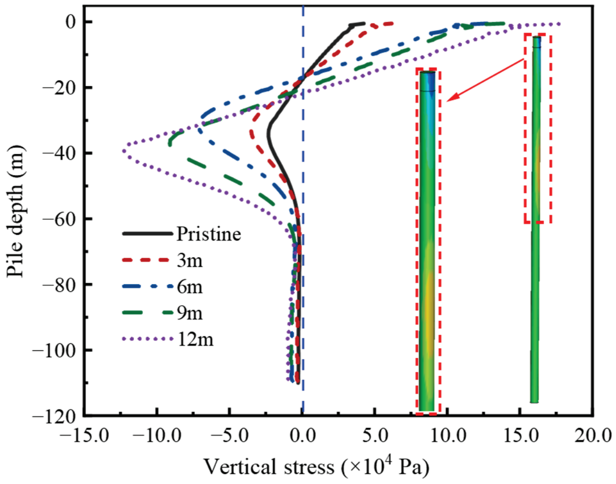

Figure 24. Vertical stress distribution diagram of pile #1 at 5.8 s.

3.3.4. Acceleration Response Analysis

The high-rise pile cap with a corrosion time of 50 years was taken again as the research subject, and the transverse acceleration time history curves of the cap at scour depths of 3 and 9 m were extracted, as shown in Figure 25. When a wave load acts on the structure, the acceleration of the cap changes abruptly, and the maximum positive acceleration and the maximum negative acceleration are roughly equal. When the scour depth is 9 m, the peak acceleration time is longer than that at 3 m. This is due to the decrease in nonlinear spring caused by the increased scour depth, which affects the overall stiffness of the structure.

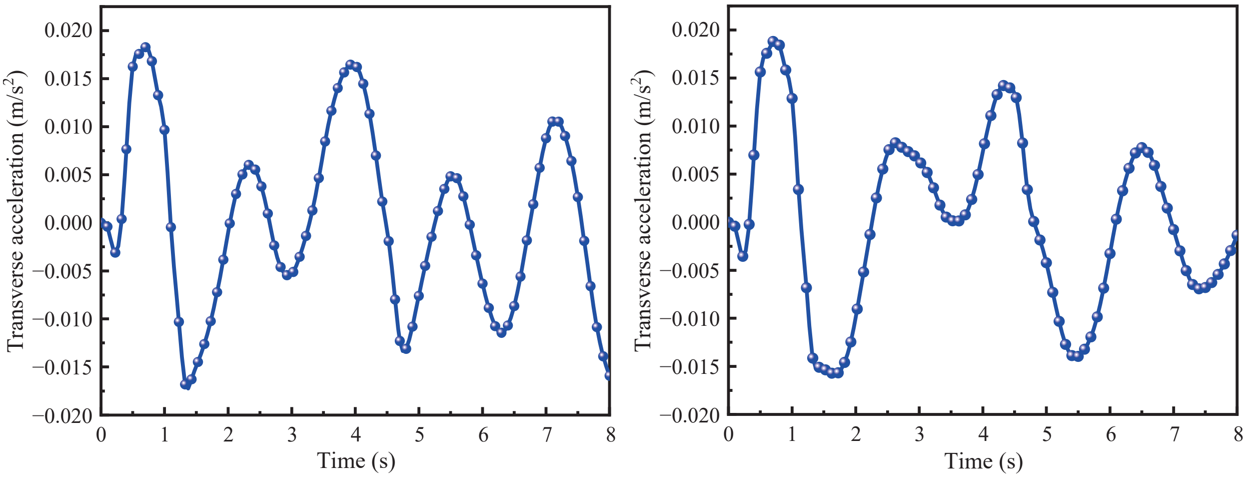

(**a**) 3 m (**b**) 9 m

Figure 25. Transverse acceleration–time relationship of the cap under different scour depths.

Figure 26 shows the frequency characteristics of the acceleration, which were extracted from the acceleration response using fast Fourier transform (FFT). Two main frequency bands can be identified from the acceleration spectrum analysis results of the cap under 3 m and 9 m scour depths. The two main frequency bands are the same: 0–50 Hz and 50–75 Hz, respectively. The 0–50 Hz frequency range typically includes low-frequency vibration modes that reflect the fundamental dynamic response of a structure. For bridges or large structures, these low-frequency modes are often linked to overall stability and long-term performance. In contrast, the 50–75 Hz range usually encompasses higher-frequency modes, which may relate to the local vibration characteristics of the structure. Within this region, the structure can display complex vibration behaviors, including higher-order modes, which can significantly impact its dynamic response.

In practice, engineers use established experience and theoretical knowledge to identify key frequency bands, with the 0–50 Hz range generally corresponding to the structure's fundamental frequency and the 50–75 Hz range possibly involving higher-order vibration modes. Within the frequency range of 0–50 Hz, the predominant frequency is 25 Hz, corresponding to 100 times the frequency of the incident wave. However, the acceleration assignment in each frequency band is different. The main vibration frequency of the structure is the second-order frequency of 62 Hz. The general rule is that the maximum acceleration assignment under 62 Hz is greater than that under 25 Hz, which also explains why the dynamic response of the structure is dominated by the second-order frequency of the pile cap. The first- and second-order frequencies correspond to different vibration modes. The first-order frequency represents the fundamental mode, while the second-order frequency represents the second major vibration mode of the structure. The second-order frequency (62 Hz) may be more significant than the first-order frequency, suggesting that the dynamic response of the structure is influenced more by higher-frequency modes, leading to a more complex vibration pattern with multiple vibration nodes.

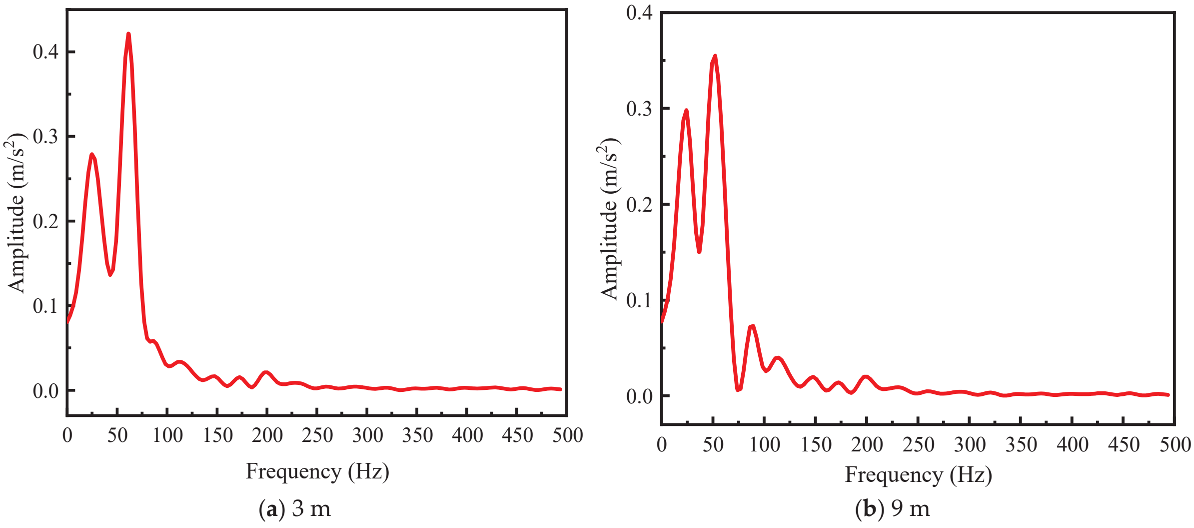

(**a**) 3 m (**b**) 9 m

Figure 26. Fourier spectrum of transverse acceleration.

In structures with a large slenderness ratio, such as high-rise pile caps, bending failure can easily be induced due to excessive displacement at the top. In the subsequent research, we focused on the breaking mode of the structure under the second-order frequency. Comparing the acceleration amplitude under the two scouring conditions in Figure 26, it can be concluded that the increase in the scouring depth reduces the acceleration amplitude.

Frequency response analysis is crucial in offshore engineering and coastal protection design because it reveals the dynamic behavior of structures at different frequencies. The fundamental frequencies of high-pile foundations (25 Hz) and higher-order frequencies (62 Hz) can be compared with the frequencies of external loads such as waves and wind. Engineers can use this comparison to avoid resonance phenomena, thereby optimizing the design and enhancing the stability and durability of the structure. Additionally, the identified frequency data help optimize material selection, structural shape, and support systems. The regular monitoring of frequency responses over time helps detect potential damage and facilitates maintenance, extending the structure's service life.

The maximum transverse acceleration of the cap under different corrosion durations (8, 50, and 100 years) and at different scour depths was calculated (Table 5), and its law is shown in Figure 27. The maximum transverse acceleration reflects the dynamic response ability of the structure in the lateral direction. High transverse acceleration may lead to increased structural vibrations or accelerated fatigue and damage. Therefore, when designing and evaluating engineering structures, attention should be paid to the magnitude and distribution of the maximum transverse acceleration. When the scour depth increases from 0 m to 12 m, the maximum transverse acceleration of the three corrosion conditions (8, 50, and 100 years) increases by 8.82%, 7.39%, and 10.56%, respectively. This indicates that as the bridge structure approaches its designated service life, it becomes increasingly susceptible to damage, so it is necessary to maintain and replace the bridge structure in time, especially the substructure.

Table 5. Maximum transverse acceleration of the cap under different corrosion times (m/s^2).

Corrosion Duration	Scour Depth				
	0 m	**3 m**	**6 m**	**9 m**	**12 m**
8 years	0.0170	0.0177	0.0181	0.0183	0.0185
50 years	0.0176	0.0183	0.0186	0.0188	0.0189
100 years	0.0180	0.0187	0.0190	0.0194	0.0199

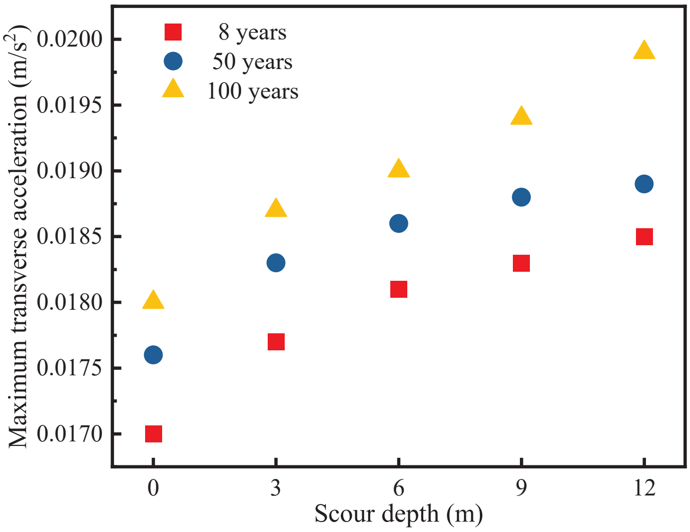

Figure 27. Scatter plot of the maximum transverse acceleration of the cap.

4. Conclusions

This study analyzed the dynamic response of high-rise pile cap structures under scouring and corrosion using a nonlinear dynamic analysis program. Parametric results were obtained for three corrosion durations (8, 50, and 100 years) and six scouring conditions through finite element analysis. Hydrodynamic characteristics, performance degradation, and long-term dynamic responses (energy, displacement, stress, and acceleration) were simulated. The main findings are as follows.

(1) Under wave action, the wave splash zone and the base of the high-rise pile cap are most vulnerable to damage. The wave force exhibits clear periodicity, mainly influenced by horizontal wave forces. The maximum positive and negative resultant wave forces are 119,712.5 N and −88,255 N, respectively.

(2) This study reveals that steel bars degrade faster in the wave splash zone, rusting in 8 years compared to 19 years in the atmospheric area. Concrete cracks develop earlier in the splash zone (after 11 years) than in the atmospheric area (28 years). Concrete strength declines earlier in the splash zone, but shows a more significant reduction in the atmospheric area.

(3) The energy fluctuation period of the high-rise pile cap matches the wave load period. Energy conversion analysis shows that the sum of internal and kinetic energy equals the total energy at all times, confirming the accuracy of the numerical model.

(4) As the scour depth increases, the transverse displacement of the cap rises, with peak displacement occurring later. Longitudinal displacement occurs earlier on the left of the bridge piles than on the right. Vertical displacement follows a cyclic pattern, with that of left-side piles first increasing and then decreasing, and that of right-side piles decreasing and then increasing. The maximum transverse displacement grows with an increase in corrosion time.

(5) There is a noticeable concentration of stress at the pile cap connection. As the scour depth increases, the transverse stress in the cap rises. Vertical tensile stress is seen at the pile top, shifting to vertical compressive stress at a depth of 35 m. Both the vertical tensile stress at the top and the compressive stress at 35 m increase with deeper scouring. At a burial depth of between 20 and 60 m, the pile stress first increases and then decreases.

(6) Wave loads cause abrupt changes in cap acceleration. At a 9 m scour depth, the acceleration peak occurs later than at 3 m. Two main frequency bands, 0–50 Hz and 50–75 Hz, are observed at scour depths of 3 and 9 m, respectively. The maximum acceleration amplitude occurs at the second-order frequency (62 Hz), indicating the importance of the structure's breaking mode at this frequency.

Although the long-term performance of high-pile caps under the influence of scouring and corrosion has been extensively investigated through comprehensive numerical studies, the modeling and analytical approaches employed in this research still require further validation via experimental testing. Future research should focus on the uncertainty of corrosion and scour rates. In addition, the impact of environmental factors such as temperature variations and pollutants on corrosion and scour should be considered to more accurately predict the long-term performance of high-rise pile cap structures.

Author Contributions: S.N.: Formal analysis; Investigation; Methodology; Modeling; Validation; Writing—Original Draft. Z.L.: Data Curation; Investigation; Methodology; Writing—Review and Editing. T.G.: Conceptualization; Supervision; Writing—Review and Editing. A.G.: Conceptualization; Methodology; Supervision; Writing—Review and Editing. S.X.: Conceptualization; Methodology; Supervision. All authors have read and agreed to the published version of the manuscript.

Funding: This work was supported by the National Key R&D Program of China (No. 2022YFB2602700), the National Science Foundation for Distinguished Young Scholars of China (No. 2125802), the International Science and Technology Cooperation Program of Jiangsu Province (No. BZ2024015), the Postgraduate Research & Practice Innovation Program of Jiangsu Province (No. KYCX24_0444), and the Research Fund for Advanced Ocean Institute of Southeast University, Nantong (No. MP202402).

Institutional Review Board Statement: Not applicable.

Informed Consent Statement: Not applicable.

Data Availability Statement: The data supporting this study's findings are available upon request from the corresponding authors.

Conflicts of Interest: The authors declare no conflicts of interest.

References

1. Chen, J.; Qu, Y.; Sun, Z. Protection mechanisms, countermeasures, assessments and prospects of local scour for cross-sea bridge foundation: A review. *Ocean Eng.* **2023**, *288*, 116145. [CrossRef]
2. Yang, R.; Li, Y.; Xu, C.; Yang, Y.; Fang, C. Directional effects of correlated wind and waves on the dynamic response of long-span sea-crossing bridges. *Appl. Ocean Res.* **2023**, *132*, 103483. [CrossRef]
3. Shi, X.; Liu, Z.; Guo, T.; Li, W.; Niu, Z.; Ling, F. Research on the Flow-Induced Vibration of Cylindrical Structures Using Lagrangian-Based Dynamic Mode Decomposition. *J. Mar. Sci. Eng.* **2024**, *12*, 1378. [CrossRef]
4. Li, C.Y.; Chi, Y.; Sun, X.Q.; Han, Y.P.; Chen, X.; Zhao, L.C.; Zhang, H. Construction technology of high-rise pile cap foundation of offshore wind power in Taiwan Strait. *IOP Conf. Ser. Earth Environ. Sci.* **2017**, *93*, 012037. [CrossRef]
5. Barnes, I.C.; Frick, K.T.; Deakin, E.; Skabardonis, A. Impact of Peak and Off-Peak Tolls on Traffic in San Francisco–Oakland Bay Bridge Corridor in California. *Transp. Res. Rec.* **2012**, *2297*, 73–79. [CrossRef]
6. Miyata, T.; Yamaguchi, K. Aerodynamics of wind effects on the Akashi Kaikyo Bridge. *J. Wind Eng. Ind. Aerodyn.* **1993**, *48*, 287–315. [CrossRef]
7. Yu, Y.; Li, J.; Li, J.; Xia, Y.; Ding, Z.; Samali, B. Automated damage diagnosis of concrete jack arch beam using optimized deep stacked autoencoders and multi-sensor fusion. *Dev. Built Environ.* **2023**, *14*, 100128. [CrossRef]

8. Yuan, W.; Liu, M. Research on the Wave Load Effect Based on Time History Analysis of Donghai Island Bridge. *Adv. Mater. Res.* **2014**, *919–921*, 587–589. [CrossRef]
9. Ma, X.; Xiong, W.; Fang, Y.; Cai, C.S. Safety assessment of ship-bridge system during sea transportation under complex sea states. *Ocean Eng.* **2023**, *286*, 115630. [CrossRef]
10. Qiu, Z.; Prabhakaran, A.; Su, L.; Zheng, Y. Performance-based seismic resilience and sustainability assessment of coastal RC bridges in aggressive marine environments. *Ocean Eng.* **2023**, *279*, 114547. [CrossRef]
11. Guo, A.; Fang, Q.; Bai, X.; Li, H. Hydrodynamic Experiment of the Wave Force Acting on the Superstructures of Coastal Bridges. *J. Bridge Eng.* **2015**, *20*, 04015012. [CrossRef]
12. Liu, Z.; Shi, X.; Guo, T.; Ren, H.; Zhang, M. Investigation on hydrodynamic response and characteristics of a submerged floating tunnel based on hydrodynamic tests. *Ocean Eng.* **2024**, *300*, 117187. [CrossRef]
13. Yang, Y.; Fahmy, M.F.M.; Guan, S.; Pan, Z.; Zhan, Y.; Zhao, T. Properties and applications of FRP cable on long-span cable-supported bridges: A review. *Compos. Part B Eng.* **2020**, *190*, 107934. [CrossRef]
14. Meier, U. Proposal for a Carbon Fibre Reinforced Composite Bridge across the Strait of Gibraltar at its Narrowest Site. *Proc. Inst. Mech. Eng. Part B Manag. Eng. Manuf.* **1987**, *201*, 73–78. [CrossRef]
15. Wang, Q.; Li, L.; Zhao, Y.; Song, Y.; Zhang, C. Feasibility assessment and application of sea sand in concrete production: A review. *Structures* **2024**, *60*, 105891. [CrossRef]
16. Alraeeini, A.S.; Nikbakht, E. Corrosion effect on the flexural behaviour of concrete filled steel tubulars with single and double skins using engineered cementitious composite. *Structures* **2022**, *44*, 1680–1694. [CrossRef]
17. Bazli, M.; Dorothea Luck, J.; Rajabipour, A.; Arashpour, M. Bond-slip performance of seawater sea sand concrete filled filament wound FRP tubes under cyclic and static loads. *Structures* **2023**, *52*, 889–903. [CrossRef]
18. Yuan, Y.; Jiang, J.; Peng, T. Corrosion Process of Steel Bar in Concrete in Full Lifetime. *ACI Mater. J.* **2010**, *107*, 562–567.
19. Ou, Y.-C.; Tsai, L.-L.; Chen, H.-H. Cyclic performance of large-scale corroded reinforced concrete beams. *Earthq. Eng. Struct. Dyn.* **2012**, *41*, 593–604. [CrossRef]
20. Akiyama, M.; Frangopol, D.M. Long-term seismic performance of RC structures in an aggressive environment: Emphasis on bridge piers. *Struct. Infrastruct. Eng.* **2014**, *10*, 865–879. [CrossRef]
21. Fan, W.; Sun, Y.; Sun, W.; Huang, X.; Liu, B. Effects of Corrosion and Scouring on Barge Impact Fragility of Bridge Structures Considering Nonlinear Soil–Pile Interaction. *J. Bridge Eng.* **2021**, *26*, 04021058. [CrossRef]
22. Liu, Z.; Niu, S.; Qian, J.; Guo, T. Investigation on flooding dynamic response and mitigation measure of river bridge. *Eng. Fail. Anal.* **2025**, *167*, 108987. [CrossRef]
23. Niu, S.; Liu, Z.; Guo, T.; Guo, A.; Liu, A. Dynamic characteristics and force analysis of box girder under tsunami action based on level-set method. *Struct. Infrastruct. Eng.* **2025**, 1–22. [CrossRef]
24. Geng, B.; Sun, K.; Gao, P.; Jin, R.; Jiang, S. Experimental and Numerical Investigations for Impact Loading on Platform Decks. *J. Mar. Sci. Eng.* **2024**, *12*, 899. [CrossRef]
25. Albalawi, W.; Taha, H.H.; El-Sapa, S. Effect of the permeability on the interaction between two spheres oscillating through Stokes-Brinkmann medium. *Heliyon* **2023**, *9*, e14396. [CrossRef] [PubMed]
26. Xu, B.; Wei, K. Numerical simulation of wave forces on elevated pile cap of sea-crossing bridges based on RANS. *Railw. Stand. Des.* **2019**, *63*, 6.
27. Deng, L.; Yang, W.; Li, Q.; Li, A. CFD investigation of the cap effects on wave loads on piles for the pile-cap foundation. *Ocean Eng.* **2019**, *183*, 249–261. [CrossRef]
28. Al-Hanaya, A.; El–Sapa, S. Impact of permeability and fluid parameters in couple stress media on rotating eccentric spheres. *Open Phys.* **2024**, *22*, 20240112. [CrossRef]
29. Hirt, C.W.; Nichols, B.D. Volume of fluid (VOF) method for the dynamics of free boundaries. *J. Comput. Phys.* **1981**, *39*, 201–225. [CrossRef]
30. Ye, X.; Zhou, X.; Wang, M.; Qiao, D.; Zhao, X.; Wang, L. Global Responses Analysis of Submerged Floating Tunnel Considering Hydroelasticity Effects. *J. Mar. Sci. Eng.* **2024**, *12*, 1854. [CrossRef]
31. Algatheem, A.M.; Taha, H.H.; El-Sapa, S. Interaction Between Two Rigid Hydrophobic Spheres Oscillating in an Infinite Brinkman–Stokes Fluid. *Mathematics* **2025**, *13*, 218. [CrossRef]
32. Weller, H.G.; Tabor, G.; Jasak, H.; Fureby, C. A tensorial approach to computational continuum mechanics using object-oriented techniques. *Comput. Phys.* **1998**, *12*, 620–631. [CrossRef]
33. Ducrozet, G.; Bouscasse, B.; Gouin, M.; Ferrant, P.; Bonnefoy, F. CN-Stream: Open-source library for nonlinear regular waves using stream function theory. *arXiv* **2019**, arXiv:1901.10577v1.
34. Karadeniz, H. Wave-Current and Fluid-Structure Interaction Effects on the Stochastic Analysis of Offshore Structures. In Proceedings of the Second International Offshore and Polar Engineering Conference, San Francisco, CA, USA, 14–19 June 1992.
35. Fan, W.; Sun, Y.; Yang, C.; Sun, W.; He, Y. Assessing the response and fragility of concrete bridges under multi-hazard effect of vessel impact and corrosion. *Eng. Struct.* **2020**, *225*, 111279. [CrossRef]

36. Third Harbor Engineering Investigation and Design Institute of the Ministry of Transport. *Code for Pile Foundation in Port Engineering*; People's Transportation Publishing House: Beijing, China, 2012.
37. *DNV-OS-J101*; Design of Offshore Wind Turbine Structures. Det Norske Veritas: Bærum, Norway, 2010.
38. American Petroleum Institute (API). Petroleum and Natural Gas Industries-Specific Requirements for Offshore Structures. Part 4-Geotechnical and Foundation Design Considerations. 2011. Available online: http://refhub.elsevier.com/S0267-7261(19)30591-3/sref25 (accessed on 15 February 2025).
39. Boulanger, R.; Curras, C.; Kutter, B.; Wilson, D.; Abghari, A. Seismic Soil-Pile-Structure Interaction Experiments and Analyses. *J. Geotech. Geoenviron. Eng.* **1999**, *125*, 750–759. [CrossRef]
40. Guo, X.; Zhang, C.; Chen, Z. Nonlinear Dynamic Response and Assessment of Bridges under Barge Impact with Scour Depth Effects. *J. Perform. Constr. Facil.* **2020**, *34*, 04020058. [CrossRef]
41. Imam, B. Chapter Six—Climate Change Impact for Bridges Subjected to Scour and Corrosion. In *Climate Adaptation Engineering*; Bastidas-Arteaga, E., Stewar, M.G., Eds.; Butterworth-Heinemann: Oxford, UK, 2019; pp. 165–206.
42. Calvi, G.M.; Priestley, M.J.N.; Kowalsky, M.J. Displacement-Based Seismic Design of Bridges. *Struct. Eng. Int.* **2013**, *23*, 112–121. [CrossRef]
43. Guo, A.; Yuan, W.; Lan, C.; Guan, X.; Li, H. Time-dependent seismic demand and fragility of deteriorating bridges for their residual service life. *Bull. Earthq. Eng.* **2015**, *13*, 2389–2409. [CrossRef]
44. Balafas, K.; Kiremidjian, A.S. Reliability assessment of the rotation algorithm for earthquake damage estimation. *Struct. Infrastruct. Eng.* **2015**, *11*, 51–62. [CrossRef]
45. Liang, Z.; Lee, G.C. Towards establishing practical multi-hazard bridge design limit states. *Earthq. Eng. Eng. Vib.* **2013**, *12*, 333–340. [CrossRef]
46. Khan, R.; Datta, T. Effect of Support Flexibility and Soil- Structure Interaction on Seismic Risk Analysis of Harp Type Cable Stayed Bridges. *Ing. Sismica* **2014**, *31*, 32–46.
47. Cairns, J.; Plizzari, G.; Du, Y.; Law, D.; Franzoni, C. Mechanical properties of corrosion-damaged reinforcement. *ACI Mater. J.* **2005**, *102*, 256–264.
48. Du, Y.G.; Clark, L.A.; Chan, A.H.C. Residual capacity of corroded reinforcing bars. *Mag. Concr. Res.* **2005**, *57*, 135–147. [CrossRef]
49. Molina, F.J.; Alonso, C.; Andrade, C. Cover cracking as a function of rebar corrosion: Part 2—Numerical model. *Mater. Struct.* **1993**, *26*, 532–548. [CrossRef]
50. Vecchio, F.J.; Collins, M.P. The Modified Compression-Field Theory for Reinforced Concrete Elements Subjected to Shear. *ACI Struct. J.* **1986**, *83*, 219–231.
51. Biondini, F.; Vergani, M. Damage modeling and nonlinear analysis of concrete bridges under corrosion. In Proceedings of the Sixth International Conference of Bridge Maintenance, Safety and Management (IABMAS 2012), Stresa, Italy, 8–12 July 2012; pp. 949–957.
52. Coronelli, D.; Gambarova, P. Structural Assessment of Corroded Reinforced Concrete Beams: Modeling Guidelines. *J. Struct. Eng.* **2004**, *130*, 1214–1224. [CrossRef]
53. Vidal, T.; Castel, A.; François, R. Analyzing crack width to predict corrosion in reinforced concrete. *Cem. Concr. Res.* **2004**, *34*, 165–174. [CrossRef]
54. Zheng, Y.; Chen, B.; Chen, W. Evaluation of the seismic responses of a long-span cable-stayed bridge located in complex terrain based on an SHM-oriented model. *Stahlbau* **2015**, *84*, 252–266. [CrossRef]
55. Johnson, P.A.; Dock, D.A. Probabilistic Bridge Scour Estimates. *J. Hydraul. Eng.* **1998**, *124*, 750–754. [CrossRef]
56. Xu, B.; Wei, K.; Qin, S.; Hong, J. Experimental study of wave loads on elevated pile cap of pile group foundation for sea-crossing bridges. *Ocean Eng.* **2020**, *197*, 106896. [CrossRef]

Journal of
Marine Science and Engineering

MDPI

Article

Global Responses Analysis of Submerged Floating Tunnel Considering Hydroelasticity Effects

Xiangji Ye [1], Xiangbo Zhou [2], Ming Wang [2], Dongsheng Qiao [2,*], Xin Zhao [1] and Li Wang [1]

[1] CCCC First Harbour Consultants Co., Ltd., Tianjin 300220, China
[2] State Key Laboratory of Coastal and Offshore Engineering, Dalian University of Technology, Dalian 116024, China
* Correspondence: qiaods@dlut.edu.cn

Abstract: To investigate the applicability and differences in wave loads and the dynamic response calculation principles for SFT on an entire-length scale, two numerical models of entire-length SFT with identical dimensions and parameters were established. These models are employed by a 3D diffraction method based on rigid-body assumptions, the potential flow theory and the Dummy-Connection-Mass (DCM) method based on the lumped mass method and Morison equation while considering hydroelasticity effects. The applicability of the potential flow theory and Morison equation for wave load calculation of SFT is presented along with the differences in their dynamic response calculation, which aim to explore the impact on SFT dynamic responses considering hydroelasticity by comparing the numerical calculation results. Furthermore, a comparison between free-end boundary and fixed-end boundary models, established using the DCM method, is conducted to examine the reasonableness of the commonly adopted free-end boundary condition.

Keywords: SFT; 3D diffraction method; DCM method; hydroelasticity effects

1. Introduction

The Submerged Floating Tunnel (SFT) represents a novel category of transportation infrastructure that spans expansive deep-water regions. Its enhanced environmental adaptability is demonstrated, offering significant advantages over conventional transportation structures. A prototypical SFT system comprises several immersed tube segments, the joints used to link them together, a series of inclined anchor-cables for constraining tube movement, a foundation situated in deep waters, and an offshore shore protection structure. The feasibility of SFT has been studied by many researchers due to its potential advantages, as it is not easily affected by extreme wind, wave loads, or deep-water seismic loads [1]. Additionally, the SFT is maintained at a submerged depth of approximately 30–50 m, thereby eliminating issues associated with maritime traffic [2]. In contrast to underground structures, which may undergo complex responses and potential damage due to seismic behavior [3], the flexible structural system of the SFT is better equipped to resist such risks [4].

The calculation of wave loads on an SFT typically involves two methods: one based on potential flow theory and the other on the Morison equation. Among them, Liu et al. [5] simplified the mooring system as linear springs and analyzed the motion response of the SFT under different cross-sectional shapes and various mooring angles based on potential flow theory. Paik et al. [6] developed a dynamic analysis program which employed the potential flow theory and boundary element method for time-domain 3D structural analysis of an SFT and provided insights into the impact of the SFT depth on hydrodynamic coefficients. Jin et al. [7] established a full time-domain 2D numerical model for an SFT, employing the HOBEM method based on potential flow theory to simulate wave loads and solve numerical results, including first- and second-order motion response. In contrast, based on the Morison equation, Xu et al. [8] developed a non-uniform wave-current environment model along the Qiongzhou Strait by considering the impact of non-uniform loads on an SFT under five operating cases through finite element analysis. Luo et al. [9] developed a hydrodynamic model to describe the coupled dynamic response of the SFT and mooring lines under regular waves to investigate the influence of parameters such as cable length and the buoyancy–weight ratio on SFT dynamic responses under wave loads. Jeong et al. [10] developed an analysis method based on practical assumptions to evaluate the structural responses of an SFT. Under the assumption of free-end boundary conditions, the structural responses of the SFT in the time-domain was effectively determined and validated using the finite element method program ABAQUS/AQUA. Furthermore, Kunisu [11] used the boundary element method based on potential flow theory to evaluate wave forces and discuss the impact of SFT size and shape on wave forces. These results were compared with those evaluated by the Morison equation. Chung et al. [12] designed and compared three methods: potential flow theory, including second-order wave force effects; Morison equation; and experimental results conducted in a 3D wave tank, performing comparative research. Previous studies have demonstrated the accuracy of both numerical methods through experimental comparisons, concluding that both can effectively calculate structural motions under wave conditions. However, these comparisons rarely focus on the response calculation results of SFT under an entire-length scale.

In order to focus on the entire-length SFT and avoid the impact of inaccurate end boundary conditions in segmented models, a boundary element model of SFT was established by Yang et al. [13] in ANSYS-AQWA 2022R2 software, and the dynamic responses under combined wave-current conditions were calculated based on the potential flow theory. Wu et al. [14] compared the numerical segmented model established in AQWA with experimental results, showing good consistency. This method was then applied to establish an entire-length SFT model to study the influence of key parameters. Zhou et al. [15] established a boundary element model of the entire-length SFT in AQWA and OrcaFlex based on the potential flow theory. The study focused on identifying the most unfavorable cable breakage position and simulating the progressive failure process of an SFT. The advantage of this method lies in its fast calculation speed and its ability to simulate entire-length models; however, the simple rigid-body assumption fails to account for hydroelasticity effects.

Some researchers have employed the Computational Fluid Dynamics (CFD) method [16] to rigorously calculate the responses of an SFT [17–19] in order to account for hydroelasticity effects. Meanwhile, physical model experiments are also frequently utilized in studies of SFT [20–22]. However, due to limitations in the site and computational resources, CFD and experimental methods are unable to simulate an entire-length SFT, leading to the frequent use of segmented models for research. Under such circumstances, only the rigid behavior of the tunnel can be observed in most cases, making it difficult to study the impact of elastic deformation on the dynamic response of an SFT on the entire-length scale. The modal superposition method has also been widely applied to study the impact of structural hydroelasticity on large structures, which can be categorized into dry-mode and wet-mode methods. The wet-mode method requires additional mass and hydrostatic stiffness components; therefore, finite element methods are typically used to determine the mode shapes and natural frequencies of the wet modal structure [23,24]. The calculation of wet modes with mooring lines using this method is highly complex. Another approach is also called the direct coupling method, which combines finite element structural dynamic simulation with 3D hydrodynamic time-domain tools [25,26]. Its advantages include the elimination of the need for pre-calculating modal characteristics, the ability to incorporate nonlinearity in the time-domain, and the capability of simulating complex structural shapes. However, this method is computationally intensive and very time-consuming. Recently, Jin and Kim [27] proposed a specifically designed Dummy-Connection-Mass (DCM) method between the tunnel and mooring lines. This method effectively captures the elastic behavior of the tunnel while minimizing numerical errors at the connection points between the mooring lines and the flexible tunnel. Kim et al. [28]

employed the time-domain DCM method to numerically simulate a deformed tunnel with multiple mooring lines. This model was validated through comparison with 2D wave tank experiments, confirming its accuracy. Jin and Kim [29] developed a program using the DCM method to address the interaction of tunnel, mooring lines and trains under wave excitation, deriving the coupled dynamics equations for the train–tunnel system. Jin et al. [30] validated the accuracy of the method through a comparative analysis of multi-body coupled DCM modeling, quasi-static calculations based on a 3D solid model in ABAQUS, and dynamic simulations using the semi-empirical Morison model in OrcaFlex.

Additionally, the end boundary conditions of an SFT are also a crucial aspect of research, with some researchers often adopting simplified end boundary conditions to mitigate the limitations of site and computational resources. In experiments, Yang et al. [31] constrained the SFT through end constraints to limit it to 2D motion (heave, sway, and roll), studying the effects of different parameters such as wave height and BWR under regular waves on the SFT. Yang et al. [32] established an SFT model with a one-degree-of-freedom vertical elastic truncated boundary condition to investigate the motion responses and hydrodynamic characteristics of the tube under wave action. Xiang et al. [33] developed differential equations for an SFT based on simply supported boundary conditions to analyze the dynamic responses of an SFT and validated the theoretical results using a finite element analysis in ABAQUS. Xiang et al. [34] compared the physical model test results and finite element simulations under simply supported boundary conditions, discussing the impact of different cable breakage factors on the dynamic response of the floating tunnel. Wang et al. [35] applied different spring stiffness constraints to match the first three modes of the truncated model with the entire-length model, and then used this to simulate the impact of various collision parameters on an SFT. However, due to the large length-to-diameter ratio of an SFT and the absence of more accurate methods for simulating segmented model end boundaries, end constraints are often ignored by most researchers, who instead base their studies on free-end boundary conditions [12,21,36,37]. Nonetheless, it is well known that an SFT is connected to land through offshore shore protection structures, which naturally prevents displacement and rotation, making them more akin to fixed-end boundary conditions. This has also been considered in some studies [38,39].

In this paper, a comparative analysis is conducted between a simplified rigid-body entire-length SFT numerical model, established based on the 3D diffraction method, and an entire-length SFT numerical model established using the DCM method. Wave loads on the entire-length SFT under different wave periods are calculated and compared using the potential flow theory and Morison equation in order to determine the applicability of these two calculation theories. With the simplified 3D diffraction method model as a reference, the dynamic response results of the two methods are compared under appropriate regular wave conditions to investigate the differences in two calculation theories in regard to response calculation and the impact of considering hydroelasticity effects on SFT dynamic responses. Additionally, the general dynamic response patterns of SFT under different conditions are explored by identifying the common conclusions derived from both methods. Furthermore, entire-length SFT models with free and fixed boundary conditions are established using the DCM method to study the influence of different end boundary conditions on the dynamic responses of the entire-length SFT.

2. Calculation Model for the Global Dynamic Responses of SFT Based on the 3D Diffraction Method

2.1. Mathematical Formulation

The 3D diffraction method, based on potential flow and boundary element methods, allows for more accurate calculation of the hydrodynamic inertial forces exerted by waves on the tunnel. In frequency-domain hydrodynamic analysis, the hydrodynamic computation software AQWA is used to numerically solve the hydrodynamic parameters of the floating structures, including the amplitude response function, first-order wave forces, second-order wave drift forces, added mass, and radiation damping. The potential flow theory assumes the fluid to be ideal, irrotational, and inviscid with incident waves of small amplitude. The first-order hydrodynamic load on the SFT are determined by defining the velocity potential and the diffraction potential [40]. The second-order wave mean drift force is based on the direct pressure integration, which is the so called "near-field" [41].

After the wave forces are calculated, the following motion equations can be solved in the frequency domain to calculate the responses of the SFT under regular waves of any frequency ω, which is represented as the Response Amplitude Operator (RAO).

$$\mathbf{M_s}(\omega)\ddot{\mathbf{x}} + \mathbf{M_a}(\omega)\ddot{\mathbf{x}} + \mathbf{C}(\omega)\dot{\mathbf{x}} + \mathbf{K_s}(\omega)\mathbf{x} = \mathbf{F}(\omega) \tag{1}$$

where $\mathbf{M_s}$, $\mathbf{M_a}$, $\mathbf{C}$, $\mathbf{K_s}$ represents the mass matrix, the added mass matrix, the system's linear damping matrix, and the system's hydrostatic stiffness matrix. $\mathbf{F}$ is the wave force per unit wave amplitude acting on the system and $\mathbf{x}$ is the displacement Response Amplitude Operator (RAO).

The dynamic analysis of mooring lines is conducted using the lumped mass method, as shown in Figure 1, which forms the mathematical foundation for modeling cable tension in OrcaFlex. The equilibrium equation is established as:

$$\mathbf{M_i a_i} = \mathbf{F_{Ti}} - \mathbf{F_{Ti\text{-}1}} + \mathbf{F_{Di}} + \mathbf{F_{Ai}} - \mathbf{W_i} \tag{2}$$

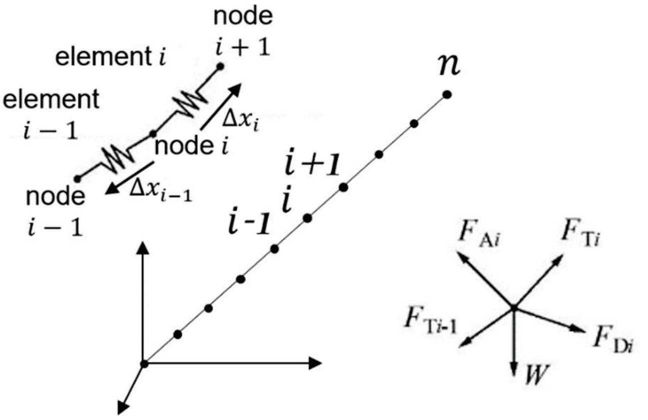

Figure 1. The force and displacement of the cable elements.

In the equation, $\mathbf{a_i}$, $\mathbf{M_i}$, $\mathbf{W_i}$ represent the acceleration vector of node i, the mass of node i and the gravitational force acting on node i. $\mathbf{F_{Ti\text{-}1}}$ and $\mathbf{F_{Ti}}$ represent the vector forces generated by chain elements $i-1$ and i. The terms $\mathbf{F_{Ai}}$, $\mathbf{F_{DTi}}$, and $\mathbf{F_{DNi}}$ denote the fluid inertial force, normal drag force, and tangential force acting on node i, respectively, which are calculated based on the Morison equation.

The frequency-domain calculation results are imported into OrcaFlex based on time-frequency transformation methods. The time-domain calculations are based on the Cummins equation, as shown in Equation (3), where $\mathbf{A}(\infty)$ represents the added mass matrix at the infinite wave frequency. $\mathbf{K}(t)$ is the retardation function, which is a convolution term related to radiation damping. $\mathbf{D}$ is the viscous damping correction matrix. The wave force $\mathbf{F_{wave}}(t)$ includes Froude–Krylov (F-K) forces, diffraction forces, and second-order drift forces. $\mathbf{F_{buoyancy}}(t)$ represents the net buoyancy force. The relationships in Equations (1) and (3) are given by Yin et al. [42]. The global research approach using the 3D diffraction method is illustrated in Figure 2.

$$\begin{aligned} &[\mathbf{M} + \mathbf{A}(\infty)]\ddot{\mathbf{x}}(t) + \int_0^t \mathbf{K}(t-\tau)\dot{\mathbf{x}}(\tau)d\tau \\ &+\mathbf{D}\dot{\mathbf{x}}(t) = \mathbf{F_{wave}}(t) + \mathbf{F_{moor}}(t) + \mathbf{F_{buoyancy}}(t) \end{aligned} \tag{3}$$

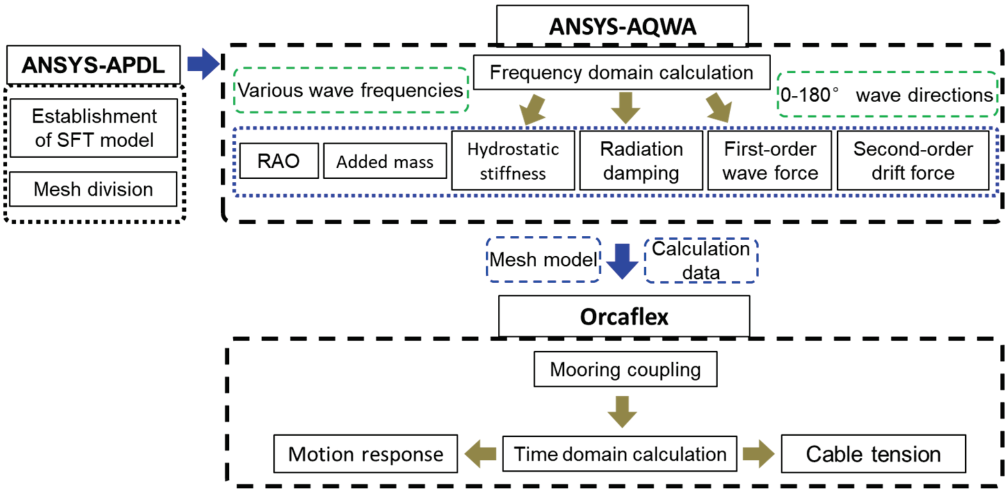

Figure 2. The numerical calculation logic of AQWA and OrcaFlex.

2.2. Numerical Model

According to the existing research on SFTs in China and abroad [13,43,44], the design parameters are chosen. For the entire-length SFT model, its total length is set as 2000 m, including 21 pairs of cables which are symmetrically arranged and spaced 100 m apart along the tunnel's axis, as shown in Figure 3. The water depth is 74 m, and a suggested clearance depth of 30 m between the SFT and the water surface is provided, with specific values being detailed in Table 1. According to Yuan et al. [36], when the ratio of length to diameter of the SFT is greater than a certain value, the influence of boundary conditions on the dynamic characteristics of the SFT could be ignored. Therefore, the entire-length model of an SFT without the boundary constraints is established to investigate the global dynamic response of an SFT. Meanwhile, each anchor-cable is assumed with the same parameter settings for the purpose of simplifying the calculation process. In the numerical model, it is assumed that the redundant buoyancy of the SFT is evenly apportioned into each cable.

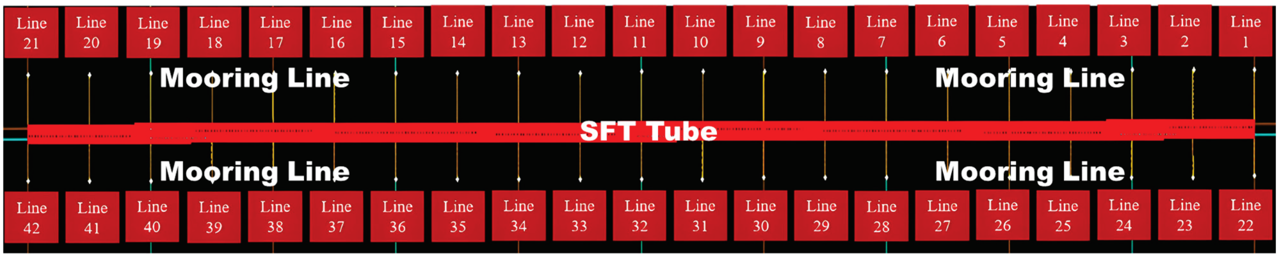

Figure 3. Model diagram of the SFT–mooring line coupling model.

Using these SFT structural parameters, a finite element model is developed, as shown in Figure 4. For the tube, the basic requirement for meshing is to satisfy one wavelength covering at least five to eight maximum size elements. At the same time, considering the balance between calculation accuracy and efficiency, a variety of schemes are compared. Finally, the SFT is divided into 25,391 panel elements based on a meshing size of 3 m in ANSYS-APDL. Furthermore, the frequency domain hydrodynamic coefficients of the SFT are calculated by AQWA based on the boundary element method. while the global dynamic response of moored floating structures can be calculated by OrcaFlex. The global dynamic responses of moored floating structures can be computed by OrcaFlex, with the input being provided by the frequency domain hydrodynamic coefficients calculated by AQWA. The time-domain calculation model based on this method has been established by the authors and a method validation has been conducted [15]. The numerical model established using this method will hereafter be referred to as Model 1.

Table 1. Design parameters of SFT.

Items	Parameter	Unit	Value
Tube	Outer diameter	m	14
	Inside diameter	m	12
	Length	m	2000
	Density	kg/m^3	2500
	Mass	kg	2.04×10^8
	EI	N m^2	3.12×10^{13}
	EA	N	1.47×10^{12}
Anchor-cables	Diameter	m	0.5
	Length	m	48.79
	Cable interval	m	100
	Mass per unit length	kg/m	1541.34
	Density	kg/m^3	7850
	Inclination angle	°	45
	Elastic modulus	MPa	206,000

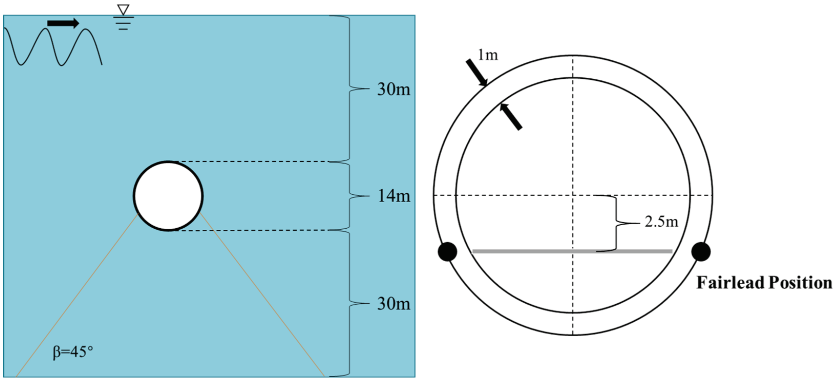

Figure 4. ANSYS/AQWA hydrodynamic calculation model diagram.

3. Calculation Model for the Global Dynamic Responses of an SFT Based on the DCM Method

3.1. Mathematical Formulation

The DCM method is a research approach that enables hydrodynamic calculations for an entire-length SFT while effectively explaining the tunnel's hydroelasticity deformation behavior. The core concept involves placing a dummy mass point at the connection position between the tunnel and mooring lines, with both the tunnel and mooring lines being modeled using the lumped mass method, as outlined in Figure 5. The entire tunnel is firstly divided into several segments by the dummy mass point with the mooring lines. At the division points, the tunnel segments are connected to the mooring lines through a dummy rigid body (i.e., dummy mass) with six degrees of freedom, allowing for the establishment of the SFT–mooring line integrated model, after which the motion responses can be calculated using Equation (4). The mass and volume of the dummy rigid body can be neglected, meaning that they enable coupling between the tunnel and mooring lines without altering the global dynamic equations [45]. Additionally, the connection between the tunnel segments and the dummy rigid body is set as infinite tensile, bending, and torsional stiffness, simulating a rigid connection that transmits forces and moments, while the mooring lines are hinged to the dummy rigid body.

The dynamic response equation of an SFT considering mooring and hydroelasticity under this method can be described by the following equation:

$$\mathbf{M}\ddot{x}(t) + \mathbf{C}\dot{x}(t) + \mathbf{K}x(t) = \mathbf{F}_{\mathbf{wave}}(t) + \mathbf{F}_{\mathbf{buoyancy}}(t) + \mathbf{F}_{\mathbf{constraint}}(t) \quad (4)$$

where **M** represents the mass matrix, **C** is the structural damping matrix, **K** is the total structural stiffness matrix including mooring stiffness, $\mathbf{F_{wave}}(t)$ is the wave load, $\mathbf{F_{buoyancy}}(t)$ is the net buoyancy, and $\mathbf{F_{constraint}}(t)$ denotes the end boundary constraint load.

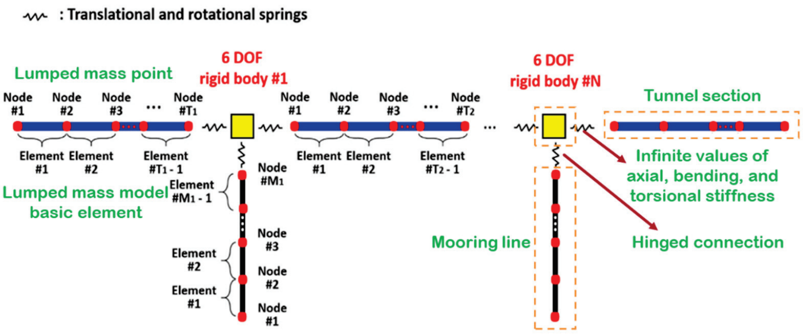

Figure 5. Dummy-Connection-Mass method [46].

The wave excitation load is calculated by the Morison equation, which is suitable for capturing the effects of the instantaneous positions throughout the tunnel after hydroelasticity deformation. Equation (5) represents the wave loads acting on the tunnel and mooring lines.

$$\mathbf{F_{wave}} = \mathrm{C_M}\rho\boldsymbol{\Delta}\mathbf{a_f} - \mathrm{C_a}\rho\boldsymbol{\Delta}\mathbf{a_r} + \frac{1}{2}\rho \mathrm{DlC_D}\mathbf{v}|\mathbf{v}| \tag{5}$$

$$\mathrm{C_M} = \mathrm{C_a} + 1 \tag{6}$$

where $\mathrm{C_M}$, $\mathrm{C_a}$, and $\mathrm{C_D}$ represent the inertia coefficient, added mass coefficient, and drag coefficient, respectively. For the circular tube form of the SFT, these values are taken as 2, 1, and 0.55, while, for the mooring lines, they are 2, 1, and 2.4, respectively. D, l, and $\boldsymbol{\Delta}$ represent the tube diameter, segment length, and displaced volume, respectively. Vectors $\mathbf{a_f}$, $\mathbf{a_r}$ and $\mathbf{v}$ denote the fluid acceleration, body acceleration, and relative velocity between the fluid and the tube, respectively.

The mass and structural stiffness matrices are determined by the structural characteristics of the tunnel, including its diameter, thickness, and material properties. These parameters are defined using the lumped mass line method in OrcaFlex. Additionally, the Rayleigh damping model is used to set the structural damping. The Rayleigh damping model specifies that the damping is proportional to the system's mass and stiffness, as shown in the following equation:

$$\mathbf{C} = \alpha\mathbf{M_T} + \beta\mathbf{K} \tag{7}$$

$$\alpha = \zeta\frac{2\omega_{n,i}\omega_{n,j}}{\omega_{n,i}+\omega_{n,j}}, \beta = \zeta\frac{2}{\omega_{n,i}+\omega_{n,j}} \tag{8}$$

where $\mathbf{M_T}$ is the total mass matrix, including the added mass matrix. α and β are the mass and stiffness proportional damping coefficients, respectively. The damping ratio is selected as 8% after comparison.

3.2. Numerical Model

The model considered in this method is also as shown in Figure 3 and Table 1 and is connected by 21 pairs of mooring lines. At this time, the SFT model is represented by 20 tunnel segments and 21 dummy-connection masses, which are massless and volumeless, based on the DCM method. The entire-length SFT model is established in the OrcaFlex 11.0 software based on the above method, as shown in Figure 6. To further investigate the influence of end boundary conditions on the dynamic responses of the entire-length SFT considering hydroelasticity, two entire-length SFT numerical models with free and fixed boundary conditions are established using the DCM method. The numerical model with free-end boundary conditions is hereafter referred to as Model 2 while the one with fixed-end boundary conditions is referred to as Model 3.

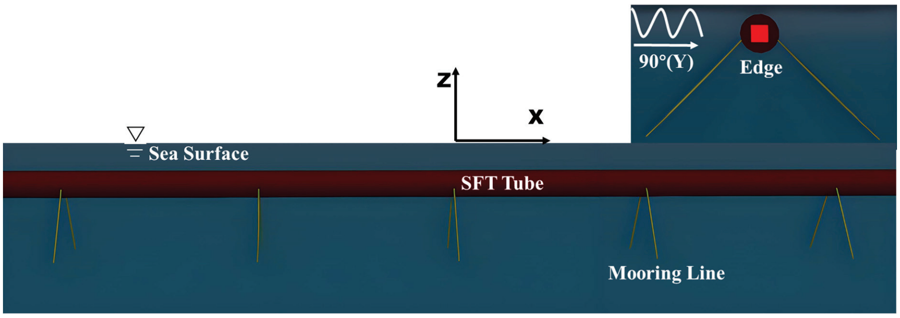

Figure 6. Entire-length model of SFT based on DCM methodology.

3.3. Verification of the Numerical Method

To verify the accuracy of the research approach, it is necessary for the results to be compared with previously published studies. In OrcaFlex, an SFT model identical to the scientific work of Jin and Kim [25] was established for comparison of certain results, as shown in Figure 7. This model has a total length of 700 m, with a tube diameter of 23 m and mooring lines arranged every 25 m near the midpoint. Each group consists of four lines, resulting in a total of 15 groups. The established model's vertical displacement and cable tension were compared under static conditions, and the horizontal displacement and cable tension were compared under a given once-in-a-century sea condition. The results, as shown in Figure 8a–d, indicate that the results are very close to those of Jin and Kim, demonstrating the accuracy of our model establishment method.

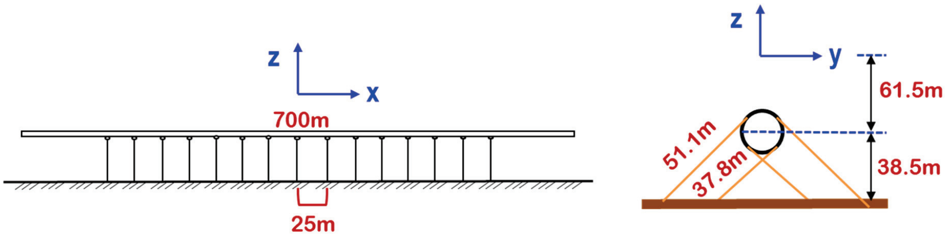

Figure 7. Jin and Kim's SFT numerical calculation model [27].

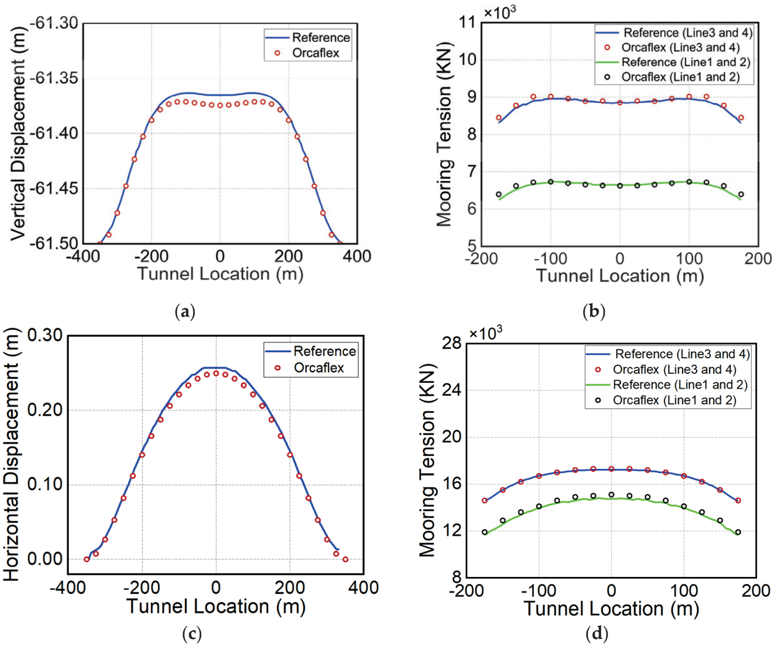

Figure 8. (**a**) Static vertical displacement; (**b**) static cable tension; (**c**) horizontal displacement under once−in−a−century sea conditions; (**d**) cable tension under once−in−a−century sea condition.

4. Comparison and Analysis

4.1. Comparison of Wave Force

Before studying the structural motion responses and cable tension, it is necessary to firstly calculate the wave loads on the structure to determine the magnitude of external excitation on the models by the two methods. For the potential flow theory in the 3D diffraction approach, under small amplitude waves, the wave excitation load consists of the first-order incident wave force (Froude–Krylov force) and the diffraction force caused by disturbed waves due to the presence of the object. Due to the significant submergence depth, the second-order drift force is minimal and thus temporarily ignored in this section, but it will be considered later in the time-domain calculation. Under the action of regular wave with unit amplitudes and 90-degree incidence, the wave loads with various wave periods acting on the entire length model of the SFT can be obtained through frequency-domain calculations performed by AQWA. The DCM method, on the other hand, is based on the Morison equation, as shown in Equation (5). In some studies [7,36], to simplify calculations, the acceleration and velocity terms related to the structure in Morison equation are often ignored, with attention only being paid to the acceleration and velocity of wave particles. In this study, time-domain calculations in OrcaFlex under wave action are used to extract fluid acceleration, structural acceleration, fluid velocity, and structural velocity at the mid-span location of the structure, as shown in Figure 9a–d The wave loads acting on the entire-length SFT are calculated using a Python program developed for this purpose.

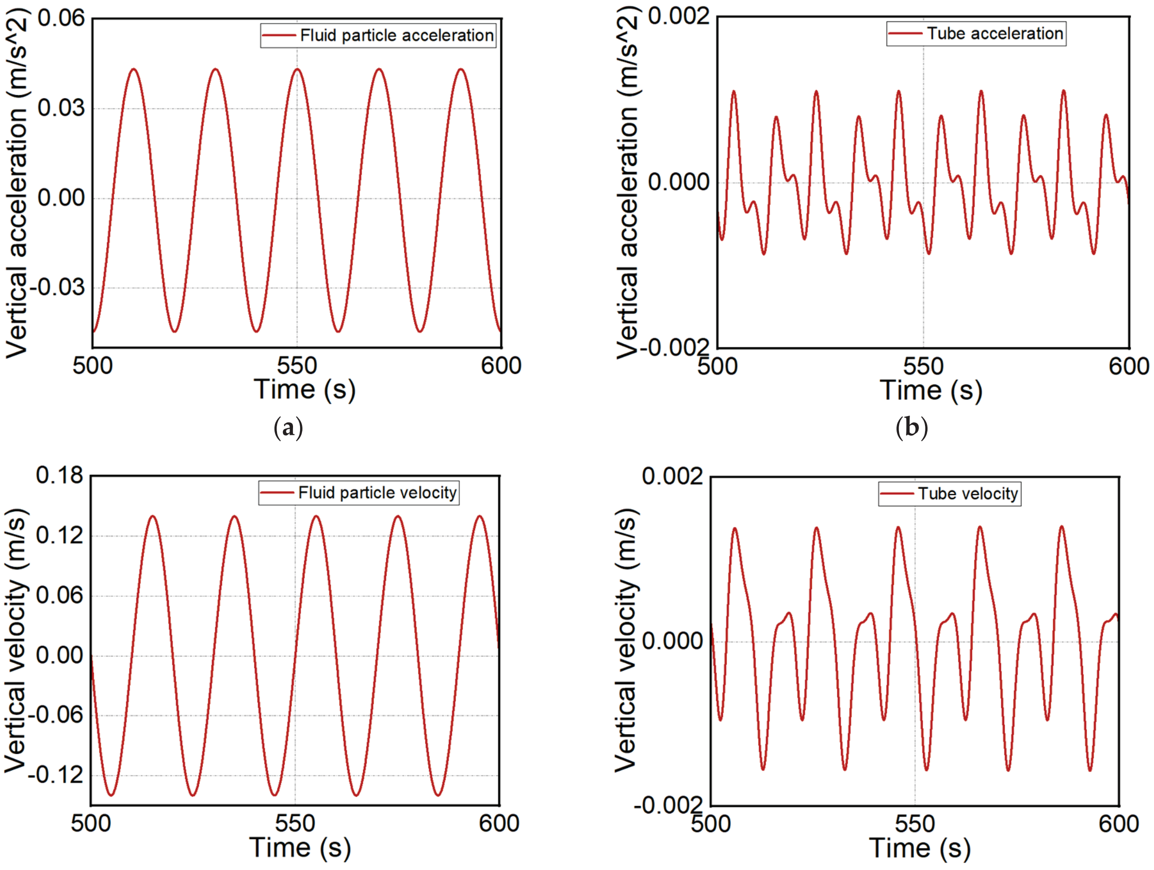

(**a**) (**b**)

(**c**) (**d**)

Figure 9. (**a**) Fluid vertical acceleration; (**b**) tube vertical acceleration; (**c**) fluid vertical velocity; (**d**) tube vertical velocity.

The maximum wave loads of different wave periods in the horizontal and vertical directions for both methods are shown in Figure 10a,b. The results indicate that the wave loads calculated by the two different methods are relatively close. For an SFT, which has a large horizontal scale, both the potential flow theory and Morison equation method can effectively calculate the wave loads on the structure. However, for future research, it is more important to focus on which method should be chosen to calculate wave loads in the simplified segment model to better map the dynamic responses of the entire-length SFT. Meanwhile, since most current research on SFT segment models adopt free-end boundaries, it is essential to ensure that the forces fit the fixed-end boundary conditions in practical engineering situations. Therefore, Model 3, with a fixed-end boundary, is employed as a reference, comparing the wave loads of Model 1 and Model 2 with free boundary conditions. The applicable conditions for the potential flow theory and Morison equation can be more accurately provided in calculations of the wave loads on the SFT. It is shown that, when the wave period is less than 20 s, i.e., when the ratio of structural diameter to wavelength (D/L) exceeds 0.03, more accurate results are provided by the potential flow theory. Conversely, when the D/L is less than 0.03, the Morison equation will be more accurate.

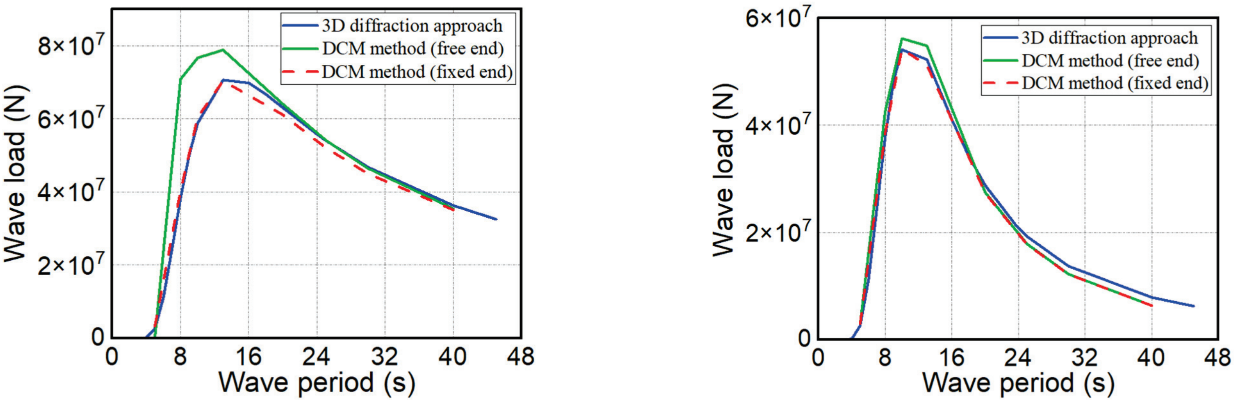

(**a**) (**b**)

Figure 10. (**a**) Horizontal wave loads; (**b**) vertical wave loads.

Furthermore, it is possible for the external excitation variable to be controlled by selecting wave periods that have similar wave load magnitudes for subsequent research, facilitating a better comparison of the two methods to investigate the impact of hydroelasticity deformation. Therefore, a wave period of 20 s is chosen as the wave condition in this research.

4.2. Comparison of Motion Responses

To compare the motion responses of the entire-length SFT, it is firstly necessary to determine the locations of the monitoring points of interest for the research. For the 3D diffraction method, the boundary element model assumes the structure as a rigid body, and since the pitch motion is minimal in the structural motion, only the motion of the structure's centroid is considered. Model 1 is always set with the free boundary condition, and by comparing it with Model 2, which also has a free boundary condition, the impact of hydroelasticity on motion responses can be studied. It can also be served as a reference for comparing Models 2 and 3 to study the effects of free- and fixed-end boundary conditions on the entire-length SFT. Additionally, since the hydroelasticity deformation of a 2000 m-long structure is considered in the DCM method, several monitoring points need to be determined for subsequent research. According to the static displacement of SFT shown in Figure 11, it is evident that different boundary conditions mainly affect the areas near the edge of the SFT. Since the SFT is a symmetric structure, three locations are chosen for this study: the mid-span, 500 m away from the mid-span, and 850 m away from the mid-span, denoted as P1, P2, and P3, respectively, to be served as monitoring points.

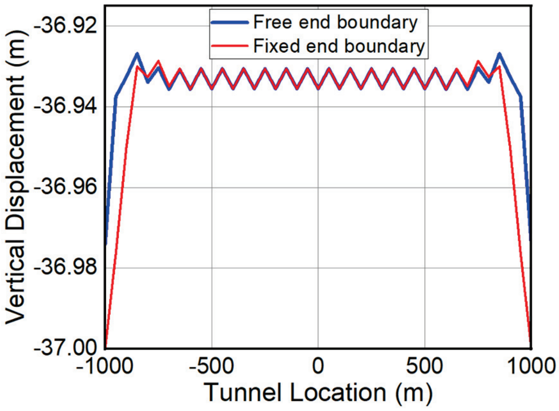

Figure 11. Static displacement of the numerical model based on the DCM method.

A regular wave with unit amplitude, a period of 20 s, and a 90° incidence angle perpendicular to the structure is applied in OrcaFlex. The vertical motion displacement of Model 1 and Model 2 are shown in Figure 12, while the vertical motion displacement of Model 1 and Model 3 are presented in Figure 13. Since it is in a deformation state transitioning from the edge of the SFT to a static equilibrium position, the displacement at P3, which is near the edge, is larger compared to other positions. Furthermore, the displacements at P1 and P2 are identical in both models with different end boundary conditions, which is consistent with their static displacement patterns. This reflects the displacement differences caused by hydroelasticity and end boundary conditions, demonstrating that the selected monitoring points are meaningful.

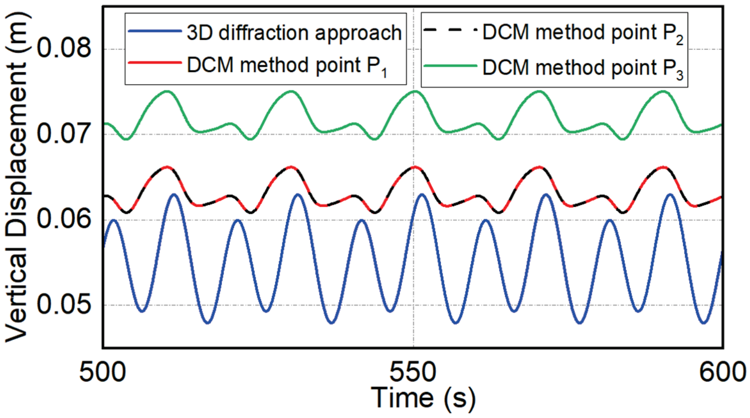

Figure 12. Vertical displacement of Model 1 and Model 2.

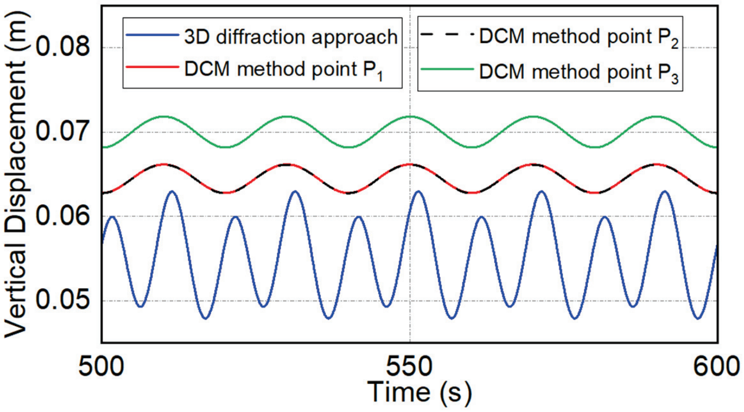

Figure 13. Vertical displacement of Model 1 and Model 3.

It can be observed that the amplitude of vertical displacement of Model 1 is 5% smaller than that at the mid-span position of Model 2 and 16% smaller than the maximum displacement at position P3. This is because the 3D diffraction method, based on the rigid-body assumption, does not consider the effect of hydroelasticity deformation in the vertical direction, resulting in a lower global movement position of the structure, which is similar to the movement situation at the end boundary position of Model 2. Moreover, this difference may cause the cable tension in Model 1 to be smaller, resulting in a larger motion magnitude.

Under the fixed-end boundary condition, it is noted that the motion amplitude of Model 3 is significantly reduced, with the maximum amplitude being recorded at 0.0718 m at position P3. In contrast, Model 2 has a larger amplitude, with the maximum displacement at position P3 being 0.0751 m, only 5% larger than that of Model 3. However, it is revealed through comparison of the amplitudes at positions P1 and P2 in both models that they are identical. This also proves that the amplitude of the motion response at various positions of the SFT under wave action is related to the displacement magnitude at the static equilibrium position.

Additionally, in Figure 12, there is a multi-frequency phenomenon in the motion response at each monitoring point, where the response frequency is always twice that of the wave. This is consistent with the findings of Yang et al. [29] in their experiments. The power spectral analysis results of vertical motion responses for different periods are shown in Figure 14a,b, indicating that the multi-frequency phenomenon is not affected, even when the wave period changes. This is because the vertical motion is coupled with the horizontal and roll motion. As shown in Figure 15, the roll and horizontal motions are nearly synchronous. When both increase, the cable tension increases, causing the SFT to move downward. Conversely, there are instances where the horizontal displacement of the SFT reaches zero twice within a wave period, as it oscillates left and right once each under the influence of regular wave. Whenever the displament is zero, the cables slacken, causing the structure to move upward, resulting in two peaks in the vertical motion. The vertical and horizontal motion trajectory of the tube mid-span are shown in Figure 16a. For the fixed-end boundary condition shown in Figure 13, the vertical and horizontal motion trajectory of the tube mid-span are shown in Figure 16b. The constraint at both ends results in very little horizontal and roll motion, thus almost eliminating this phenomenon. However, it can be anticipated that this phenomenon will still occur if the length of the SFT increases.

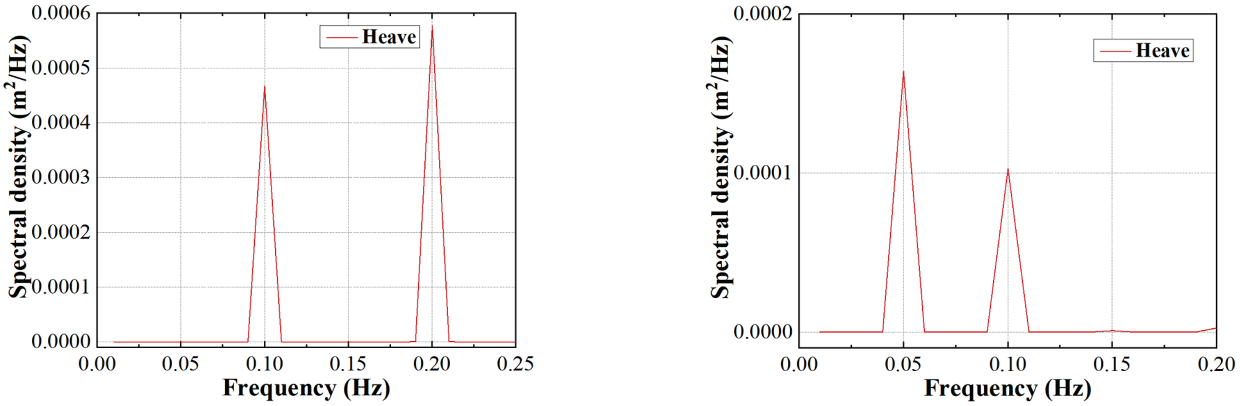

(**a**) (**b**)

Figure 14. (**a**) Spectral density under 10s wave period; (**b**) spectral density under 20s wave period.

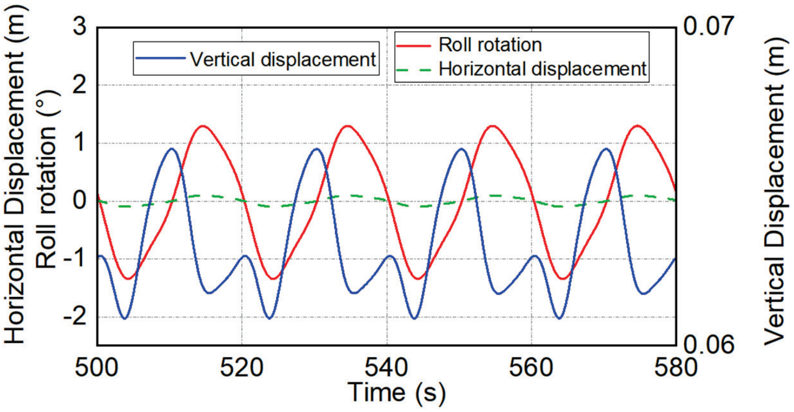

Figure 15. Coupling effect of motion response.

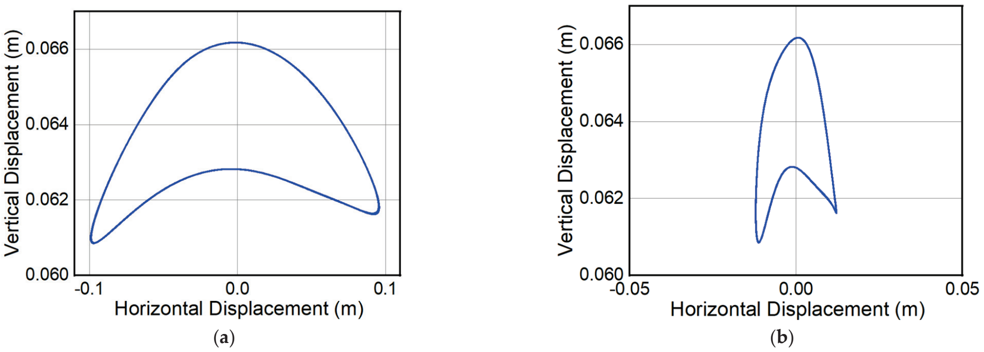

(**a**)
(**b**)

Figure 16. (**a**) Motion trajectory of Model 2; (**b**) motion trajectory of Model 3.

The horizontal motion responses of Model 1 and Model 2 are shown in Figure 17 and the horizontal motion responses of Model 1 and Model 3 are shown in Figure 18. It can be seen that, under free-end boundary conditions, the horizontal motion of the SFT is almost unaffected by hydroelasticity deformation, as identical displacement is evident at each point. Under fixed-end boundary conditions, the closer the displacement is to the edge, the greater the influence of the fixed ends becomes, leading to reduction in the displacement value. The horizontal motion amplitude of the SFT calculated based on Model 1 is 0.752 m, which is much greater than the 0.096 m at position P1 of Model 2. It is evident that the 3D diffraction method overestimates the horizontal displacement of the structure, possibly due to the smaller average position of the vertical motion leading to reduced cable tension. Therefore, it is necessary to compare the cable tension of the structure.

Additionally, under fixed-end boundary conditions, the motion amplitude of Model 3 is minimal at only 0.012 m. In contrast, the mid-span amplitude of Model 2 is 6.9 times greater than that of Model 3. Since the horizontal displacement differences in the SFT along the tube are relatively small, Figure 19a,b summarize the maximum horizontal values of positions along the tube of the two models under wave action. It can be seen that, under free-end boundary conditions, the horizontal displacement pattern of the SFT is still approximately the same as in the static equilibrium state. However, under the constraint of the fixed-end boundary, the horizontal displacement of the SFT is more restricted, with the maximum occurring at the mid-span and the minimum occurring at the two ends. This means that the constraint load of the end boundary has a significant impact on the global horizontal motion response of the SFT. The reason is that, unlike the vertical direction, which is subjected to substantial buoyancy, the SFT does not exhibit significant hydroelasticity deformation in the horizontal direction. Overall, all positions tend to move together under wave forces, and the end boundary constraints greatly limit this motion. Therefore, the choice of end boundary condition should be made carefully in related studies.

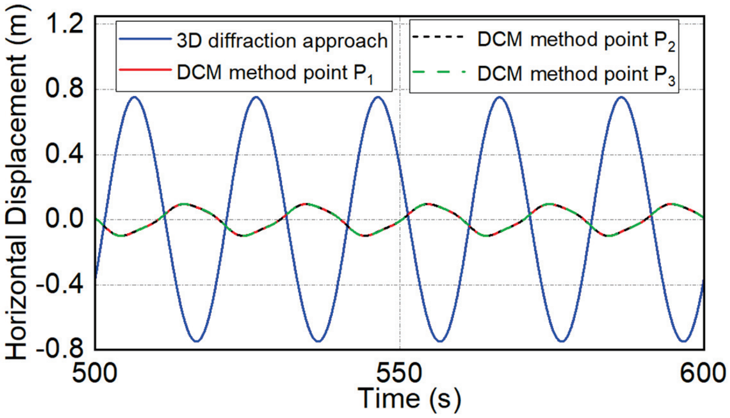

Figure 17. Horizontal displacement of Model 1 and Model 2.

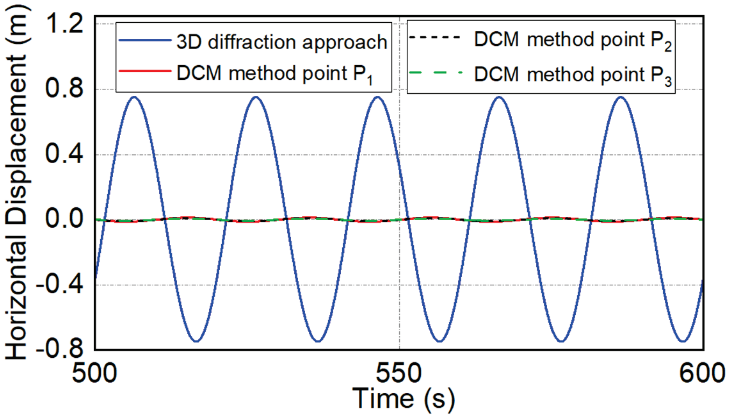

Figure 18. Horizontal displacement of Model 1 and Model 3.

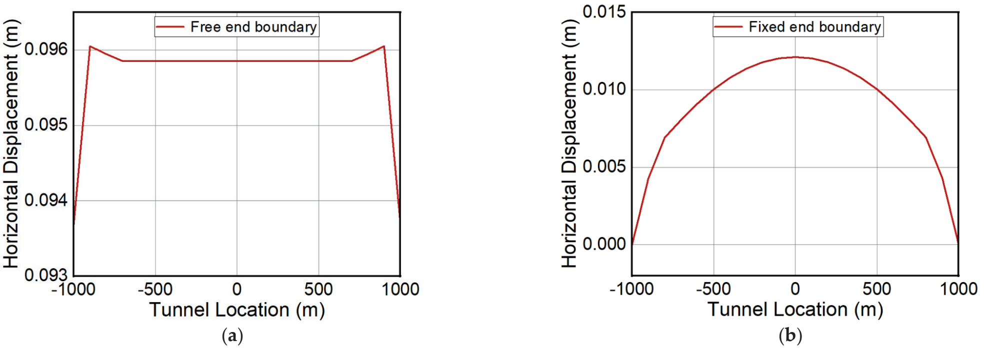

(**a**)

(**b**)

Figure 19. (**a**) Maximum horizontal displacement of each position of Model 2; (**b**) maximum horizontal displacement of each position of Model 3.

4.3. Comparison of Cable Tension

Static equilibrium calculation is firstly performed on the structure in OrcaFlex to determine the static equilibrium position of the SFT and the corresponding cable tension, as presented in Table 2. Since the mooring system is primarily utilized to counteract the substantial buoyancy of the SFT, vertical displacement has a significant impact on cable tension. For Model 1, which is based on the rigid-body assumption, vertical displacement is consistent throughout the static equilibrium state, resulting in identical anchor line tensions. Therefore, attention for the research is focused solely on the wave-facing anchor line Line32 at mid-span. In contrast, for Model 2, positive vertical deformation occurs throughout the tube due to hydroelasticity, except at the edges. This difference leads to greater vertical displacement of the SFT under wave action when hydroelasticity is considered, resulting in increased cable tension.

Table 2. Cable tension in static equilibrium position.

Cable Position	Model 1		Model 2		Model 3	
	Cable Tension (N)	Vertical Displacement (m)	Cable Tension (N)	Vertical Displacement (m)	Cable Tension (N)	Vertical Displacement (m)
Mid-span Line32	3.67×10^7	0.0614	3.85×10^7	0.0645	3.85×10^7	0.0645
500 m away Line37	3.67×10^7	0.0614	3.85×10^7	0.0645	3.85×10^7	0.0645
800 m away Line40	3.67×10^7	0.0614	3.94×10^7	0.0661	4.02×10^7	0.0674
900 m away Line41	3.67×10^7	0.0614	4.02×10^7	0.0675	3.01×10^7	0.05
Edge Line42	3.67×10^7	0.0614	1.66×10^7	0.0259	6.59×10^6	0

Furthermore, it can be observed that different end boundary conditions result in significant displacement variations at position P3 near the edge of the entire-length SFT based on the comparison between Model 2 and Model 3, along with Figure 11, which in turn causes notable differences in cable tension in the vicinity of the edge. It is noteworthy that, for Model 2, with a free-end boundary, the cable that is most affected is Line41, located 900 m from the mid-span, whereas for Model 3, with a fixed-end boundary, the most affected cable is Line40, situated 800 m from the mid-span. This discrepancy arises from the different end constraints, which result in variations in the distance required for the SFT tube to transition from the end boundary to the section where the vertical displacement is approximately consistent in the equilibrium position. Consequently, for Model 2, the primary focus is directed towards the cables Line32, Line37, and Line41, while, for Model 3, attention is directed towards the cables Line32, Line37, and Line40, with the cable positions being illustrated in Figure 20.

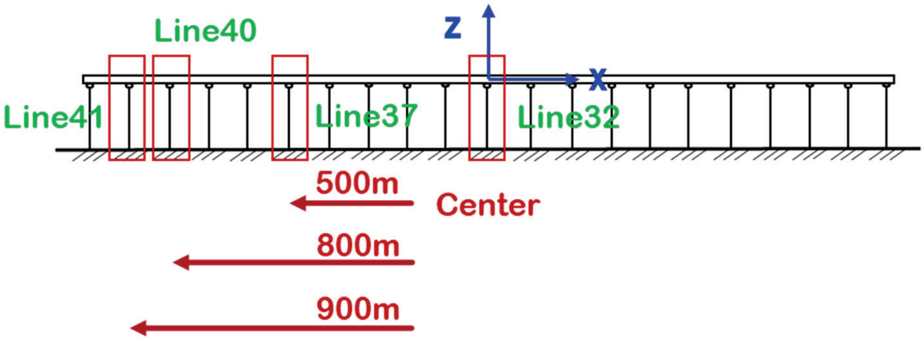

Figure 20. Location of the cables under investigation.

Subsequently, a regular wave with a unit amplitude and period of 20 s was applied perpendicularly to the SFT at 90° incidence. The cable tension of Model 1 and Model 2 is illustrated in Figure 21, while the cable tension of Model 1 and Model 3 is presented in Figure 22. The tension amplitude of the mid-span cable Line32 of the SFT, calculated based on Model 1, was found to be 6% lower than that calculated for Model 2 and 9.7% lower than the maximum tension cable Line41 in Model 2. This observation corroborates the findings in Section 4.2, which can be attributed to the lower average vertical motion position of Model 1, resulting in the reduced tension of the cables during SFT movement, thereby leading to lower cable tension.

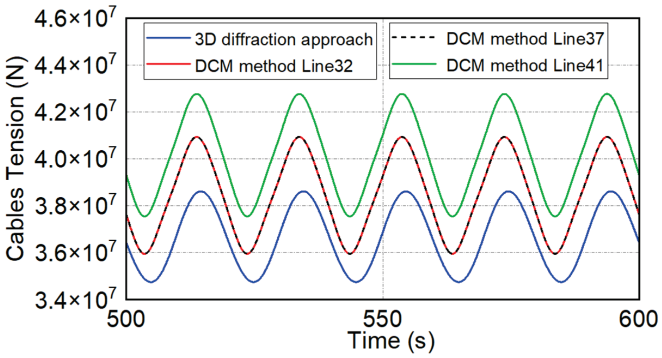

Figure 21. Cable tension of Model 1 and Model 2.

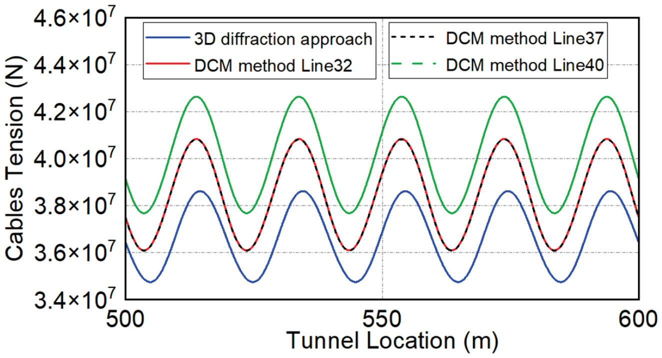

Figure 22. Cable tension of Model 1 and Model 3.

In summary, as illustrated in Figure 23, through comparison of Model 1 and Model 2, it is discovered that, when hydroelasticity effects are taken into account, there is a higher static equilibrium position and a vertical displacement of the SFT, which results in greater cable tension and, consequently, smaller horizontal displacement. As shown in Figure 24, by comparing Model 2 and Model 3, it is observed that, despite the differences in end boundary conditions, due to the large length-to-diameter ratio and redundant buoyancy of the entire-length SFT, the vertical displacement and cable tension conditions are found to be very similar. However, owing to the constraint of the end boundary, significant differences are observed between the two models in terms of horizontal displacement and the location of maximum cable tension.

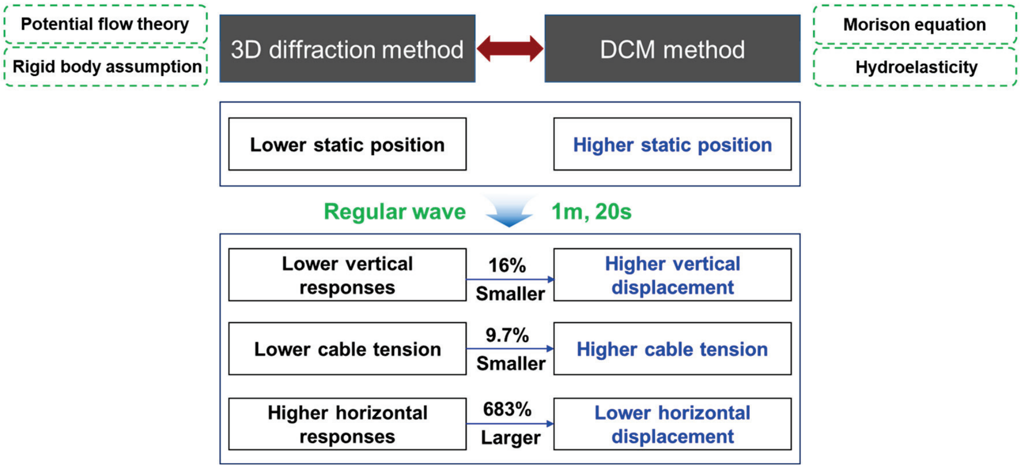

Figure 23. Comparison results of two methods.

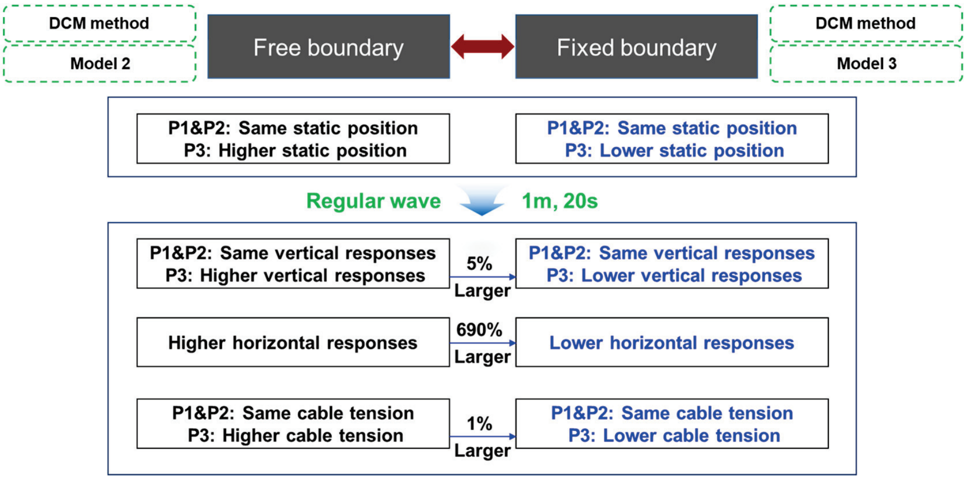

Figure 24. Comparison results of the two end boundary conditions.

5. Conclusions

In this study, the impact of hydroelasticity on the global dynamic responses of the SFT was investigated by comparing the 3D diffraction method based on rigid-body assumption and the potential flow theory with the DCM method while considering hydroelasticity effects based on the Morison equation. The reasonability of the commonly adopted free-end boundary condition was also examined by comparing models with free-end and fixed-end boundary condition established using the DCM method. The conclusions are as follows:

(1) For large-scale floating structures like an SFT, both potential flow theory and the Morison equation can be effectively used to calculate wave loads on the structure. When the ratio of structure diameter to wavelength (D/L) is greater than 0.03, the results calculated by potential flow theory are found to be more realistic. Conversely, when D/L is less than 0.03, the Morison equation is determined to be more in touch with reality.

(2) Under the influence of hydroelasticity, due to the effect of redundant buoyancy, there is a significant upward deformation in the vertical direction of an SFT. As a result, the SFT as a whole exhibits a higher static equilibrium position and larger vertical displacement under wave action, which leads to greater cable tension and consequently smaller horizontal displacement.

(3) Due to the large length-to-diameter ratio and the redundant buoyancy of the full-length SFT, it is feasible to use a simplified free-end boundary condition to simulate actual conditions when studying vertical displacement and cable tension. However, the constraint of the end boundary has a significant impact on the horizontal displacement of the SFT and the location of the maximum cable tension, which should be treated with caution in the related investigation.

However, there are considerable limitations to the present investigation. With the lack of experimental results for the entire-length SFT, the applicability of the wave load recommendations can only be inferred from the comparison with the model based on the fixed-end boundary constraints. In addition, the hydroelasticity effect of the 3D diffraction method was not considered in the comparison of the two methods and further development of suitable simulation methods is necessary in the future.

Author Contributions: Conceptualization, X.Y. and D.Q.; Methodology, D.Q. and L.W.; Software, X.Z. (Xiangbo Zhou); Validation, M.W.; Formal analysis, X.Z. (Xiangbo Zhou); Investigation, L.W.; Resources, X.Y. and D.Q.; Data curation, X.Z. (Xin Zhao); Writing—original draft, X.Z. (Xiangbo Zhou); Writing—review & editing, D.Q.; Supervision, X.Y., M.W., X.Z. (Xin Zhao) and L.W.; Project administration, X.Y. and X.Z. (Xin Zhao). All authors have read and agreed to the published version of the manuscript.

Funding: This work was supported by the National Key R&D Program of China [Grant No. 2022YFB2602800], and Science and Technology Projects of Liaoning Province [Grant No. 2023011352-JH1/110].

Institutional Review Board Statement: Not applicable.

Informed Consent Statement: Not applicable.

Data Availability Statement: Data are contained within the article.

Conflicts of Interest: Authors Xiangji Ye, Xin Zhao, Li Wang were employed by the company CCCC First Harbour Consultants Co., Ltd. The remaining authors declare that the research was conducted in the absence of any commercial or financial relationships that could be construed as a potential conflict of interest.

References

1. Jin, C.; Kim, M. Dynamic and structural responses of a submerged floating tunnel under extreme wave conditions. *Ocean Syst. Eng.* **2017**, *7*, 413–433.
2. Wu, Z.; Ni, P.; Mei, G. Vibration response of cable for submerged floating tunnel under simultaneous hydrodynamic force and earthquake excitations. *Adv. Struct. Eng.* **2018**, *21*, 1761–1773. [CrossRef]
3. Zucca, M.; Valente, M. On the limitations of decoupled approach for the seismic behaviour evaluation of shallow multi-propped underground structures embedded in granular soils. *Eng. Struct.* **2020**, *211*, 110497. [CrossRef]
4. Martinelli, L.; Domaneschi, M.; Shi, C. Submerged floating tunnels under seismic motion: Vibration mitigation and seaquake effects. *Procedia Eng.* **2016**, *166*, 229–246. [CrossRef]
5. Liu, Y.; Jin, R.J.; Geng, B.L.; Zhang, H.Q.; Ran, C. Influence of anchor cable inclination angle on motion response of submerged floating tunnel with different section. *Chin. J. Hydrodyn.* **2020**, *35*, 237–247.
6. Paik, I.Y.; Oh, C.K.; Kwon, J.S.; Chang, S.P. Analysis of wave force induced dynamic response of submerged floating tunnel. *KSCE J. Civ. Eng.* **2004**, *8*, 543–550. [CrossRef]
7. Jin, R.; Gou, Y.; Geng, B.; Zhang, H.; Liu, Y. Coupled dynamic analysis for wave action on a tension leg-type submerged floating tunnel in time domain. *Ocean Eng.* **2020**, *212*, 107600. [CrossRef]
8. Xu, G.; Chen, X.; Xue, S.; Townsend, J.F.; Chen, X.; Tang, M. Numerical assessment of non-uniform terrain and inhomogeneous wave–current loading effects on the dynamic response of a submerged floating tunnel. *Ocean Eng.* **2023**, *288*, 115942. [CrossRef]
9. Luo, W.; Huang, B.; Tang, Y.; Ding, H.; Li, K.; Cheng, L.; Ren, Q. Numerical simulation of dynamic response of submerged floating tunnel under regular wave conditions. *Shock Vib.* **2022**, *2022*, 4940091. [CrossRef]
10. Jeong, K.; Kim, S. Structural response of submerged floating tunnels with free-end boundary condition based on an analytical approach. *Appl. Ocean Res.* **2024**, *143*, 103861. [CrossRef]
11. Kunisu, H. Evaluation of wave force acting on submerged floating tunnels. *Procedia Eng.* **2010**, *4*, 99–105. [CrossRef]
12. Chung, W.C.; Jin, C.; Kim, M.; Hwang, J.Y. Comparison study and forensic analysis between experiment and coupled dynamics simulation for submerged floating tunnel segment with free ends under wave excitations. *CMES Comput. Model. Eng. Sci.* **2023**, *136*, 413–433. [CrossRef]
13. Yang, S.; Hu, Q.; Wu, Z.W.; Mou, L.W.; Wei, C.X. Dynamic response for submerged floating tunnel during local anchor cable breakage under wave and current load. *Ship Eng.* **2021**, *43*, 149–154.
14. Wu, Z.; Zhang, C.; Mou, L.; Mei, G.; Garg, A. Dynamic performance of submerged floating tunnel with different mooring styles subjected to anchor cable failure. *Front. Struct. Civ. Eng.* **2023**, *17*, 1443–1464. [CrossRef]
15. Zhou, X.-B.; Qiao, D.-S.; Wang, M.; Tang, G.-Q.; Lu, L.; Ou, J.-P. Global Dynamic Responses and Progressive Failure of Submerged Floating Tunnel under Cable Breakage Conditions. *China Ocean Eng.* **2024**, *38*, 676–688. [CrossRef]
16. Gao, J.; Mi, C.; Song, Z.; Liu, Y. Transient gap resonance between two closely-spaced boxes triggered by nonlinear focused wave groups. *Ocean Eng.* **2024**, *305*, 117938. [CrossRef]
17. Dong, M.-S.; Miao, G.-P.; Yong, L.-C.; Niu, Z.-R.; Pang, H.-P.; Hou, C.-Q. Effect of escape device for submerged floating tunnel (SFT) on hydrodynamic loads applied to SFT. *J. Hydrodyn.* **2012**, *24*, 609–616. [CrossRef]
18. Zou, P.X.; Bricker, J.D.; Uijttewaal, W.S.J. Impacts of extreme events on hydrodynamic characteristics of a submerged floating tunnel. *Ocean Eng.* **2020**, *218*, 108221. [CrossRef]
19. Xu, W.; Song, Z.; Liu, G.; Sun, Y. Numerical Analysis of the Impact Parameters on the Dynamic Response of a Submerged Floating Tunnel under Coupling Waves and Flows. *Sustainability* **2023**, *15*, 15241. [CrossRef]
20. Oh, S.H.; Park, W.S.; Jang, S.C.; Kim, D.H. Investigation on the behavioral and hydrodynamic characteristics of submerged floating tunnel based on regular wave experiments. *KSCE J. Civ. Environ. Eng. Res.* **2013**, *33*, 1887–1895. [CrossRef]
21. Mou, L.W.; Pan, L.F.; Xiao, Y.Y.; Wang, D.X.; Wu, Z.W.; Gu, B.T. Experimental investigation for dynamic response of submerged floating tunnel with different mooring styles under random waves. *Ship Eng.* **2022**, *44*, 172–178.
22. Pan, W.; Cui, C.; Chen, C.; Xie, M.; Gu, Q.; Yang, Z. Optimization Analysis of the Arrangement of the Submerged Floating Tunnel Subjected to Waves. *J. Mar. Sci. Eng.* **2024**, *12*, 764. [CrossRef]

23. Humamoto, T.; Fujita, K. Wet-Mode Superposition for Evaluating the Hydroelastic Response of Floating Structures with Arbitrary Shape. In Proceedings of the ISOPE International Ocean and Polar Engineering Conference, Kitakyushu, Japan, 26–31 May 2002. ISOPE-I-02-044.
24. Senjanović, I.; Tomić, M.; Tomašević, S. An explicit formulation for restoring stiffness and its performance in ship hydroelasticity. *Ocean Eng.* **2008**, *35*, 1322–1338. [CrossRef]
25. Kim, K.-H.; Bang, J.-S.; Kim, J.-H.; Kim, Y.; Kim, S.-J.; Kim, Y. Fully coupled BEM-FEM analysis for ship hydroelasticity in waves. *Mar. Struct.* **2013**, *33*, 71–99. [CrossRef]
26. Das, S.; Cheung, K.F. Hydroelasticity of marine vessels advancing in a seaway. *J. Fluids Struct.* **2012**, *34*, 271–290. [CrossRef]
27. Jin, C.; Kim, M.H. Time-domain hydro-elastic analysis of a SFT (submerged floating tunnel) with mooring lines under extreme wave and seismic excitations. *Appl. Sci.* **2018**, *8*, 2386. [CrossRef]
28. Kim, S.-J.; Jin, C.; Lee, I.; Kim, G.-J.; Kim, M.; Kwak, H.-G. Efficient time-domain approach for hydroelastic-structural analysis including hydrodynamic pressure distribution on a moored SFT. *Mar. Struct.* **2023**, *90*, 103402. [CrossRef]
29. Jin, C.; Kim, M.H. Tunnel-mooring-train coupled dynamic analysis for submerged floating tunnel under wave excitations. *Appl. Ocean Res.* **2020**, *94*, 102008. [CrossRef]
30. Jin, C.; Kim, G.-J.; Kim, S.-J.; Kim, M.; Kwak, H.-G. Discrete-module-beam-based hydro-elasticity simulations for moored submerged floating tunnel under regular and random wave excitations. *Eng. Struct.* **2023**, *275*, 115198. [CrossRef]
31. Yang, Z.; Li, J.; Zhang, H.; Yuan, C.; Yang, H. Experimental study on 2D motion characteristics of submerged floating tunnel in wave. *J. Mar. Sci. Eng.* **2020**, *8*, 123. [CrossRef]
32. Yang, Z.; Li, J.; Xu, Y.; Ji, X.; Sun, Z.; Ouyang, Q.; Zhang, H. Experimental study on the wave-induced dynamic response and hydrodynamic characteristics of a submerged floating tunnel with elastically truncated boundary condition. *Mar. Struct.* **2023**, *88*, 103339. [CrossRef]
33. Xiang, Y.; Chen, Z.; Yang, Y.; Lin, H.; Zhu, S. Dynamic response analysis for submerged floating tunnel with anchor-cables subjected to sudden cable breakage. *Mar. Struct.* **2018**, *59*, 179–191. [CrossRef]
34. Xiang, Y.; Chen, Z.; Bai, B.; Lin, H.; Yang, Y. Mechanical behaviors and experimental study of submerged floating tunnel subjected to local anchor-cable failure. *Eng. Struct.* **2020**, *212*, 110521. [CrossRef]
35. Wang, M.; Qiao, D.; Zhou, X.; Tang, G.; Lu, L.; Ou, J. Dynamic responses analysis of submerged floating tunnel under impact load. *Brodogr. Int. J. Nav. Archit. Ocean Eng. Res. Dev.* **2024**, *75*, 75208. [CrossRef]
36. Yuan, X.; Liu, J.; Zhou, J.; Guo, A. Effect of cable layout on hydrodynamic response of submerged floating tunnel under wave action. *Ocean Eng.* **2023**, *280*, 114257. [CrossRef]
37. Ding, H.; Huang, B.; Cheng, L.; Li, K.; Ren, Q. Hydrodynamic experiment of submerged floating tunnel under regular wave and current actions during construction period. *Mar. Struct.* **2024**, *93*, 103508. [CrossRef]
38. Seo, S.-I.; Mun, H.-S.; Lee, J.-H.; Kim, J.-H. Simplified analysis for estimation of the behavior of a submerged floating tunnel in waves and experimental verification. *Mar. Struct.* **2015**, *44*, 142–158. [CrossRef]
39. Chung, W.C.; Jin, C.; Kim, M.; Kim, S. Parametric Study on Mooring System Design of Submerged Floating Tunnel under Extreme Wave and Seismic Excitation. *J. Mar. Sci. Eng.* **2023**, *11*, 2357. [CrossRef]
40. Ghafari, H.; Dardel, M. Parametric study of catenary mooring system on the dynamic response of the semi-submersible platform. *Ocean Eng.* **2018**, *153*, 319–332. [CrossRef]
41. Li, B. Operability study of walk-to-work for floating wind turbine and service operation vessel in the time domain. *Ocean Eng.* **2021**, *220*, 108397. [CrossRef]
42. Yin, L.; Qiao, D.; Li, B.; Liang, H.; Yan, J.; Tang, G.; Ou, J. Modeling and controller design of an offshore wind service operation vessel with parallel active motion compensated gangway. *Ocean Eng.* **2022**, *266*, 112999. [CrossRef]
43. Chen, X.; Chen, Z.; Cai, S.; Xu, W.; Zhuo, X.; Lv, J.; Zhao, J. Numerical investigation of dynamic responses and mooring forces of submerged floating tunnel driven by surface wave. *Sci. Rep.* **2020**, *10*, 18836. [CrossRef]
44. Wu, Z.; Yang, S.; Tang, L.; Ma, H.; Mou, L.; Xiao, Y. Experimental investigation and analysis for hydrodynamic behaviours and progressive collapse phenomenon of submerged floating tunnel under anchor cables' breakage. *Ships Offshore Struct.* **2022**, *17*, 1924–1938. [CrossRef]
45. Kim, S.J.; Jin, C.; Kim, M.H. Dynamics of a moored submerged floating tunnel under tsunami waves. *Ocean Eng.* **2024**, *291*, 116333. [CrossRef]
46. Jin, C.; Bakti, F.P.; Kim, M.H. Time-domain coupled dynamic simulation for SFT-mooring-train interaction in waves and earthquakes. *Mar. Struct.* **2021**, *75*, 102883. [CrossRef]

Journal of
Marine Science and Engineering

Article

Failure Behavior and Surrounding Soil Stress Responses of Suction Anchor in Low-Strength Muddy Clay

Jiwei Luo [1,*], Xiaoqiang Liu [1], Xianpeng Liu [1], Dianjun Zuo [1], Xiaoyu An [1] and Liqiang Yu [2]

[1] National Engineering Research Center of Port Hydraulic Construction Technology, Tianjin Research Institute for Water Transport Engineering, Ministry of Transport, Tianjin 300456, China
[2] Hebei Construction & Investment Offshore Wind Power Co., Ltd., Tangshan 063611, China; hbjtyu@126.com
* Correspondence: luojiweim@126.com

Abstract: Anchorage failure of a suction anchor is more likely to occur in low-strength muddy clay. This paper focuses on the failure behaviors of suction anchors and muddy clay stress responses. The centrifugal model test was used to study the loading processes of suction anchors with various pulling angles. Firstly, the multi-stage developing process of anchoring force was analyzed according to the test results. Numerical modeling was used to validate the test results. The displacement of the suction anchor and muddy clay soil were analyzed using the numerical results. Then, the numerical and testing results were compared to analyze the horizontal soil pressure responses around the suction anchors. It was found that the change in loading direction affected the distribution and development of soil stress. The horizontal soil resistance played a crucial role in improving the bearing capacity. The soil stress variation and anchor displacement revealed that the suction anchors exhibited multi-attitude coupling movement during the inclined pulling. The vertical pulling suction anchor showed shear–slip failure behaviors, while the inclined pulling suction anchors showed compression–shear–slip coupling failure behaviors. The results of this study provide insight into the interaction mechanism between suction anchors and muddy clay, serving as a reference for the design and application of suction anchors.

Keywords: centrifugal model test; suction anchor; failure behavior; muddy clay

1. Introduction

With the development of anchoring technology in offshore engineering, suction anchors are extensively being used as deep water foundations [1,2]. A suction anchor is a cylindrical structure with a large diameter that is open at the bottom and closed at the top. The anchor is placed on the seabed and sinks into the soil under self-weight, thereby forming a closed environment. Subsequently, the internal water is pumped out, generating a considerable differential pressure. Then, the suction anchor is installed into the seabed gradually under pressure [3]. Installing a suction anchor is both cost-effective and convenient compared to piling in deep water, and a suction anchor can provide high bearing capacity. Suction anchors with taut wire have excellent stability and high deformation control accuracy, which can be used to tension leg oil platforms [4], floating wind turbines [5,6], and submerged floating tunnels [7].

The offshore floating structures experience a complex combination of wind, wave, and current loads [8], and all loads are transferred to the anchor foundation. Therefore, the bearing capacity of a suction anchor is vital for the safety of offshore structures, and this has become a hotspot of current research [9–13]. Researchers have focused on suction anchors' bearing capacity under static and dynamic loads. In terms of the loading direction effect, various studies have been conducted by researchers. Wang et al. [14] assessed the lateral bearing capacity of suction bucket foundation. Wang and Chen [15] focused on the suction caisson's vertical loading effect. Monajemi et al. [16] investigated the suction anchor's reaction under inclined loading.

For the bearing capacity under dynamic load, Li et al. [17] and Shen et al. [18] investigated the excess pore pressure accumulation around the suction anchor. Cheng et al. [19] utilized a stiffness degradation model to analyze the cyclic behavior of suction anchors. Previous studies [20–23] have shown that the bearing capacity of a suction anchor under dynamic load was 60 to 90 percent of that under static load. For the bearing capacity under static load, the previous research pays more attention to the length/diameter ratio (L/D) [2] and mooring position [24] of suction anchors, which significantly influences the bearing capacity. The mooring position, which ensures that the anchor purely translates, is known as the optimal loading point of suction anchors (i.e., when a horizontal or inclined load is experienced) [4]. However, loading on the optimal point is ideal. Slight rotation during the loading and deformation process of a suction anchor is inevitable and makes the mechanical behaviors of the suction anchor more complex.

A series of analytical methods, including upper bound plastic limit analyses [25], limiting equilibrium analyses [26], and vertical–horizontal (V-H) failure envelope analyses [9], are used to describe the bearing mechanism and calculation methods of suction anchors. Numerical simulation methods are applied to the parameter analysis of suction anchors. Koh et al. [27] analyzed the installation effect using a coupled effective stress–pore pressure large deformation finite element (LDFE) approach. Yang et al. [28] and Cheng et al. [29] analyzed suction anchors' bearing and failure performance based on numerical methods. Hu et al. [30] conducted numerical simulations to study the local scour around suction anchors. Analytical and numerical simulation methods have obtained many important results, which have greatly contributed to the design and construction technology of suction anchors. However, the mechanical analysis of suction anchors via theoretical analysis and numerical simulation is simplified, meaning that it may not accurately reflect the operational states of suction anchors.

In contrast, test methods play a crucial role in revealing the bearing capacity and mechanical state of a suction anchor. Saue et al. [31] and Utsunomiya et al. [32] reported suction anchors' installation and working effect using field test results. Wang and Li [33], Cheng et al. [34], and Lee and Do [35] performed a 1 g scale model test to study the deformation and loading capacity of suction anchors. Andersen et al. [36], Kim et al. [37], and Zhu et al. [38] conducted centrifugal model tests to study the installation process and pullout bearing performance of suction anchors. Among these test methods, the centrifugal model test can reflect the natural stress state of the seabed [39], which can accurately simulate the loading process of suction anchors using small models.

In summary, previous studies have obtained valuable insights into the bearing capacity of anchors. Investigations into the interaction mechanism between the seabed and the suction anchors have primarily been conducted through analytical methods and numerical simulations, which make it challenging to reflect the natural state of soil stress in the bearing capacity evolution of suction anchors. The research results regarding anchors in other forms, such as pile anchors [40] and plate anchors [41], provide significant references but cannot be applied to suction anchors directly.

Therefore, for this study, we used a centrifugal model test to investigate the bearing capacity of suction anchors in low-strength muddy clay. The evolution process of the anchoring force with different loading angles was analyzed based on the test results. Numerical modeling was used to validate the test results of anchoring force development, which also showed the displacement characteristic of the soil and suction anchor. The soil pressures around the suction anchors were analyzed based on a comparative numerical and testing analysis. The centrifugal test results revealed the interaction mechanism between a suction anchor and muddy clay soil, and the influence of the loading direction on the interaction mechanism was investigated. The failure behaviors of suction anchors were clarified according to the anchoring force development, the anchor movement, and the mechanical responses of the muddy clay soil.

2. Design and Implementation of Centrifugal Model Test

2.1. Model Scale and Main Design Scheme

In this paper, the centrifugal model test was carried out to study the interaction between suction anchors and muddy clay soil. The test was conducted in the centrifuge laboratory of Tianjin Research Institute For Water Transport Engineering, Ministry of Transport. The TK-C500 geotechnical centrifuge used in the test (shown in Figure 1) has an effective capacity of 500 g·t.

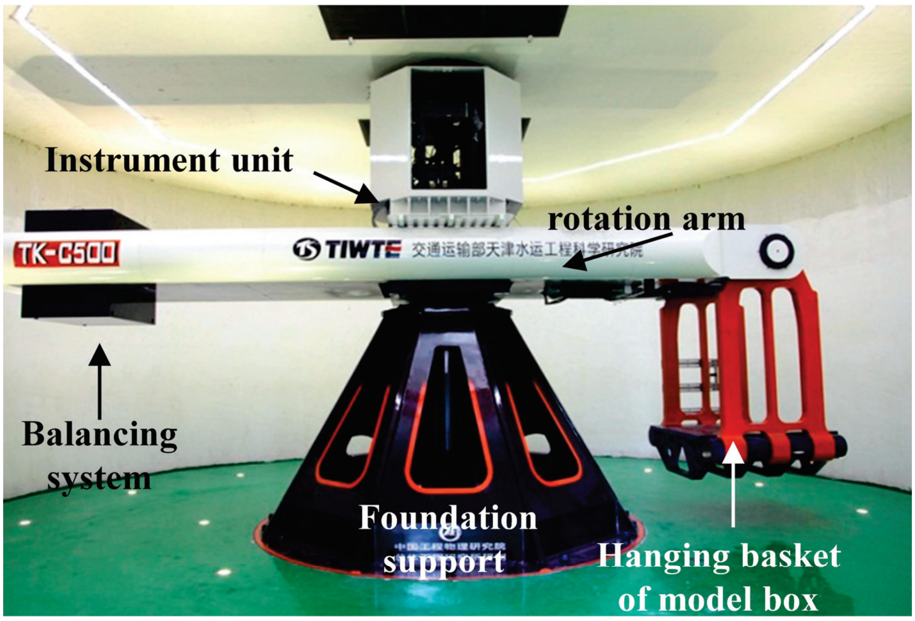

Figure 1. The TK-C500 geotechnical centrifuge used for the model test.

Geotechnical centrifuge modeling works by creating in situ soil stresses on a reduced model scale but at higher centrifugal acceleration [42]. The similarity principle is shown in Equation (1).

$$\rho g h = \rho \times \mathrm{n} g \times h/\mathrm{n} \tag{1}$$

where ρ is the soil density, g is the gravitational acceleration, h is the prototype dimension, ng is the centrifugal acceleration, h/n is the model dimension, and n is the model scale. When the centrifugal acceleration increases to ng, the in situ stress becomes equal for both the reduced-scale model and full-scale prototype. Table 1 shows the similarity relationship between the model and prototype.

Table 1. Similarity relationship of model and prototype.

Parameters	Units	Model/Prototype
Acceleration	m/s^2	n/1
Linear dimensions	m	1/n
Stress	kPa	1/1
Strain	-	1/1
Density	Kg/m^3	1/1
Force	N	$1/n^2$
Bending moment	N·m	$1/n^3$
Axial rigidity	N	$1/n^2$
Flexural rigidity	$N{\cdot}m^2$	$1/n^4$
Consolidation time	s	$1/n^2$
Permeability coefficient	m/s	n/1
Viscosity coefficient	Pa·s	1/1
Seepage time	s	$1/n^2$

The arrangement of the suction anchors for the centrifugal model test is shown in Figure 2. The pulling angles were set to 90°, 69°, and 51°, respectively, to investigate the influence of loading direction on the bearing capacity and failure behaviors of the suction anchors. In the 90° vertical pulling test, the loading position was at the top center of the suction anchor to maintain coaxial with the anchor body. The optimal loading point is at the lower part for suction anchors subject to horizontal or inclined load. Therefore, the loading position was 160 mm from the bottom of the suction anchor in the 69° and 51° inclined pulling tests, which differed from the vertical pulling test. Since the suction anchors' displacement values were much smaller than the cable length, the loading angle change was relatively small and considered negligible in the inclined pulling test.

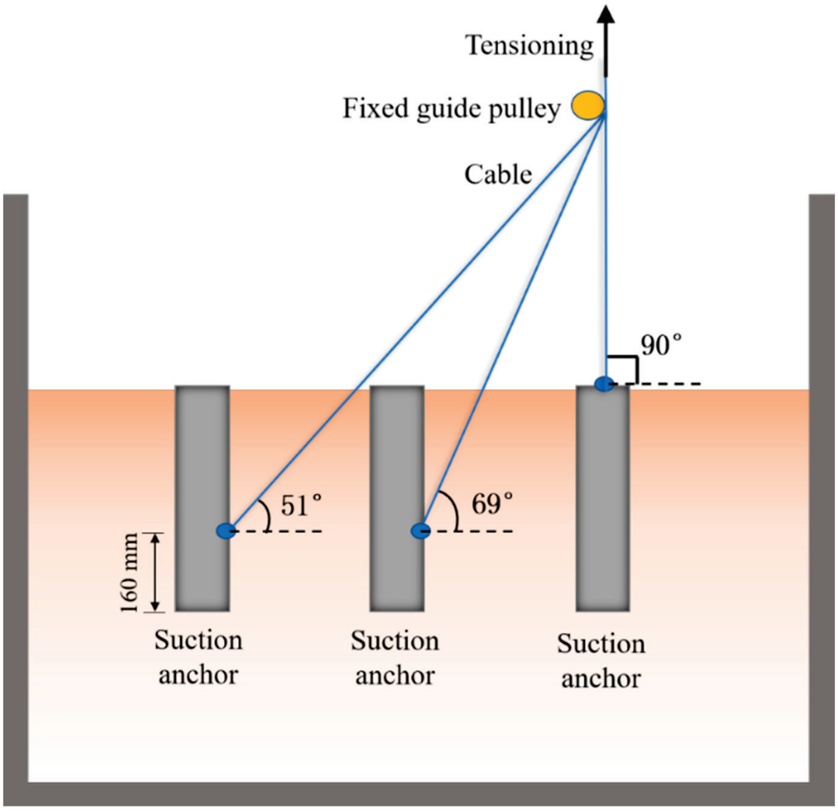

Figure 2. Arrangement of suction anchors in centrifugal model test.

In the centrifugal model test, a relatively small model scale is helpful, as this can improve the test's accuracy. Therefore, a model scale of n = 50 was chosen based on various factors, including the structural characteristics of the suction anchors, the size of the model box, the pulling angle, the space demands of the loading device, and the boundary conditions. The centrifuge acceleration was set to 50 g according to the similarity principle. The parameters of the prototype and the model suction anchor are shown in Table 2. The model anchor was a thin-walled cylinder with a diameter of 80 mm and a thickness of 0.8 mm. The top was closed with a reserved small hole for vacuum pumping, and the bottom was open, as shown in Figure 3a. The cable was attached to the anchor top or body through a padeye.

Table 2. Testing parameters of prototype and model suction anchors.

	Diameter *D*	**Length *L***	**Thickness *t***	**Material**	**Elastic Modulus**	**Similarity Ratio**
Prototype suction anchor	4 m	20 m	40 mm	steel	210 GPa	1:50
Model suction anchor	80 mm	400 mm	0.8 mm			

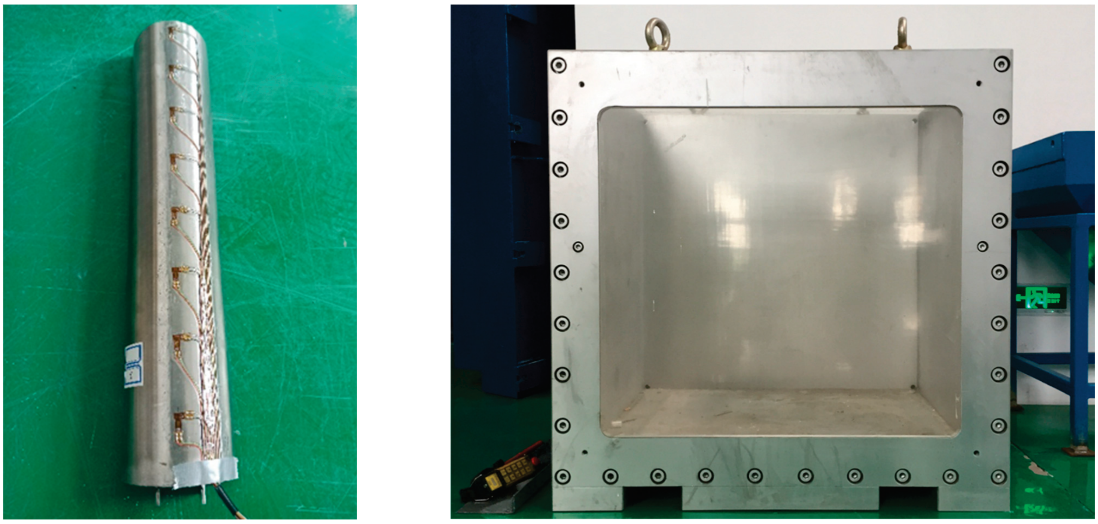

(**a**) (**b**)

Figure 3. The model box and suction anchor in the test: (**a**) the model suction anchor; (**b**) the model box.

2.2. Test Equipment and Preparation

In the test, the model box had a bottom size of 1000 × 1000 mm, and the simulated range was 50 × 50 m, according to the model scale of n = 50. The thickness of the model soil was 700 mm, and the simulated seabed depth was 35 m. The model box is shown in Figure 3b.

The pressure cells were used to measure the soil pressure around the suction anchor. For the suction anchor experiencing inclined pulling, two groups of pressure sensors were arranged on each side of the anchor, with a vertical arrangement of six sensors per group. The pressure cell distribution is shown in Figure 4. Considering the horizontal movement of the suction anchor, the front pressure cells may be disturbed by the anchor body in the loading process. Hence, the front pressure cells were arranged with larger spacings to deal with the impact of anchor movement. The cable was made of steel wire rope, and a strain gauge unit measured the cable force.

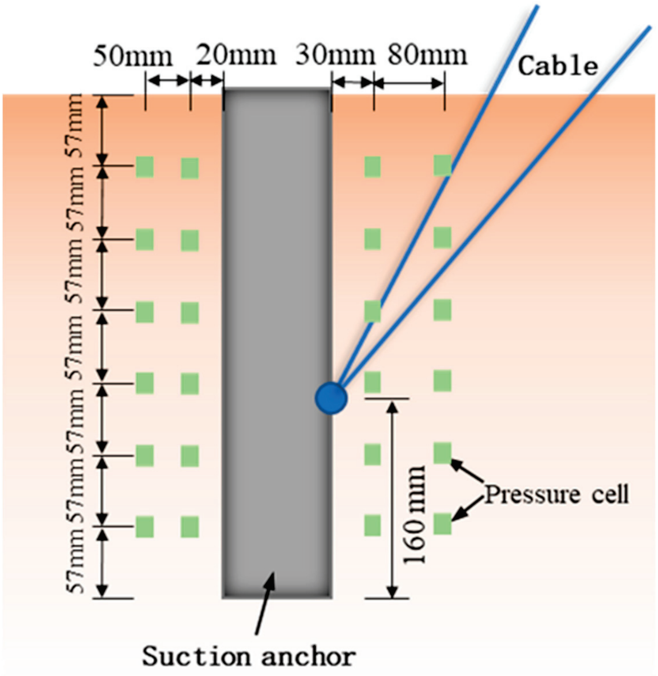

Figure 4. Arrangement of pressure cells around the suction anchor.

The low-strength muddy clay seabed model was made of kaolin. The vane shear test was used to evaluate the consolidated soil strength. The test results (Figure 5) showed that the undrained shear strength of the surface layer was about 10 kPa, and the strength at a depth of 400 mm nearly reached 50 kPa. The soil strength distribution in the model is shown in the following formula:

$$S_u = S_{u0} + kz \tag{2}$$

where S_u is the undrained shear strength, kPa; S_{u0} is the undrained shear strength of surface soil (the average linear fitting value of four groups' test data is $S_{u0} = 8.75$ kPa); k is the strength gradient (the average linear fitting value of four groups' test data is $k = 0.935$ kPa/m); z is the soil depth, m.

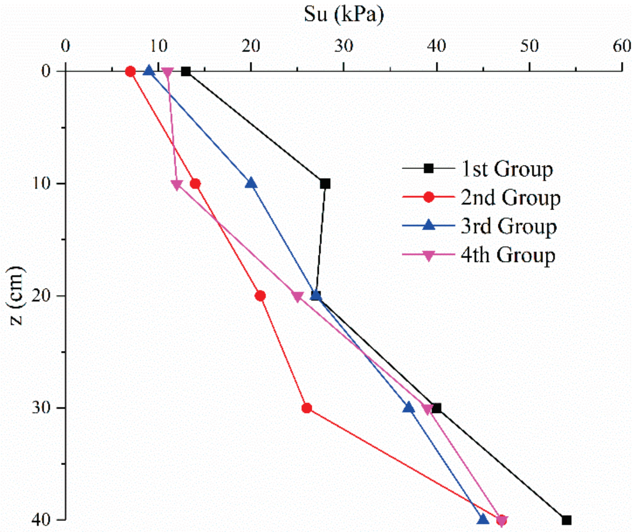

Figure 5. The undrained shear strength of muddy clay in the centrifugal model test.

The sinking process of the suction anchor was simulated to reflect its natural working state. The reserved hole on the top of the suction anchor was connected to the vacuum pump via a rubber pipe. The negative pressure caused by the vacuum was applied to the suction anchor. Then, the suction anchor gradually sunk into the clay to the predetermined position, as shown in Figure 6.

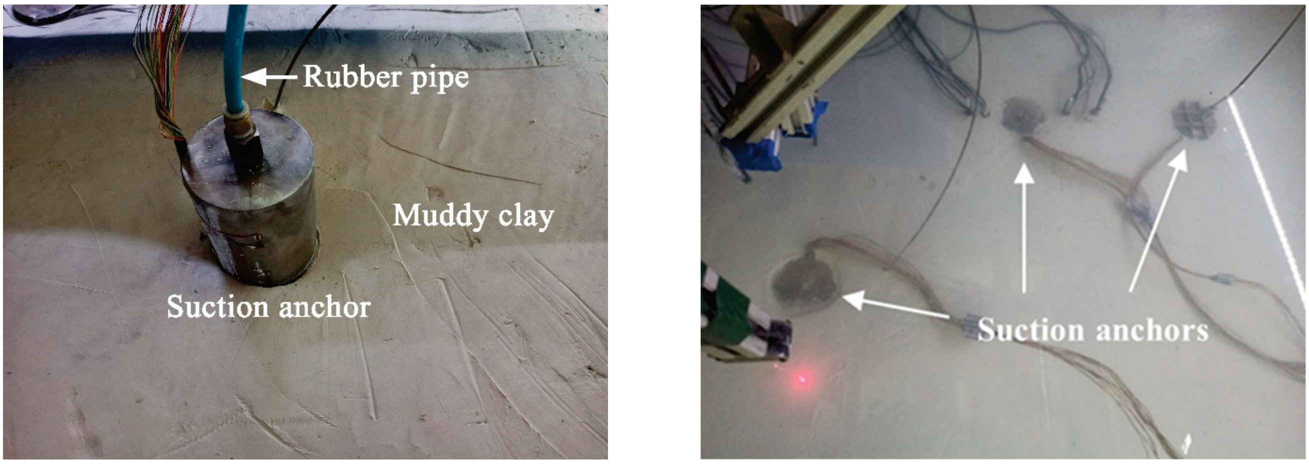

(**a**) (**b**)

Figure 6. Installation of the model suction anchor: (**a**) suction anchor sinking process; (**b**) suction anchor distribution in the model box.

A camera was arranged on the top side of the model box, as shown in Figure 7, to capture the motion pattern and failure behaviors of the suction anchor in the loading process. Tension sensors were set at the bottom of the loading device to test the pulling load. The loading device was directly connected to the suction anchor through the cable in the vertical pulling test. The pulley was used to guide the cable tensioning direction in the inclined pulling test, as shown in Figure 7.

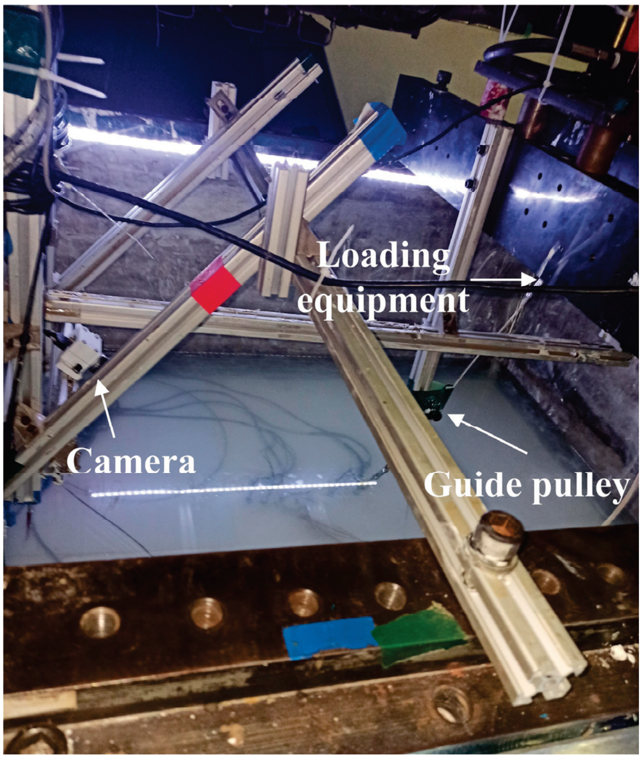

Figure 7. Loading device in model test.

2.3. Geotechnical Centrifuge Operation and Model Loading

The geotechnical centrifuge was started after the installation of the test device. The gravity acceleration of the model was gradually increased to 50 g. Once all sensor data were stable under 50 g acceleration, the pulling test of the suction anchors was conducted. Then, a fixed speed load of 0.06 mm/s was applied to the suction anchor. The tensioning force of the cable and horizontal soil pressures around the inclined pulling suction anchors were constantly monitored in the loading process. The loading stopped until the suction anchors reached the maximum bearing capacity and showed a slowly stable decrease in bearing capacity. Finally, the monitoring equipment and the geotechnical centrifuge were closed and the model test was completed.

3. Loading Failure Process and Mechanical Behavior of Suction Anchor

3.1. The 90° Vertical Pulling Test

This paragraph describes the behavior of a suction anchor that has been subjected to a 90° vertical pulling load. The anchoring force and displacement of the suction anchor are shown in Figure 8. Initially, the anchoring force was 0 when the anchor cable was relaxed. Then, the anchoring force increased rapidly with the loading displacement after the cable was tensioned. The anchoring force increased linearly when it was within 70% of the maximum value. The average growth rate $\Delta F/\Delta D$ of the anchoring force was 0.194 kN/mm. Afterward, the force growth rate gradually declined. The rapid growth stage ended when the anchoring force reached 95% of the maximum value, with an average growth rate of 0.098 kN/mm. Then, the anchoring force gradually increased to the maximum value of 1.007 kN, and the vertical displacement reached 7.465 mm. The anchoring force slowly fluctuated and decreased after crossing the maximum value, which remained close to the maximum. Then, the anchoring force significantly declined to 0.987 kN, with an average rate of −0.019 kN/mm. Finally, the anchoring force showed a relatively stable and slow decline stage, with an average decline rate of -2.77×10^{-3} kN/mm. The suction anchor was gradually pulled out of the muddy clay soil at this stage, and the contact area between the anchor body and the soil decreased. Therefore, the anchoring force decreased until the suction anchor was pulled out of the soil and lost its bearing capacity.

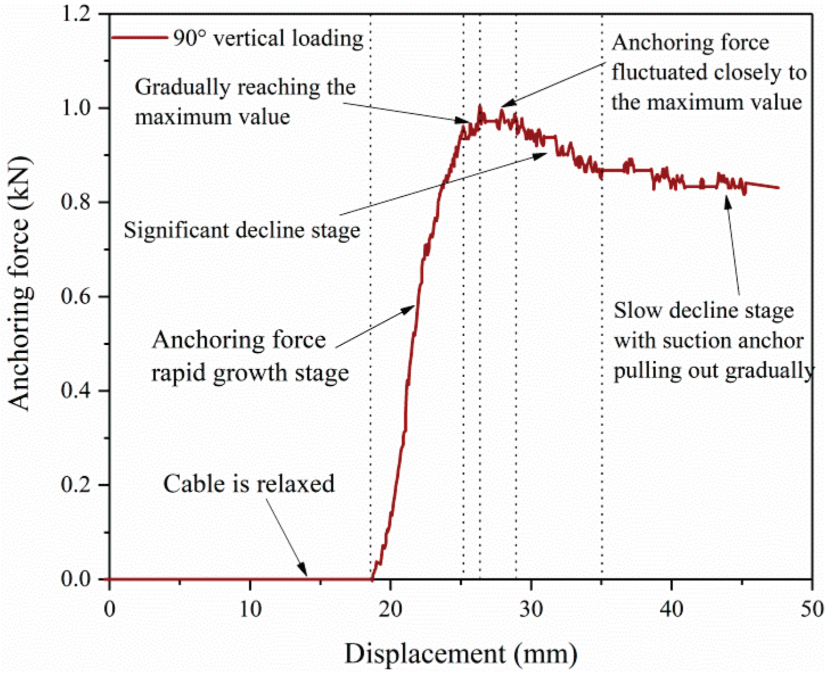

Figure 8. Anchoring force and displacement of the suction anchor in the 90° pulling test.

According to the model similarity theory, the anchoring force of the prototype suction anchor can be calculated using the following equation. The maximum anchoring force of the prototype suction anchor was 2517.5 kN.

$$\frac{F_P}{F_M} = \mathrm{n}^2 \tag{3}$$

where F_P is the anchoring force of the prototype suction anchor, F_M is the anchoring force of the model suction anchor, and n = 50 is the model similarity ratio.

3.2. The 69° Inclined Pulling Test

The anchoring force and displacement of the suction anchor under a 69° inclined load are shown in Figure 9. The reserved cable length between the loading device and suction anchor was insufficient. The muddy clay soil was secondarily consolidated with high gravity while the centrifuge accelerated to 50 g. The muddy clay soil and suction anchor showed secondary settlement and caused cable tensioning. Consequently, the initial anchoring force was not zero but 0.069 kN during the loading process. Upon the application of the pulling load, the anchoring force increased rapidly to the maximum value of 1.181 kN, with an average growth rate of 0.142 kN/mm. The anchoring force of the prototype suction anchor, calculated using Equation (3), was 2952.5 kN. Afterwards, the anchoring force fluctuated with the increase in displacement. It approached the maximum value until the bearing capacity began to decrease. Then, the anchoring force showed a significant decline stage, with an average rate of -9.22×10^{-3} kN/mm. Finally, the anchoring force experienced a slow decline stage, and the average rate was −0.00169 kN/mm. The bearing capacity decreased with the decrease in contact area between the anchor and muddy clay.

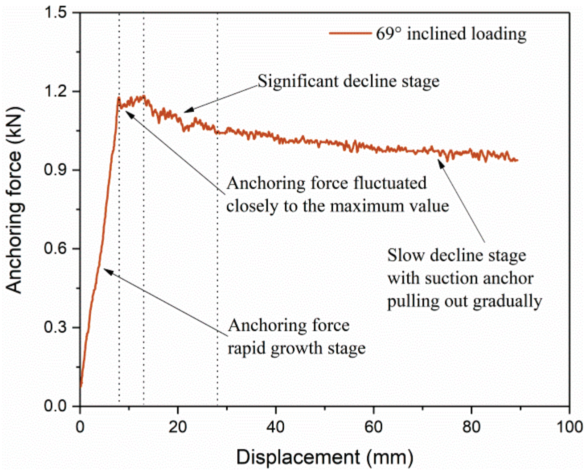

Figure 9. Anchoring force and displacement of the suction anchor in the 69° pulling test.

3.3. The 51° Inclined Pulling Test

Figure 10 shows the anchoring force and displacement of the suction anchor under a 51° inclined load. The cable was initially relaxed and buried in the muddy clay soil and gradually reached the tension state, overcoming the soil resistance. The anchoring force was small in the early stage of the pulling test. Then, the pulling load was transferred to the suction anchor after the cable was tensioned. The anchoring force increased rapidly to 95% of the maximum value, with an average growth rate of 0.108 kN/mm. The growth rate of the anchoring force was slightly lower at an earlier time of the rapid growth stage, mainly because the cable in the soil had not been fully tensioned and straightened. After the cable was fully straightened, the anchoring force increased more rapidly with the displacement. Subsequently, the anchoring force fluctuated to the maximum value of 1.458 kN, and the converted force of the prototype suction anchor was 3645.0 kN. It differed from the other two tests in that the anchoring force did not significantly decline after reaching the maximum value while displaying a slow decline stage directly with an average rate of -2.05×10^{-3} kN/mm.

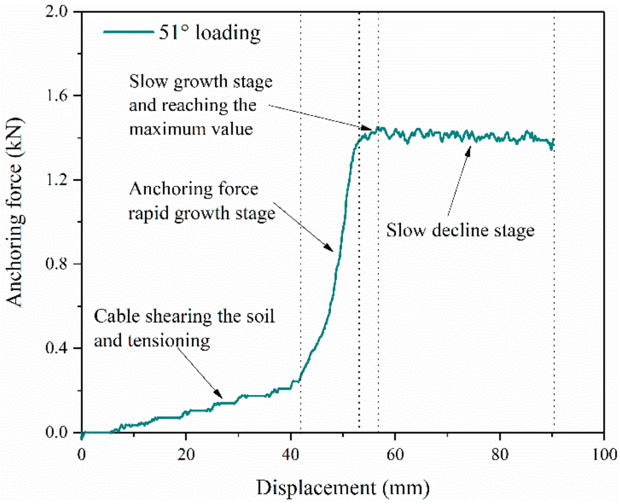

Figure 10. Anchoring force and displacement of the suction anchor in the 51° pulling test.

3.4. Influence of Loading Direction on Bearing Capacity of Suction Anchor

Comparing the test results, it is evident that the loading direction significantly impacts the bearing capacity of the suction anchor. The maximum anchoring force of the model and prototype suction anchors in each test is shown in Table 3.

Table 3. Test results related to the maximum anchoring force.

Test Group	Size (L × D × t)	90° Loading	69° Loading	51° Loading
Model suction anchor	400 × 80 × 0.8 mm	1.007 kN	1.181 kN	1.458 kN
Prototype suction anchor	20 × 4 × 0.04 m	2517.5 kN	2952.5 kN	3645.0 kN

For the prototype suction anchor, the bearing capacity in the 69° inclined pulling test was 435.0 kN larger than that in the vertical pulling test, which showed an increase of 17.3%. Moreover, the bearing capacity of 51° pulling was 1127.5 kN larger than that in the vertical pulling test, which showed an increase of 44.8%. The bearing capacity of the suction anchor increased, with the loading direction tending to be horizontal. When subjected to an inclined pulling load, the bearing capacity of the suction anchor was significantly improved due to horizontal soil pressure. The lateral soil pressure's contribution to the bearing capacity increased with the decrease in loading angle. Therefore, when the suction anchor is subjected to an inclined pulling load, the horizontal soil pressure is critical to the interaction between the suction anchor and the muddy clay soil.

3.5. Numerical Modeling on the Prototype Suction Anchor Used in the Centrifugal Model Test

The 3D finite difference software based on fast lagrangian analysis of continua, FLAC3D, was used for the numerical modeling of the prototype suction anchor. The model was created with 60,925 zones and 66,540 grid points, and its meshing and geometry shown in Figure 11. The *x*–*y*–*z* dimensions of the model were 40 m, 40 m, and 40.5 m, respectively. The normal displacements of the lateral boundaries were fixed, and the *x*-*y*-*z* displacements of the bottom boundary were fixed. The suction anchor was installed in the model's center along the z-axis. The Mohr-Coulomb constitutive model was used for the muddy clay soil, and the Elastic constitutive model was used for the suction anchor. The Interface Elements built into the FLAC3D software were used to model the contact surface between the suction anchor and the soil, which can be sheared and slid. The cable structure elements (cableSELs) were used to model the cable in the test. The parameters of the muddy clay soil and suction anchor are shown in Table 4.

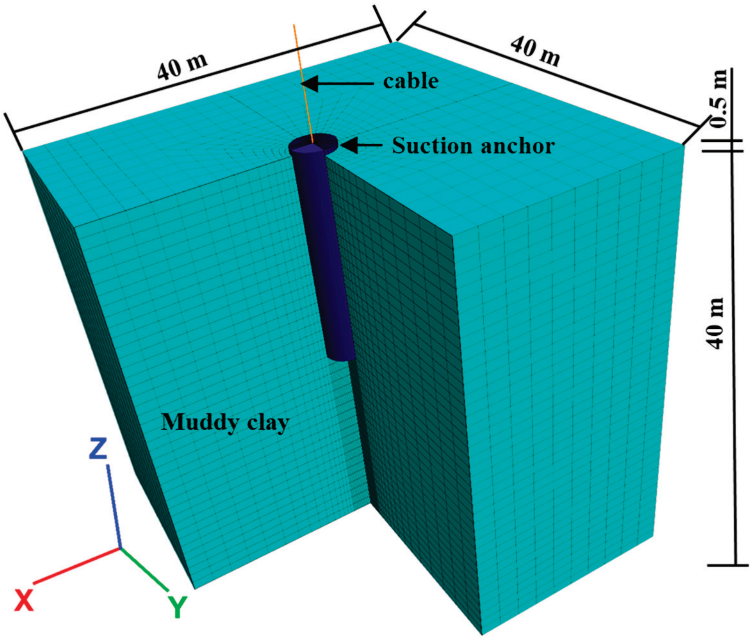

Figure 11. Numerical model of prototype suction anchor and muddy clay soil.

Table 4. Parameters of muddy clay soil and suction anchor.

	Muddy Clay Soil				Suction Anchor	
Parameter	**c/kPa**	**φ/°**	**E/MPa**	**ν**	**E/GPa**	**ν**
Value	8.75	3.57	0.85	0.50	205	0.275

According to the similarity principle, the prototype suction anchor's numerical results can be compared to the prototype results converted from the test [13,37]. The anchoring force and displacement of the prototype suction anchor can be obtained from the test results based on the similarity relationship shown in Table 1. The load–displacement curves obtained from centrifugal model tests and numerical simulations are compared in Figure 12. The numerical results demonstrated that the initial anchoring force increased linearly with loading. The growth rate of anchoring force decreased with continuous loading, and the suction anchor gradually reached the maximum bearing capacity. Subsequently, the anchoring force significantly declined until it reached a stable stage, indicating that anchoring failure had occurred. The load–displacement characteristics were consistent between the testing and numerical results. There was a rapid growth stage of anchoring force, a slower increasing stage, a significant decline stage after reaching the maximum value, and a relatively stable stage, with anchoring failure in both curves. The bearing capacity obtained from the centrifugal test and numerical simulation showed the same trend as the variation in the loading angle. The maximum anchoring force of the testing results was close to the numerical results, with the same loading angle. The above results showed that the centrifugal testing results are consistent with the numerical modeling results. Therefore, the centrifugal testing results are reliable.

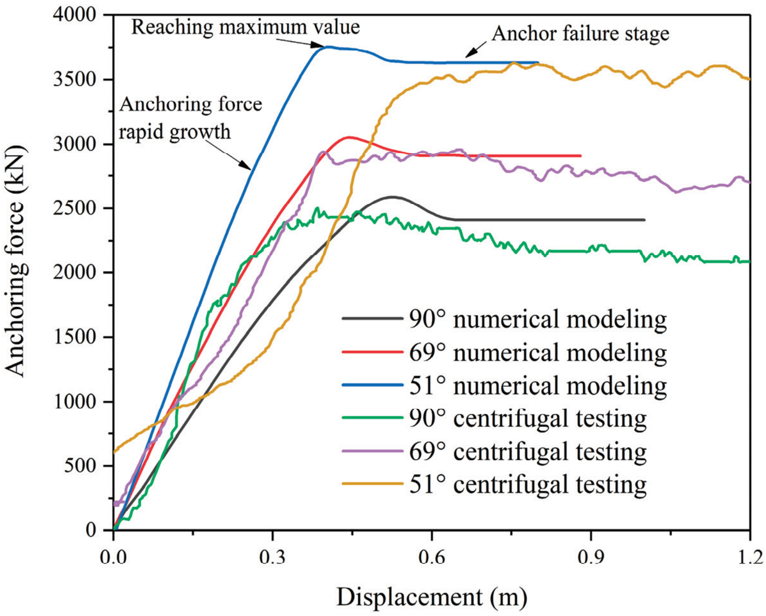

Figure 12. Load–displacement curves of centrifugal model test and numerical modeling.

Figures 13 and 14 show the vertical and horizontal displacement of the muddy clay soil and suction anchor during the loading process. The soil displacement during the 90° vertical loading presented a symmetrical distribution. As the anchoring force increased, the soil mainly moved vertically, and the soil closer to the suction anchor experienced greater displacement. The soil exhibited significant vertical displacement, with the anchoring force reaching the maximum value. After that, the soil displacement showed slight increases as the anchor entered a failure state. This indicates that the soil could no longer provide sufficient resistance for the suction anchor. During the 90° loading process, the horizontal displacement of the soil was minimal. While loading to failure, the vertical displacement of the suction anchor was much greater than that of the soil. This suggests that the contact surface between the suction anchor and the soil underwent slip failure. In the 69° loading model, the soil displacement in front of the suction anchor (the right side) was more significant than the rear. The soil displacement rapidly increased until the anchoring force reached its maximum value. Afterward, the soil displacement developed slightly as the suction anchor was loaded to failure. Compared to the 90° loading, the vertical displacement decreased while the horizontal displacement increased. The vertical displacement of the suction anchor was significantly greater than the soil's. The movement of the suction anchor was characterized by pulling upward to sliding and slight forward and slight backward rotation. In the 51° loading model, the asymmetric displacement distribution was further enhanced. The soil displacement showed rapid accumulation, with the anchor loading to its maximum bearing capacity. Then, the horizontal deformation of soil continued to increase, while the vertical deformation increased less until reaching the failure stage. Compared to 69° loading, the vertical displacement of the suction anchor and soil in the same loading stage decreased while the horizontal displacement continued to increase. The suction anchor also showed a slight increase in inclination. It can be concluded that the failure deformation of the suction anchor with inclined loading is pulling upward to sliding, accompanied by slight horizontal displacement and inclined deformation.

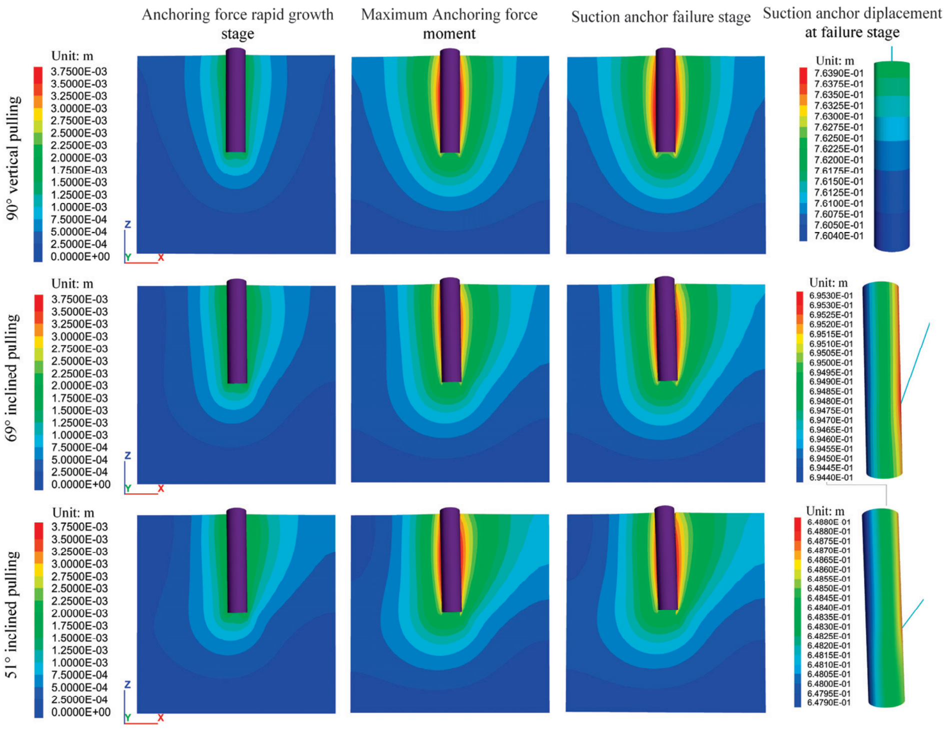

Figure 13. Vertical (z-axis) displacements of muddy clay soil and suction anchor.

The distribution of horizontal soil pressure (σ_{xx}) during the loading process is shown in Figure 15. The horizontal soil pressure barely changed in the 90° loading model because the suction anchor showed vertical sliding failure and had little squeezing effect on the soil. During the 69° loading, the soil pressure in front of the anchor increased significantly with the increase in loading force, while the back soil pressure decreased. This indicates that the horizontal movement of the anchor resulted in soil compression. There were slight changes in soil pressure during the loading from maximum anchoring force to the failure stage. The changing characteristics of soil pressure were similar in the 51° and 69° pulling processes, while the variation of soil pressure was more significant in the 51° loading model. This indicates that the anchor had a more significant squeezing effect on the soil in the horizontal direction. As the loading direction tended to be horizontal, the suction anchor compressed the soil laterally. This caused the horizontal pressure of the soil to increase, providing resistance for the anchor. As a result, the suction anchor could achieve a greater bearing capacity.

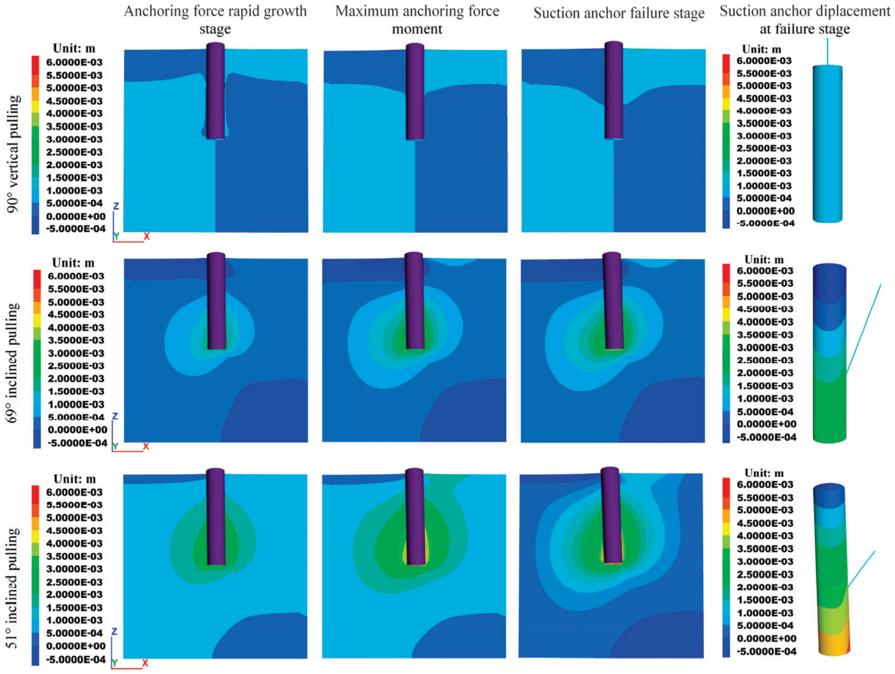

Figure 14. Horizontal (x-axis) displacements of muddy clay soil and suction anchor.

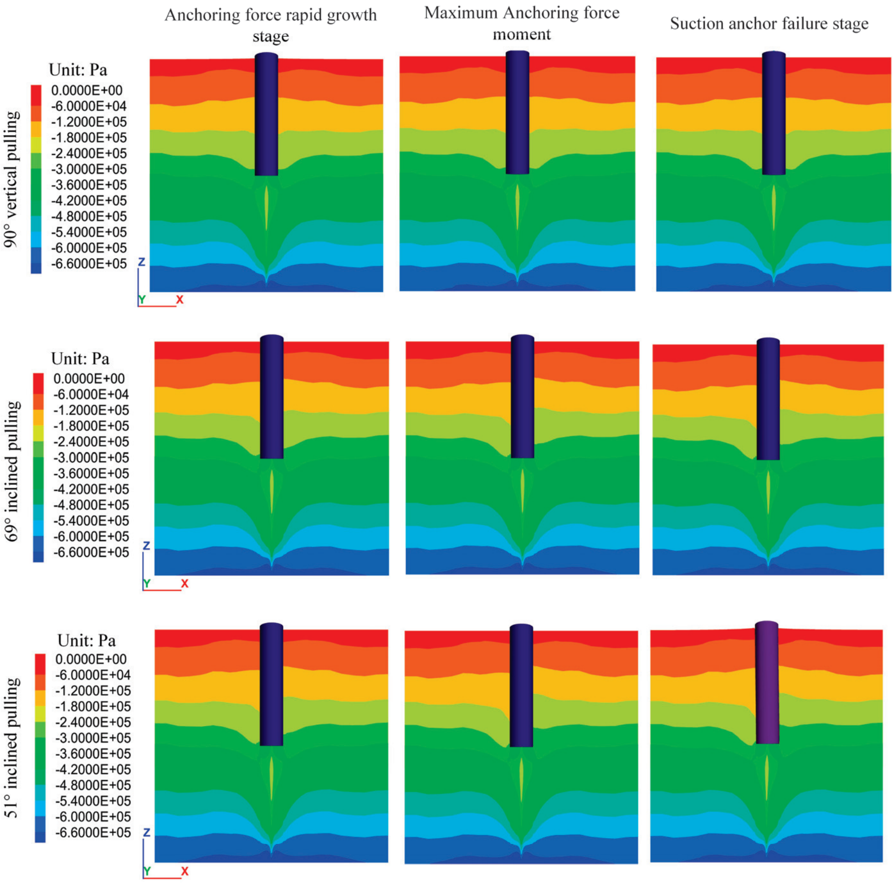

Figure 15. Horizontal soil pressure (σ_{xx}) distribution of muddy clay soil.

4. Interaction Mechanism between Suction Anchor and Soil

4.1. Mechanical Behaviors of Soil with Suction Anchor Loading

In this section, the interaction between the suction anchor and muddy clay will be analyzed based on the monitoring results of horizontal soil pressures in the inclined pulling tests of the suction anchors.

Figure 16 shows the monitoring results of horizontal soil stresses around the suction anchor in the 69° pulling test. The monitoring arrangement is shown in Figure 4. The development stages of the anchoring force in the 69° pulling process (as shown in Figure 9) are marked in Figure 16 by dotted lines for better comparisons. The suction anchor was loaded when the pressure sensor data stabilized. The soil pressures in front of the suction anchor dramatically increased to a peak value. The peak value coincided with the end of the anchoring force rapid growth stage. This phenomenon was related to the generation and dissipation of excess pore water pressure caused by soil compression.

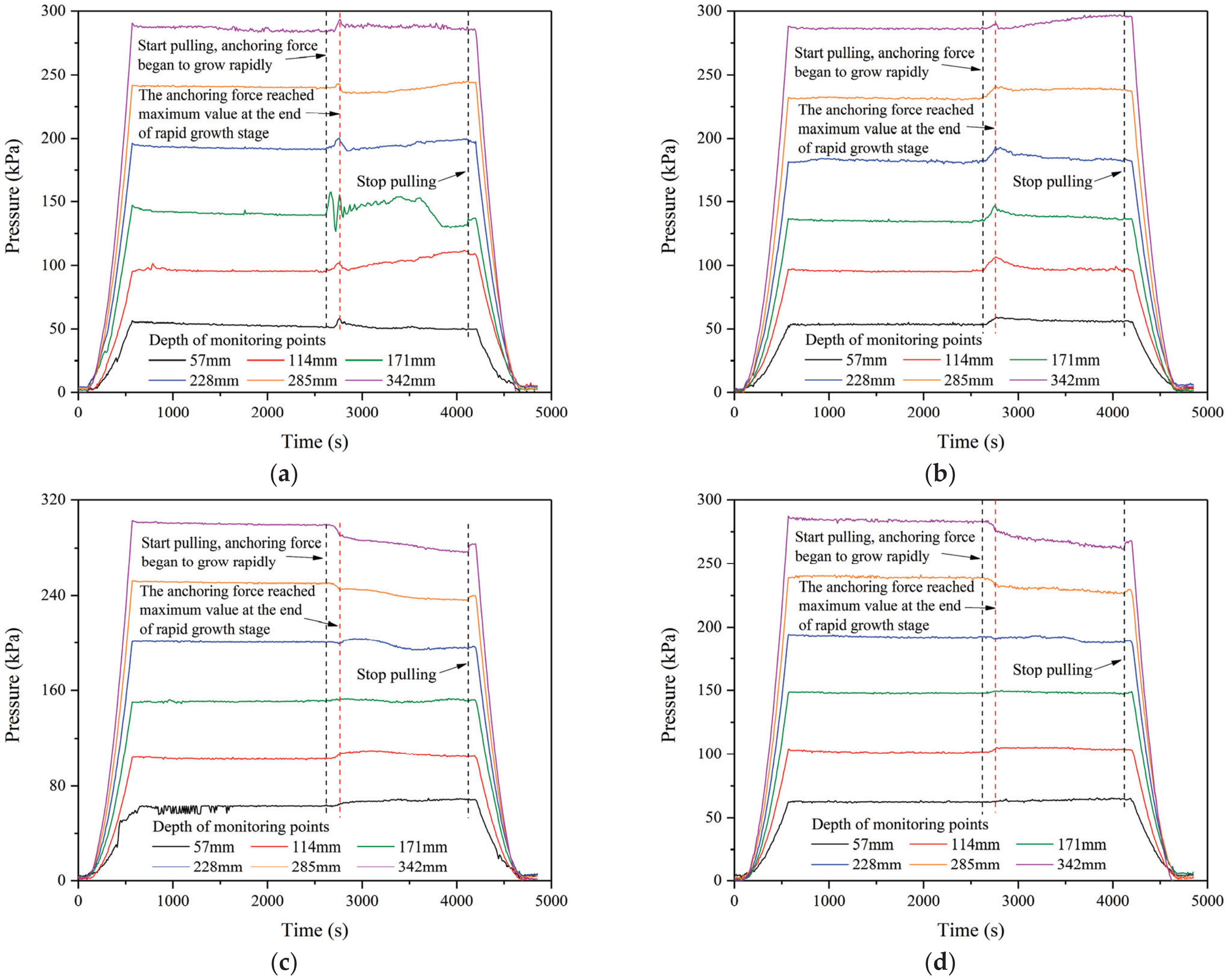

(**a**) (**b**) (**c**) (**d**)

Figure 16. Soil pressures around the suction anchor in the 69° inclined pulling test: (**a**) 30 mm in front of suction anchor; (**b**) 80 mm in front of suction anchor; (**c**) 20 mm behind suction anchor; (**d**) 50 mm behind suction anchor.

The front soil pressures initially declined after exceeding the peak values and tended to differentiate at various measuring points. The soil pressures 30 mm in front of the suction anchor are shown in Figure 16a. The pressure at 57 mm depth exhibited a decline, followed by a slight increase, before ultimately stabilizing. The soil pressure at the depths of 114~285 mm declined briefly. Then, it increased, especially at depths of 114~171 mm, indicating that the soil was compressed forward and upward. Moreover, the soil pressure at 171 mm depth underwent significant changes due to the cable's disturbance. The bottom soil pressure at 342 mm depth was the largest, but it decreased slightly after crossing the peak value and tended to stabilize. The increases in the top and bottom soil pressures were relatively small. It can be concluded that the top pressure was easily released to the free surface, and the pressure increase was inconspicuous. The displacement of the suction anchor also formed a free surface at the bottom, which caused the release of soil pressure. Therefore, the subsequent growth of the bottom soil pressure was minimal.

The horizontal soil pressures 80 mm in front of the suction anchor are shown in Figure 16b. The pressures at the depths of 57~285 mm slightly decreased after crossing the peak value and tended to stabilized. In general, the soil pressures showed an upward trend. The bottom pressure slightly decreased after exceeding the peak value, followed by an increase with the pulling process. Figure 16a,b showed that the front soil pressure was greatly affected by suction anchor pulling during the anchoring force rapid growth stage. The suction anchor's influence on the soil pressure declined with increasing distance. The results also showed that the interaction between the suction anchor and muddy clay varied during the rapid growth stage and the subsequent stage of the anchoring force. The suction anchor compressed the soil and showed rapid anchoring force growth at the earlier loading time. At the same time, the soil pressures quickly reached peak values. However, the muddy clay soil produced plastic shear deformation with the movement of the suction anchor, causing soil stress redistribution.

The soil stress behind the suction anchor differentiated evidently with development. The soil pressures 20 mm behind the suction anchor are shown in Figure 16c. The soil pressure at 57 mm depth remained stable after an initial increase during the loading process. The soil pressure at 114 mm depth showed an initial increase, followed by stability, and then a slight decrease. The soil pressure at 171 mm depth showed the behaviors of increase–decrease–increase–stable, with minimal changes. The development trend of soil pressure at 228 mm depth was the same as that at 171 mm, but with more noticeable changes. The soil pressures at 285 mm and 342 mm depths showed significant differences. The soil pressures decreased rapidly in the anchoring force rapid growth stage. Then, it decreased slower until the end of loading.

The soil pressures 50 mm behind the suction anchor are shown in Figure 16d. The soil pressure developments were consistent with the pressures 20 mm behind the suction anchor (Figure 16c). The variation ranges of the soil pressures at 57~228 mm depths were minor, while the variation ranges of soil pressure at depths of 285 mm and 342 mm were nearly the same. The more accessible stress release near the bottom free surface caused this phenomenon while the suction anchor was pulled out of the muddy clay.

Figure 17 shows the horizontal soil pressures around the 51° pulling suction anchor. The development stages of the anchoring force in the 51° pulling process (as shown in Figure 10) are marked in Figure 17 by dotted lines for better comparisons. The cable was initially relaxed and gradually tightened with pulling. At this time, the cable would shear and compress the soil along the movement direction, causing an increase or local decrease in soil stress. Subsequently, the suction anchor moved forward and compressed the soil, which caused significant increases in soil pressures and a rapid growth stage for the anchoring force. The soil pressures differentiated with development during loading. Simultaneously, the anchoring force slowly increased to the maximum value. Figure 17a shows the soil pressures 30 mm in front of the suction anchor. The soil pressures at depths of 285 mm and 342 mm reached the peak values with the rapid growth of the anchoring force. Then, the soil pressure development was consistent with the 69° pulling test (Figure 16a). Nevertheless, the pressures at the 57~228 mm depths continued to increase in the fluctuation growth stage of the anchoring force, and there were no periodic peak values. Finally, the soil pressures increased slowly with the continuous loading of the suction anchor.

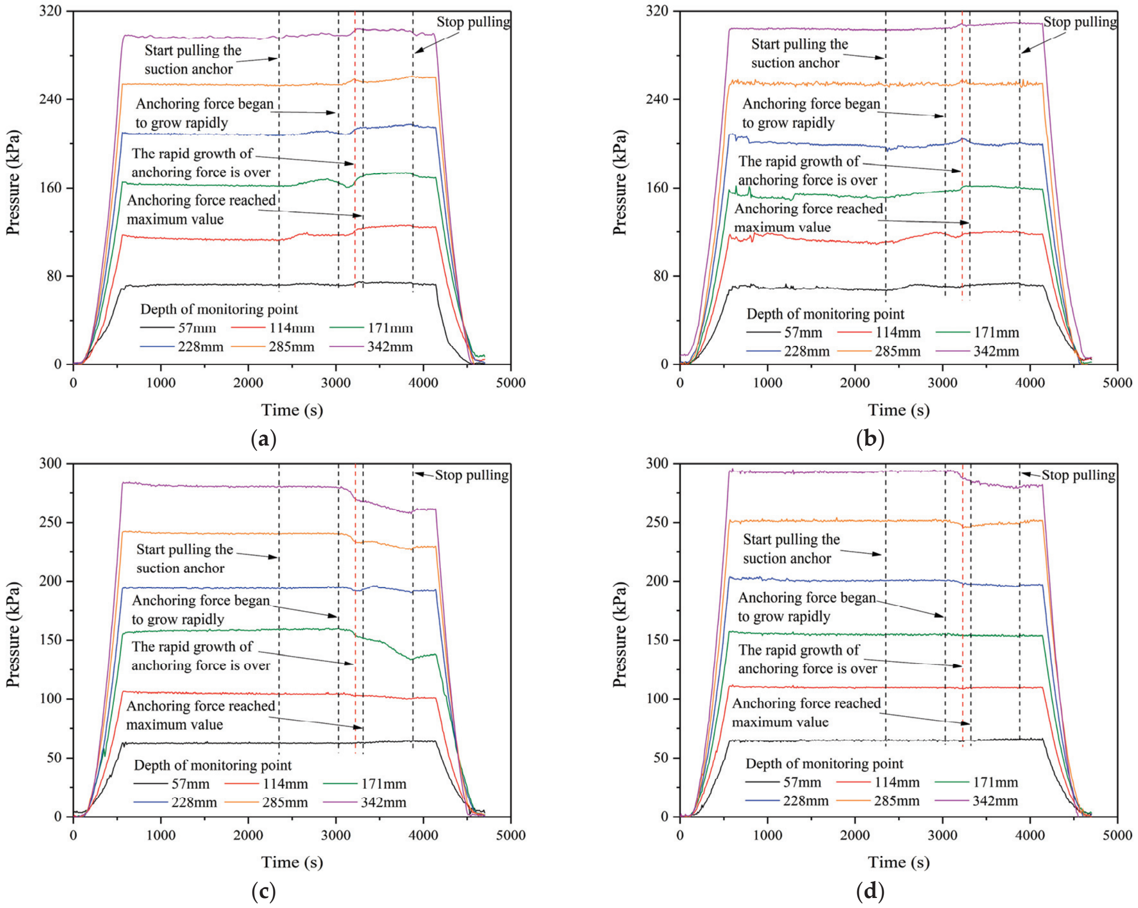

(**a**) (**b**) (**c**) (**d**)

Figure 17. Soil pressures around the suction anchor in the 51° inclined pulling test: (**a**) 30 mm in front of suction anchor; (**b**) 80 mm in front of suction anchor; (**c**) 20 mm behind suction anchor; (**d**) 50 mm behind suction anchor.

The horizontal soil pressures 80 mm in front of the 51° pulling suction anchor are shown in Figure 17b. The soil pressure developments were consistent with the test results 30 mm in front of the suction anchor. It should be noted that the soil pressures at 228~342 mm depths reached their peak values and then decreased. These soil pressure responses were related to the generation and dissipation of excess pore water pressure caused by soil compression. The excess pore water pressures in the upper range were small and easily dissipated. Therefore, the soil pressures at 57~171 mm depths increased rapidly at first and tended to increase slowly or stabilize with the continuous loading of the suction anchor.

The horizontal soil pressures 20 mm behind the suction anchor are shown in Figure 17c. The soil pressure at 57 mm depth increased slightly. This indicates that the suction anchor inclined backward, causing its upper part to compress the soil. The soil pressure at 114 mm depth decreased slightly with the pulling of suction anchor. The soil pressure at 171 mm depth showed a noticeable decrease, which was due to local stress release caused by the soil and anchor moving forward. The soil pressure at 228 mm depth showed a decrease–increase–decrease changing process. The soil pressure decreased to a minimum value with the rapid growth of the anchoring force in this process. At depths of 285 mm and 342 mm, the soil pressures exhibited a sharp decline in the anchoring force rapid growth stage. Then, the soil pressures decreased slowly with the continuous loading of the suction anchor.

Figure 17d shows the soil pressures 50 mm behind the suction anchor. The loading suction anchor barely affected the soil pressures at 57~171 mm depths. Nevertheless, the soil pressures at 228~342 mm depth were affected and showed similar responses. The bottom soil pressures decreased significantly with the suction anchor moving forward. At the same time, the anchoring force increased rapidly. The pressure variations were less than those observed 20 mm behind the suction anchor.

4.2. Distribution Characteristics of Soil Pressures around Suction Anchors

Three representative states have been selected to display the pressure distributions in the loading process: the initial state of soil pressure, the soil pressure at the end of the anchoring force rapid growth stage, and the soil pressure at the end of the pulling test. The horizontal soil pressure distribution around the 51° and 69° pulling suction anchors is shown in Figure 18.

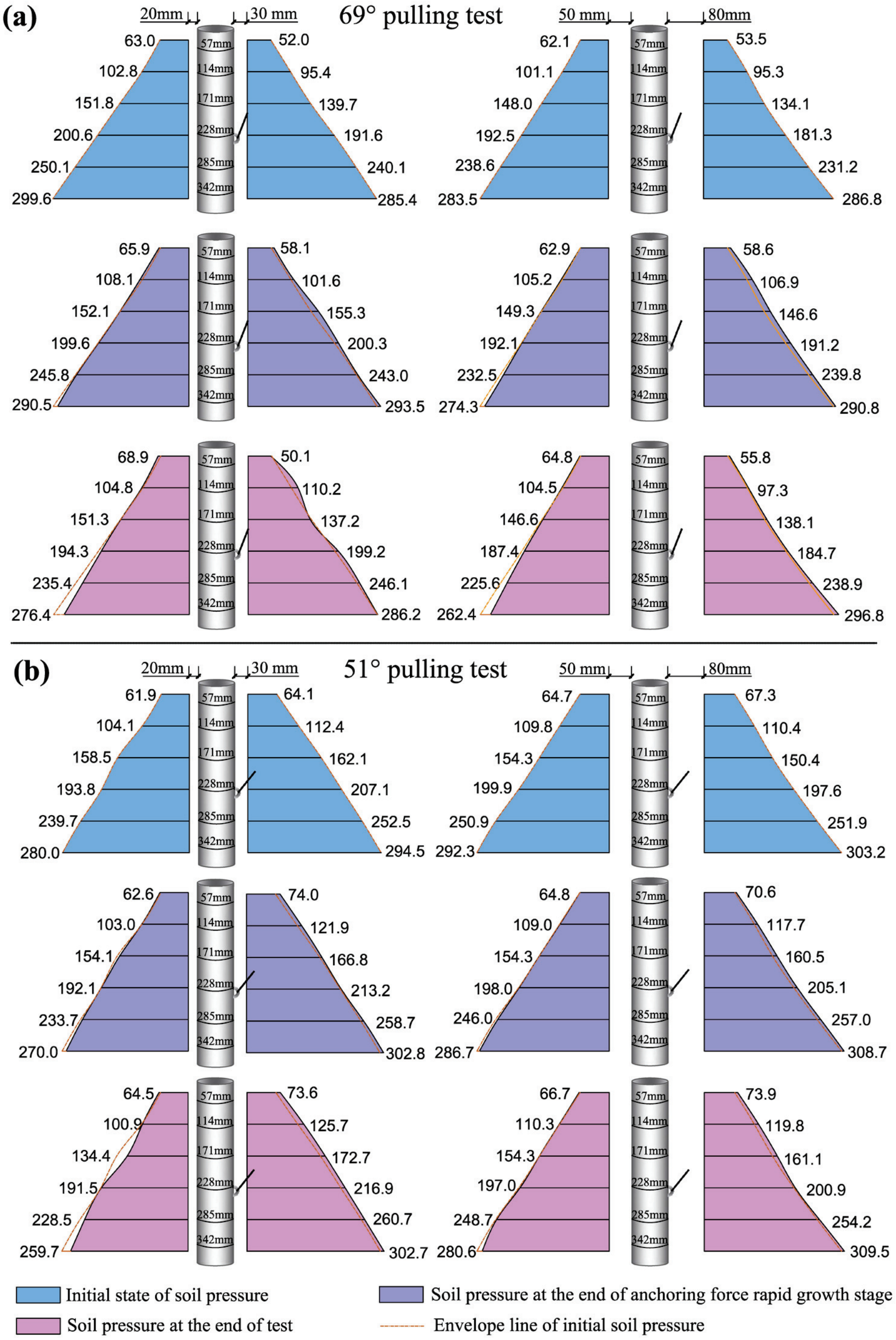

Figure 18. The horizontal soil pressure distribution around the suction anchors in the following tests: (**a**) the 69° pulling test; (**b**) the 51° pulling test.

The horizontal soil pressures were approximately linearly distributed along the depth. The soil pressures around the 69° pulling suction anchor are shown in Figure 18a. The soil pressures 30 mm in front of the suction anchor showed marked increases of 2.9~15.6 kPa during the anchoring force rapid growth stage. The increase in the soil pressures 80 mm in front of the suction anchor was 4.0~12.5 kPa, slightly smaller than the former. However, the pressures did not increase linearly with the soil depth. This indicates that the soil compression caused by the suction anchor was not uniform. Due to the dissipation of excess pore water pressure, some soil pressures decreased at the end of the test, but on the whole, the pressures showed a growing trend with the continuous pulling of the suction anchor. Notably, the soil pressures 80 mm in front of the anchor were linearly distributed. In contrast, the soil pressures at 30 mm showed a nonlinear distribution. This indicates that the muddy clay soil near the suction anchor was severely disturbed.

Comparing the pressures behind the suction anchor, it can be seen that the soil pressures of the upper part showed an increasing trend. In contrast, the soil pressures of the lower part showed a decreasing trend. This contrast indicated that the anchor body was inclined backward while moving forward. The loading position in the suction anchor's lower part caused this response. At the end of the test, only the top pressure behind the suction anchor continued to increase while the pressures at other monitoring points decreased. In the vertical direction, the bottom pressures showed the largest decrease. In the horizontal direction, the soil pressures near and behind the suction anchor were more likely to show larger decreases.

The soil pressure around the 51° pulling suction anchor is shown in Figure 18b. Similar to the 69° pulling test, the soil pressures in front of the suction anchor increased variously during the pulling process. The pressures near the suction anchor experienced greater increases. The soil pressures behind the suction anchor also showed the differentiation of the upper and lower parts. The top pressure 20 mm behind the suction anchor increased, while the others showed a decreasing trend. For the soil pressures 50 mm behind the suction anchor, the upper three monitoring points had either stable or increased soil pressures, while the lower points showed marked decreases. These results indicate that the anchor body was inclined backward while the suction anchor compressed and sheared the front soil.

Comparing the pressure changes on both sides of the suction anchor, the pressure decreases regarding the back side were more significant than the pressure increases regarding the front side. Because the muddy clay soil, where the suction anchors were located, had low strength, the soil on the front side quickly reached the plastic flow state when the suction anchor was pulled forward. Therefore, it was difficult for the muddy clay soil to provide strong resistance to the suction anchor. The stress release on the back side caused decreases in soil pressures. The anchor body inclined backward as the loading position was at the front lower part of the anchor body. Therefore, the upper soil behind the anchor body was compressed, and the soil pressures showed increasing responses. Comparing the pressure changes in the 51° and 69° pulling tests, the soil pressures of the front sides showed larger increases under the 51° pulling load. It was demonstrated that the compressing effect on the front side was more significant, with the loading direction tending to be horizontal.

By comparing the soil stress distribution in Figures 15 and 18, the same characteristics can be found: the soil pressure in front of the suction anchor increased, while the pressure behind it decreased. The pressure changes were more significant in the soil closer to the suction anchor. Moreover, the pressure changes at the lower part were more pronounced. The centrifugal test results were consistent with the numerical results. There were also minor differences. The soil pressure changes in the numerical simulation were more uniform than those in the centrifugal test. Because the soil was assumed to be homogeneous and continuous in the numerical simulation despite not being so in reality, it was impossible to achieve an absolute uniformity of soil, even in the laboratory. Furthermore, the loading motion of the suction anchors caused soil disturbance, leading to differences in soil pressure distribution. Therefore, the non-uniformity of the soil and the disturbance caused by the suction anchor resulted in more complex soil stress responses.

4.3. Failure Mechanism of Suction Anchors in Muddy Clay

The movement of suction anchors and the deformation of muddy clay soil after the test are shown in Figure 19. The relevant displacement profiles of the suction anchors are shown in Figure 20. The suction anchor was vertically pulled up from the soil in the 90° pulling test. The shear–slip failure behaviors occurred on the internal and external contact surfaces between the suction anchor and muddy clay. The shear stress on the contact surface gradually reached the bond shear strength by pulling the suction anchor. Then, shear–slip failure occurred on the surface, and the contact surface area decreased gradually. Therefore, the suction anchor lost its bearing capacity gradually with continuous pulling.


(**a**) (**b**) (**c**)

Figure 19. The movement of the suction anchors and the deformation of the muddy clay soil after the following tests: (**a**) the 90° pulling test; (**b**) the 69° pulling test; (**c**) the 51° pulling test.

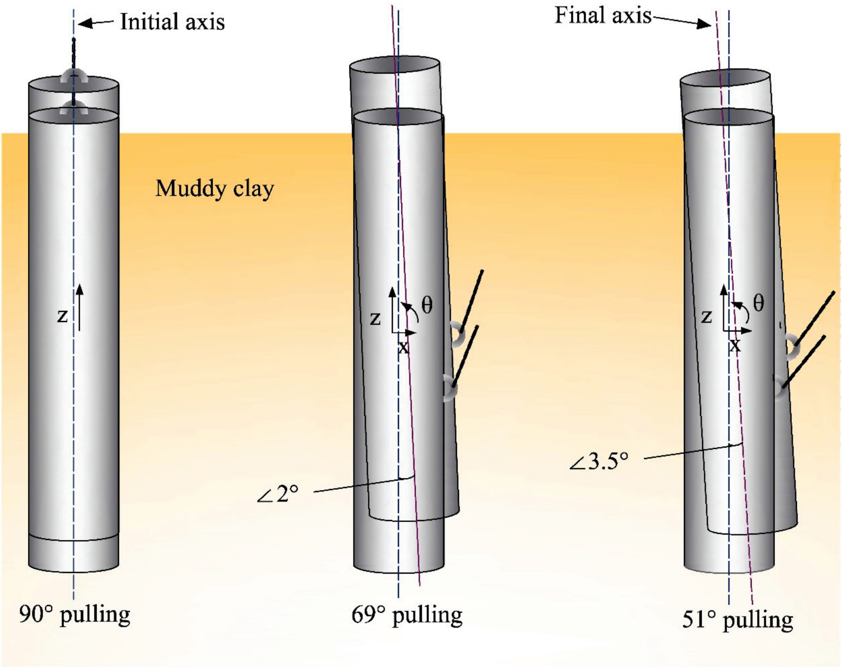

Figure 20. The displacement profiles of the suction anchors in the centrifugal model test.

The inclined pulling suction anchors were loaded at the lower part of the anchor body. According to Figures 19b,c and 20, as well as the previous analysis, the suction anchors showed multi-attitude coupling characteristics of rotation and moved forward and upward, which complicated the interaction between the suction anchors and soil.

The vertical sliding displacement was relatively significant, whereas the horizontal and rotational movements under the lateral soil resistance were less significant. As the loading direction shifted towards the horizontal, there was an increase in both the horizontal and rotational displacement of the suction anchor. According to the horizontal soil pressure distribution around the suction anchor, the front-side pressure tended to transform into passive soil pressure. In contrast, the back-side pressure tended to transform into active soil pressure. The front-side soil pressures increased with the loading angle decrease, providing higher resistance to the suction anchor. Due to the combined rotation and horizontal displacement of the suction anchor, there was an enhanced soil compression effect in the lower and middle parts, resulting in notable changes in soil pressure. The interaction between the suction anchor and the soil led to the inclined loading suction anchors' compression–shear–slip coupling failure behaviors. At the initial loading stage, the suction anchor compressed the soil, and the shear stress on the contact surface increased. The suction anchor then moved forward and caused the yielding failure of the muddy clay soil. At the same time, the shear stress of the contact surface reached the shear strength, resulting in the slip of the suction anchor. Therefore, the suction anchor gradually lost its bearing capacity and pulled out of the soil.

5. Conclusions

For this paper, the centrifugal model test was carried out to study the mechanical characteristics of suction anchors in low-strength muddy clay. The pulling load was applied to the suction anchors with vertical and inclined angles. The results showed that the anchoring force developments of suction anchors in muddy clay were complicated multi-stage processes, including the rapid growth stage, the slow growth stage, the fluctuating maintenance stage, the significant decline stage, and the slow decline stage of the anchoring force. Moreover, the anchoring force's slow growth or significant decline stage might not be evident. The comparative test results showed that the inclined pulling suction anchors had larger bearing capacities than the vertical pulling suction anchor. Furthermore, the reduction in the inclined pulling angle caused an increase in the horizontal resistance of the muddy clay soil. Therefore, the bearing capacity of the suction anchor was improved. Numerical modeling was used to validate the test results of anchoring force development. The load–displacement relationship in the numerical simulation and centrifugal test showed consistency. The displacement distribution and evolution of the suction anchors and muddy clay soil were analyzed based on the numerical results. During the loading process, the soil displacement continued to increase until the anchors reached maximum bearing capacity. Following this, the soil displacement developed slightly with the suction anchor loaded to failure.

The horizontal soil stresses around the suction anchors were obtained in the inclined pulling tests, which provided valuable insights into the stress responses, including the development and distribution of soil stresses. The centrifugal test and numerical simulation showed consistent soil stress responses. The suction anchors significantly interacted with the muddy clay soil in the pulling process. The influence of the loading direction on the interaction mechanism was investigated based on the comparative analysis. The failure mechanism of the suction anchors in the muddy clay was summarized according to the testing and numerical results. The vertical pulling suction anchor showed shear–slip failure behaviors. However, the inclined pulling suction anchors had more complicated failure behaviors. The motion of suction anchors showed multi-attitude coupling characteristics of rotation and moved forward and upward while subjected to the inclined pulling load. The interaction between the suction anchors and the soil led to the compression–shear–slip coupling failure behaviors of the suction anchors subjected to inclined pulling.

The bearing capacity of a suction anchor depends on the interaction between the anchor and the soil. When the contact interface between the suction anchor and the soil reaches its ultimate strength, the suction anchor can bear the maximum load. In challenging geological conditions, including in muddy and soft clay, the design of suction anchors should take into account the negative effect of low-strength soil on anchoring capacity. It is suggested to fully utilize the lateral resistance of soil or increase the critical slip strength in structural optimization to improve the bearing capacity of suction anchors. The findings of this paper are essential for clarifying the mechanical characteristics of suction anchors in muddy clay, providing references for the deep water anchorage of offshore platforms, floating wind turbines, and submerged floating tunnels.

It should be noted that calculating the bearing capacity of suction anchors in muddy clay of varying strengths is challenging. This study conducted centrifugal tests on low-strength muddy clay under one specific condition, without fully considering changes in soil strength. To enhance design support for suction anchors, we recommend carrying out future research via comparative tests under varying conditions. These conditions could include different soil properties, diameter/length ratios, and loading positions. Such tests would provide a comprehensive understanding of the bearing capacity of suction anchors in various conditions.

Author Contributions: Conceptualization, J.L. and X.L. (Xiaoqiang Liu); methodology, J.L.; software, J.L.; validation, X.A.; formal analysis, J.L. and D.Z.; investigation, L.Y. and D.Z.; resources, J.L.; data curation, J.L. and X.A.; writing—original draft preparation, J.L.; writing—review and editing, J.L.; supervision, X.L. (Xianpeng Liu); project administration, J.L. and X.L. (Xianpeng Liu). All authors have read and agreed to the published version of the manuscript.

Funding: This work was funded by the National Key Research and Development Program of China (grant number: 2022YFB2602800), the National Natural Science Foundation of China (grant number: 52308401), the Transportation Technology Development Project of Tianjin (grant number: 2022-43), and the Fundamental Research Funds for the Central Research Institutes (grant numbers: TKS20220102, TKS20220207, and TKS20200101).

Institutional Review Board Statement: Not applicable.

Informed Consent Statement: Not applicable.

Data Availability Statement: The data presented in this study are available from the corresponding author upon email request (luojiweim@126.com).

Conflicts of Interest: Author Liqiang Yu was employed by the company: Hebei Construction & Investment Off-shore Wind Power Co., Ltd. The remaining authors declare that the research was conducted in the absence of any commercial or financial relationships that could be construed as a potential conflict of interest.

References

1. Arany, L.; Bhattacharya, S. Simplified load estimation and sizing of suction anchors for spar buoy type floating offshore wind turbines. *Ocean Eng.* **2018**, *159*, 348–357. [CrossRef]
2. Wang, M.; Nacci, V.; Demars, K. Behavior of underwater suction anchor in soil. *Ocean Eng.* **1975**, *3*, 47–62. [CrossRef]
3. Dyvik, R.; Andersen, K.H.; Hansen, S.B.; Christophersen, H.P. Field tests of anchors in clay. I: Description. *J. Geotech. Geoenviron.* **1993**, *119*, 1515–1531. [CrossRef]
4. Liu, H.; Yang, Y.; Peng, J. A Unified Model for Analyzing Comprehensive Behaviors of Deepwater Anchors. *J. Mar. Sci. Eng.* **2021**, *9*, 913. [CrossRef]
5. Ahn, J.; Lee, H.; Kim, Y.-T. Finite element analysis of the holding capacity of shallow suction caisson anchors. *Mar. Georesour. Geotechnol.* **2015**, *33*, 33–44. [CrossRef]
6. Wang, P.; Lu, H.; Wang, M.; Nagarajaiah, S.; Du, X. Experimental and numerical investigations on seismic responses of wind turbine structures with amplifying damping transfer system. *Soil Dyn. Earthq. Eng.* **2023**, *175*, 108277. [CrossRef]
7. Yang, Z.; Li, J.; Zhang, H.; Yuan, C.; Yang, H. Experimental Study on 2D Motion Characteristics of Submerged Floating Tunnel in Waves. *J. Mar. Sci. Eng.* **2020**, *8*, 123. [CrossRef]
8. Wang, C. Nonlinear waves and wave-structure interactions in marine hydrodynamics—Recent progress. *Sci. China Technol. Sci.* **2012**, *55*, 3253–3256. [CrossRef]
9. Zdravkovic, L.; Potts, D.; Jardine, R. A parametric study of the pull-out capacity of bucket foundations in soft clay. *Geotechnique* **2001**, *51*, 55–67. [CrossRef]
10. Bang, S.; Jones, K.; Kim, Y.S.; Cho, Y. Horizontal capacity of embedded suction anchors in clay. *Ocean Eng.* **2011**, *133*, 011104. [CrossRef]
11. Du, J.; Du, S.; Wang, Z. A Comparison of Pull-out Capacity of Suction Anchors in Clay and Sand. *Appl. Mech. Mater.* **2014**, *614*, 613–617. [CrossRef]

12. Koh, K.X.; Hossain, M.S.; Kim, Y. Installation and monotonic pullout of a suction caisson anchor in calcareous silt. *J. Geotech. Geoenviron. Eng.* **2017**, *143*, 04016098. [CrossRef]
13. Sassi, K.; Zehzouh, S.; Blanc, M.; Thorel, L.; Cathie, D.; Puech, A.; Colliat-Dangus, J.L. Effect of seabed trenching on the holding capacity of suction anchors in soft deepwater Gulf of Guinea clays. In Proceedings of the Offshore Technology Conference, Houston, TX, USA, 30 April–3 May 2018.
14. Wang, X.; Yang, X.; Zeng, X. Lateral capacity assessment of offshore wind suction bucket foundation in clay via centrifuge modelling. *J. Renew. Sustain. Energy* **2017**, *9*, 033308. [CrossRef]
15. Wang, H.; Cheng, X. Undrained bearing capacity of suction caissons for offshore wind turbine foundations by numerical limit analysis. *Mar. Georesour. Geotechnol.* **2016**, *34*, 252–264. [CrossRef]
16. Monajemi, H.; Razak, H.A. Finite element modeling of suction anchors under combined loading. *Mar. Struct.* **2009**, *22*, 660–669. [CrossRef]
17. Li, H.; Chen, X.; Hu, C.; Wang, S.; Liu, J. Accumulation of Pore Pressure in a Soft Clay Seabed around a Suction Anchor Subjected to Cyclic Loads. *J. Mar. Sci. Eng.* **2019**, *7*, 308. [CrossRef]
18. Shen, K.; Wang, L.; Guo, Z.; Jeng, D.S. Numerical investigations on pore-pressure response of suction anchors under cyclic tensile loadings. *Eng. Geol.* **2017**, *227*, 108–120. [CrossRef]
19. Cheng, X.; Wang, P.; Li, N.; Liu, Z.; Zhou, Y. Predicting the cyclic behaviour of suction anchors based on a stiffness degradation model for soft clays. *Comput. Geotech.* **2020**, *122*, 103552. [CrossRef]
20. Randolph, M.; House, A. Analysis of suction caisson capacity in clay. In Proceedings of the Offshore Technology Conference, Houston, TX, USA, 6–9 May 2002.
21. Andersen, K.H.; Dyvik, R.; Schrøder, K.; Hansteen, O.E.; Bysveen, S. Field tests of anchors in clay II, Predictions and interpretation. *J. Geotech. Eng.* **1993**, *119*, 1532–1549. [CrossRef]
22. Clukey, E.C.; Morrison, M.J.; Gamier, J.; Corte, J.F. The response of suction caissons in normally consolidated TLP loading conditions. In Proceedings of the Offshore Technology Conference, Houston, TX, USA, 1–4 May 1995.
23. Chen, W.; Randolph, M.F. Uplift Capacity of Suction Caissons under Sustained and Cyclic Loading in Soft Clay. *J. Geotech. Geoenviron. Eng.* **2007**, *133*, 1352–1363. [CrossRef]
24. Fu, D.; Zhang, Y.; Yan, Y.; Jostad, H.P. Effects of tension gap on the holding capacity of suction anchors. *Mar. Struct.* **2020**, *69*, 102679. [CrossRef]
25. Aubeny, C.; Murff, J.D. Simplified limit solutions for the capacity of suction anchors under undrained conditions. *Ocean Eng.* **2005**, *32*, 864–877. [CrossRef]
26. Jones, K.D.; Bang, S.; Cho, Y. Pullout capacity of embedded suction anchors in sand. *Ocean Eng.* **2007**, *34*, 2107–2114. [CrossRef]
27. Koh, K.X.; Wang, D.; Hossain, M.S. Numerical simulation of caisson installation and dissipation in kaolin clay and calcareous silt. *Bull. Eng. Geol. Environ.* **2018**, *77*, 953–962. [CrossRef]
28. Yang, Q.; Pan, G.; Liu, H.; Wang, Q. Bearing capacity of offshore umbrella suction anchor foundation in silty soil under varying loading modes. *Mar. Georesour. Geotechnol.* **2018**, *36*, 781–794. [CrossRef]
29. Cheng, L.; Hossain, M.S.; Hu, Y.; Kim, Y.H.; Ullah, S.N. Failure envelope of suction caisson anchors subjected to combined loadings in sand. *Appl. Ocean Res.* **2021**, *114*, 102801. [CrossRef]
30. Hu, R.; Liu, H.; Leng, H.; Yu, P.; Wang, X. Scour Characteristics and Equilibrium Scour Depth Prediction around Umbrella Suction Anchor Foundation under Random Waves. *J. Mar. Sci. Eng.* **2021**, *9*, 886. [CrossRef]
31. Saue, M.; Aas, P.M.; Andersen, K.H.; Solhjell, E. Installation of suction anchors in layered soils. In Proceedings of the Offshore Site Investigation Geotechnics 8th International Conference Proceeding, Oslo, Norway, 12–14 September 2017; pp. 507–515.
32. Utsunomiya, T.; Sekita, K.; Kita, K.; Sato, I. Demonstration Test for Using Suction Anchor and Polyester Rope in Floating Offshore Wind Turbine. In Proceedings of the International Conference on Ocean, Offshore and Arctic Engineering, Trondheim, Norway, 25–30 June 2017.
33. Wang, J.; Li, S. Analysis procedure of the cyclic bearing capacity for suction anchors in soft clays. *Mar. Georesour. Geotechnol.* **2015**, *33*, 546–555. [CrossRef]
34. Cheng, X.; Yang, A.; Li, G. Model tests and finite element analysis for the cyclic deformation process of suction anchors in soft clays. *Ocean Eng.* **2018**, *151*, 329–341. [CrossRef]
35. Lee, J.; Do, J. Effects of the Installation Method, Loading Condition, and Failure Mechanism on the Behavior of Suction Piles under Monotonic Horizontal Loading. *J. Mar. Sci. Eng.* **2021**, *9*, 1333. [CrossRef]
36. Andersen, K.H.; Jeanjean, P.; Luger, D.; Jostad, H.P. Centrifuge tests on installation of suction anchors in soft clay. *Ocean Eng.* **2005**, *32*, 845–863. [CrossRef]
37. Kim, S.; Choo, Y.W.; Kim, J.H.; Kim, D.S.; Kwon, O. Pullout resistance of group suction anchors in parallel array installed in silty sand subjected to horizontal loading—Centrifuge and numerical modeling. *Ocean Eng.* **2015**, *107*, 85–96. [CrossRef]
38. Zhu, B.; Dai, J.; Kong, D.; Feng, L.; Chen, Y. Centrifuge modelling of uplift response of suction caisson groups in soft clay. *Can. Geotech. J.* **2020**, *57*, 1294–1303. [CrossRef]
39. Zhang, Y.; He, K.; Li, X.; Ye, J. Centrifuge Shaking Table Test on the Seismic Dynamics of Revetment Breakwater and a Nearby Aircraft Runway Built on Reclaimed Coral Sand Foundation. *J. Mar. Sci. Eng.* **2023**, *11*, 41. [CrossRef]
40. Reese, L.C.; Beard, R.M. A design method for an anchor pile in a mooring system. In Proceedings of the Offshore Technology Conference, Houston, TX, USA, 28 April–1 May 1973.

41. Bhattacharya, P. Pullout capacity of shallow inclined anchor in anisotropic and nonhomogeneous undrained clay. *Geomech. Eng.* **2017**, *13*, 825–844.
42. Ng, C.W.W.; Shi, J.; Hong, Y. Three-dimensional centrifuge modelling of basement excavation effects on an existing tunnel in dry sand. *Can. Geotech. J.* **2013**, *50*, 874–888. [CrossRef]

Journal of
Marine Science
and Engineering

Article

Influence of Blade Flexibility on the Dynamic Behaviors of Monopile-Supported Offshore Wind Turbines

Yongqing Lai [1], Wei Li [1], Ben He [1], Gen Xiong [1], Renqiang Xi [2,3,*] and Piguang Wang [3]

[1] Key Laboratory for Far-Shore Wind Power Technology of Zhejiang Province, PowerChina Huadong Engineering Corporation Limited, Hangzhou 311122, China; lai_yq@hdec.com (Y.L.); li_w@hdec.com (W.L.); he_b2@hdec.com (B.H.); xiong_g@ecidi.com (G.X.)
[2] School of Mechanical Engineering and Rail Transit, Changzhou University, Changzhou 213164, China
[3] The Key Laboratory of Urban Security and Disaster Engineering of Ministry of Education, Beijing University of Technology, Beijing 100124, China; wangpiguang1985@bjut.edu.cn
* Correspondence: xirenqiang@cczu.edu.cn

Abstract: At present, monopile-supported offshore wind turbines (MOWTs) are widely used in offshore wind farms. The influence of blade flexibility on the dynamic behaviors of MOWTs excited by waves and earthquakes was investigated in this study. Numerical analysis models were established for 5 MW and 10 MW MOWTs, incorporating flexible and rigid blade configurations. The modes and natural frequencies of the full system were compared between these two numerical models, and their dynamic responses were evaluated under wave-only and earthquake-only excitations. It was revealed that the influence of blade flexibility on the first- and second-order modes of the system can be neglected. The dynamic response of these MOWTs under wave excitation can be predicted by the rigid blade model, where the maximum relative difference is less than 5%. However, higher-order modes of the system are significantly affected by the blade flexibility. Under high-frequency excitations, these higher-order modes of the system are remarkably stimulated. Additionally, a large relative difference, exceeding 50%, is detected when the rigid blade model is used to predict the seismic response of the two MOWTs. Consequently, the blade flexibility should be adequately modeled when predicting the dynamic response of OWTs.

Keywords: blade flexibility; dynamic characteristics; dynamic response; offshore wind turbines; Fourier amplitude spectra

1. Introduction

Offshore wind energy offers greater abundance and stability than onshore, and its exploration has less impact on the environment [1]. Consequently, offshore wind energy is a promising option. According to the Global Wind Energy Council [2], the global installed capacity of offshore wind power reached 8.8 GW in 2022. To reduce the levelized cost of wind power, more and more large-scale wind turbines have been installed [3]. However, these wind turbines are more susceptible to dynamic excitations due to the large mass of the rotor–nacelle assembly (RNA) and the flexibility of the support structure. Therefore, accurately predicting the dynamic behavior of offshore wind turbines (OWTs) is crucial to ensure their structural integrity and economic viability.

Currently, the majority of commercial offshore wind energy plants are located in nearshore areas and utilize bottom-fixed support structures. Bottom-fixed OWTs are subjected to long-term dynamic forces from the marine environment [4]. Additionally, in regions with significant seismic hazards, bottom-fixed OWTs face damage risks induced by strong ground motion [5]. The bottom-fixed OWTs consist of a foundation, substructures, tower, nacelle, and rotor [6]. Therefore, the dynamic analysis of OWTs requires appropriate modeling of structural characteristics, whether through theoretical analysis [7] or experiment [8].

The rotor, which consists of blades and a hub, is the crucial component of OWTs. It plays a vital role in converting wind energy into electricity by rotating with the low-speed shaft of the drivetrain system [9]. Currently, there are two types of modeling methods for the dynamic analysis of OWTs in terms of blades. The first type involves establishing a blade model with distributed mass and stiffness properties, which is referred to as the flexible blade model in this study. The beam element is usually used to model the mass, stiffness, and damping distribution of blades [10,11]. To decouple the aero-elastic effect, aerodynamic damping was introduced into the numerical model through a viscous damper [12] or modal damping [13]. This improvement allows for the dynamic response of OWTs under wind and other load excitations to be computed in general software. For example, the commercial finite element software ABAQUS was used to establish a numerical model for MOWTs excited by wind, waves, and earthquakes [14,15]. Along this line, researchers have developed a detailed blade model to analyze the dynamic behavior of the DTU 10 MW wind turbine under seismic action [16,17], where the skin and spar of blades are modeled by the shell element. However, the complex modeling or manufacturing methods, as well as the limited blade structural information, constrain the application of flexible blade models in numerical simulations and experimental research.

The second type of method treats the rotor as a rigid body and only considers its inertial effects. Although there may be some differences in determining the total mass and inertia moment of the RNA, the commonality among these methods is that blade stiffness is not taken into account. Consequently, it is referred to as the rigid blade model in the current study. Bazeos et al. [18] established a finite element model for a 450 kW wind turbine. In this research, the RNA was modeled by a concentrated mass and its aerodynamic loads were simplified as a quasi-static concentrated force. Based on this model, seismic responses of wind turbines at the operational state were analyzed [19], and the dominant role of earthquake load at high-seismic-hazard regions was emphasized [20]. However, it is difficult to consider the aero-elastic effect by using this model, which restricts the applicability of this simplified model.

As wind turbines grow larger, the flexibility of the blades increases, necessitating the consideration of the aero-elastic effect when computing the aerodynamic loads on the rotor [21]. To meet this requirement, researchers computed the hub-height aerodynamic loads using aero-elastic software and then established a finite element model using the hydro-geotech code USFOS [22,23], where the RNA was also simplified as a concentrated mass. This model has been utilized to investigate the dynamic behavior of OWTs under various loads, such as extreme wind and wave conditions [24], earthquakes [25,26], normal ocean states [27], etc. In summary, rigid blade models have been proposed and improved by researchers. Additionally, these models have been widely applied in the dynamics of OWTs, including theoretical analysis [28], experimental research [29], and numerical simulations [30]. However, the applicability of these models has not been reported.

On the whole, the influence of blade flexibility on the dynamic response of OWTs stems from the impact of blade oscillation velocity on aerodynamic loads and the effect of blade stiffness on the system's dynamic characteristics. The former has already become a consensus in the wind power industry, and researchers have demonstrated the impact of blade flexibility on aerodynamic loadings through numerical analysis [31] and wind tunnel experiments [32]. As for the influence of blade stiffness on dynamic characteristics and the dynamic response of OWTs, the existing research is quite limited. Arany et al. [33] proposed a closed solution for the first-mode natural frequency of MOWTs by modeling the RNA as a concentrated mass. This solution was validated by comparison with experimental results. To some extent, their work suggests that the rigid blade model may be used to predict the natural frequency of MOWTs. The rigid blade model has been extensively used to analyze the dynamic response of different loadings. However, to the best of the author's knowledge, no researchers have investigated whether it is applicable for predicting higher-order modes and dynamic responses of multi-megawatt OWTs.

To address the research gap in this field, the present study explored the influence of blade flexibility on the dynamic behaviors of MOWTs. The outline of this study is as follows: firstly, the characteristics of 5 MW and 10 MW MOWTs, the properties of the blade, load cases, the numerical model, and methodology are summarized; secondly, the modes and natural frequencies of 5 MW and 10 MW MOWTs are analyzed by using flexible and rigid blade models, respectively; thirdly, the dynamic response of 5 MW and 10 MW MOWTs excited by waves and earthquakes only are analyzed and compared; finally, some conclusions are summarized.

2. Model, Load Cases, and Methodology

2.1. Characteristics of MOWTs

This study aimed to explore the influence of blade flexibility on the dynamic behaviors of multi-megawatt OWTs. Specifically, two MOWTs were analyzed, one utilizing the NREL 5 MW reference wind turbine [34] and the other incorporating an update on the DTU 10 MW wind turbine [35]. Both of them are upwind horizontal axis wind turbines with three blades. Their control systems adopt variable speed and blade pitch technology. These reference wind turbines have been extensively utilized in previous studies [36,37]. The main characteristics of the two MOWTs are summarized in Table 1. Detailed information on the two wind turbines can be found in the literature [34,35].

Table 1. Properties of the 5 MW and 10 MW monopile-supported OWTs.

Part	Property	NREL 5 MW	DTU 10 MW
Blade	Rotor diameter	126 m	178.3 m
	Hub height	90 m	119 m
	Cut-in, rated, and cut-out wind speed	3 m/s, 11.4 m/s, and 25 m/s	4 m/s, 11.4 m/s, and 25 m/s
	Cut-in and rated rotor speed	6.9 rpm and 12.1 rpm	6.0 rpm and 12.1 rpm
	Length	61.5 m	86.35 m
	Overall mass	53,220 kg	122,442 kg
	Structural damping ratio	0.5%	0.5%
Hub and nacelle	Hub diameter	3 m	5.6 m
	Hub mass	56,780 kg	105,520 kg
	Nacelle mass	240,000 kg	446,036 kg
Tower	Bottom and top outer diameter	6 m and 3.87 m	7.8 m and 5.3 m
	Bottom and top wall thickness	0.027 m and 0.019 m	0.05 m and 0.03 m
	Overall mass	347,460 kg	673,998 kg
	Structural damping ratio	1%	1%
Monopile	Total length	66 m	69 m
	Outer diameter	6 m	7.8 m
	Wall thickness	0.060 m	0.085 m

2.2. Properties of the Blade

Wind turbine blades are slender members and exhibit characteristics of cantilevered beams [9]. Functionally, the structure of a blade can be divided into two components: the skin and the spar [17]. The skin forms the outer geometry of the blade and endures a portion of the aerodynamic and mechanical loads. The spar plays a crucial role as the load-bearing element, typically comprising a spar cap and a spar web, as shown in Figure 1. The spar cap supports the bending loads generated by the aerodynamic and mechanical forces. The spar web resides within the hollow section of the spar cap, providing reinforcement, enhancing stiffness, and preventing structural buckling [38]. The spar cap is usually constructed using unidirectional fabrics, while the spar web adopts a sandwich structure.

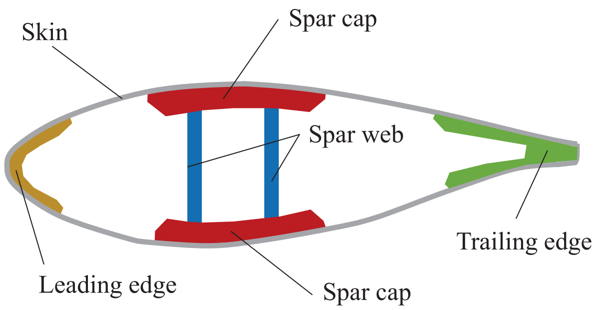

Figure 1. Structure of the blade.

To meet the structural requirements, a variable cross-section is employed in the blade design. Taking the 10 MW turbine as an example, the FFA-W series airfoils are utilized [35]. The airfoils along the blade span include FFA-W3-241, FFA-W3-301, FFA-W3-360, FFA-W3-480, and FFA-W3-600, with relative thicknesses of 24.1%, 30.1%, 36%, 48%, and 60%, respectively. The variations in blade mass and cross-sectional stiffness as a function of the radial distance "*r*" are presented in Figures 2 and 3 for the 5 MW and 10 MW wind turbines, respectively. This study aimed to investigate the influence of blade flexibility on the dynamic behaviors of the support structure. Consequently, the blade was modeled as a beam with varying cross-sections.

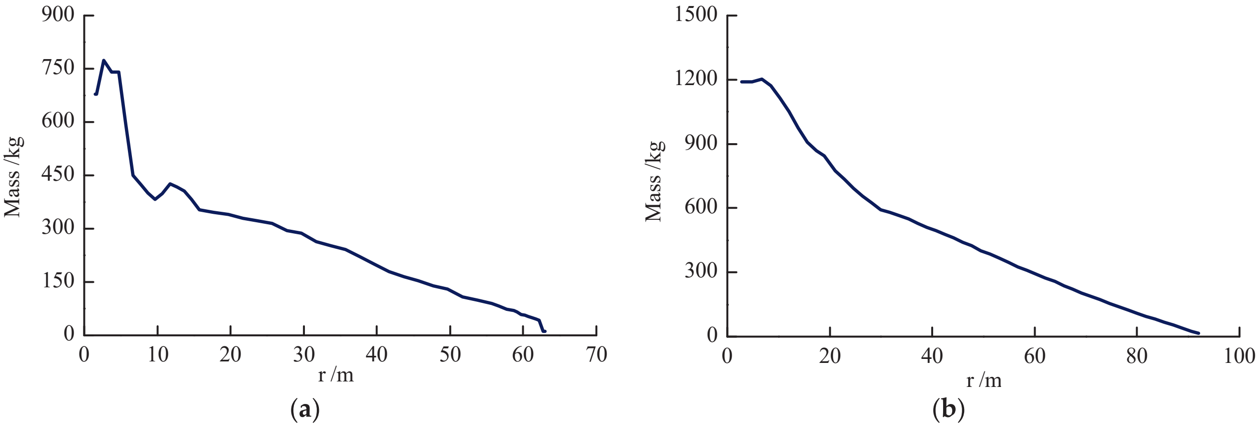

Figure 2. Mass distribution of the blade: (**a**) NREL 5 MW; (**b**) DTU 10 MW.

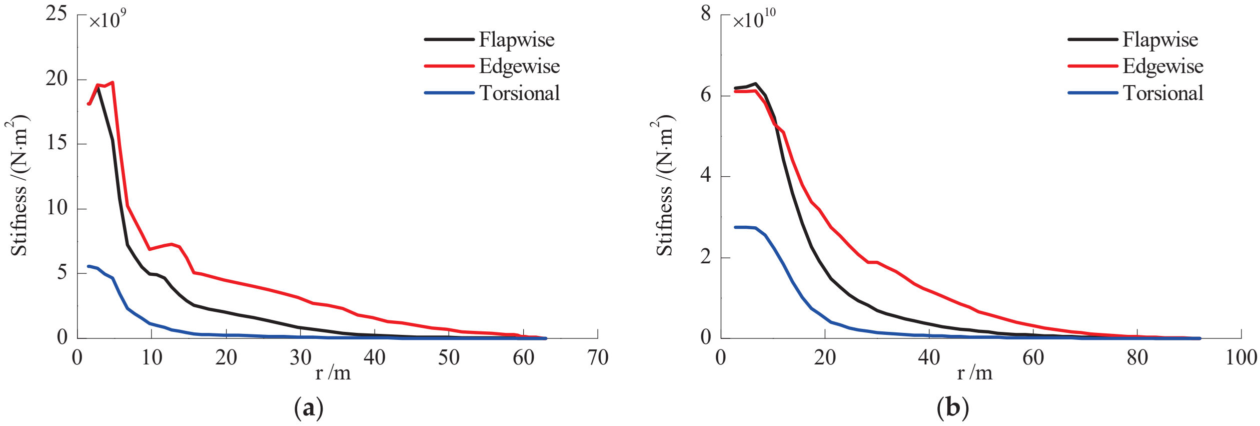

Figure 3. Stiffness distribution of the blade: (**a**) NREL 5 MW; (**b**) DTU 10 MW.

2.3. Load Cases

To assess the impact of blade flexibility, both low-frequency and high-frequency excitations were applied to these two OWTs. For bottom-fixed OWTs, although both wind and waves are low-frequency excitations, wind loadings on blades are significantly affected by the aero-elastic effect and control system. Under the wind excitation, the blade flexibility influences the dynamic responses of OWTs through the combined effect of wind loads and system dynamic characteristics. Based on the purpose of this work, the wind turbines were assumed to be in the parked condition, neglecting the influence of wind. Consequently, the low-frequency and high-frequency excitations were generated by waves and earthquakes, respectively.

In this study, an irregular wave model was used to represent the real sea state. A power spectrum should be selected to describe the amplitude of the wave component. The JONSWAP spectrum is frequently utilized in the dynamic analysis of MOWTs. It is also proposed by guidelines of the offshore wind energy community [39] and the report of 10 MW MOWTs [35]. Consequently, the JONSWAP spectrum used in this study is as follows:

$$S(f) = \frac{\alpha g^2}{(2\pi)^4} f^{-5} \exp\left(-\frac{5}{4}\left(\frac{f}{f_\mathrm{p}}\right)^{-4}\right) \gamma^{\exp\left(-0.5\left(\frac{f-f_\mathrm{p}}{\sigma \cdot f_\mathrm{p}}\right)^2\right)} \tag{1}$$

where f represents the wave frequency, f_p denotes the spectral peak frequency, g is the acceleration of gravity, α represents the generalized Phillips' constant, σ is the spectral width parameter, and γ denotes the peak-enhancement factor. These parameters are either constants or can be determined based on their relationship with the significant wave height H_s and peak period T_p.

In designing the support structures for these two OWTs, the metocean data of the Ijmuiden Shallow Water Site were used. This site is located in the Dutch North Sea and the water depth is 21.4 m MSL. The coordinates of this site are 52°33′00″ east and 4°03′30″ north. The metocean data are based on 3 h average values for a period of 22 years (January 1979–December 2000). The dynamic analysis of these OWTs employed the wave parameters of this site. The most significant wave height and peak periods are summarized in Table 2. More details about the metocean condition of this site can be found in the report by Fischer et al. [40].

Table 2. Parameters of the wave spectrum.

Load Cases	Significant Wave Height H_s (m)	Peak Period T_p (s)	Description
1	1.67	5.89	Hub mean wind speed 12 m/s
2	3.72	8.11	Hub mean wind speed 26 m/s
3	4.75	9.09	Hub mean wind speed 32 m/s
4	6.06	9.71	Return period 1 year

The input earthquakes were selected considering the recommendation of the Applied Technology Council (ATC) [41]. These records include far-field, near-field, and pulse-like seismic motions, as specified in Table 3. Both the wave and seismic motions are parallel to the horizontal projection of the normal vector of the rotor plane. The interaction between water and the oscillated monopile is considered by the updated added mass method proposed by Wang et al. [30].

Table 3. Earthquake ground motions.

No.	Earthquake, Year	Station/Component	No.	Earthquake, Year	Station/Component
1	Kocaeli, 1999	Arcelik/000	28	Duzce, 1999	Duzce/180-pulse
2	Duzce, 1999	Bolu/000	29	Imperial Valley-06, 1979	El Centro Array-6/230
3	Loma Prieta, 1989	Capitola/000	30	Imperial Valley-06, 1979	El Centro Array-7/140
4	Chi-Chi, 1999	CHY101/E	31	Erzican, 1992	Erzincan/s
5	Imperial Valley, 1979	Delta/262	32	Kocaeli, 1999	Izmit/090
6	Kocaeli, 1999	Duzce/180	33	Landers, 1992	Lucerne/260
7	Imperial Valley, 1979	El Centro Array-11/140	34	Cape Mendocino, 1992	Petrolia/090
8	Loma Prieta, 1989	Gilroy Array-3/090	35	Superstition Hills-02, 1987	Parachute Test Site/225
9	Hector Mine, 1999	Hector/090	36	Northridge-01, 1994	Rinaldi Receiving Sta/228
10	Superstition Hills, 1987	El Centro Imp. Co./090	37	Loma Prieta, 1989	Saratoga-Aloha/090
11	Northridge, 1994	Canyon Country-WLC/000	38	Irpinia, Italy-01, 1980	Sturno/270
12	Northridge, 1994	Beverly Hills-Mulhol/009	39	Northridge-01, 1994	Sylmar-Olive View/360
13	Kobe, 1995	Nishi-Akashi/000	40	Chi-Chi, 1999	TCU065/E
14	San Fernando, 1971	LA-Hollywood Stor./090	41	Chi-Chi, 1999	TCU102/E
15	Superstition Hills, 1987	Poe Road (temp)/360	42	Northridge-01, 1994	LA-Sepulveda VA/7360
16	Cape Mendocino, 1992	Rio Dell Overpass/270	43	Imperial Valley-06, 1979	Bonds Corner/140
17	Kobe, 1995	Shin-Osaka/000	44	Loma Prieta, 1989	BRAN/000
18	Friuli, 1976	Tolmezzo/000	45	Imperial Valley-06, 1979	Chihuahua/282
19	Landers, 1992	Yermo Fire Station/270	46	Loma Prieta, 1989	Corralitos/000
20	Manjil, 1990	Abbar/T	47	Gazli, 1976	Karakyr/gaz0
21	Darfield, 2010	Christchurch Cathedral College/26w	48	Nahanni, 1985	Site 2/240
22	ChiChi, 1999	Chy104/chy104-n-004	49	Nahanni, 1985	Site 1/010
23	Mexico, 2010	Calexico Fire Station/ cxo090	50	Northridge-01, 1994	Northridge-Saticoy/090
24	Mexico, 2010	Cerro Prieto Geothermal/ geo000	51	Chi-Chi, 1999	TCU067/E
25	Darfield, 2010	Christchurch Hospital/ hcs89w	52	Chi-Chi, 1999	TCU084/E
26	Chi-Chi, 1999	TCU070/tcu070-n	53	Kocaeli, 1999	Yarimca/330
27	Chi-Chi, 1999	TCU109/tcu109-n			

2.4. Numerical Model

To examine the influence of blade flexibility, the natural frequencies and mode shapes of the system were compared using both flexible and rigid blade models. Finite element models were created for these two MOWTs using the ADINA software [42], with three-dimensional beam elements utilized to simulate the blades and support structure. The length of the blade and monopile element was set to 1 m, and the length of the tower element was set to 2 m. The blades and support structures are both made of linear elastic materials whose parameters are summarized in Table 4. Since the ADINA software does not have a rigid material, the Young's modulus of the blade was increased by 10,000 times in the rigid blade model, which corresponds to material 3 in Table 4. This approach allows for neglecting the deformation of the blade and treating it as a rigid body.

Table 4. Material properties of wind turbines.

ID	Mass Density ρ (kg/m^3)	Young's Modulus E /GPa	Poisson's Ratio μ	Shear Modulus G /GPa	Description
1	1500	20	0.2	8.33	Flexible blade
2	7800	200	0.3	76.92	Support structure
3	1500	200,000	0.2	83,300	Rigid blade

The cross-sections of the tower and monopile for these two OWTs were modeled by the 'pipe' form of ADINA, and the outer and wall thickness was determined based on Table 1. Considering that the blades are composed of multiple materials and have a complex structure, their sections were modeled using the 'general' form in the ADINA software. The area A, moment of inertia I, and polar moment of inertia I_p of the cross-section for blades were determined via the following equations:

$$A = \frac{\overline{m}}{\rho} \tag{2}$$

$$I = \frac{EI}{E} \tag{3}$$

$$I_\mathrm{p} = \frac{GI_\mathrm{p}}{G} \tag{4}$$

where $\overline{m}$, EI, and GI_p are the distributed mass per length, bending stiffness, and torsional stiffness, respectively; ρ, E, and G are the material mass density, Young's modulus, and Poisson's ratio, respectively. These distributed properties of the cross-section are summarized in the corresponding report [34,35]. The hub and generator are represented as concentrated masses, while the nacelle, for which stiffness data are unavailable, is considered a rigid body.

The dynamic responses of the two MOWTs under investigation were simulated using the GL-Bladed software [43], with beam elements employed to represent the blades and tower. For the blade, the cross-section properties, i.e., distributed mass, stiffness, and airfoil, should be directly inputted by users. The rigid blade model was implemented by disabling the 'flexibility' option of the blade in the GL-bladed software. For the tower and monopile, this software calculates the distributed mass and stiffness data based on their geometry dimension and material properties. These models adopt the same mesh size as those established in ADINA.

These numerical models incorporate the beam on the nonlinear Winkler foundation (BNWF) model to simulate the soil–structure interaction (SSI) between the soil and monopile foundation. The horizontal reaction curve of the foundation employs an improved model that takes into account the size effect of large-diameter piles, as shown in the following [44]:

$$P = \mathrm{AP_u} \tan\mathrm{h}\left[\frac{k_0 z_0 \left(\frac{D}{\mathrm{D_0}}\right)^m \left(\frac{z}{z_0}\right)^n}{\mathrm{AP_u}} y\right] \tag{5}$$

where A is a factor accounting for the cyclic or static loading conditions, evaluated by A = 0.9 for cyclic loading; $\mathrm{P_u}$ is the ultimate lateral resistance at depth z; k_0 is the initial stiffness of the foundation; z_0 = 2.5 m is the reference depth; z is the depth below the original seafloor; y is the lateral deflection at depth z; D is the monopile outside diameter; $\mathrm{D_0}$ = 1.0 m is the reference diameter of the monopile; and m = 0.5 and n = 0.6 are dimensionless coefficients.

In fact, the horizontal reaction curve is commonly referred to as the p-y curve. The support structures of both MOWTs are designed for the site depicted in Figure 4, where γ and φ are the effective soil unit weight and soil internal friction angle, respectively. As a result, these parameters were utilized to establish the SSI model for the two OWTs. The

BNWF model was implemented by using springs along the pile shaft under the seabed. Given that modal analysis is conducted for linear systems, the initial slope of p-y curves was used as the stiffness of springs for modal analysis in ADINA. In dynamic analysis, these p-y curves are used as the force–displacement relationship of springs for the GL-bladed model.

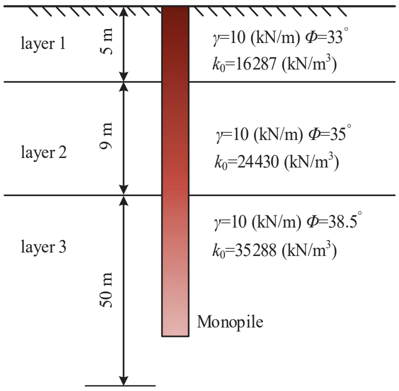

Figure 4. Soil profile of a typical marine site.

2.5. Methodology

During modal analysis, in order to ensure the non-singularity of the stiffness matrix, the RNA is rigidly connected to the tower top. Soil springs are placed along the pile shaft. In the standard finite element procedure, the motion equation of the system can be represented as follows:

$$[\boldsymbol{M}]\{\ddot{\boldsymbol{u}}\} + [\boldsymbol{K}]\{\boldsymbol{u}\} = \{0\} \tag{6}$$

where $[\boldsymbol{M}]$ and $[\boldsymbol{K}]$ are the mass and stiffness matrices, respectively; $\{\boldsymbol{u}\}$ and $\{\ddot{\boldsymbol{u}}\}$ are the displacement and acceleration vectors, respectively. In this equation, the difference between the flexible blade model and the rigid blade model lies only in the stiffness matrix. The Enriched Bathe subspace iteration method [45] was employed to implement the modal analysis for the flexible blade and rigid blade models.

In GL-bladed, the principle of virtual work is utilized to integrate the motion equations of the system, which can be expressed as the following:

$$[\boldsymbol{M}]\{\ddot{\boldsymbol{u}}\} + [\boldsymbol{C}]\{\dot{\boldsymbol{u}}\} + [\boldsymbol{K}]\{\boldsymbol{u}\} = \{\boldsymbol{f}\} \tag{7}$$

where $[\boldsymbol{C}]$ is the damping matrix, $\{\dot{\boldsymbol{u}}\}$ is the velocity vector, and $\{\boldsymbol{f}\}$ is the load vector. For structural damping, as recommended in the report, the damping ratio for all modes was assumed to be 0.5%. The foundation damping is generated by radiation and hysteresis effects. The model developed by Makris and Gazetas [46] was used to determine the foundation damping as follows:

$$c_\mathrm{s} = 6\sqrt{\rho_\mathrm{s} G_\mathrm{s}} D \left(\frac{\omega_1 D}{\sqrt{G_\mathrm{s}/\rho_\mathrm{s}}} \right)^{-1/4} + 2\beta_\mathrm{s} \frac{k_\mathrm{s}}{\omega_1} \tag{8}$$

where c_s is the foundation damping coefficient; ρ_s and G_s are the density and shear modulus of the soil, respectively; ω_1 is the first-order natural angular frequency of the support structure; k_s is the initial stiffness of the p-y curves; and β_s is the hysteresis damping ratio with a value of 5%. The shear modulus of the soil for the site illustrated in Figure 4 was taken from the literature [47]. For the sake of brevity, it is not listed here again. The Morison equation was used to calculate wave loadings, which are applied to the support structures under the sea surface. The input seismic acceleration was converted into inertial forces by GL-bladed and applied to the entire system. Subsequently, these loads are integrated into the load vector in Equation (7). To improve the computational efficiency, the fourth-order Runge–Kutta method with a variable time step was used to solve the motion equations of the system.

For the dynamic analysis implemented in GL-bladed, a modal reduction method was applied to reduce computational burden by considering a reduced number of support structures and blade modes. The full finite element model was used as the benchmark method to explore the modal reduction models required for computational accuracy, considering different mode numbers. Taking the Duzce record (no. 28 of Table 3) as the input earthquake, the 5 MW and 10 MW MOWTs use 8 and 12 modes for the blades, respectively, while their support structures use 20 modes. Their seismic responses are shown in Figures 5 and 6. The modal reduction models exhibited high agreement with the full finite element models. In addition, more studies with other input earthquakes indicate that these modal reduction models achieve a balance between computational accuracy and efficiency, and they are used for implementing dynamic analysis.

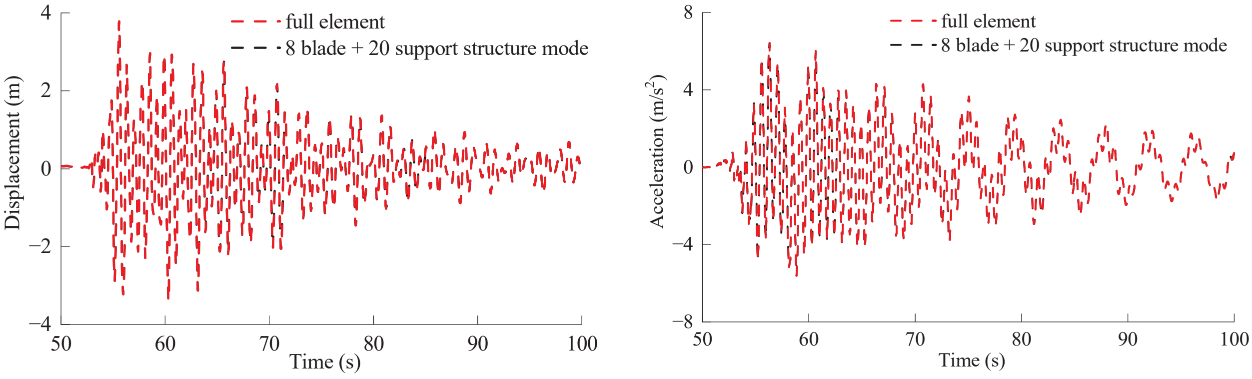

(**a**) (**b**)

Figure 5. Seismic response of the 5 MW MOWT: (**a**) displacement of the blade tip; (**b**) tower-top acceleration.

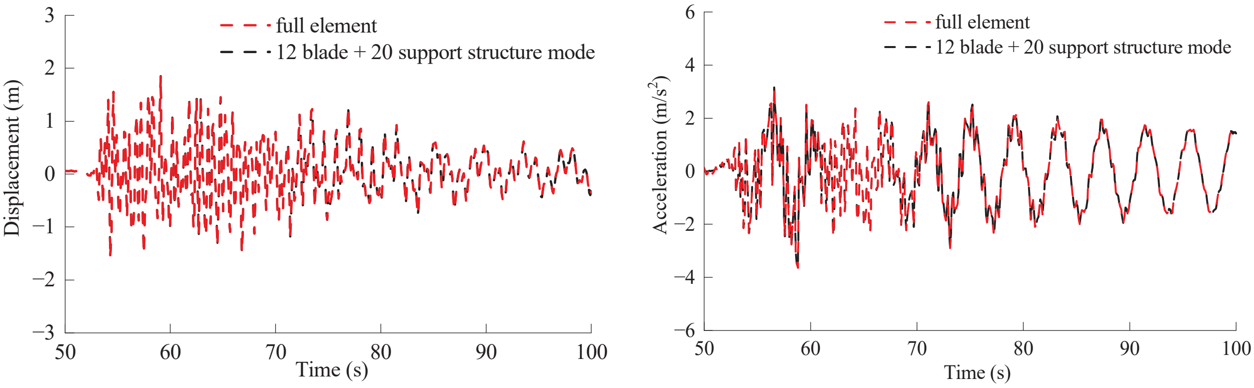

(**a**) (**b**)

Figure 6. Seismic response of the 10 MW MOWT: (**a**) displacement of the blade tip; (**b**) tower-top acceleration.

3. Results and Discussion

This section utilizes two software packages, namely ADINA and GL-Bladed, to conduct all numerical analyses. These commercial software packages have been certified for their accuracy, as documented in their respective user manuals. Therefore, the validation of numerical modes focuses on assessing the reliability of the modeling process, which is implemented by a comparative analysis with existing studies.

3.1. Dynamic Characteristic Analysis of the 5 MW and 10 MW MOWTs

In this section, the natural frequencies and mode shapes of 5 MW and 10 MW MOWTs were analyzed using the 'Frequency/Modes' module of ADINA. Table 5 presents a subset of natural frequencies for the 5 MW MOWT using flexible blade and rigid blade models.

The natural frequencies of the first two mode shapes obtained from the flexible blade model showed a high agreement with the existing research [48]. This indicates that the 5 MW MOWT model of this study provides a reliable representation. According to the table, the natural frequencies of the first two mode shapes derived from both rigid blade and flexible blade models exhibited disparities of less than 1%. Hence, the model simplifying the rotor–nacelle assembly as a rigid mass body can effectively predict the first- and second-mode natural frequencies of the full system.

Table 5. Full-system natural frequencies of the 5 MW MOWT.

Flexible Blade Model			**Rigid Blade Model**			**Existing Result [48]**		
Mode	**Frequency /Hz**	**Description**	**Mode**	**Frequency /Hz**	**Description**	**Mode**	**Frequency /Hz**	**Description**
1	0.2474	1st Tower Side-to-Side	1	0.2479	1st Tower Side-to-Side	1	0.245	1st Tower Side-to-Side
2	0.2487	1st Tower Fore–Aft	2	0.2484	1st Tower Fore–Aft	2	0.247	1st Tower Fore–Aft
3	0.6451	1st Blade Asymmetric Edgewise	3	1.2384	2nd Tower Fore–Aft			
4	0.6674	1st Blade Symmetric Edgewise	4	1.2818	2nd Tower Side-to-Side			
5	0.6733	1st Blade Asymmetric Edgewise	5	1.4965	1st Tower Torsion			
6	1.0189	1st Blade Asymmetric Flapwise						
7	1.1191	1st Blade Symmetric Flapwise						
8	1.1928	1st Tower Torsion						
9	1.4092	2nd Tower Fore–Aft and 2nd Blade Asymmetric Edgewise						
10	1.4665	2nd Tower Side-to-Side and 2nd Blade Asymmetric Flapwise						

According to Table 5, it is evident that the rigid blade model fails to accurately capture the modes primarily influenced by blade deformation, specifically the third, fourth, fifth, sixth, and seventh modes. This observation is further supported by a visual comparison of modes for the 5 MW MOWT, as depicted in Figures 7 and 8. The rigid blade model exhibited a significant discrepancy in estimating the natural frequencies associated with higher-order modes. For instance, the first torsional mode of the tower was overestimated by 25%, while the second fore–aft and the second side-to-side tower modes were underestimated by 12% and 13%, respectively. The rigid blade model can only provide reliable predictions for the first two natural frequencies.

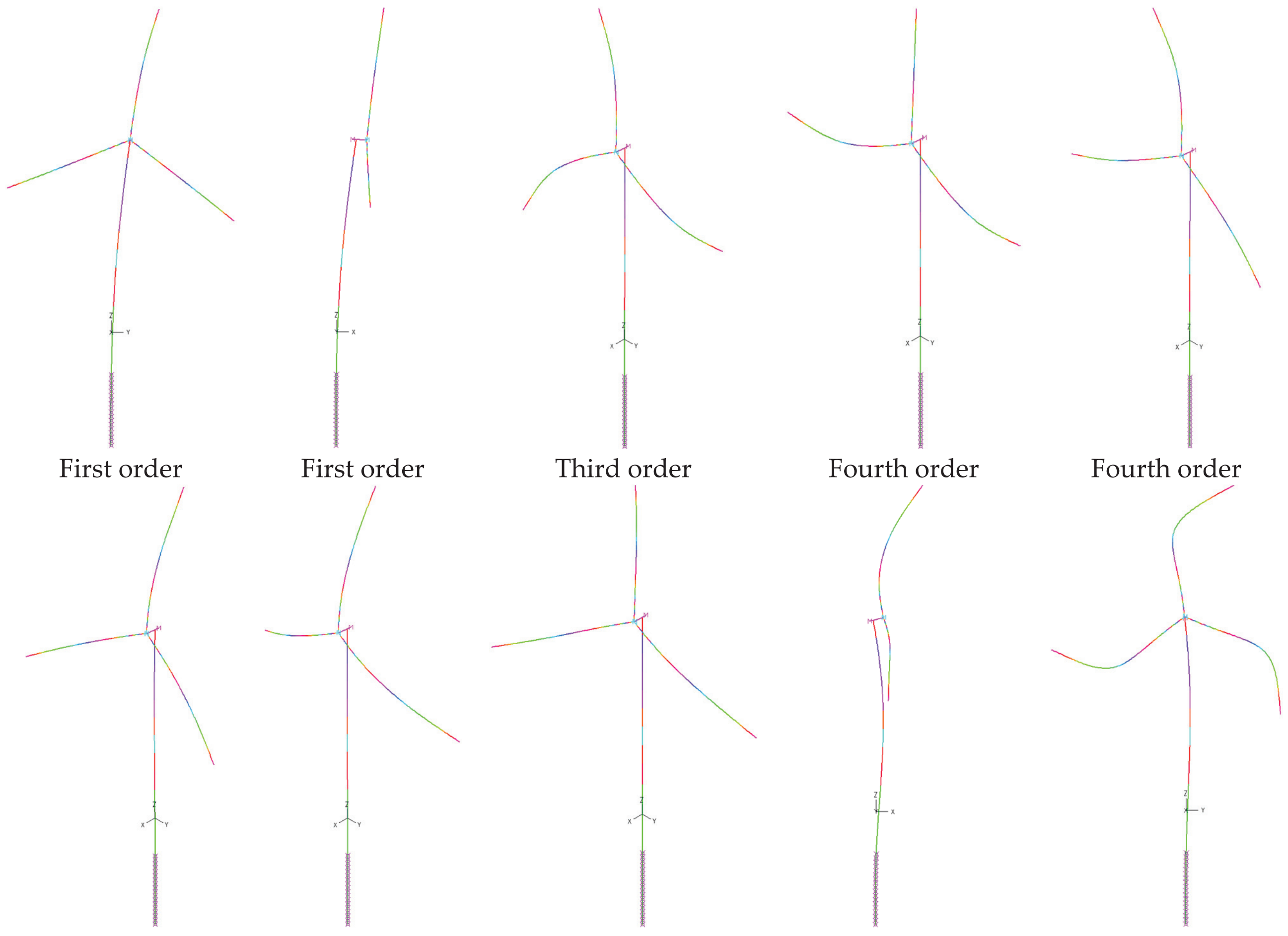

First order First order Third order Fourth order Fourth order

Sixth order Seventh order Eighth order Ninth order Tenth order

Figure 7. First ten mode shapes of the 5 MW MOWT using the flexible blade model.

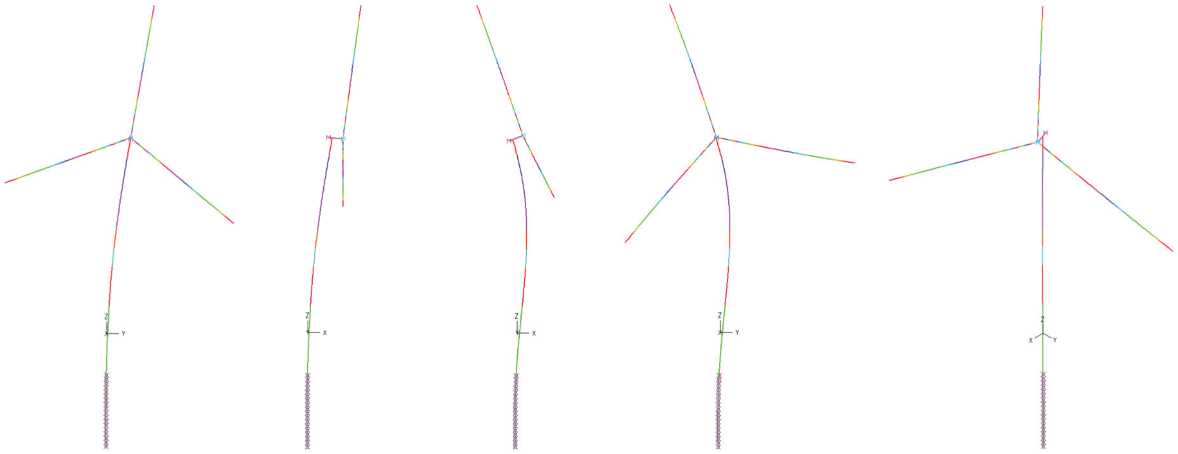

First order Second order Third order Fourth order Fifth order

Figure 8. First five mode shapes of 5 MW MOWT using the rigid blade model.

The natural frequencies of the 10 MW MOWT are compared in Table 6, and the corresponding modes are illustrated in Figures 9 and 10. The results of the flexible blade model closely match those in our previous study [49], with a relative error of less than 1.0%. The disparities between the flexible blade and rigid blade models showed similarities to those observed for the 5 MW MOWT. Specifically, the rigid blade model exhibited a

19% overestimation in the first torsional mode of the tower, while the second fore–aft and the second side-to-side tower modes of the tower were underestimated by 11% and 13%, respectively.

Table 6. Full-system natural frequencies of the 10 MW MOWT.

Flexible Blade Model			Rigid Blade Model			Existing Result [49]		
Mode	**Frequency /Hz**	**Description**	**Mode**	**Frequency /Hz**	**Description**	**Mode**	**Frequency /Hz**	**Description**
1	0.2138	1st Tower Side-to-side	1	0.2147	1st Tower Side-to-side	1	0.217	1st Tower Side-to-Side
2	0.2152	1st Tower Fore–Aft	2	0.2158	1st Tower Fore–Aft			
3	0.4896	1st Blade Asymmetric Edgewise	3	1.0740	1st Tower Torsion			
4	0.5078	1st Blade Symmetric Edgewise	4	1.1169	2nd Tower Fore–Aft			
5	0.5138	1st Blade Asymmetric Edgewise	5	1.2096	2nd Tower Side-to-side			
6	0.6811	1st Blade Asymmetric Flapwise						
7	0.8331	1st Blade Symmetric Flapwise						
8	0.9069	1st Tower Torsion						
9	1.2496	2nd Tower Fore–Aft and 2nd Blade Asymmetric Edgewise						
10	1.3817	2nd Tower Side-to-side and 2nd Blade Asymmetric Flapwise						

The natural frequencies of the first five modes of the full system using the rigid blade model are presented in Table 7. For comparison, the natural frequencies of corresponding modes of the system using the flexible blade model are provided, along with the relative difference between them. It is important to note that the term ‘corresponding’ refers to the similarity in tower deflection shapes between the two models. From Table 7, it is evident that the flexible blade model predicts significantly different natural frequencies for higher tower modes in the fore–aft direction of wind turbines.

Table 7. Natural frequencies for the fore–aft tower modes.

5 MW MOWT				10 MW MOWT			
Mode	**Rigid (Hz)**	**Flexible (Hz)**	**Relative Difference (%)**	**Mode**	**Rigid (Hz)**	**Flexible (Hz)**	**Relative Difference (%)**
1	0.2484	0.2487	−0.12	1	0.2158	0.2152	0.27
2	1.26	1.41	−10.01	2	1.12	1.25	−10.41
3	2.52	3.04	−17.11	3	2.2	2.96	−25.66
4	4.56	4.94	−8.33	4	3.91	4.87	−19.72
5	7.41	7.88	−6.34	5	6.27	7.04	−10.94

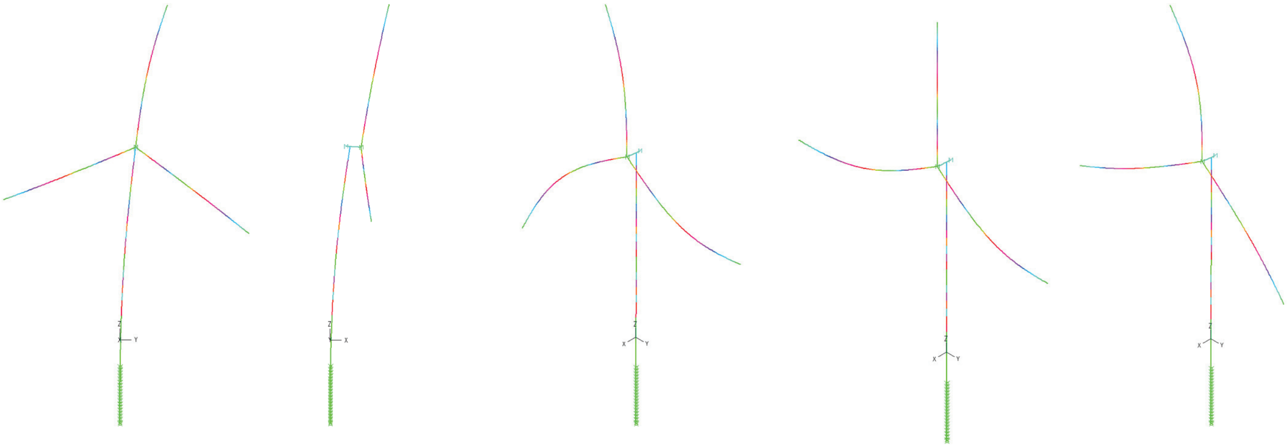

First order Second order Third order Fourth order Fifth order

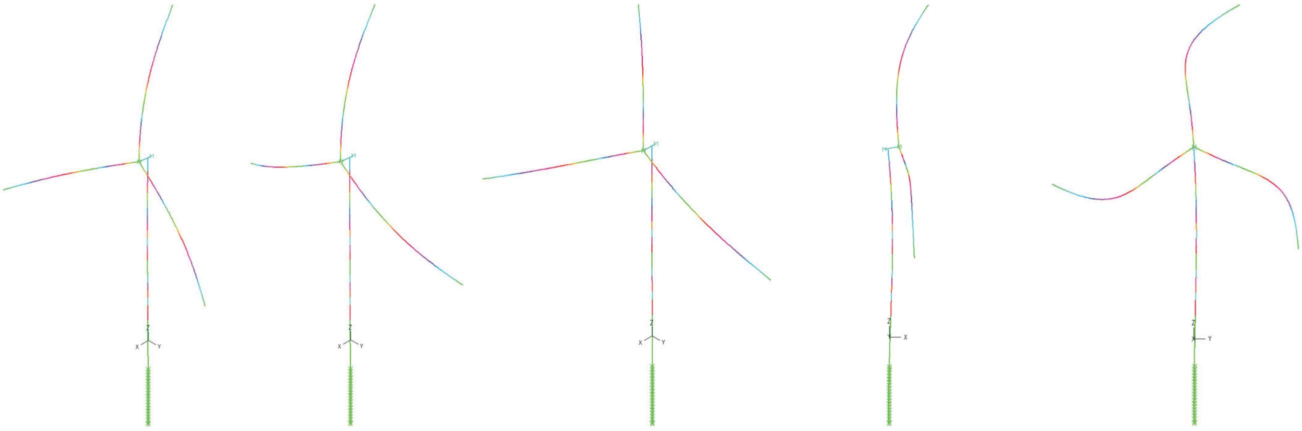

Sixth order Seventh order Eighth order Ninth order Tenth order

Figure 9. First ten mode shapes of the 10 MW MOWT using the flexible blade model.

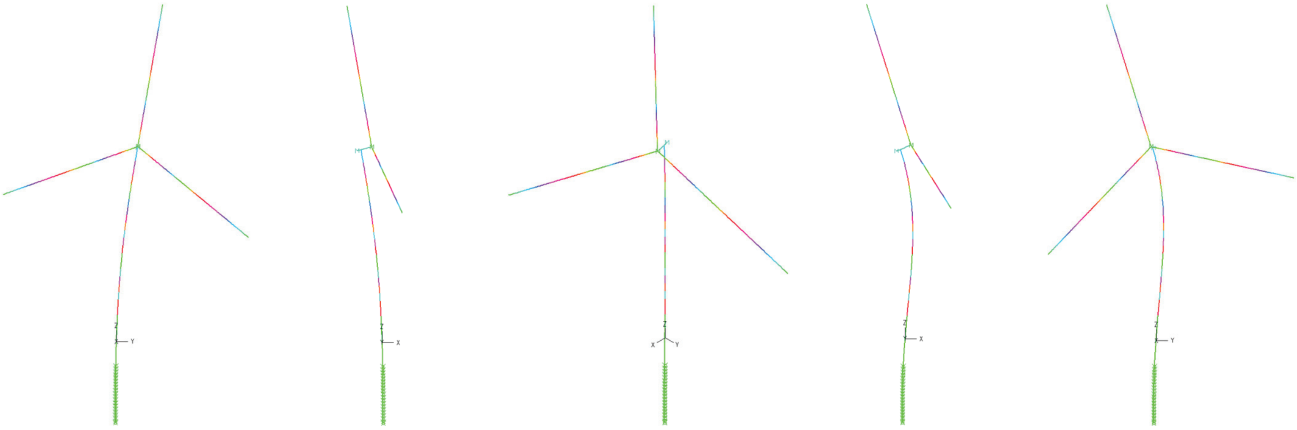

First order Second order Third order Fourth order Fifth order

Figure 10. First five mode shapes of the 10 MW MOWT using the rigid blade model.

This section compares the variations in natural frequencies and mode shapes predicted by the flexible blade and rigid blade models of MOWTs. It can be concluded that the rigid flexibility has little influence on the natural frequencies of the first and second modes of the full system. However, the examination of higher-order modes and their natural frequencies reveals that blade flexibility significantly influences their natural frequencies.

3.2. Dynamic Response of the 5 MW and 10 MW MOWTs Excited by Wave Load

For load case 1 of Table 2, Figure 11 depicts the time histories of tower-top acceleration and their Fourier amplitude spectra obtained from both the flexible and rigid blade models for the 5 MW MOWT. The tower-top accelerations obtained from these models exhibited a high degree of consistency in this load case. For MOWTs, wave loads are typically characterized as low-frequency excitations, resulting in the prevalence of low-order modes in the structural dynamic response. Furthermore, Figure 11b demonstrates that the tower-top acceleration was primarily characterized by low frequencies. Considering the satisfactory agreement between the two models in predicting the low-order dynamic characteristics of MOWTs, the prediction relative difference in the dynamic response of the system under wave excitations would be relatively minimal. In this context, the relative difference in the analysis results of the two models can be defined as

$$\delta = \frac{|R_\mathrm{r} - R_\mathrm{f}|}{R_\mathrm{f}} \times 100\% \tag{9}$$

where R_f and R_r represent the response amplitude of MOWTs using the flexible blade model and rigid blade model, respectively. Figure 12 illustrates the relative difference in tower-top displacement, acceleration, mudline shear force, and bending moment obtained from both methods for the 5 MW MOWT. The maximum relative difference was less than 5%, indicating the high precision of the rigid blade model.

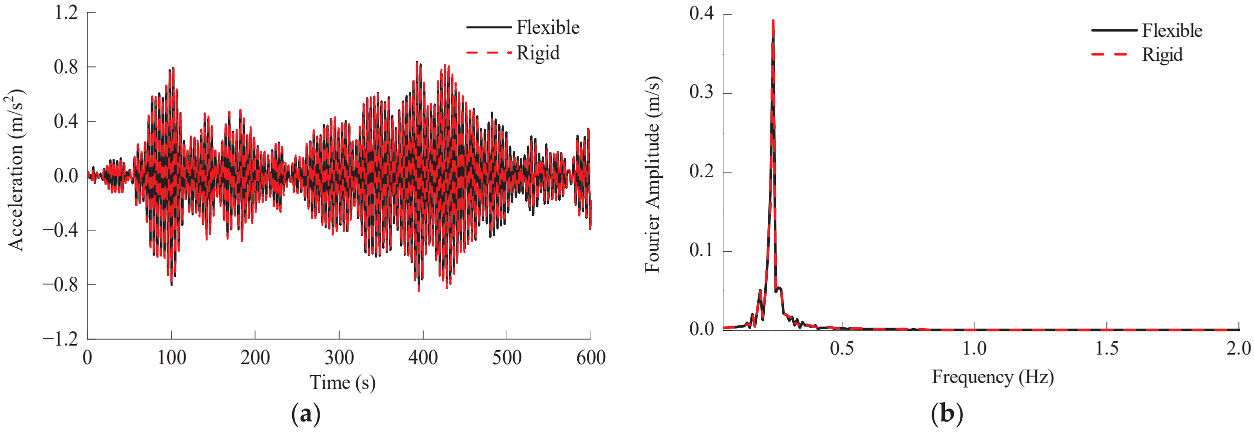

Figure 11. Nacelle response of the 5 MW MOWT using the flexible and rigid blade models: (**a**) nacelle acceleration time history; (**b**) nacelle Fourier amplitude.

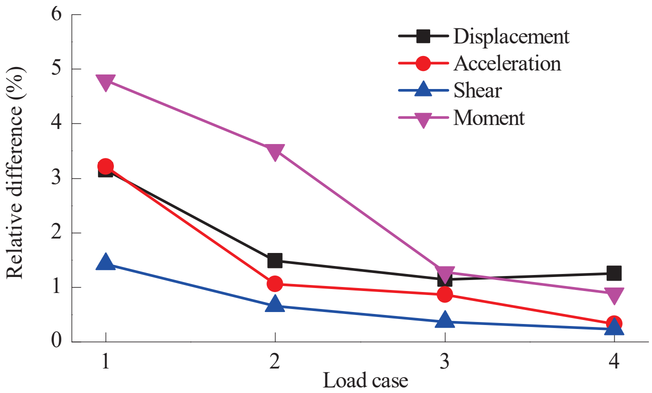

Figure 12. Response difference of the 5 MW MOWT between the flexible and rigid blade models.

The discrepancies between the two models for the 10 MW MOWT were similarly insignificant. Figure 13 displays the time histories of tower-top acceleration and their corresponding Fourier amplitude spectra obtained from both models for the 10 MW MOWT. Furthermore, Figure 14 offers a comprehensive depiction of the relative difference in tower-top displacement, acceleration, mudline shear force, and bending moment obtained from both methods for the 10 MW MOWT. All of these relative differences were less than 4%, which reveals that the flexibility of the blade has a negligible influence on predicting the dynamic response of the 10 MW MOWT excited by the wave.

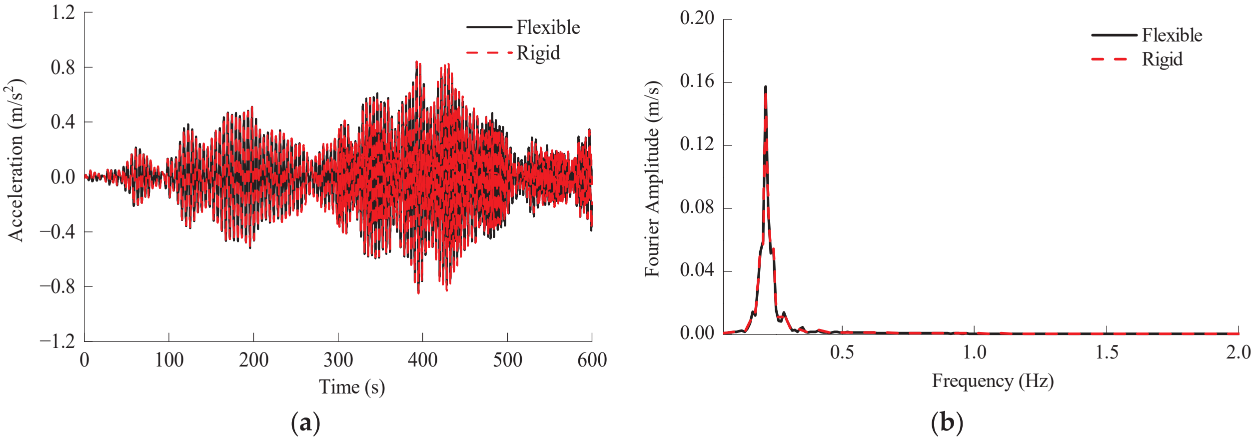

(**a**) (**b**)

Figure 13. Nacelle response of the 10 MW MOWT using the flexible and rigid blade models: (**a**) nacelle acceleration time history; (**b**) nacelle Fourier amplitude.

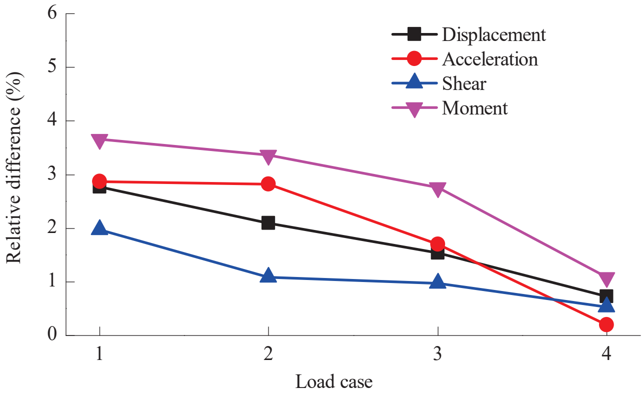

Figure 14. Response difference of the 10 MW MOWT between the flexible and rigid blade models.

This section investigates the disparities in predicting the dynamic response of MOWTs under wave excitations using both the flexible blade and rigid blade models. The results indicate that the relative differences between the two models for the selected indicators of structural dynamic response were below 5%, which meets the engineering margin requirement. Given that wave loads are characterized as low-frequency excitations and that blade flexibility has minimal impact on the low-order modes of MOWTs, the influence of blade flexibility on the dynamic response of MOWTs under wave excitations is insignificant.

3.3. Seismic Response of 5 MW and 10 MW MOWTs

For these two MOWTs, the decay of free vibration suggests a damping ratio of approximately 1% for the first mode. Therefore, Figure 15 illustrates the response spectra of the seismic records listed in Table 3 with a damping ratio of 1%. In this context, the non-dimensional amplification factor response spectrum is utilized, which is calculated as follows:

$$\beta(T) = \frac{S_a}{a_{\max}} \tag{10}$$

where S_a represents the absolute acceleration response spectrum value of the seismic motion, while a_{max} denotes the corresponding peak acceleration. This collection of earthquake records covers a broad range of periods, with a particular focus on the period interval [0.06 s, 3.8 s], where the amplification factor response spectrum can exceed 3.0. This interval encompasses the first 40 or so mode shapes of the 5 MW and 10 MW MOWTs. Therefore, the use of this set of strong earthquake records to examine the disparities between the flexible blade and rigid blade models is representative.

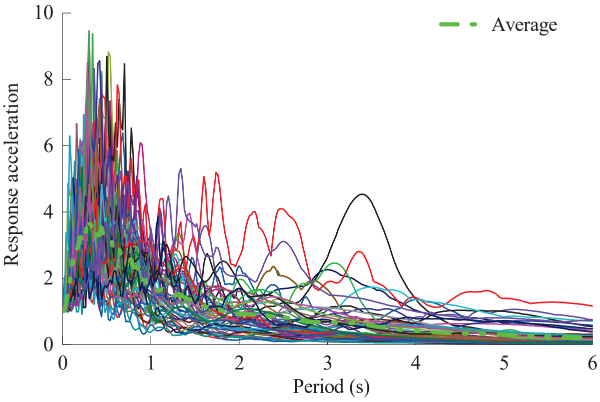

Figure 15. Non-dimensional response acceleration of input ground motion (the solid lines represent the response spectra of different seismic records).

Figure 16 depicts a horizontal acceleration time history recorded by the Bolu station during the 1999 Duzce earthquake in Turkey and the 1% damped response spectrum. The primary period of this seismic record is 0.32 s, which qualifies as high-frequency excitation for both wind turbines in this study. For the 5 MW MOWT, Figure 17 presents the tower-top acceleration time history and the corresponding Fourier amplitude spectrum obtained from both the flexible blade and rigid blade models. The peak acceleration of the nacelle for the flexible blade model was 4.84 m/s^2, while it was 6.47 m/s^2 for the rigid blade model, resulting in a relative difference of 33.8%. The Fourier amplitude spectra for the first mode of both models were 0.86 and 0.90, respectively, indicating minimal differences. However, for the second, third, and fourth modes of the tower, the Fourier spectra values obtained from the rigid blade model were significantly greater than those from the flexible blade model. According to the natural frequencies listed in Table 5 and the acceleration response spectrum in Figure 16b, the response spectrum value corresponding to the second mode of the tower in the rigid blade model was 0.60, whereas it was 0.43 in the flexible blade model. This discrepancy leads to a higher predicted peak acceleration of the nacelle from the rigid blade model compared to the flexible model.

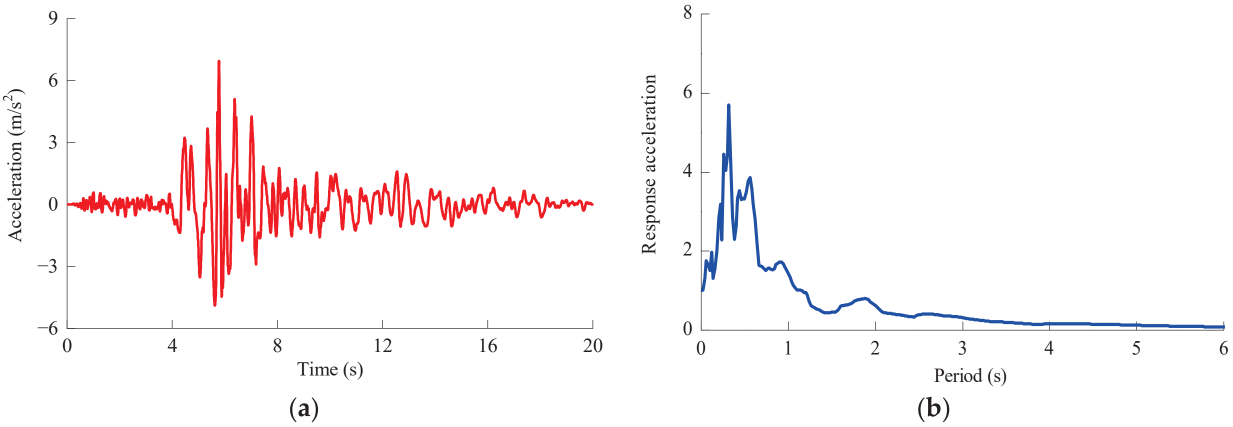

(**a**) (**b**)

Figure 16. Bolu record of the 1999 Duzce earthquake in Turkey: (**a**) acceleration time history; (**b**) non-dimensional response acceleration.

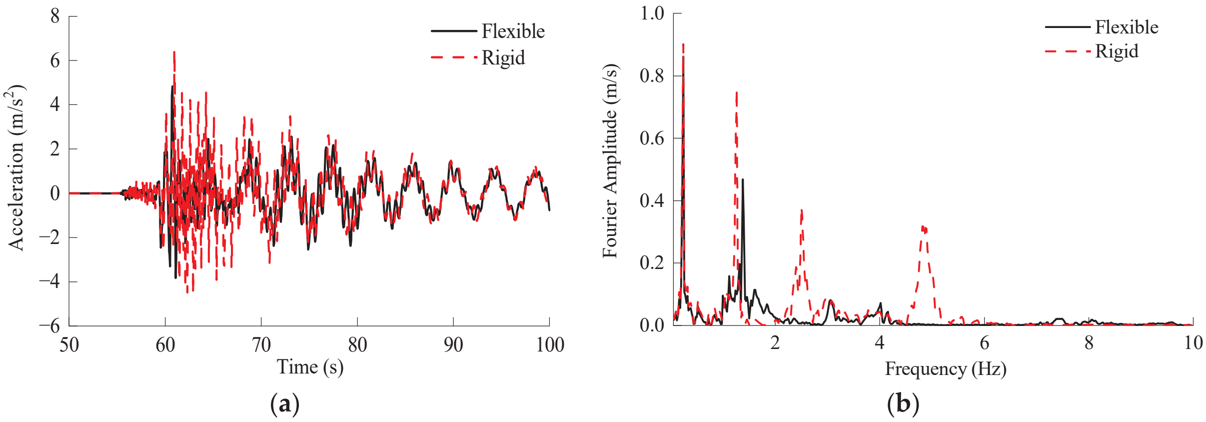

(**a**) (**b**)

Figure 17. Nacelle acceleration of 5 MW MOWT excited by the Bolu record: (**a**) nacelle acceleration time history; (**b**) Fourier amplitude spectra.

For the 5 MW MOWT, Figure 18a illustrates the time history of the mudline bending moment of the monopile obtained from both the flexible blade and rigid blade models. The peak mudline bending moment for the flexible blade model was 123.5 MN·m, whereas it was 163.3 MN·m for the rigid blade model, resulting in a relative difference of 38.7%. To normalize the bending moment time history, the following formula was employed:

$$\overline{M}(t) = \frac{M(t)}{M_{\mathrm{fr,max}}} \tag{11}$$

where $\overline{M}(t)$ is the dimensionless bending moment time history, M(t) represents the tower bending moment time history, and $M_{\mathrm{fr,max}}$ is the maximum tower bending moment predicted by both the flexible blade and rigid blade models. The Fourier spectra of the dimensionless bending moment were analyzed and are presented in Figure 18b for both the flexible blade and rigid blade models of the 5 MW MOWT. The Fourier amplitude spectra for the first mode of both models were 0.238 and 0.24, respectively, indicating minimal difference. However, for the second tower mode, the Fourier spectra value obtained from the rigid blade model was significantly greater than that from the flexible blade model. Since the second tower mode is substantially excited in the rigid blade model, the mudline bending moment was higher compared to the flexible model.

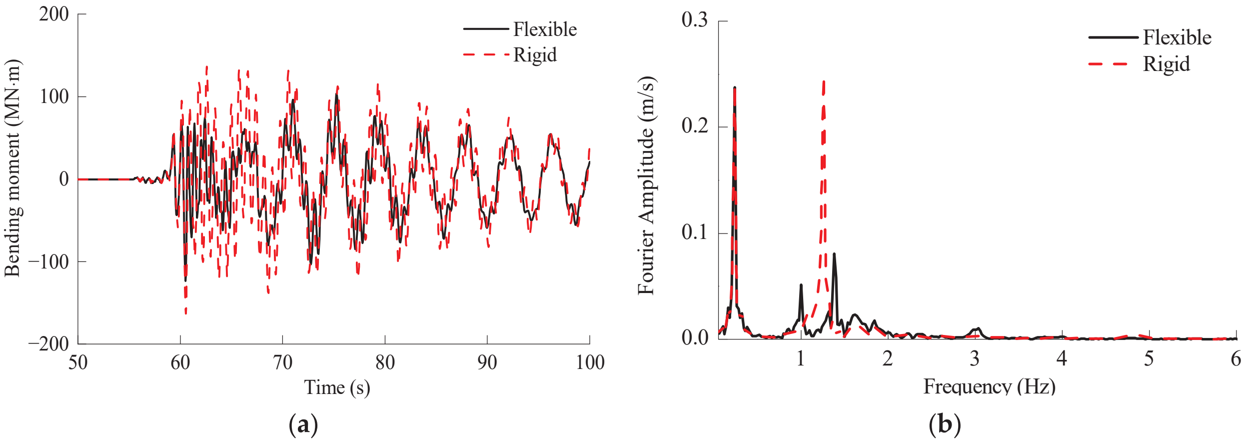

(**a**) (**b**)

Figure 18. Mudline bending moment of the 5 MW MOWT excited by the Bolu record: (**a**) mudline bending moment of the monopile; (**b**) Fourier amplitude spectra.

For the 10 MW MOWT, Figure 19 depicts the tower-top acceleration time history and the corresponding Fourier amplitude spectrum obtained from both the flexible blade and rigid blade models. The peak acceleration of the nacelle was 5.95 m/s^2 for the flexible blade model, while it was 8.31 m/s^2 for the rigid blade model, resulting in a relative difference of 39.6%. Regarding the first four modes of the tower, the Fourier spectra values for the rigid blade model were significantly higher than those for the flexible blade model. Figure 20 displays the time history of the mudline bending moment and its Fourier amplitude spectrum for both the flexible blade and rigid blade models. The peak bending moment of the mudline was 278.7 MN·m for the flexible blade model, while it was 348.2 MN·m for the rigid blade model, resulting in a relative difference of 24.9%. In addition, it can be concluded that the Fourier spectra corresponding to the second mode of the rigid blade model were significantly greater than that of the flexible blade model according to Figure 20b.

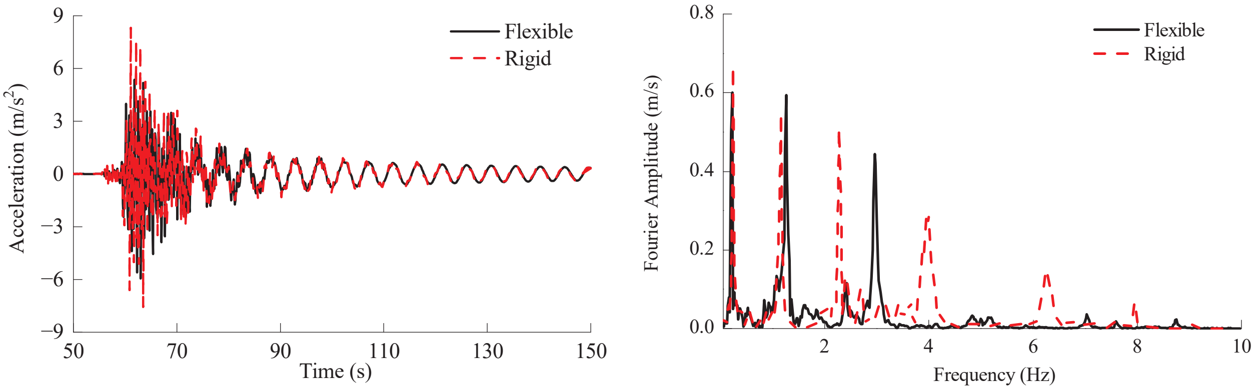

(**a**) (**b**)

Figure 19. Nacelle acceleration of the 10 MW MOWT excited by the Bolu record: (**a**) nacelle acceleration time history; (**b**) Fourier amplitude spectra.

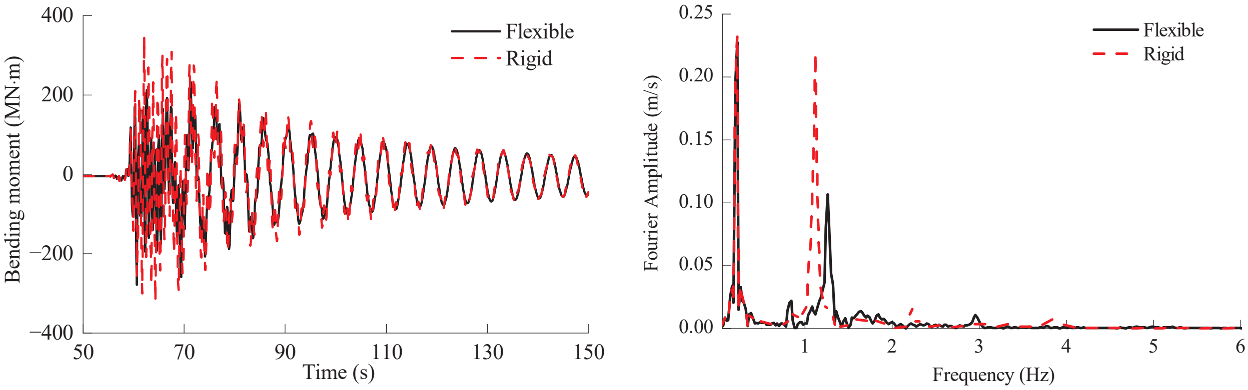

(**a**) (**b**)

Figure 20. Mudline bending moment of the 10 MW MOWT excited by the Bolu record: (**a**) mudline bending moment of the monopile; (**b**) Fourier amplitude spectra.

Figure 21 presents a horizontal acceleration time history recorded by the Capitola station during the 1989 Loma Prieta earthquake and the 1% damped response spectrum. The dominant period of this seismic record is 0.28 s, which is also high-frequency excitation for these wind turbines. For the 5 MW MOWT, Figure 22 displays the tower-top acceleration time history and the corresponding Fourier amplitude spectrum obtained from both the flexible blade and rigid blade models. The peak acceleration of the nacelle was 6.59 m/s^2 for the flexible blade model, while it was 4.84 m/s^2 for the rigid blade model, resulting in a relative difference of −26.6%. In terms of the second mode of the system, the Fourier spectra value obtained from the flexible blade model was approximately 5 times that of the rigid blade model. Considering the natural frequencies listed in Table 5 and the acceleration response spectrum in Figure 21b, the response spectrum value corresponding to the second mode frequency of the tower was 0.95 for the rigid blade model and 0.51 for the flexible blade model. This disparity leads to a significantly higher predicted peak acceleration of the nacelle from the flexible blade model compared to the rigid model.

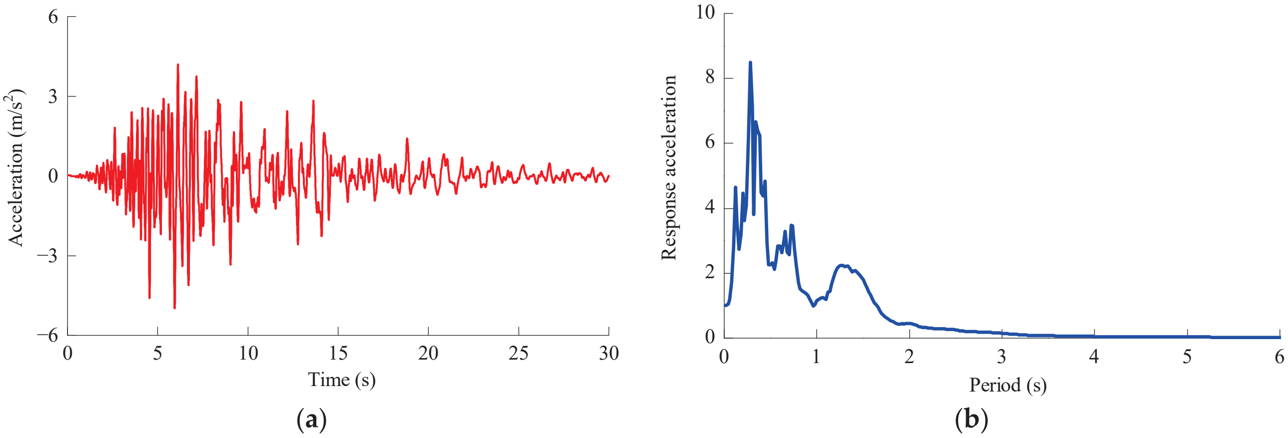

Figure 21. Capitola record of the 1989 Loma Prieta earthquake: (**a**) acceleration time history; (**b**) non-dimensional response acceleration.

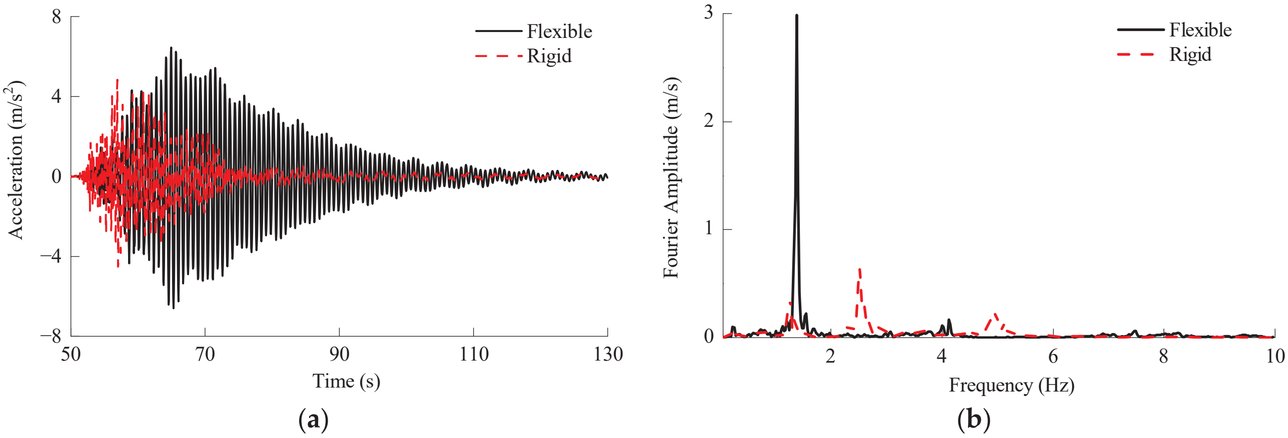

Figure 22. Nacelle acceleration of the 5 MW MOWT excited by Capitola record: (**a**) nacelle acceleration time history; (**b**) Fourier amplitude spectra.

Figure 23a presents the time history of the mudline bending moment for the 5 MW MOWT obtained from both the flexible blade and rigid blade models. The flexible blade model predicts a maximum mudline bending moment of 167.9 MN·m, while the rigid blade model predicts a value of 102.1 MN·m, resulting in a relative difference of −39.3%. Additionally, Figure 23b illustrates the dimensionless Fourier amplitude spectra of the mudline bending moment, comparing the results obtained from both models. The spectra for the first mode were 0.0336 and 0.034, respectively, indicating a small difference. However, for the second tower mode, the flexible blade model exhibited significantly higher Fourier spectrum values compared to the rigid blade model. This discrepancy arises from the significant excitation of the second tower mode in the flexible blade model, resulting in a higher mudline bending moment compared to the prediction of the rigid blade model.

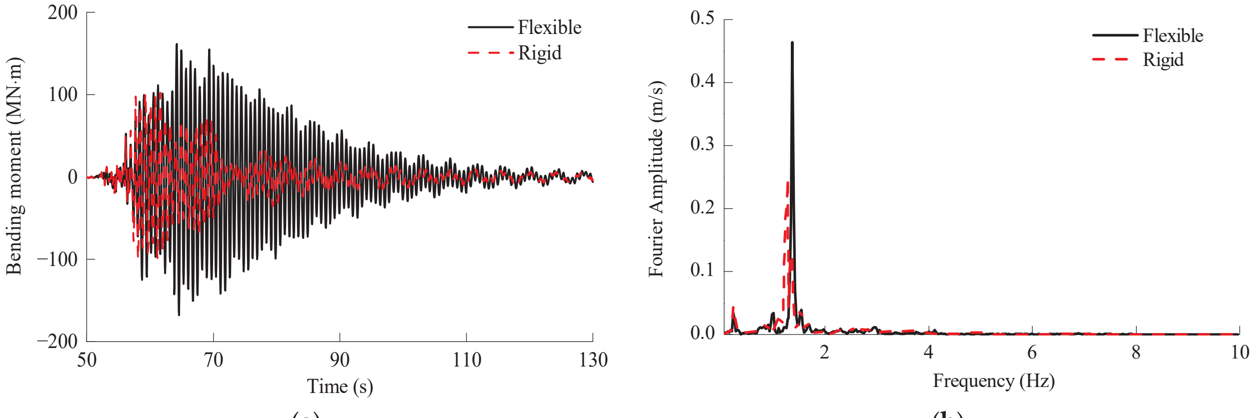

(a)

(b)

Figure 23. Mudline bending moment of the 5 MW MOWT excited by the Capitola record: (**a**) mudline bending moment of the monopile; (**b**) Fourier amplitude spectra.

Figure 24 illustrates the tower-top acceleration time history and its Fourier amplitude spectra for the 10 MW MOWT, obtained from these two different analysis models. The peak nacelle acceleration was 5.41 m/s^2 for the flexible blade model, while the rigid blade model predicted a value of 6.86 m/s^2, resulting in a relative difference of 26.8%. The Fourier spectrum values for the third and fourth tower modes were significantly higher in the rigid blade model compared to the flexible blade model. In Figure 25a, the time history of the mudline bending moment is depicted for both the flexible blade and rigid blade models. The flexible blade model estimated a peak mudline bending moment of 207.3 MN·m, while the rigid blade model predicted a value of 162.1 MN·m, resulting in a relative difference of −21.8%. Figure 25b displays the dimensionless Fourier amplitude spectra of the mudline bending moment for the 10 MW MOWT. Obviously, the Fourier spectra value corresponding to the second tower mode was significantly higher in the flexible blade model compared to the rigid blade model.

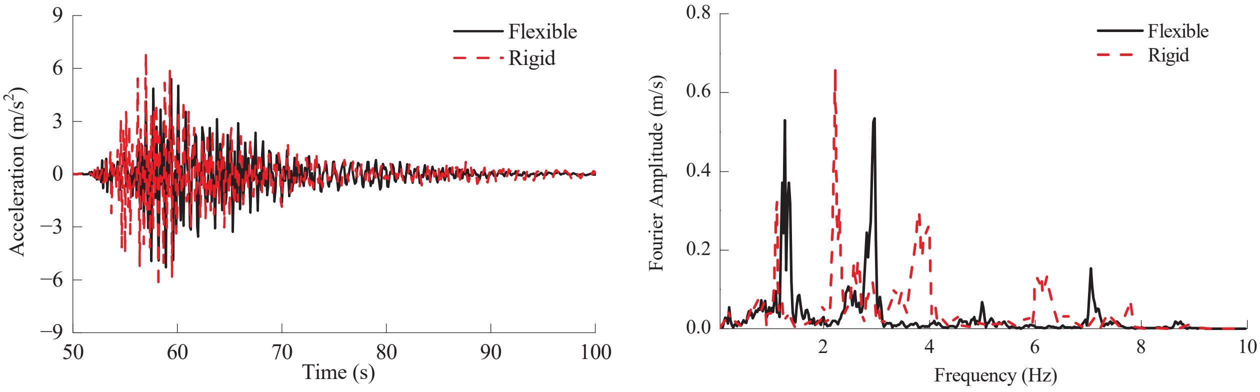

(a)

(b)

Figure 24. Nacelle acceleration of the 10 MW MOWT excited by the Capitola record: (**a**) nacelle acceleration time history; (**b**) Fourier amplitude spectra.

The rigid blade model fails to adequately capture the dynamic characteristics of these two MOWTs, including higher-order natural frequencies and modes. Additionally, the low damping exhibited by the MOWT in the parked state exacerbates the oscillation of the acceleration response spectra. As a result, when subjected to seismic excitation, the rigid blade model is prone to significant inaccuracies in predicting the dynamic response of the OWTs. Specifically, for the same MOWT and input seismic motion, the rigid blade model may significantly overestimate or underestimate various system response parameters. For example, this includes the tower-top acceleration and mudline bending moment of the 10 MW MOWT when exposed to the Capitola seismic record.

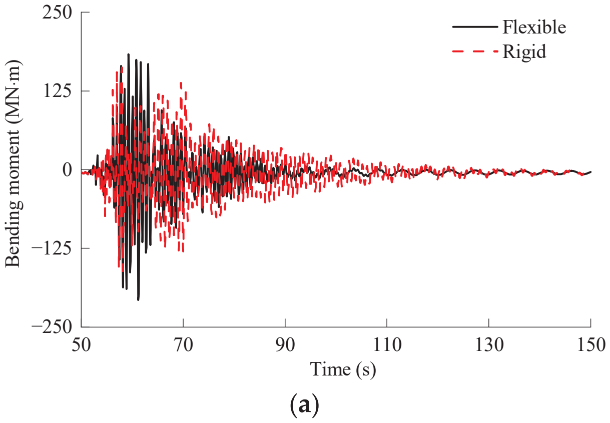

Figure 25. Mudline bending moment of the 10 MW MOWT excited by the Capitola record: (**a**) mudline bending moment of the monopile; (**b**) Fourier amplitude spectra.

In seismic load cases, the relative difference in the seismic response of MOWTs caused by the overestimation or underestimation of the rigid blade model can be defined as follows:

$$\delta_E = \frac{R_{\mathrm{E,r}} - R_{\mathrm{E,f}}}{R_{\mathrm{E,f}}} \times 100\% \tag{12}$$

where $R_{\mathrm{E,f}}$ represents the peak response obtained from the flexible blade model under seismic excitation and $R_{\mathrm{E,r}}$ represents the peak response obtained from the rigid blade model under seismic excitation. Figure 26 depicts the relative difference in nacelle acceleration predicted by the rigid blade model for both the 5 MW and 10 MW MOWTs when subjected to the seismic motions listed in Table 3. For the 5 MW MOWT, 29 seismic excitations resulted in a nacelle acceleration relative difference that exceeded the range of [−15%, 15%]. Similarly, for the 10 MW turbine, this number was 26. Figure 27 illustrates the relative difference in the mudline bending moment predicted by the rigid blade model for both turbines. In the case of the 5 MW MOWT, 31 seismic excitations led to a peak mudline bending moment relative difference beyond the range of [−15%, 15%], while for the 10 MW turbine, this number was 28. Considering the precision requirements in seismic engineering, models with relative differences exceeding 15% should be improved to enhance accuracy. Hence, the flexibility of the blades may have a noteworthy impact on the seismic response of MOWTs.

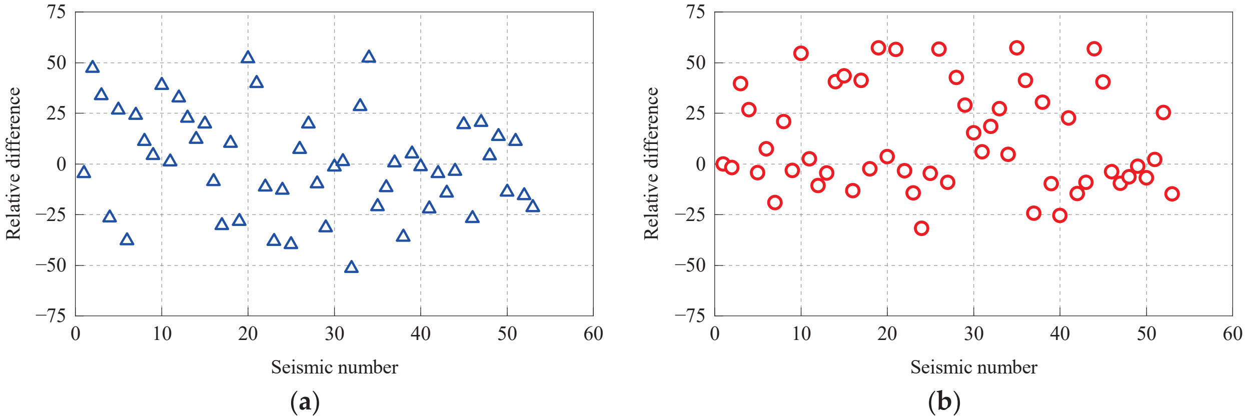

Figure 26. Relative difference in nacelle peak acceleration: (**a**) error for the 5 MW MOWT; (**b**) error for the 10 MW MOWT.

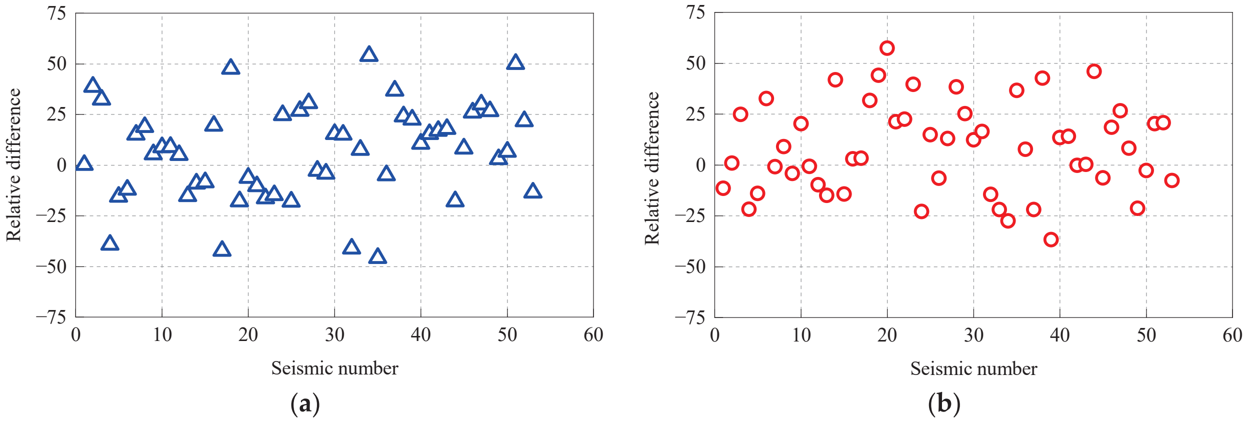

(**a**) (**b**)

Figure 27. Relative difference of the mudline bending moment: (**a**) error for the 5 MW MOWT; (**b**) error for the 10 MW MOWT.

If the rigid blade model is used due to a lack of stiffness data of the blades, it is crucial that it undergo a comprehensive model verification process. This verification should include parameters that have an impact on the safety of the turbine and support structures. Additionally, selecting an adequate number of seismic motions is essential to minimize the possibility of incorrect outcomes. For example, Figure 28 demonstrates the difference in nacelle displacement predicted by the rigid blade model for the aforementioned two MOWTs. If only a subset of seismic motions from Table 3 is considered, focusing solely on nacelle displacement response, it may lead to an improper conclusion regarding the suitability of the rigid model for predicting the seismic response of these two MOWTs.

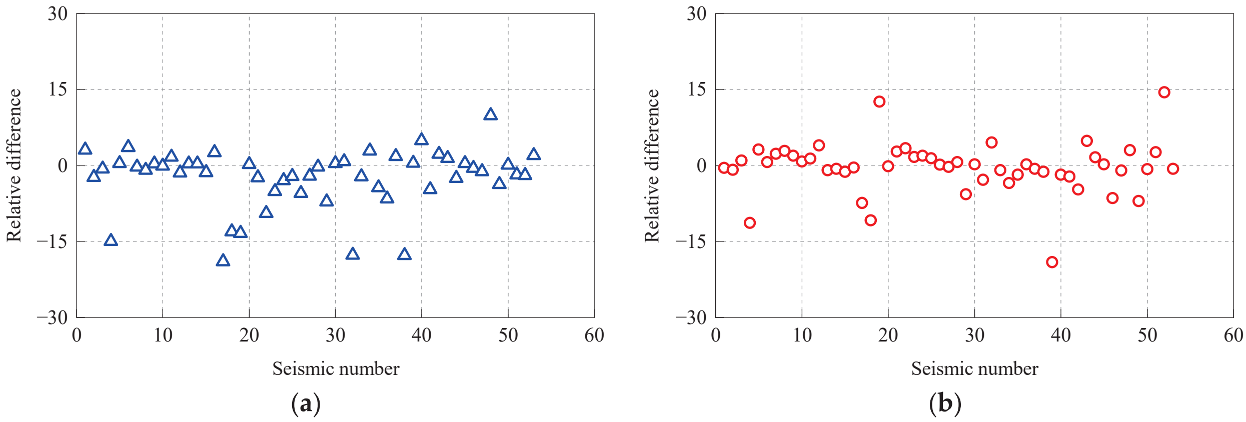

(**a**) (**b**)

Figure 28. Relative error of nacelle displacement: (**a**) error for the 5 MW MOWT; (**b**) error for the 10 MW MOWT.

4. Conclusions and Outlook

It is usually difficult to obtain the structural properties of blades for commercial wind turbines. In this circumstance, the flexibility of blades is neglected, and the rotor is simplified as a rigid body. This study examined the structural models of the 5 MW and DTU 10 MW MOWTs considering flexible blade and rigid blade configurations. The discrepancies in predicting natural frequencies and modes between these two models were analyzed, and the differences in the dynamic response of wind turbines under wave and seismic excitations were evaluated. Based on these findings, the following conclusions can be drawn:

1. The rigid blade model failed to account for the flexible deformation of the blades, which led to the exclusion of blade-deformation-dominated modes when determining the system modes. Moreover, it introduced significant differences when calculating

the higher-order natural frequencies. For instance, the frequency of the second fore–aft tower mode for the 5 MW and 10 MW MOWTs was underestimated by 12% and 13%, respectively. Therefore, the flexibility of the blades can have a remarkable impact on the higher-order modes and natural frequencies of MOWTs.

2. The dynamic response of both MOWTs under wave excitations was mainly governed by the first tower mode, with the blade flexibility having a minimal influence. The rigid blade model effectively predicted the deformation and internal forces of the supported structure of MOWTs in this load case. Taking nacelle acceleration and the mudline bending moment, for example, the maximum discrepancy between the rigid and flexible blade models was less than 5%. Hence, the flexibility of the blades has a negligible impact on the dynamic response of MOWTs solely excited by waves.
3. The seismic excitation generally consists of rich high-frequency components that strongly stimulate higher-order tower modes. As a result, the rigid blade model tended to substantially underestimate or overestimate the peak seismic response of these two MOWTs. For example, in terms of nacelle acceleration and the mudline bending moment, the maximum relative difference between the rigid blade and flexible blade model exceeded 50%. Therefore, blade flexibility has a notable influence on the seismic response of MOWTs.

Based on the aforementioned conclusions, several modeling requirements of blades for the dynamic analysis of MOWTs can be identified. When analyzing the low-order modes and dynamic responses of OWTs under wave excitations, the influence of blade flexibility can be neglected. The rotor can be simplified as a lumped mass, requiring only its total mass and moment of inertia. However, when analyzing the high-order modes and dynamic response of OWTs under seismic excitations, it is necessary to consider the flexibility of blades. In this situation, the structural model should, at minimum, accurately represent the distribution characteristics of blade mass and stiffness. Although these conclusions and prospects are based on the numerical simulations conducted in this study, relevant experimental research and theoretical analyses can also draw inspiration from them.

Author Contributions: Conceptualization, Y.L. and R.X.; methodology, W.L.; software, Y.L. and G.X.; validation, Y.L., R.X. and P.W.; formal analysis, B.H. and R.X.; investigation, Y.L., W.L., R.X. and P.W.; resources, W.L.; data curation: B.H. and G.X.; writing—original draft preparation, Y.L.; writing—review and editing, Y.L., B.H. and R.X.; visualization, W.L., B.H. and G.X.; supervision, Y.L. and R.X.; project administration, Y.L. and R.X.; funding acquisition, Y.L. and R.X. All authors have read and agreed to the published version of the manuscript.

Funding: This research is funded by the China Postdoctoral Science Foundation (2022M722960), Zhejiang Provincial Natural Science Foundation of China (LQ23E090003), National Natural Science Foundation of China (52278480) and Postdoctoral Science Preferential Funding of Zhejiang Province.

Institutional Review Board Statement: Not applicable.

Informed Consent Statement: Not applicable.

Data Availability Statement: The data presented in this study are available in this article (tables and figures).

Conflicts of Interest: The authors declare no conflict of interest.

References

1. Subbulakshmi, A.; Verma, M.; Keerthana, M.; Sasmal, S.; Harikrishna, P.; Kapuria, S. Recent advances in experimental and numerical methods for dynamic analysis of floating offshore wind turbines-an integrated review. *Renew. Sustain. Energy Rev.* **2022**, *164*, 112525. [CrossRef]
2. GWEC. Global Wind Report: Annual Market Update 2022. *Global Wind Energy Council.* 2023. Available online: https://gwec.net/wp-content/uploads/2020/04/GWEC-Global-Wind-Report-2019.pdf (accessed on 20 July 2023).
3. Veers, P.S.; Dykes, K.; Lantz, E.; Barth, S.; Bottasso, C.L.; Carlson, O.; Clifton, A.; Green, J.; Green, P.; Holttinen, H.; et al. Grand challenges in the science of wind energy. *Science* **2019**, *366*, eaau2027. [CrossRef] [PubMed]

4. Yeter, B.; Garbatov, Y. Structural integrity assessment of fixed support structures for offshore wind turbines: A review. *Ocean Eng.* **2022**, *244*, 110271. [CrossRef]
5. Wang, W.; Li, X.; Pan, Z.; Zhao, Z. Motion control of pentapod offshore wind turbines under earthquakes by tuned mass damper. *J. Mar. Sci. Eng.* **2020**, *7*, 224. [CrossRef]
6. Jahani, K.; Langlois, R.G.; Afagh, F.F. Structural dynamics of offshore wind turbines: A review. *Ocean Eng.* **2022**, *251*, 111136. [CrossRef]
7. Leng, D.; Yang, Y.; Xu, K.; Li, Y.; Xie, Y. Vibration control of offshore wind turbine under multiple hazards using single variable-stiffness tuned mass damper. *Ocean Eng.* **2021**, *236*, 109473. [CrossRef]
8. Ko, Y.-Y.; Li, Y.-T. Response of a scale-model pile group for a jacket foundation of an offshore wind turbine in liquefiable ground during shaking table tests. *Earthq. Eng. Struct. Dyn.* **2020**, *49*, 1682–1701. [CrossRef]
9. Manwell, J.F.; McGowan, J.G.; Rogers, A.L. *Wind Energy Explained: Theory, Design and Application*, 2nd ed.; Wiley: Sussex, UK, 2010.
10. Failla, G.; Santangelo, F.; Foti, G.; Scali, F.; Arena, F. Response-spectrum uncoupled analyses for seismic assessment of offshore wind turbines. *J. Mar. Sci. Eng.* **2018**, *6*, 85. [CrossRef]
11. Zhao, Z.; Dai, K.; Lalonde, E.R.; Meng, J.; Li, B.; Ding, Z.; Bitsuamlak, G. Studies on application of scissor-jack braced viscous damper system in wind turbines under seismic and wind loads. *Eng. Struct.* **2019**, *196*, 109294. [CrossRef]
12. Fan, J.; Li, Q.; Zhang, Y. Collapse analysis of wind turbine tower under the coupled effects of wind and near-field earthquake. *Wind Energy* **2019**, *22*, 407–419. [CrossRef]
13. Santangelo, F.; Failla, G.; Arena, F.; Ruzzo, C. On time-domain uncoupled analyses for offshore wind turbines under seismic loads. *Bull. Earthq. Eng.* **2018**, *16*, 1007–1040. [CrossRef]
14. Zuo, H.; Bi, K.; Hao, H. Dynamic analyses of operating offshore wind turbines including soil-structure interaction. *Eng. Struct.* **2018**, *157*, 42–62. [CrossRef]
15. Zuo, H.; Bi, K.; Hao, H.; Xin, Y.; Li, J.; Li, C. Fragility analyses of offshore wind turbines subjected to aerodynamic and sea wave loadings. *Renew. Energy* **2020**, *160*, 1269–1282. [CrossRef]
16. Ali, A.; Risi, R.D.; Sextos, A. Finite element modeling optimization of wind turbine blades from an earthquake engineering perspective. *Eng. Struct.* **2020**, *222*, 111105. [CrossRef]
17. Huang, H.S. Simulations of 10mw wind turbine under seismic loadings. *Compos. Struct.* **2022**, *279*, 114686. [CrossRef]
18. Bazeos, N.; Hatzigeorgiou, G.D.; Hondros, I.D.; Karamaneas, H.; Karabalis, D.L.; Beskos, D.E. Static, seismic and stability analyses of a prototype wind turbine steel tower. *Eng. Struct.* **2002**, *24*, 1015–1025. [CrossRef]
19. Lavassas, I.; Nikolaidis, G.; Zervas, P.; Efthimiou, E.; Doudoumis, I.; Baniotopoulos, C. Analysis and design of the prototype of a steel 1-MW wind turbine tower. *Eng. Struct.* **2003**, *25*, 1097–1106. [CrossRef]
20. Martinez-Vazquez, P.; Gkantou, M.; Baniotopoulos, C. Strength demands of tall wind turbines subject to earthquakes and wind load. *Procedia Eng.* **2017**, *199*, 3212–3217. [CrossRef]
21. Hansen, M.O.L.; Sørensen, J.N.; Voutsinas, S.; Sørensen, N.; Madsen, H.A. State of the art in wind turbine aerodynamics and aero-elasticity. *Prog. Aerosp. Sci.* **2006**, *42*, 285–330. [CrossRef]
22. Dong, W.; Moan, T.; Gao, Z. Long-term fatigue analysis of multi-planar tubular joints for jacket-type offshore wind turbine in time domain. *Eng. Struct.* **2011**, *33*, 2002–2014. [CrossRef]
23. Abhinav, K.A.; Saha, N. Coupled hydrodynamic and geotechnical analysis of jacket offshore wind turbine. *Soil Dyn. Earthq. Eng.* **2015**, *73*, 66–79. [CrossRef]
24. Taflanidis, A.A.; Loukogeorgaki, E.; Angelides, D.C. Offshore wind turbine risk quantification/evaluation under extreme environmental conditions. *Reliab. Eng. Syst. Saf.* **2013**, *115*, 19–32. [CrossRef]
25. Jiang, W.; Lin, C.; Sun, M. Seismic responses of monopile-supported offshore wind turbines in soft clays under scoured conditions. *Soil Dyn. Earthq. Eng.* **2021**, *142*, 106549. [CrossRef]
26. Yeh, P.H.; Chung, S.H.; Chen, B.F. Multiple TLDs on motion reduction control of the offshore wind turbines. *J. Mar. Sci. Eng.* **2020**, *8*, 470. [CrossRef]
27. Jalbi, S.; Nikitas, G.; Bhattacharya, S.; Alexander, N. Dynamic design considerations for offshore wind turbine jackets supported on multiple foundations. *Mar. Struct.* **2019**, *67*, 102631. [CrossRef]
28. Feyzollahzadeh, M.; Mahmoodi, M.J.; Yadavar-Nikravesh, S.M.; Jamali, J. Wind load response of offshore wind turbine towers with fixed monopile platform. *J. Wind. Eng. Ind. Aerodyn.* **2016**, *158*, 122–138. [CrossRef]
29. Wang, X.; Zeng, X.; Yang, X.; Li, J. Seismic response of offshore wind turbine with hybrid monopile foundation based on centrifuge modelling. *Appl. Energy* **2019**, *235*, 1335–1350. [CrossRef]
30. Wang, P.; Zhao, M.; Du, X.; Liu, J.; Xu, C. Wind, wave and earthquake responses of offshore wind turbine on monopile foundation in clay. *Soil Dyn. Earthq. Eng.* **2018**, *113*, 47–57. [CrossRef]
31. Yu, D.O.; Kwon, O.J. Predicting wind turbine blade loads and aeroelastic response using a coupled CFD-CSD method. *Renew. Energy* **2014**, *70*, 184–196. [CrossRef]
32. Bayati, I.; Belloli, M.; Bernini, L.; Zasso, A. Aerodynamic design methodology for wind tunnel tests of wind turbine rotors. *J. Wind. Eng. Ind. Aerodyn.* **2017**, *167*, 217–227. [CrossRef]

33. Arany, L.; Bhattacharya, S.; Macdonald, J.H.G.; Hogan, S.J. Closed form solution of eigen frequency of monopile supported offshore wind turbines in deeper waters incorporating stiffness of substructure and ssi. *Soil Dyn. Earthq. Eng.* **2016**, *83*, 18–32. [CrossRef]
34. Jonkman, J.; Butterfield, S.; Musial, W.; Scott, G. *Definition of a 5-MW Reference Wind Turbine for Offshore System Development*; National Renewable Energy Laboratory: Golden, CO, USA, 2009. Available online: https://www.osti.gov/biblio/947422 (accessed on 1 July 2023).
35. Bak, C.; Zahle, F.; Bitsche, R.; Kim, T.; Yde, A.; Henriksen, L.C.; Hansen, M.H.; Blasques, J.P.A.A.; Gaunaa, M.; Natarajan, A. *Description of the DTU 10-MW reference wind turbine*; DTU Wind Energy: Frederiksborgvej, Roskilde, Denmark, 2013. Available online: https://orbit.dtu.dk/files/55645274/The_DTU_10MW_Reference_Turbine_Christian_Bak.pdf (accessed on 1 July 2023).
36. Lee, J.W.; Lee, J.S.; Han, J.H.; Shin, H.K. Aeroelastic analysis of wind turbine blades based on modified strip theory. *J. Wind. Eng. Ind. Aerodyn.* **2012**, *110*, 62–69. [CrossRef]
37. Tran, T.T.; Kim, D.H. The coupled dynamic response computation for a semi-submersible platform of floating offshore wind turbine. *J. Wind. Eng. Ind. Aerodyn.* **2015**, *147*, 104–119. [CrossRef]
38. Meng, H.; Jin, D.; Li, L.; Liu, Y. Analytical and numerical study on centrifugal stiffening effect for large rotating wind turbine blade based on NREL 5MW and WindPACT 1. *5MW models. Renew. Energy* **2022**, *183*, 321–329. [CrossRef]
39. DNV. *Design of Offshore Wind Turbine Structures*; Det Norske Veritas: Bærum, Norway, 2013.
40. Fischer, T.; De Vries, W.E.; Schmidt, B. *UpWind design basis WP4: Offshore foundations and support structures*; EU UpWind project: Stuttgart, Germany, 2010. Available online: https://repository.tudelft.nl/islandora/object/uuid:a176334d-6391-4821-8c5f-9c91b6b32a27/datastream/OBJ/download (accessed on 1 July 2023).
41. ATC. *Quantification of Building Seismic Performance Factors*; Report No FEMA-P695; Applied Technology Council: Redwood City, CA, USA, 2009.
42. ADINA. *ADINA Theory and Modeling Guide*; ADINA R&D Inc.: Watertown, MA, USA, 2014.
43. Bossanyi, E.A. *Bladed for Windows User Manual*; Garrad Hassan and Partners: Bristol, UK, 2016.
44. Sun, Y.L.; Xu, C.S.; Du, X.L.; Du, X.P.; Xi, R.Q. A modified p-y curve model of large-monopiles of offshore wind power plants. *Eng. Mech.* **2020**, *8*, 44–53. [CrossRef]
45. Kim, K.T.; Bathe, K.J. The Bathe subspace iteration method enriched by turning vectors. *Comput. Struct.* **2017**, *186*, 11–21. [CrossRef]
46. Makris, N.; Gazetas, G. Dynamic pile-soil-pile interaction. Part II: Lateral and seismic response. *Earthq. Eng. Struct. Dyn.* **1992**, *21*, 145–162. [CrossRef]
47. Xi, R.Q.; Xu, C.S.; Du, X.L.; Naggar, M.H.; Wang, P.G.; Liu, L.; Zhai, E.D. Framework for dynamic response analysis of monopile supported offshore wind turbine excited by combined wind-wave-earthquake loading. *Ocean Eng.* **2022**, *247*, 110743. [CrossRef]
48. Yang, Y.; Li, C.; Bashir, M.; Wang, J.; Yang, C. Investigation on the sensitivity of flexible foundation models of an offshore wind turbine under earthquake loadings. *Eng. Struct.* **2019**, *183*, 756–769. [CrossRef]
49. Xi, R.Q.; Wang, P.G.; Du, X.L.; Xu, C.S. Dynamic analysis of 10 MW monopile supported offshore wind turbine based on fully coupled model. *Ocean Eng.* **2021**, *234*, 109346. [CrossRef]

Journal of
Marine Science
and Engineering

MDPI

Article

Influence of Auxiliary Pipelines of the Deepwater Drilling Riser on the Dynamic Characteristics of the Subsea Wellhead

Jinduo Wang, Yanbin Wang *, Deli Gao, Rui Li and Liurui Guo

MOE Key Laboratory of Petroleum Engineering China University of Petroleum (Beijing), Beijing 102249, China; wjd9412@163.com (J.W.); gaodeli_team@126.com (D.G.); 15004604457@163.com (R.L.); glr201228@163.com (L.G.)
* Correspondence: wangyanbin@cup.edu.cn

Abstract: During deepwater drilling, the subsea wellhead will be subjected to dynamic loads transmitted from the marine environment, floating drilling platform, riser, and blowout preventer (BOP). Therefore, complex dynamic responses will be induced, which will seriously affect the safety of the subsea wellhead. In this paper, considering the effect of auxiliary pipelines on the riser, a novel entire mechanical model of the floating platform–riser–BOP–subsea wellhead is established. By using the finite-difference method, the governing equations are solved. Finally, the dynamic bending moment and stress distribution of the subsea wellhead are obtained. Moreover, the model is verified by numerical simulation in Orcaflex. On this basis, the influence of the wave height, wave period, sludge height of the subsea wellhead, rotational stiffness of the lower flexible joint, and wall thickness of the conductor on the dynamic characteristics of the subsea wellhead is discussed. Analysis results show that the theoretical analysis results are in good agreement with the numerical simulation. The auxiliary pipelines have important influence on the dynamic characteristics of the subsea wellhead. Wave period is the most important factor affecting the mechanical behavior of the subsea wellhead. Wave height, wall thickness of the conductor, and sludge height are secondary factors affecting the mechanical behavior of the subsea wellhead. The rotational stiffness of the lower flexible joint has little influence on the mechanical behavior of the subsea wellhead. By solving the optimized mechanical model proposed in this paper, the dynamic characteristic of the subsea wellhead conforms more to the actual deepwater drilling conditions. This study has reference significance for the design and mechanical control of the subsea wellhead in deepwater drilling.

Keywords: deepwater drilling riser; auxiliary pipelines; subsea wellhead; dynamic analysis

1. Introduction

With the increase in the world demand for oil and gas resources, the exploration and development of oil and gas in deepwater areas have received more and more attention [1–3]. The deepwater drilling riser and subsea wellhead are indispensable equipment for deepwater drilling engineering, and its safety and efficiency are the premise for developing deepwater oil and gas resources [4–6]. However, the riser will generate complex mechanical behavior under the combined action of the marine environment, floating platform, and operating load, and will transmit the vibration load to the subsea wellhead through the BOP, inducing a dynamic response on the subsea wellhead, which seriously affects the safety of the subsea wellhead [7–10]. Therefore, it is of great significance to analyze the dynamic response of the subsea wellhead and obtain the main control factors of the dynamic behavior.

At present, much research has been carried out on the mechanical analysis of the deepwater drilling riser and subsea wellhead, which provides significant basis for the safe and efficient development of oil and gas in deepwater areas. In terms of riser mechanics, Burke [11] established the dynamic analysis equation of the riser, where the Morison equation was used to describe the wave current, and the dynamic response of the riser was solved and discussed. Egeland et al. [12] modified the lateral vibration governing equation of the riser by changing the boundary conditions at the top of the riser, with consideration of the random wave and drilling platform, and analyzed the influence of random wave parameters on the vibration characteristics of the riser. Tian et al. [13] simulated the vortex-induced vibration of a riser system with 4~10 auxiliary pipelines, which showed that the auxiliary pipelines have an obvious effect on the dynamic response of the riser. Wu et al. [14] obtained the f-vortex-induced vibration characteristics of the deepwater drilling riser considering the auxiliary pipelines. Han et al. [15] established the mechanical model of the deepwater drilling riser considering the effect of buoyancy blocks and the nonlinear dynamic characteristic effects of drilling fluid in the riser. Gao et al. [16] studied the dynamic behavior of the deepwater drilling riser by using the principle of vibration mechanics. Kong et al. [17] studied the vortex-induced vibration of the riser system considering six auxiliary pipelines of the drilling riser by numerical simulation. Wang et al. [18] proposed the dynamic model for the riser-recoil response, which was solved by the finite-element model and the Newmark–β method. Yang et al. [19] proposed a model for the natural frequency and vibration of the deepwater drilling riser to avoid resonance. Karun et al. [20] carried out a theoretical analysis of the deepwater drilling riser, and studied the effect of the internal wave on the large-amplitude dynamic response of the riser. Zhang et al. [21] proposed an assessment method for the deepwater drilling riser under the influence of extreme sea conditions. Zhao et al. [22] studied the dynamic model on the recoil control of the deepwater drilling riser system. Liu et al. [23] proposed a deepwater drilling riser recoil-control method based on the control theory. Chen et al. [24] established an analysis method to determine the safe operation window of the deepwater riser based on the allowable offset of the drilling platform in different directions. Wang et al. [25–31] established a systematic analysis method for the mechanical behavior of the deepwater drilling riser under complex marine environments and drilling loads, which provided a scientific basis for the design and control of the deepwater drilling riser. The mechanical analysis on the riser system, including static analysis, vibration analysis, and recoil analysis, is related to the resilience issue. It is necessary to discuss and study the current research on the resilience of pipelines and other systems. Argyroudis et al. [32] proposed a novel framework for the quantitative resilience assessment of critical infrastructure. Mina et al. [33] studied the resilience of unburied high-pressure/high-temperature pipelines with different outside diameter-to-wall thickness ratios and subjected to the action of thermal loads. Ouyang et al. [34] proposed a novel resilience-assessment method of interdependent infrastructure systems. Zelaschi et al. [35] studied the resilience response of the bridges in a road network based on a three-dimensional finite-element model.

In terms of the subsea wellhead, Valka et al. [36] discussed the transfer mechanism of loads acting on the subsea wellhead, and introduced the key points to be considered in the entire mechanical modeling of the subsea wellhead. Evans et al. [37] discussed the influence of the riser system configuration and operation parameters on subsea wellhead fatigue damage. Williams et al. [38,39] studied the transmission mechanism of stress acting on the subsea wellhead, and evaluated the effect of the motion of the floating drilling platform on the fatigue damage of the subsea wellhead. Pedro et al. [40] studied the dynamic bending moment of the subsea wellhead, and pointed out that the frequency-domain method has certain limitations in the global response analysis. Det Norske Veritas GL (DNVGL) proposed two recommended practices for the fatigue-damage evaluation of the subsea wellhead [41,42]. Jaiswal et al. [43] conducted a numerical simulation study on the mechanical behavior of the floating drilling platform–riser–BOP–subsea wellhead, and evaluated the effect of the dynamic wave load on the fatigue damage of the subsea wellhead. McNeill et al. [44–46] analyzed the fatigue damage of the subsea wellhead using a semianalytical method. Li et al. [47] simulated the wave and current loads with finite-element software, and calculated the fatigue life of the subsea wellhead. Wang et al. [48] proposed a subsea wellhead fatigue analysis method which is more suitable for practical engineering applications. Li et al. [49] developed a local stress–strain method based on a semidecoupled model to predict the fatigue damage of the subsea wellhead. Chen et al. [50] summarized the factors affecting the fatigue damage of the subsea wellhead system qualitatively and quantitatively. Pestana et al. [51,52] conducted a theoretical analysis of the recoil response of the riser after emergency detachment using a nonlinear damping-spring model. Mai et al. [53,54] presented new modeling of the behavior of an underwater vehicle operating in the littoral sea, and a new simulation method of the full equations of the combined rigid-body motion of an underwater vehicle, and the flexible motion of the umbilical cable was derived. Wang et al. [55–57] established an analysis frame for the fatigue assessment of the subsea wellhead with consideration of the coupling effect of temperature and pressure.

To sum up, a lot of research has been carried out on the mechanical analysis and design control of the deepwater drilling riser and subsea wellhead, which provides scientific guidance for the safety of deepwater drilling engineering. However, the rare published literature on the mechanical characteristics of the riser and subsea wellhead has considered the influence of the auxiliary pipelines of the drilling riser, which results in analysis results different from the reality situation. The former method models for the riser dynamic usually ignored the influence of auxiliary pipelines on the riser. Ignoring the auxiliary pipelines may reduce the calculation time to solving the models, but the results do not conform to the actual deepwater drilling conditions. Therefore, it is necessary to establish a practical mechanical model to analyze the mechanical behavior of the riser and the subsea wellhead. Therefore, considering the influence of the auxiliary pipelines of the riser and the movement of the floating platform, the novel entire dynamic analysis model and governing equations of the floating platform–riser–BOP–subsea wellhead are established in this paper. On this basis, the influence of auxiliary pipelines on the dynamic response of the subsea wellhead has been analyzed emphatically. This study has guiding significance for the accurate analysis of the mechanical response of the subsea wellhead.

The subsequent sections of the paper are structured as follows: Section 2 considers the auxiliary pipelines of the drilling riser, and establishes the novel entire mechanical model of the floating platform–riser–BOP–subsea wellhead. Section 3 elaborates the solution process of the mechanical model by the finite-difference method. Section 4 first compares the theoretical calculation and numerical simulation results to validate the model proposed in this paper. Then, the influence of the wave height, wave period, sludge height of the subsea wellhead, rotational stiffness of the lower flexible joint, and wall thickness of the conductor on the dynamic behavior of the subsea wellhead are discussed by sensitivity analysis. Finally, the main controlling factors which affect the dynamic characteristics of the subsea wellhead are revealed by orthogonal experiments. Section 5 discusses all the results of this paper, including the model establishment, validation, and sensitivity analysis results. Finally, the primary conclusions of the paper are summarized in Section 6.

2. Mechanical Model

2.1. Mechanical Model of the Floating Platform–Riser–BOP–Subsea Wellhead

In order to simplify the mechanical model and mathematical derivation, the following assumptions are adopted in this paper. The riser is assumed as an isotropic linear elastic material, and the mechanical characteristics are regarded as constant along the water depth. The propagation directions of the wave and current are in the same plane. The top and the bottom of the riser are connected to the floating drilling platform and BOP through the upper and lower flexible joint, respectively, which is considered as a hinged restraint, as shown in Figure 1.

Based on the above assumptions, the mechanical model of the riser is established based on the principles of elasticity. In the governing Equation (1), the elastic modulus does not vary with the length of the riser, and the mechanical model established in this article is in a two-dimensional plane. The governing equation of the riser can be expressed as [58]:

$$EI\frac{\partial^4 y(x,t)}{\partial x^4} - T(x)\frac{\partial^2 y(x,t)}{\partial x^2} + m\frac{\partial^2 y}{\partial t^2} = f(x,t) \tag{1}$$

where E is the elastic modulus of the riser, Pa; I is the inertia moment of riser, m^4; $y(x,t)$ is the lateral displacement of the riser, m; x is the axial length of the riser, m; $f(x,t)$ is the wave current force on the riser, N/m; $T(x)$ is the axial tension of the riser per length, N/m; m is the total weight of the riser per length, kg/m.

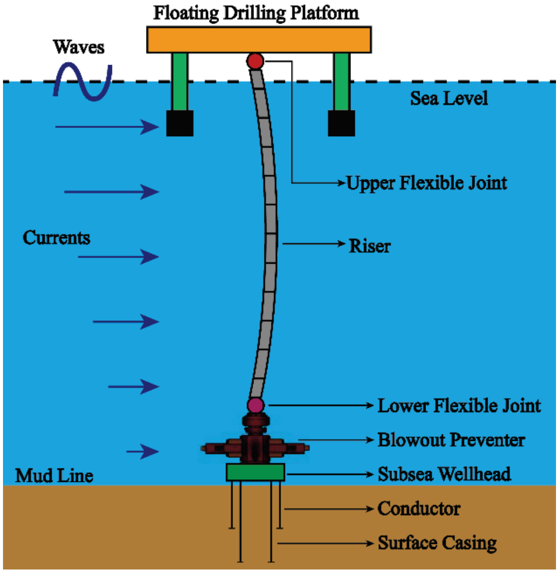

Figure 1. The system of the floating drilling platform–riser–BOP–subsea wellhead.

The top of the riser is connected to the floating platform through the upper flexible joint, which can be considered as a hinged restraint. The displacement at the top of the riser is equal to the displacement of the platform; additionally, the bending moment is equal to the rotational stiffness of the upper flexible joint. Therefore, the top boundary condition of Equation (1) can be expressed as:

$$\begin{cases} y(0,t) = S(t) \\ EI\frac{\partial^2 y(0,t)}{\partial x^2} - K_1\frac{\partial y(0,t)}{\partial x} = 0 \end{cases} \tag{2}$$

where $S(t)$ is the dynamic motion of the floating platform, m; K_1 is the rotational stiffness of the upper flexible joint, N·m/rad.

The bottom of the riser is connected to the BOP through the lower flexible joint, which can be considered as a hinged restraint. The displacement at the bottom of the riser is 0; additionally, the bending moment is equal to the rotational stiffness of the lower flexible joint. Therefore, the bottom boundary condition of Equation (1) can be expressed as:

$$\begin{cases} y(L,t) = 0 \\ EI\frac{\partial^2 y(L,t)}{\partial x^2} - K_2\frac{\partial y(L,t)}{\partial x} = 0 \end{cases} \tag{3}$$

where K_2 is the rotational stiffness of the lower flexible joint, N·m/rad; L is the riser length, m.

The forces acting on the riser system include axial forces and wave–current forces. The axial force includes the floating weight of the main rise and auxiliary pipelines, as well as the weight of drilling fluid inside the riser.

The top tension of the riser can be expressed as [59]:

$$T_0 = W_s f_{wt} - B_n f_{bt} + A_i L(\rho_m - \rho_w) \tag{4}$$

where W_s is the weight of the riser in seawater, N; f_{wt} is the submersion coefficient, which is 1.05 in this paper; B_n is the buoyancy force of the buoyancy joint, N; f_{bt} is the effective coefficient, which is 0.96 in this paper; A_i is the area of the riser inner diameter, m^2; ρ_m is the density of drilling fluid, kg/m^3; ρ_w is the density of seawater, kg/m^3.

2.2. Model of the Auxiliary Pipelines

The auxiliary pipelines mainly include kill lines, hydraulic lines, choke lines, and booster lines. The function of the choke and kill lines is to reduce the pressure loss caused by fluid flow in the riser. The booster line, which is connected with the mud pump on the floating platform, is used to increase the flow rate of the drilling fluid in the riser. The hydraulic pipelines are used to control the BOP in drilling engineering [60]. The distribution of the main riser pipe and auxiliary pipelines are shown in Figure 2.

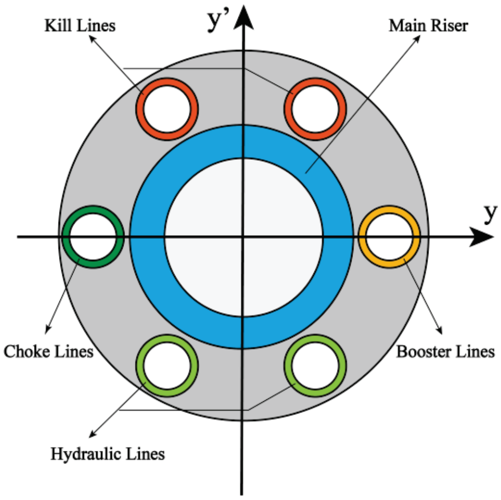

Figure 2. The main riser pipe and auxiliary pipelines.

The auxiliary pipelines are distributed around the main riser pipe, which will affect the bending stiffness of the riser system. Therefore, considering the auxiliary pipelines of the riser, the governing Equation (1) can be written as:

$$E(I+I_a)\frac{\partial^4 y(x,t)}{\partial x^4}-T(x)\frac{\partial^2 y(x,t)}{\partial x^2}+(m+m_a)\frac{\partial^2 y}{\partial t^2}=f(x,t) \tag{5}$$

where I_a is the inertia moment of the riser auxiliary pipelines, m^4; m_a is the weight of the auxiliary pipelines per length, kg/m.

$$\begin{cases} I_a = I_1 + I_2 + I_3 + I_4 \\ I_1 = a[\frac{\pi\left(D_1^4-d_1^4\right)}{64}+\alpha^2\frac{\pi\left(D_1^2-d_1^2\right)}{4}] \\ I_2 = b[\frac{\pi\left(D_2^4-d_2^4\right)}{64}+\beta^2\frac{\pi\left(D_2^2-d_2^2\right)}{4}] \\ I_3 = c[\frac{\pi\left(D_3^4-d_3^4\right)}{64}+\gamma^2\frac{\pi\left(D_3^2-d_3^2\right)}{4}] \\ I_4 = e[\frac{\pi\left(D_4^4-d_4^4\right)}{64}+\delta^2\frac{\pi\left(D_4^2-d_4^2\right)}{4}] \end{cases} \tag{6}$$

where a is the number of kill lines, dimensionless; D_1 is the outer diameter of the kill lines, m; d_1 is the inner diameter of kill lines, m; b is the number of hydraulic lines, dimensionless; D_2 is the outer diameter of the hydraulic lines, m; d_2 is the inner diameter of the hydraulic lines, m; c is the number of choke lines, dimensionless; D_3 is the outer diameter of the choke lines, m; d_3 is the inner diameter of the choke lines, m; e is the number of booster lines, dimensionless; D_4 is the outer diameter of the booster lines, m; d_4 is the inner diameter of the booster lines, m; α is the distance between the kill lines center and the y-axis, m; β is the distance between the hydraulic lines center and the y-axis, m; γ is the distance between the choke lines center and the y-axis, m; δ is the distance between the booster lines center and the y-axis, m.

When considering the auxiliary pipelines, Equation (2) can be written as:

$$\begin{cases} y(0,t) = S(t) \\ E(I+I_a)\frac{\partial^2 y(0,t)}{\partial x^2} - K_1\frac{\partial y(0,t)}{\partial x} = 0 \end{cases} \tag{7}$$

Equation (3) can be written as:

$$\begin{cases} y(L,t) = 0 \\ E(I+I_a)\frac{\partial^2 y(L,t)}{\partial x^2} - K_2\frac{\partial y(L,t)}{\partial x} = 0 \end{cases} \tag{8}$$

In Section 2.2, considering the auxiliary pipelines, a novel entire mechanical model of the deepwater drilling riser is established. The novel governing equation is shown as Equation (5), and the novel boundary conditions are shown as Equations (7) and (8).

2.3. Marine Environmental Loads and Platform Motion

The wave–current force on the riser can be calculated by the Morrison equation [61], which is:

$$f(x,t) = \frac{\pi}{4}\rho_w C_M D^2 \frac{\partial v_w}{\partial t} + \frac{1}{2}\rho_w C_D D(v_w + v_c)|v_w + v_c| \tag{9}$$

where C_M is the inertial coefficient, dimensionless; C_D is the drag coefficient, dimensionless; v_c is the current velocity, m/s; v_w is the horizontal velocity of wave particle, m/s.

Generally, the lateral motion of the floating platform will affect the dynamic characteristics of the deepwater drilling riser. The motion of the platform can be described by Equation (10) [62]:

$$S(t) = S_0 + S_L \sin\left(\frac{2\pi t}{T_L} - \alpha_L\right) + \sum_{n-1}^{N} A_n \cos(k_n x_p - \omega_n t + \varphi_n) \tag{10}$$

where S_L is the amplitude drift of the platform, m; T_L is the drift period of the platform, s; S_0 is the static offset of the platform, m; α_L is the phase angle of the drift motion, usually taken as 0; A_n is the amplitude of the random wave, m; k_n is the wave number, dimensionless; x_p is the horizontal position of the platform, m; ω_n is the wave circle frequency, rad/s; t is the time, s; φ_n is the phase angle of the wave, rad.

2.4. Mechanical Model of the Subsea Wellhead

The physical structure and mechanical load of the subsea wellhead are shown in Figure 3.

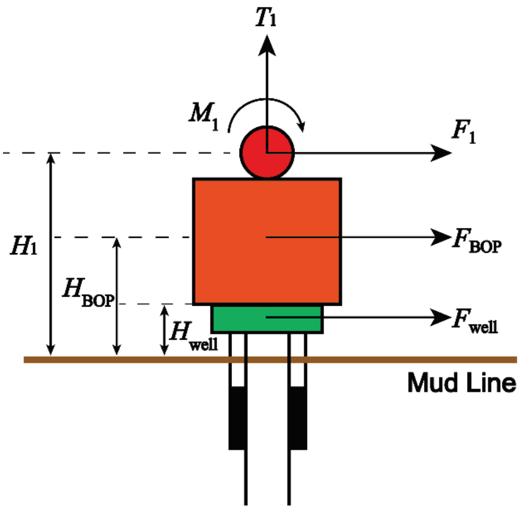

Figure 3. Mechanical model of the subsea wellhead.

The total bending moment on the subsea wellhead is:

$$M = F_{BOP} \cdot H_{BOP} + F_{well} \cdot H_{well} + F_1 \cdot H_1 + M_1 \tag{11}$$

where F_{BOP} is the current force on the BOP, N; H_{BOP} is the height from the mud line to the center of gravity of the BOP, m; F_1 is the current force on the lower flexible joint, N; H_1 is the distance between the mud line and the lower flexible joint, m; M_1 is the bending moment on the subsea wellhead transmitted from the riser, N·m; F_{well} is the current force on the subsea wellhead, N; H_{well} is the sludge height of the subsea wellhead, m.

After mathematical derivation, Equation (11) can be written as:

$$M = \int_0^{H_{BOP}} \frac{1}{2} C_D \rho_w v_c^2 D_{BOP} dy \times H_{BOP} + \int_0^{H_{well}} \frac{1}{2} C_D \rho_w v_c^2 D_{well} dy \times H_{well} + \int_0^{H_1} \frac{1}{2} C_D \rho_w v_c^2 D_{\mathrm{F}} dy \times H_1 + M_1 \tag{12}$$

where M is the total bending moment on the subsea wellhead, N·m; D_{F} is the diameter of the lower flexible joint, m.

After the bending moment on the subsea wellhead is obtained, the maximum stress, located at the outer wall of the subsea wellhead, generated by the bending moment can be calculated according to the basic principles of material mechanics, which is:

$$\sigma_{max} = \frac{M \cdot H_{well}}{I_{well}} \tag{13}$$

where I_{well} is the inertia moment of the conductor, m^4.

3. Model Solution

In this paper, the finite-difference method is used to solve the governing Equation (5). The riser is divided into n segments in the x direction, and $n + 1$ nodes are obtained. The length of each segment is h, and the nodes are numbered from top to bottom. The first node at the top is 1, and the last node at the bottom is $n + 1$, and i is the node number. The time is divided into m segments, and $m + 1$ time nodes are obtained. The time scale of each segment is k, and j is the time node. Therefore, $y(i,j)$ can be used to represent the riser displacement at position i and time j, and $f(i,j)$ represents the external load at position i at time j.

The discretized governing equation of Equation (5) can be written as:

$$E(I + I_a) \frac{y_{i+2}^j - 4y_{i+1}^j + 6y_i^j - 4y_{i-1}^j + y_{i-2}^j}{h^4} - T(i) \frac{y_{i+1}^j - 2y_i^j + y_{i-1}^j}{h^2} + (m + m_a) \frac{y_i^{j+1} - 2y_i^j + y_i^{j-1}}{k^2} = f(i,j) \tag{14}$$

where the axial force at position i can be written as:

$$T(i) = T_0 - i[A_i \rho_m g + (A_o - A_i)\rho_s g + A_F \rho_s g] \tag{15}$$

where ρ_s is the density of the riser, kg/m^3; A_o is the area of the riser outer diameter, m^2; A_F is the cross-sectional area of the auxiliary pipelines, m^2.

After mathematical derivation, Equation (14) can be expressed as:

$$A y_{i+2}^j + B_i y_{i+1}^j + C_i y_i^j + D_i y_{i-1}^j + E y_{i-2}^j = F f(i,j) \tag{16}$$

where,

$$\begin{cases} A = k^2 E(I + I_a) \\ B_i = -4k^2 E(I + I_a) - k^2 h^2 T(i) \\ C_i = 6k^2 E(I + I_a) + 2k^2 h^2 T(i) - 2h^4 (m + m_a) \\ D_i = -4k^2 E(I + I_a) - k^2 h^2 T(i) \\ E = k^2 E(I + I_a) \\ F = k^2 \end{cases} \tag{17}$$

The top boundary condition can be written as:

$$\begin{cases} y(0,j) = S(j) \\ E(I+I_a)\frac{\partial^2 y(0,j)}{\partial x^2} - K_1\frac{\partial y(0,j)}{\partial x} = E(I+I_a)\frac{y_1^j - 2y_0^j + 6y_{-1}^j}{h^2} - K_1\frac{y_1^j - y_0^j}{h} \end{cases} \tag{18}$$

The bottom boundary condition can be written as:

$$\begin{cases} y(L,j) = 0 \\ E(I+I_a)\frac{\partial^2 y(L,j)}{\partial x^2} - K_2\frac{\partial y(L,j)}{\partial x} = E(I+I_a)\frac{y_{L+1}^j - 2y_L^j + y_{L-1}^j}{h^2} - K_2\frac{y_{L+1}^j - y_L^j}{h} \end{cases} \tag{19}$$

The matrix form of the governing equation can be expressed as:

$$\begin{bmatrix} 0 & 1 & 0 & 0 & 0 & \cdots & 0 & 0 & 0 \\ 1 & -2 & 1 & 0 & 0 & \cdots & 0 & 0 & 0 \\ E & D_1 & C_1 & B_1 & A & \cdots & 0 & 0 & 0 \\ 0 & E & D_2 & C_2 & B_2 & \cdots & 0 & 0 & 0 \\ \vdots & \vdots & \vdots & \vdots & \vdots & \ddots & \vdots & \vdots & \vdots \\ 0 & 0 & 0 & 0 & 0 & \cdots & C_{n+1} & B_{n+1} & A \\ 0 & 0 & 0 & 0 & 0 & \cdots & -2 & 1 & 0 \\ 0 & 0 & 0 & 0 & 0 & \cdots & 2 & -2 & 1 \end{bmatrix} \begin{bmatrix} y_{-1} \\ y_0 \\ y_1 \\ y_2 \\ \vdots \\ y_{n+1} \\ y_{n+2} \\ y_{n+3} \end{bmatrix} = \begin{bmatrix} S(j) \\ 0 \\ Fy(1,j) \\ Fy(2,j) \\ \vdots \\ Fy(n+1,j) \\ 0 \\ 0 \end{bmatrix} \tag{20}$$

In order to demonstrate the process of model solving more clearly, the computational flow chart of the model solution is shown in Figure 4.

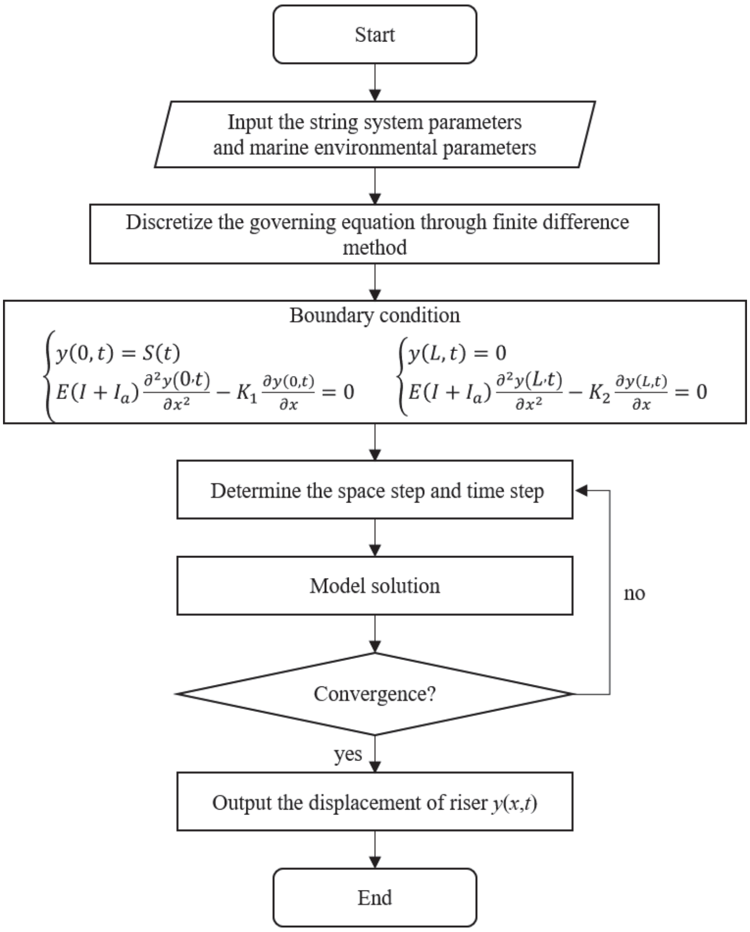

Figure 4. Computational flow chart of the model solution.

4. Case Study

4.1. Case Study

4.1.1. Model Validation

Taking a deepwater drilling as an example, the parameters of the marine environment and platform are shown in Table 1, and the configuration parameters of the riser system are shown in Table 2. Five auxiliary pipelines are arranged around the main riser pipe, including one choke line, one kill line, one booster line, and two hydraulic lines. The auxiliary pipelines configuration is shown in Table 3.

Table 1. Marine environmental and platform parameters.

Parameter	Value
Water depth (m)	1524
Density of seawater (kg/m^3)	1025
Density of drilling fluid (kg/m^3)	1200
Rotational stiffness of the upper flexible joint (kN·m/rad)	573
Rotational stiffness of the lower flexible joint (kN·m/rad)	5500
Drag coefficient	1.2
Added mass coefficient	1
Wave height (m)	8 m
Wave period (s)	13 s
Sea surface current velocity (m/s)	1 m/s
The static offset of the platform (m)	0 m
The amplitude drift of the platform (m)	10 m
The drift period of the platform (s)	200 s
Outer diameter of the conductor (m)	0.162
Wall thickness of the conductor (m)	0.0254
The sludge height of the subsea wellhead (m)	3 m

Table 2. Riser system configuration.

Riser Components	Number	Length/m	Weight/t
BOP	1	16.780	331.640
Riser joint (bare)	12	22.860	12.831
Buoyancy joint 1	27	22.860	0.415
Buoyancy joint 2	26	22.860	2.540
Riser joint 1	1	6.096	5.510
Riser joint 2	1	4.572	4.520
Riser joint 3	1	3.048	3.448
Riser joint 4	1	1.524	2.458

Table 3. Auxiliary pipelines configuration.

Name	Number	Outer Diameter/m	Inner Diameter/m
Main riser pipe	1	0.5334	0.4890
Choke line	1	0.1715	0.1143
Kill line	1	0.1715	0.1143
Booster line	1	0.1270	0.1016
Hydraulic line	2	0.1080	0.0889

The model validation has been carried out through comparing the results obtained by the method proposed in this paper and the numerical simulation in Orcaflex. In order to make the comparison results more intuitive, in the process of model verification, the bending moment and stress of the first half of the platform drift period have been chosen. The comparison results are shown in Figures 5 and 6.

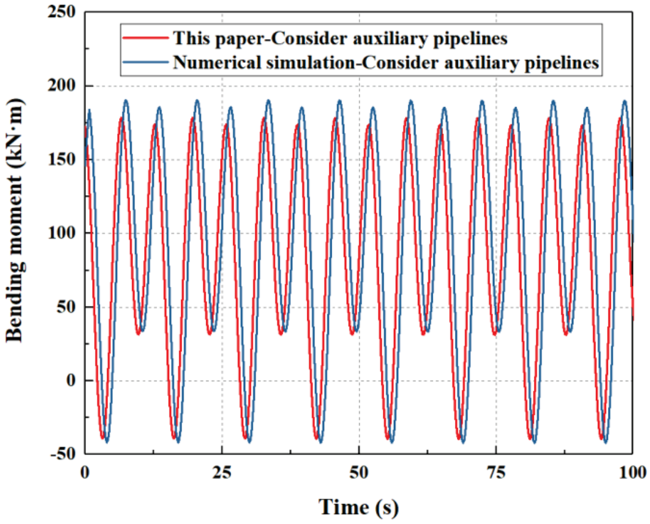

Figure 5. Model validation considering auxiliary pipelines.

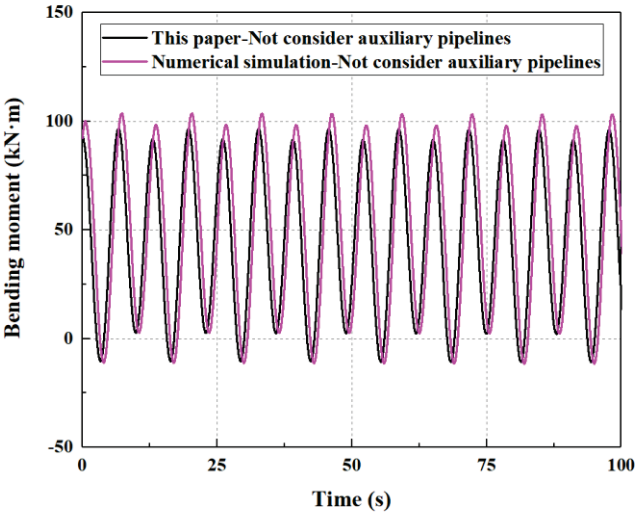

Figure 6. Model validation not considering auxiliary pipelines.

The results show that, if the auxiliary pipelines are considered, the maximum bending moment is 178.5 kN·m calculated by the method proposed in this paper, while the maximum bending moment is 190.5 kN·m calculated by the numerical simulation. If the auxiliary pipelines are not considered, the maximum bending moment is 96.6 kN·m by the method proposed in this paper, while the maximum bending moment is 103.6 kN·m by the numerical simulation. If the auxiliary pipeline of the riser is considered, the error between the theoretical results and the numerical simulation is about 6.7%, while the error between the theoretical results and the numerical simulation is about 7.2% if the auxiliary pipelines are not considered. Additionally, the results between the numerical simulation and the theoretical calculation have the same order of the amplitude, and the oscillation periods between the numerical simulation and the theoretical calculation are the same. Therefore, the correctness of the model proposed in this paper has been verified.

4.1.2. Results of the Case Study

The total bending moment of the subsea wellhead consists of the bending moment transmitted from the riser system, the bending moment at the lower flexible joint, the bending moment at the BOP, and the bending moment generated by the current at the subsea wellhead. The bending moments generated by the above four aspects are shown in Figures 7 and 8.

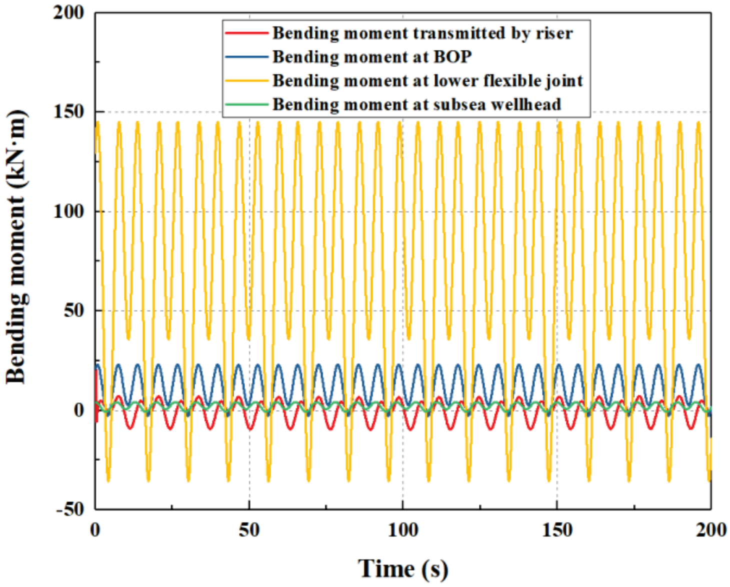

Figure 7. Bending moment on the subsea wellhead considering the auxiliary pipelines.

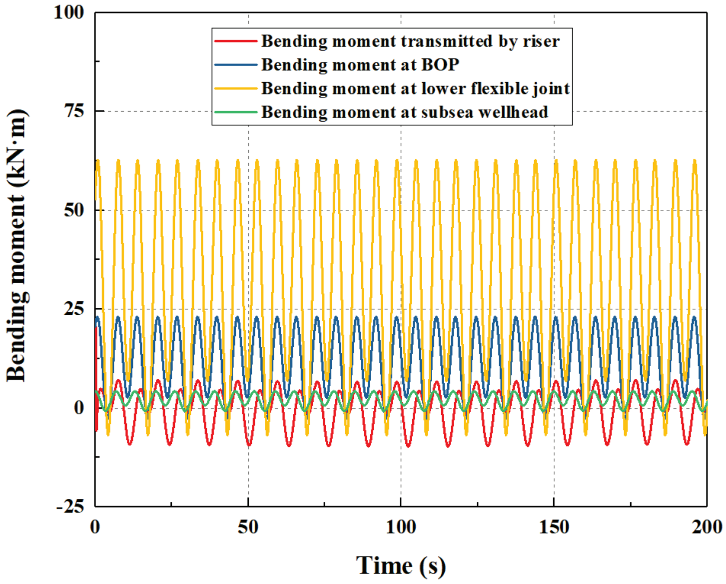

Figure 8. Bending moment on the subsea wellhead without considering the auxiliary pipelines.

As shown in Figures 7 and 8, on the whole, the auxiliary pipelines have great influence on the bending moment of the subsea wellhead. In particular, the bending moment at the lower flexible joint has the greatest effect on the total bending moment of the subsea wellhead, successively followed by the bending moment at the BOP, the bending moment at the riser, and the bending moment on the subsea wellhead.

The total time-varying bending moment and stress on the subsea wellhead are shown in Figures 9 and 10, respectively.

As shown in Figures 9 and 10, the auxiliary pipelines have a significant effect on the mechanical characteristics of the subsea wellhead. If the auxiliary pipelines are not considered, the maximum bending moment and bending stress on the subsea wellhead are 96.6 kN·m and 72.6 MPa. If the auxiliary pipelines are considered, the maximum bending moment and bending stress on the subsea wellhead are 178.5 kN·m and 134.2 MPa. The results show that the maximum difference between the bending moment and the bending stress of the subsea wellhead are 81.9 kN·m and 61.6 MPa, and the bending moment and bending stress on the subsea wellhead increase by 84.8% if the auxiliary pipelines are considered. Therefore, this paper suggests that the auxiliary pipelines should be considered in the process of the subsea wellhead dynamic analysis.

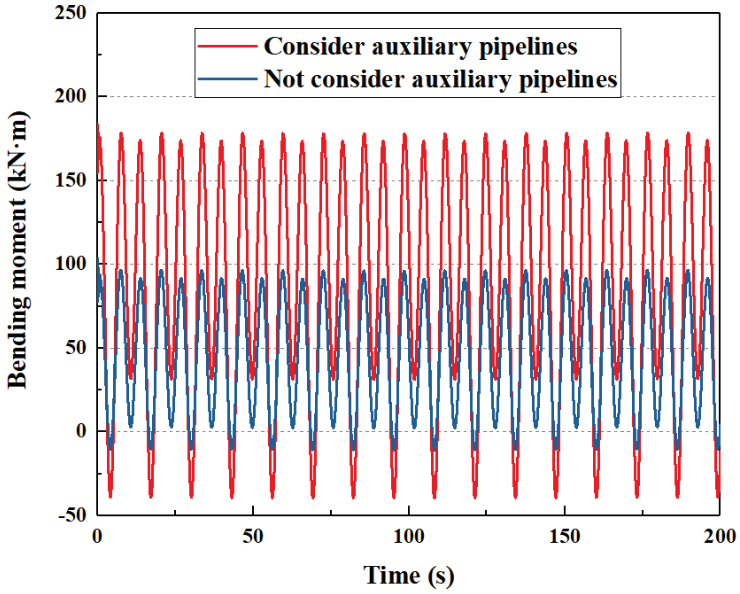

Figure 9. Total bending moment on the subsea wellhead.

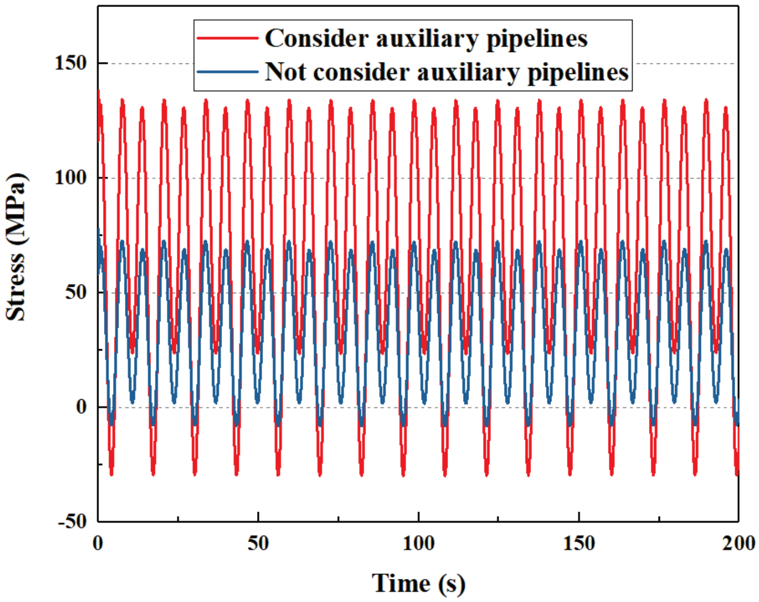

Figure 10. Bending stress on the subsea wellhead.

4.2. Sensitivity Analysis

4.2.1. Auxiliary Pipelines

Due to different drilling conditions, the types and numbers of auxiliary pipelines are different. This paper selects four types of auxiliary pipeline configurations, which are three auxiliary pipelines (choke line, kill line, and booster line), four auxiliary pipelines (choke line, kill line, booster line, and hydraulic line), five auxiliary pipelines (choke line, kill line, booster line, and two hydraulic lines), and six auxiliary pipelines (choke line, two kill lines, booster line, and two hydraulic lines). The influence of auxiliary pipelines on the dynamic response of the subsea wellhead is shown in Figures 11 and 12.

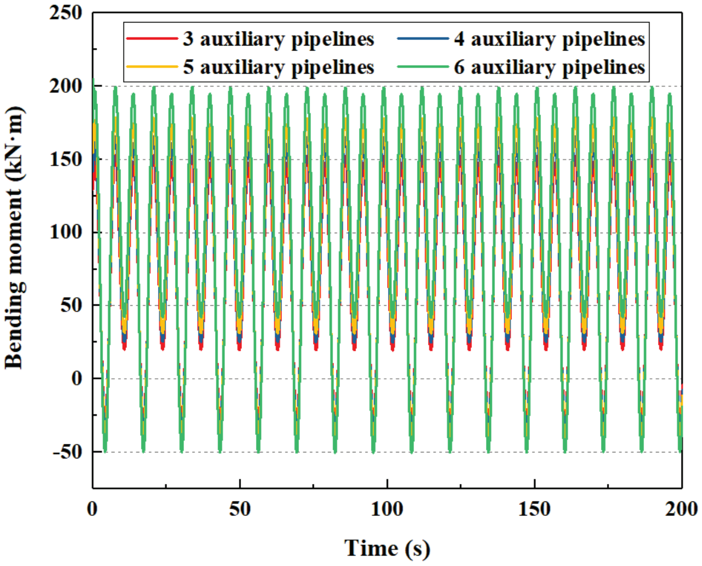

Figure 11. The influence of auxiliary pipelines of bending moment on the subsea wellhead.

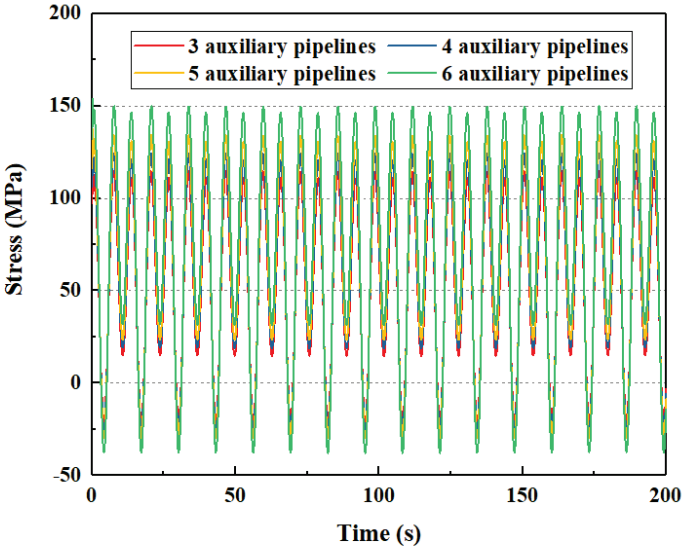

Figure 12. The influence of auxiliary pipelines of bending stress on the subsea wellhead.

As shown in Figures 11 and 12, the auxiliary pipelines have an influence on the total bending moment and bending stress on the subsea wellhead. As shown in Table 4, when the number of auxiliary pipelines increases from three to six, the maximum bending moment at the subsea wellhead increases from 152.6 kN·m to 199.3 kN·m, and the maximum bending stress increases from 114.7 MPa to 149.8 Mpa.

Table 4. The maximum bending moment and stress on the subsea wellhead under different configurations of auxiliary pipelines.

The Number of Auxiliary Pipelines	The Maximum Bending Moment/kN·m	The Maximum Bending Stress/MPa
3	152.6	114.7
4	165.5	124.4
5	178.5	134.2
6	199.3	149.8

4.2.2. Sludge Height of the Subsea Wellhead

If the sludge height of the subsea wellhead is 2 m, 3 m, 4 m, and 5 m, respectively, the mechanical behavior of the subsea wellhead is shown in Figures 13 and 14.

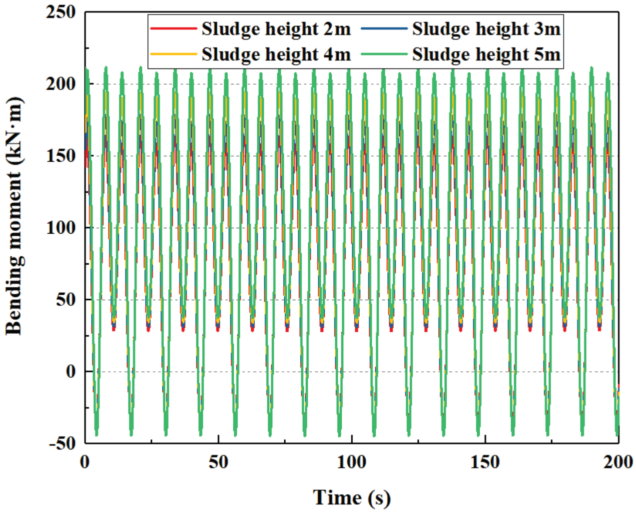

Figure 13. The influence of sludge height of bending moment on the subsea wellhead.

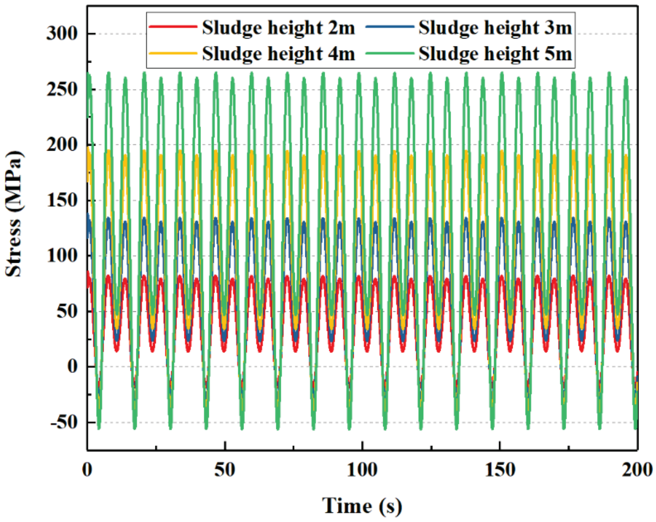

Figure 14. The influence of sludge height of bending stress on the subsea wellhead.

As shown in Figures 13 and 14, the sludge height has effect on the bending moment and stress of the subsea wellhead, and the effect on the bending stress is more significant. As shown in Table 5,when the sludge height increases from 2 m to 5 m, the maximum bending moment at the wellhead increases from 163.8 kN·m to 211.7 kN·m. The maximum bending stress increases from 82.1 Mpa to 265.2 Mpa.

Table 5. The maximum bending moment and stress on the subsea wellhead under different sludge heights.

Sludge Height	The Maximum Bending Moment/kN·m	The Maximum Bending Stress/MPa
2 m	163.8	82.1
3 m	178.5	134.2
4 m	194.3	194.7
5 m	211.7	265.2

4.2.3. Wall Thickness of the Conductor

If the wall thickness of the conductor is 0.5 in, 1.0 in, 1.5 in, and 2.0 in, respectively, the mechanical behavior of the subsea wellhead is shown in Figures 15 and 16.

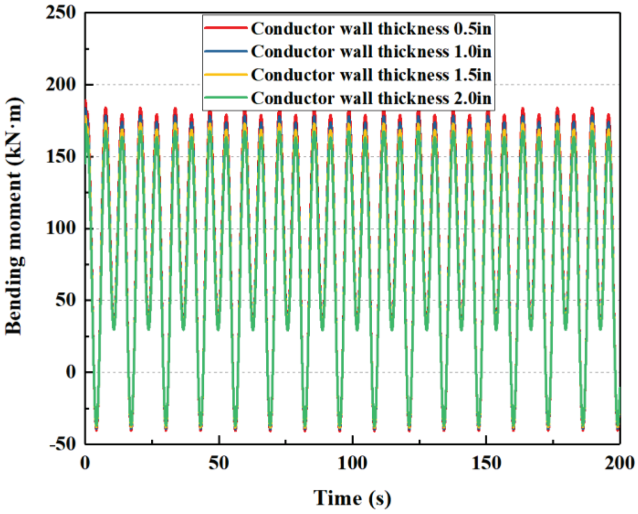

Figure 15. The influence of conductor wall thickness of bending moment on the subsea wellhead.

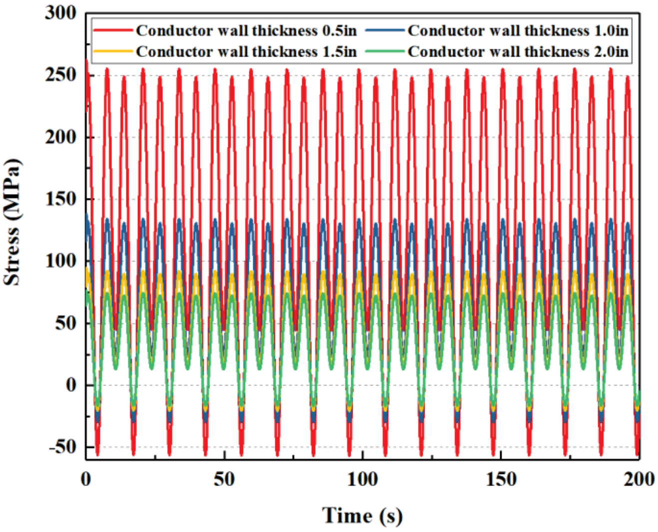

Figure 16. The influence of conductor wall thickness of bending stress on the subsea wellhead.

As shown in Figures 15 and 16, the wall thickness of the conductor has little effect on the total bending moment of the subsea wellhead, and has a certain effect on the bending stress. As shown in Table 6, When the wall thickness of the conductor increases from 0.5 in to 2.0 in, the maximum bending moment is reduced from 183.9 kN·m to 167.8 kN·m, while the maximum bending stress is reduced from 255.2 MPa to 74.2 MPa.

Table 6. The maximum bending moment and stress on the subsea wellhead under different wall thicknesses of the conductor.

Wall Thickness of Conductor	The Maximum Bending Moment/kN·m	The Maximum Bending Stress/MPa
0.5 in	183.9	255.2
1.0 in	178.5	134.2
1.5 in	173.1	92.1
2.0 in	167.8	74.2

4.2.4. Rotational Stiffness of the Lower Flexible Joint

If the rotational stiffness of the lower flexible joint is 4000 kN·m, 5500 kN·m, 7000 kN·m, and 8500 kN·m, respectively, the mechanical behavior of the subsea wellhead is shown in Figures 17 and 18.

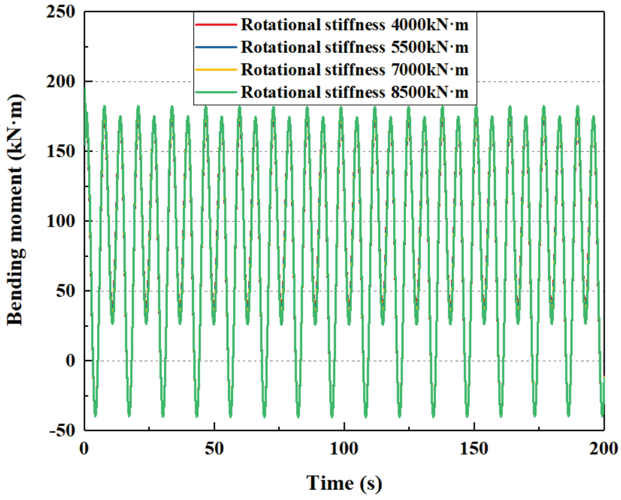

Figure 17. The influence of rotational stiffness of bending moment on the subsea wellhead.

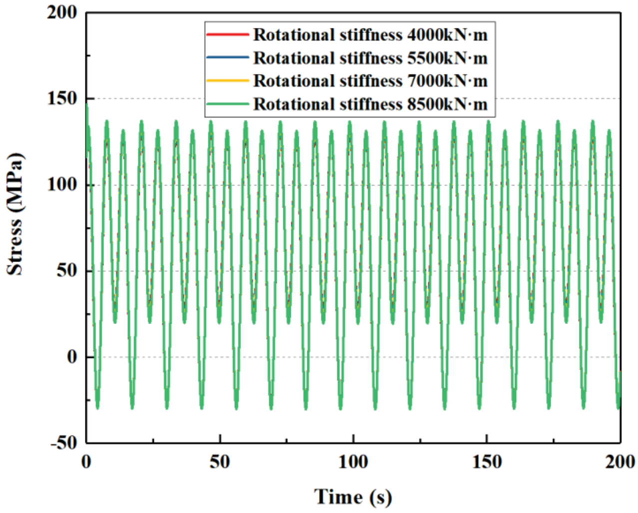

Figure 18. The influence of rotational stiffness of bending stress on the subsea wellhead.

As shown in Figures 17 and 18, the rotational stiffness of the lower flexible joint has little influence on the total bending moment and stress on the subsea wellhead. As shown in Table 7, when the rotational stiffness of the lower flexible joint increases from 4000 kN·m to 8500 kN·m, the maximum bending moment at the wellhead increases from 176.5 kN·m to 182.6 kN·m, and the maximum bending stress increases from 24.2 Mpa to 28.2 Mpa.

Table 7. The maximum bending moment and stress on the subsea wellhead under different rotational stiffnesses of the flexible joint.

Rotational Stiffness of Flexible Joint	The Maximum Bending Moment/kN·m	The Maximum Bending Stress/MPa
4000 kN·m	176.5	132.7
5500 kN·m	178.5	134.2
7000 kN·m	180.5	135.7
8500 kN·m	182.6	137.3

4.2.5. Wave Height

If the wave height is 6 m, 8 m, 10 m, and 12 m, respectively, the mechanical behavior of the subsea wellhead is shown in Figures 19 and 20.

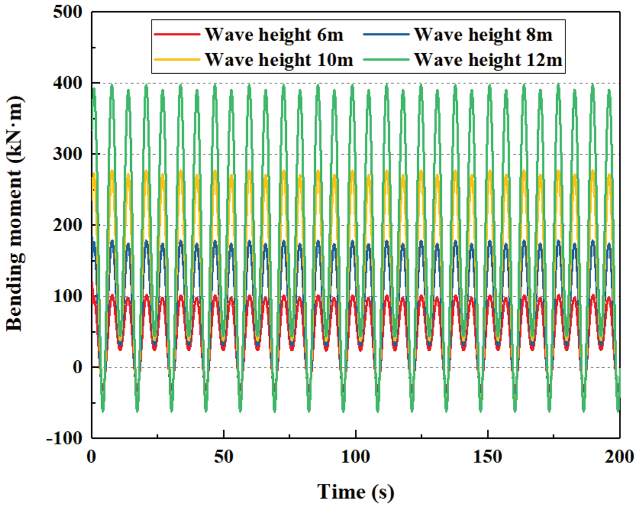

Figure 19. The influence of wave height of bending moment on the subsea wellhead.

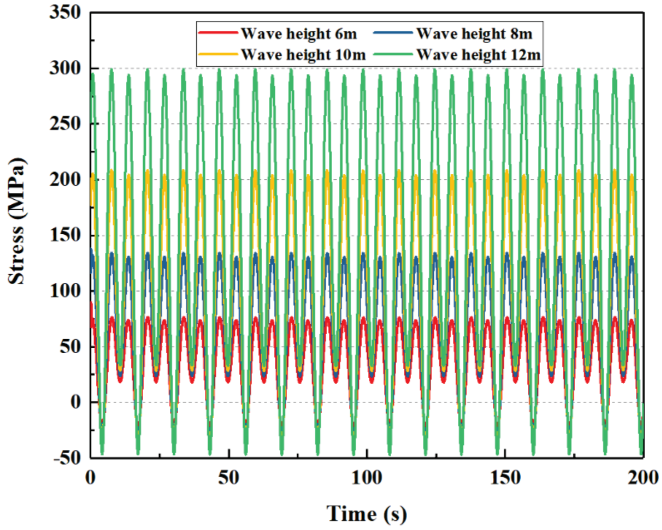

Figure 20. The influence of wave height of bending stress on the subsea wellhead.

As shown in Figures 19 and 20, the wave height has a great influence on the total bending moment and the stress on the subsea wellhead. As shown in Table 8, when the wave height increases from 6 m to 12 m, the maximum bending moment at the wellhead increases from 101.7 N·m to 397.9 kN·m, and the maximum bending stress increases from 76.5 MPa to 299.1 MPa.

Table 8. The maximum bending moment and stress of the subsea wellhead under different wave heights.

Wave Height	The Maximum Bending Moment/kN·m	The Maximum Bending Stress/MPa
6 m	101.7	76.5
8 m	178.5	134.2
10 m	277.3	208.5
12 m	397.9	299.1

4.2.6. Wave Period

If the wave period is 10 s, 13 s, 16 s, and 19 s, respectively, the mechanical behavior of the subsea wellhead is shown in Figures 21 and 22.

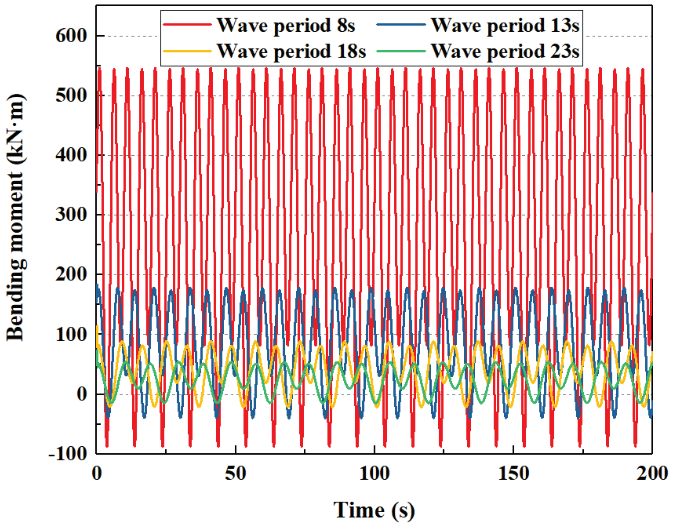

Figure 21. The influence of wave period of bending moment on the subsea wellhead.

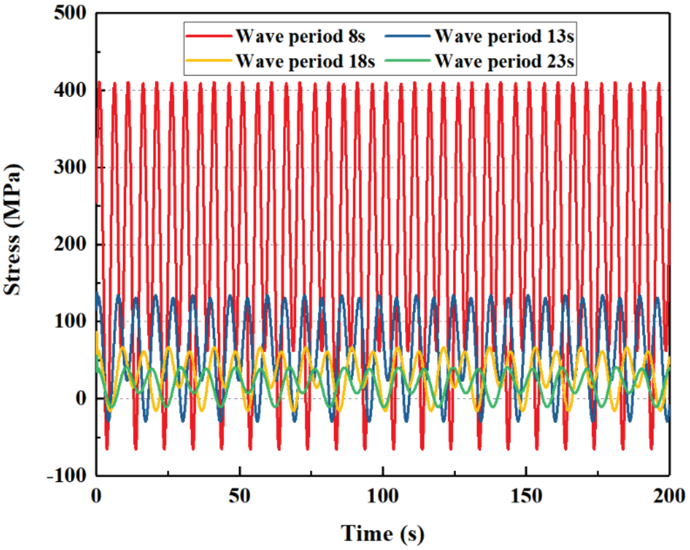

Figure 22. The influence of wave period of bending stress on the subsea wellhead.

As shown in Figures 21 and 22, the wave period has a significant effect on the total bending moment and the stress on the subsea wellhead. As shown in Table 9, when the wave period increases from 10 s to 19 s, the maximum value of the wellhead bending moment decreases from 545.5 kN·m to 54.0 kN·m, and the maximum bending stress increases from 410.0 Mpa to 40.6 Mpa.

Table 9. The maximum bending moment and stress of subsea wellhead under different wave periods.

Wave Periods	The Maximum Bending Moment/kN·m	The Maximum Bending Stress/MPa	Cycle Periods/s
10 s	545.5	410.0	10 s
13 s	178.5	134.2	13 s
16 s	88.5	66.5	16 s
19 s	54.0	40.6	19 s

4.3. Orthogonal Experiment

The influence of the sludge height, wall thickness of the conductor, rotational stiffness of the lower flexible joint, wave height, and wave period on the mechanical behavior of the subsea wellhead are obtained through the analysis of numerical examples. However, the grade of the main control factors affecting the bending stress of the subsea wellhead is still unclear. It is necessary to use an orthogonal experimental method to determine the main control factors affecting the bending stress of the subsea wellhead. The orthogonal experiment results are shown in Table 10.

Table 10. The results of the orthogonal experimental.

Number	Sludge Height (m)	Wall Thickness of Conductor (in)	Rotational Stiffness of Lower Flexible Joint (kN·m)	Wave Height (m)	Wave Period (s)	The Maximum Bending Moment (kN·m)	The Maximum Bending Stress (MPa)
1	2	0.5	4000	6	10	275.4	262.4
2	2	1.0	5500	8	13	170.5	85.4
3	2	1.5	7000	10	16	128.0	45.0
4	2	2.0	8500	12	19	115.9	32.2
5	3	0.5	5500	10	19	83.5	119.4
6	3	1.0	4000	12	16	192.6	144.8
7	3	1.5	8500	6	13	104.2	54.9
8	3	2.0	7000	8	10	547.8	227.9
9	4	0.5	7000	12	16	212.0	404.1
10	4	1.0	8500	10	19	92.4	92.6
11	4	1.5	4000	8	10	611.0	429.4
12	4	2.0	5500	6	13	110.8	61.4
13	5	0.5	8500	8	13	215.7	514.0
14	5	1.0	7000	6	10	390.2	488.8
15	5	1.5	5500	12	19	136.3	119.7
16	5	2.0	4000	10	16	156.3	108.3
Stress level K1	106.25	324.975	236.225	216.875	352.125		
K2	136.75	202.9	96.475	314.175	178.925		
K3	246.875	162.25	291.45	91.325	175.55		
K4	307.7	107.45	173.425	175.2	90.975		
Difference between maximum and minimum	201.45	217.525	194.975	222.85	261.15		
Grade of main control factors	4	3	5	2	1		

The results show that the wave period is the most important factor affecting the mechanical behavior of the subsea wellhead. Wave height, wall thickness of the conductor, and sludge height are the secondary factors, and the rotational stiffness of the lower flexible joint has the least influence. The bending stress increases with the increase in the sludge height, the rotational stiffness of the lower flexible joint, and the wave height, while the bending stress decreases with the increase in the wall thickness of the conductor and the wave period. Through the orthogonal experimental analysis, it can be seen that the marine environmental parameters have the most obvious influence on the mechanical behavior of the subsea wellhead. Therefore, in addition to selecting a small wave height and large wave period, it is particularly important to optimize the sludge height of the wellhead, the wall thickness of the conductor, and the rotational stiffness of the lower flexible joint to control the safety of the subsea wellhead.

5. Discussion

(1) The mechanical model and analysis method of the dynamic response of the subsea wellhead have been established, considering the auxiliary pipelines and floating drilling platform. The model is verified by numerical simulation. The dynamic bending moment and stress of the subsea wellhead have been obtained;

(2) The auxiliary pipelines have an important influence on the dynamic characteristics of the subsea wellhead. If the auxiliary pipelines are considered, the bending moment and stress on the subsea wellhead are significantly increased. Therefore, this study suggests that the auxiliary pipelines should be considered in the dynamic analysis of the subsea wellhead to obtain a more realistic dynamic response of the subsea wellhead;

(3) Wave period is the most important factor affecting the mechanical behavior of the subsea wellhead. Wave height, wall thickness of the conductor, and sludge height are secondary factors affecting the mechanical behavior of the subsea wellhead. The rotational stiffness of the lower flexible joint has little influence on the mechanical behavior of the subsea wellhead.

6. Conclusions

(1) The contribution of this paper is to optimize the entire mechanical model of the floating platform–riser–BOP–subsea wellhead by considering the effect of auxiliary pipelines on the riser. Furthermore, the more accurate bending moment and stress transmitted to the subsea wellhead have been obtained. Comparing the theoretical calculation results with the numerical simulation results, the calculation accuracy is 93.3%. Subsequently, through sensitivity analysis and orthogonal experiments, the influence factors of the mechanical characteristics of the subsea wellhead have been discussed, and the main controlling factors affecting the mechanical characteristics of the subsea wellhead have been obtained;

(2) In the future, in order to further verify the reliability of the theoretical model, indoor testing or ocean tests can be carried out subsequently to obtain real subsea wellhead mechanical-response results. By comparing the test results with the theoretical calculation results, the confidence of the theoretical model can be increased;

(3) This research can lay the foundation for developing independent mechanical analysis software for the deepwater subsea wellhead system, and ultimately achieve application in deepwater drilling engineering.

Author Contributions: Conceptualization, Y.W. and J.W.; methodology, J.W. and Y.W.; validation, J.W., R.L. and L.G.; formal analysis, J.W.; investigation, J.W. and Y.W.; resources, Y.W. and D.G.; writing—original draft preparation, J.W.; writing—review and editing, Y.W.; supervision, project administration and funding acquisition, D.G. All authors have read and agreed to the published version of the manuscript.

Funding: This research was funded by the Natural Science Foundation of China (grant no. 52322110 and grant no. 52074310). This research was also funded by the Science Foundation of China University of Petroleum, Beijing (grant no. 2462021QNXZ006). This research was also funded by the Ministry of Industry and Information Technology (grant no. CJ05N20).

Institutional Review Board Statement: Not applicable.

Informed Consent Statement: Not applicable.

Data Availability Statement: Not applicable.

Acknowledgments: The authors would like to thank the editors and reviewers for their many constructive suggestions and comments that helped improve the quality of the paper.

Conflicts of Interest: The authors declare that we do not have any commercial or associative interest that represent a conflict of interest in connection with the work submitted.

Nomenclature

BOP	Blowout preventer
E	Elastic modulus of the riser, Pa
I	Inertia moment of the riser, m^4
$y(x,t)$	Lateral displacement of the riser, m
x	Axial length of the riser, m
$f(x,t)$	Wave current force on the riser, N/m
$T(x)$	Axial tension of the riser per length, N/m
M	Total weight of the riser per length, kg/m
$S(t)$	Dynamic motion of the floating platform, m
K_1	Rotational stiffness of the upper flexible joint, N·m/rad
K_2	Rotational stiffness of the lower flexible joint, N·m/rad
L	Riser length, m
W_s	Weight of the riser in seawater, N
f_wt	Submersion coefficient, which is 1.05 in this paper
B_n	Buoyancy force of the buoyancy joint, N
f_bt	Effective coefficient, which is 0.96 in this paper
A_i	Area of the riser inner diameter, m^2
ρ_m	Density of the drilling fluid, kg/m^3
ρ_w	Density of seawater, kg/m^3
I_a	Inertia moment of the riser auxiliary pipelines, m^4
m_a	Weight of the auxiliary pipelines per length, kg/m
a	Number of kill lines, dimensionless
D_1	Outer diameter of the kill lines, m
d_1	Inner diameter of the kill lines, m
b	Number of hydraulic lines, dimensionless
D_2	Outer diameter of the hydraulic lines, m
d_2	Inner diameter of the hydraulic lines, m
c	Number of choke lines, dimensionless
D_3	Outer diameter of the choke lines, m
d_3	Inner diameter of the choke lines, m
e	Number of booster lines, dimensionless
D_4	Outer diameter of the booster lines, m
d_4	Inner diameter of the booster lines, m
α	Distance between the kill lines center and the y-axis, m
β	Distance between the hydraulic lines center and the y-axis, m
γ	Distance between the choke lines center and the y-axis, m
δ	Distance between the booster lines center and the y-axis, m
C_M	Inertial coefficient, dimensionless
C_D	Drag coefficient, dimensionless
v_c	Current velocity, m/s
v_w	Horizontal velocity of the wave particle, m/s
S_L	Amplitude drift of the platform, m
T_L	Drift period of the platform, s
S_0	Static offset of the platform, m
α_L	Phase angle of the drift motion, usually taken as 0
A_n	Amplitude of the random wave, m
k_n	Wave number, dimensionless
x_p	Horizontal position of the platform, m
ω_n	Wave circle frequency, rad/s
t	Time, s

φ_{n}	Phase angle of the wave, rad
F_{BOP}	Current force on the BOP, N
H_{BOP}	Height from the mud line to the center of gravity of the BOP, m
F_1	Current force on the lower flexible joint, N
H_1	Distance between the mud line and the lower flexible joint, m
M_1	Bending moment on the subsea wellhead transmitted from the riser, N·m
F_{well}	Current force on the subsea wellhead, N
H_{well}	Sludge height of the subsea wellhead, m
M	Total bending moment on the subsea wellhead, N·m
D_{F}	Diameter of the lower flexible joint, m
I_{well}	Inertia moment of the conductor, m^4
ρ_{s}	Density of the riser, $\mathrm{kg/m}^3$
A_{o}	Area of the riser outer diameter, m^2
A_F	Cross-sectional area of the auxiliary pipelines, m^2

References

1. Watson, P.A.; Iyoho, A.W.; Meize, R.A.; Kunning, J.R. Management Issues and Technical Experience in Deepwater and Ultra-Deepwater Drilling. In Proceedings of the Offshore Technology Conference, Houston, TX, USA, 2–5 May 2005. [CrossRef]
2. John, S.; William, D.; Rick, G.; Todd, D. More Ultradeepwater Drilling Problems. In Proceedings of the SPE/IADC Drilling Conference, Amsterdam, The Netherlands, 20–22 February 2007. [CrossRef]
3. Charlez, P.; Simondin, A. A Collection of Innovative Answers to Solve the Main Problematic Encountered When Drilling Deep Water Prospects. In Proceedings of the Offshore Technology Conference, Houston, TX, USA, 5–8 May 2003. [CrossRef]
4. Cunha, J.C. Innovative Design for Deepwater Exploratory Well. In Proceedings of the IADC/SPE Drilling Conference, Dallas, TX, USA, 2–4 March 2004. [CrossRef]
5. Yang, J.; Cao, S.J. Current situation and developing trend of petroleum drilling technologies in deep water. *Oil Drill. Prod. Technol.* **2008**, *30*, 10–13. [CrossRef]
6. Zhang, X.D.; Wang, H.J. Progress and outlook of deepwater drilling technologies. *Nat. Gas Ind.* **2010**, *30*, 46–48. [CrossRef]
7. Wang, Y.H.; Wang, W.H.; Jiang, X.X. South China sea deepwater drilling challenges and solutions. *Pet. Drill. Tech.* **2011**, *39*, 50–55. [CrossRef]
8. Yang, J.H. Overview of global deepwater drilling business. *Pet. Sci. Technol. Forum* **2014**, *33*, 46–50. [CrossRef]
9. Chen, G.M.; Liu, X.Q.; Chang, Y.J.; Xu, L.B. Advances in technology of deepwater drilling riser and wellhead. *J. China Univ. Pet. (Ed. Nat. Sci.)* **2013**, *37*, 129–139. [CrossRef]
10. Gao, D.L.; Wang, Y.B. Progress in tubular mechanics and design control techniques for deep-water drilling. *Pet. Sci. Bull.* **2016**, *1*, 61–80. [CrossRef]
11. Burke, B.G. An Analysis of Marine Risers for Deep Water. In Proceedings of the Offshore Technology Conference, Dallas, TX, USA, 29 April–2 May 1969. [CrossRef]
12. Egeland, O.; Wiik, T.; Natvig, B. Dynamic Analysis of Marine Risers. In Proceedings of the Offshore South East Asia Show, Singapore, Singapore, 9–12 February 1982. [CrossRef]
13. Tian, Q.L.; Huang, X.L.; Wang, J.S. Vortex-induced vibration of the riser with affiliated pipes based on discrete vortex method. *Chin. J. Hydrodyn.* **2016**, *31*, 633–640. [CrossRef]
14. Wu, W.; Wang, J.; Jiang, S.; Sheng, L. Flow and flow control modeling for a drilling riser system with auxiliary pipelines. *Ocean. Eng.* **2016**, *123*, 204–222. [CrossRef]
15. Han, C.J.; Guo, M.; Wang, X.X.; Yan, T. Research on lateral vibration mechanism of offshore drilling riser. *Control Instrum. Chem. Ind.* **2019**, *46*, 1028–1031.
16. Gao, H.; Li, X.Y.; Liu, F.; Ma, H.F.; Chen, Y. Mechanical behavior of riser in drilling and production vessels used for gas hydrate. *Nat. Gas Technol. Econ.* **2020**, *14*, 33–40.
17. Kong, T.T.; Wang, J.S.; Wu, W.B.; Xu, L.B.; Sheng, L.X.; Li, C.W. Two-dimensional numerical simulation of VIV for an actual drilling riser system considering auxiliary lines. *J. Vib. Shock.* **2021**, *40*, 15–22. [CrossRef]
18. Wang, X.L.; Liu, X.Q.; Zhang, N.; Li, Y.W.; Chang, Y.J.; Chen, G.M.; Xu, L.B.; Sheng, L.X.; Li, C.W. Improved recoil dynamic analysis of the deepwater riser system after emergency disconnection. *Appl. Ocean. Res.* **2021**, *113*, 102719. [CrossRef]
19. Yang, J.; Abimbola, F. Modal analysis of deepwater drilling riser in freestanding disconnected mode. *Ocean. Eng.* **2022**, *260*, 112001. [CrossRef]
20. Klaycham, K.; Athisakul, C.; Chucheepsakul, S. Large amplitude vibrations of a deepwater riser conveying oscillatory internal fluid flow. *Ocean. Eng.* **2020**, *217*, 107966. [CrossRef]
21. Zhang, N.; Chang, Y.; Shi, J.; Chen, G.; Zhang, S.; Cai, B. Fragility assessment approach of deepwater drilling risers subject to harsh environments using Bayesian regularization artificial neural network. *Ocean. Eng.* **2021**, *225*, 108793. [CrossRef]
22. Zhao, Y.; Sun, Y.; Zhang, B.; Han, Q.; Zhang, X. Recoil control of deepwater drilling riser systems via optimal control with feedforward mechanisms. *Ocean. Eng.* **2022**, *257*, 111690. [CrossRef]

23. Liu, X.; Liu, Z.; Wang, X.; Zhang, N.; Qu, N.; Chang, Y.; Chen, G. Recoil control of deepwater drilling riser system based on optimal control theory. *Ocean. Eng.* **2021**, *220*, 108473. [CrossRef]
24. Chen, K.; Huang, J.; Feng, C.; Han, X.Y.; Wei, M.J.; Xia, C.Y. Analysis on safe operation window of deepwater riser system. *J. Saf. Sci. Technol.* **2021**, *17*, 79–84. [CrossRef]
25. Wang, Y.; Gao, D. Influence of the damping matrix and mud discharge on the recoil response of deepwater drilling riser after emergency disconnection. *Ocean. Eng.* **2021**, *222*, 108591. [CrossRef]
26. Wang, Y.; Gao, D.; Fang, J. Static analysis of deep-water marine riser subjected to both axial and lateral forces in its installation. *J. Nat. Gas Sci. Eng.* **2014**, *19*, 84–908. [CrossRef]
27. Wang, Y.; Gao, D. On the static mechanics of the tubular system during installation of the surface casing in deepwater drilling. *Appl. Ocean. Res.* **2021**, *110*, 102599. [CrossRef]
28. Wang, Y.; Luan, T.; Gao, D.; Wang, J. Research progress on recoil analysis and control technology of deepwater drilling risers. *Energies* **2022**, *15*, 6897. [CrossRef]
29. Wang, Y.; Gao, D. Study on the marine environment limiting conditions of deepwater drilling for natural gas hydrate. *Appl. Energy* **2022**, *312*, 118802. [CrossRef]
30. Wang, Y.B.; Wang, J.D.; Gao, D.L.; Xin, S.L. Analysis of the effect of floating platform motion on the lateral dynamic characteristics of deepwater drilling riser during installation. *J. Northeast. Pet. Univ.* **2022**, *46*, 98–106.
31. Wang, Y.B.; Gao, D.L. Recoil response of deepwater drilling riser during emergency disconnection based on a multi-degrees-of-freedom system. *Acta Pet. Sin.* **2020**, *41*, 1259–1265. [CrossRef]
32. Argyroudis, S.; Mitoulis, S.; Hofer, L.; Zanini, M.; Tubaldi, E.; Frangopol, D. Resilience assessment framework for critical infrastructure in a multi-hazard environment: Case study on transport assets. *Sci. Total Environ.* **2020**, *714*, 136854. [CrossRef]
33. Mina, D.; Karapour, H.; Forcellini, D. Resilience of HP/HT pipelines to combined seismic and thermal loadings. *Ocean. Eng.* **2023**, *275*, 114098. [CrossRef]
34. Ouyang, M.; Wang, Z. Resilience assessment of interdependent infrastructure systems: With a focus on joint restoration modeling and analysis. *Reliab. Eng. Syst. Saf.* **2015**, *141*, 74–82. [CrossRef]
35. Zelaschi, C.; De, A.; Giardi, F.; Forcellini, D.; Monteiro, R.; Papadrakakis, M. Performance Based Earthquake Engineering Approach Applied to Bridges in a Road Network. In Proceedings of the 5th International Conference on ECCOMAS, Crete Island, Greece, 25–27 May 2015. [CrossRef]
36. Valka, W.A.; Fowler, J.R. The Design and Analysis of a TLP Subsea Wellhead. In Proceedings of the Offshore Technology Conference, Houston, TX, USA, 6–9 May 1985. [CrossRef]
37. Evans, J.; McGrail, J. An Evaluation of the Fatigue Performance of Subsea Wellhead Systems and Recommendations for Fatigue Enhancements. In Proceedings of the Offshore Technology Conference, Houston, TX, USA, 2–5 May 2011. [CrossRef]
38. Williams, D.; Ashton, P. Determination of the Effect of Second Order Motions of Moored MODU on Wellhead Fatigue. In Proceedings of the International Conference on Ocean, Offshore and Arctic Engineering, San Francisco, CA, USA, 8–13 June 2014. [CrossRef]
39. Williams, D. Calibration of Stress Transfer Function for Wellhead Fatigue. In Proceedings of the International Conference on Ocean, Offshore and Arctic Engineering, St. John's, NL, Canada, 31 May–5 June 2015. [CrossRef]
40. Pedro, R.; Hamilton, M.; Bhalla, K. Assessing Uncertainties in Wellhead System Fatigue Life Prediction. In Proceedings of the Offshore Technology Conference, Houston, TX, USA, 4–7 May 2015. [CrossRef]
41. *DNVGL-RP-E104*; Recommended Practice: Wellhead Fatigue Analysis. DNVGL: Oslo, Norway, 2018.
42. *DNVGL-RP-0142*; Recommended Practice: Wellhead Fatigue Analysis. DNVGL: Oslo, Norway, 2015.
43. Jaiswal, V.; Feng, L.; Saraswat, R.; Healy, B.; Horte, T.; Sharma, P. Fatigue Analysis of Non-rigid Locked Wellhead. In Proceedings of the International Ocean and Polar Engineering Conference, Rhodes, Greece, 26 June–1 July 2016.
44. Mcneill, S.; Agarwal, P.; Kluk, D.; Bhalla, K.; Young, R.; Burman, S.; Liapis, S.; Jain, S.; Jhingran, V.; Hodges, S.; et al. Subsea Wellhead and Riser Fatigue Monitoring in a Strong Surface and Submerged Current Environment. In Proceedings of the Offshore Technology Conference, Houston, TX, USA, 5–8 May 2014. [CrossRef]
45. Mcneill, S.; Agarwal, P.; Kluk, D.; Bhalla, K. Exploring the Benefits of Wellhead Fatigue Monitoring. In Proceedings of the Offshore Technology Conference, Houston, TX, USA, 4–7 May 2015. [CrossRef]
46. Mcneill, S.; Agarwal, P.; Bhalla, K.; Ge, M.; Leonard, J. Wellhead Fatigue Monitoring During Subsea Well Plug and Abandonment Activities. In Proceedings of the Offshore Technology Conference, Houston, TX, USA, 1–4 May 2017. [CrossRef]
47. Li, Z.; Gong, D.W.; Guo, Y.B.; Chen, H.D.; Liu, H.X.; Zhao, X.Z. Mechanical analysis of the wave-induced fatigue in the subsea wellhead. *Offshore Oil* **2019**, *39*, 90–96. [CrossRef]
48. Wang, Y.; Li, Z.; Luo, W.; Wang, W.; Yang, J.; Li, J.; Sun, H.; Wang, J. Fatigue life prediction method for subsea wellhead welds based on the nonlinear fatigue accumulation model. *Ocean. Eng.* **2022**, *248*, 110828. [CrossRef]
49. Li, J.; Chang, Y.; Xiu, Z.; Liu, H.; Xue, A.; Chen, G.; Xu, L.; Sheng, L. A local stress-strain approach for fatigue damage prediction of subsea wellhead system based on semi-decoupled model. *Appl. Ocean. Res.* **2020**, *102*, 102306. [CrossRef]
50. Chen, G.M.; Li, J.Y.; Chang, Y.J.; Wang, K.; Xiu, Z.X.; Liu, H.L.; Xu, L.B.; Sheng, L.X. Influencing factors for fatigue damage of underwater wellhead system of deepwater oil and gas. *Acta Pet. Sin.* **2019**, *40*, 141–151. [CrossRef]
51. Pestana, R.; Roveri, F.; Franciss, R.; Ellwanger, G. Marine riser emergency disconnection analysis using scalar elements for tensioner modelling. *Appl. Ocean. Res.* **2016**, *59*, 83–92. [CrossRef]

52. Wang, Y.; Gao, D. Mechanical analysis on recoil response of deepwater drilling riser based on a complex mode method. *J. China Univ. Pet.* **2020**, *44*, 58–63. [CrossRef]
53. Mai, T.; Hyeung, S.; Jinil, K.; Dae, H.; Sang, K. A study on hovering motion of the underwater vehicle with umbilical cable. *Ocean. Eng.* **2017**, *135*, 137–157. [CrossRef]
54. Mai, T.; Mien, V.; Duc, H.; Quang, T.; Tuan, T.; Sang, D.; Hyeung, S. Study on dynamic behavior of unmanned surface vehicle-linked unmanned underwater vehicle system for underwater exploration. *Sensors* **2020**, *20*, 1329. [CrossRef]
55. Wang, Y.; Gao, D.; Wang, J.; Ning, B. Investigation on influence of temperature and pressure on fatigue damage of subsea wellhead in deepwater drilling. *J. Pet. Sci. Eng.* **2022**, *212*, 110328. [CrossRef]
56. Wang, Y.B.; Zeng, J.; Gao, D.L. Effect of annular pressure on the fatigue damage of deepwater subsea wellheads. *Nat. Gas Ind.* **2020**, *40*, 116–123. [CrossRef]
57. Wang, Y.; Gao, D.; Fang, J. Finite element analysis of deepwater conductor bearing capacity to analyze the subsea wellhead stability with consideration of contact interface models between pile and soil. *J. Pet. Sci. Eng.* **2015**, *126*, 48–54. [CrossRef]
58. Wang, Y.B. Research on Mechanical Behavior of Deepwater Conductor and Drilling Riser in Installations. Ph.D. Thesis, China University of Petroleum, Beijing, China, 2016.
59. Zhou, R.X.; Zhou, B.; Li, L.; Wang, K.J.; Wang, J.X.; Yang, Y.M. Influence of the top tension of riser on the stability of subsea wellhead system. *Oil Drill. Prod. Technol.* **2018**, *40*, 98–100. [CrossRef]
60. Wang, P. Dynamic Response and Mechanical Coupling Behavior of Deep Water Riser System. Ph.D. Thesis, Northeast Petroleum University, Daqing, China, 2014.
61. Wang, S.Q.; Liang, B.C. *Wave Mechanics for Ocean Engineering*, 1st ed.; China Ocean University Press: Qingdao, China, 2013.
62. Sexton, R.M.; Agbezuge, L.K. Random Wave and Vessel Motion Effects on Drilling Riser Dynamics. In Proceedings of the Offshore Technology Conference, Dallas, TX, USA, 3–6 May 1976. [CrossRef]

MDPI AG
Grosspeteranlage 5
4052 Basel
Switzerland
Tel.: +41 61 683 77 34

Journal of Marine Science and Engineering Editorial Office
E-mail: jmse@mdpi.com
www.mdpi.com/journal/jmse

Academic Open
Access Publishing

mdpi.com

ISBN 978-3-7258-6453-9